Experiments in a turbine cascade for the validation of turbulence and transition models

Moore, H

Moore, H (1995) *Experiments in a turbine cascade for the validation of turbulence and transition models*, Durham theses, Durham University. Available at Durham E-Theses Online: http://etheses.dur.ac.uk/5356/

Experiments In A Turbine Cascade For The Validation Of Turbulence And Transition Models

by

H. Moore

A Thesis submitted in partial fulfilment
of the requirements for the degree of
Doctor of Philosophy

School of Engineering and Computer Sciences

The University of Durham
1995

Declaration

The work contained in this thesis has not been submitted elsewhere for any other degree or qualification, and unless otherwise referenced it is the author's own work.

Big whirls have little whirls
That feed off their velocity;
And little whirls have smaller whirls
And so on to viscosity.

L.F. Richardson (1926)

Acknowledgements

I am most grateful to my supervisor Dr. David Gregory–Smith whose guidance and encouragement have been of great help throughout this project.

I would also like to thank all the staff in the school of Engineering who have provided assistance to me during my period as a research student. In particular thanks must go to Mr. Ray Mand and Mr. Michael Page in the thermodynamics laboratory, all the technicians in the mechanical and electrical workshops who built pieces of apparatus for me and to Mr. Trevor Nancarrow for his support in the use of the departmental computer network.

The help of Mr. John Coupland and other members of the Aerothermal methods group at Rolls–Royce, Derby is also much appreciated. In particular, their assistance in exporting and running Rolls–Royce software has been of great value.

Finally, the financial support of Rolls–Royce Plc and the Engineering and Physical Sciences Research Council is also gratefully acknowledged.

Experiments In A Turbine Cascade For The Validation Of Turbulence And Transition Models

H. Moore

Abstract

This thesis presents a detailed investigation of the secondary flow and boundary layers in a large scale, linear cascade of high pressure turbine rotor blades. The puropose of the data is to provide a suitable test case to aid the design and validation of the turbulence and transition models used in computational fluid dynamics.

Hot–wire measurements have been made on a number of axial planes upstream, within and downstream of the blades to give both the mean flow conditions and all six components of Reynolds stress. Suitable inlet conditions have been defined at one axial chord upstream of the blade leading edge where the velocity and turbulence have been measured in both the freestream and endwall boundary layer. The turbulence dissipation rate has also been measured in order to define fully the inlet flow, a quantity that is usually missing in other data.

Measurements through the blade show that the turbulence generation associated with the secondary flows is considerable and that all three shear stress components are significant. Intermittency measurements close to the endwall and blade surfaces show that the boundary layers are mostly laminar or transitional. The new endwall boundary layer, that forms behind the separation line, was found to be initially laminar. On the suction surface transition occurs over the latter part of the blade and on the pressure surface the accelerating flow causes relaminarisation.

A number of calculations using a mixing length and high and low Reynolds number k–ϵ calculations show that reasonable overall results may be obtained. The lack, or failure, of transition modelling caused profile losses to be generally overpredicted and there was little evidence that the more sophisticated models produced better results. No model accurately predicted the individual turbulence quantities largely due to the inadequacy of the Boussinesq assumption for this type of flow. Good transition modelling appears to be more important than turbulence modelling in terms of the overall results.

Contents

LIST OF FIGURES

LIST OF TABLES

Nomenclature

C_{ax}	Blade axial chord
s	Blade pitch
h	Blade half span
U_1,U_2,U_3	Mean velocity components
u_1,u_2,u_3	Fluctuating velocity components (hot–wire coordinates)
u,v,w	Fluctuating velocity components (streamwise coordinates)
V_u	Inlet velocity
τ_w	Wall shear stress
C_f'	Local skin friction factor
δ^*	Displacement thichness
θ	Momentum thichness
H	Shape factor (δ^*/θ)
η	Intermittency
ρ	Density
μ	Laminar viscosity
μ_T	Turbulent viscosity
k	Turbulent kinetic energy
ϵ	Turbulent dissipation rate
L	Mixing length scale
L_∞	Freestream mixing length scale

Coefficients (defined in Appendix B)

C_{sk}	Secondary kinetic energy coefficient
C_{tk}	Turbulent k.e. coefficient
C_{ps}	Static pressure loss coefficient
C_{p0}	Total pressure loss coefficient
$C_{p0\infty}$	Mixed out total pressure loss coefficient

Three–dimensional CFD calculations

	Mixing length model
MLA	Coarse grid, fully turbulent, $L_\infty = 9.36mm$
MLB	Coarse grid, fully turbulent, $L_\infty = 0.936mm$
MLF	Fine grid, fully turbulent, $L_\infty = 0.936mm$
MLV	Coarse grid, laminar regions, $L_\infty = 0.936mm$

	k–ϵ model
KSS	Standard high Reynolds number
KSO	High Reynolds number with S–Ω modification
LSO	Low Reynolds number with S–Ω modification

(S–Ω modification due to Kato & Launder [1993])

Chapter I

Introduction

In the field of fluid mechanics increasing use is being made of computer based methods for the design of components. Within the gas turbine industry Computational Fluid Dynamics (CFD) is now used for the design and analysis of all major engine components – intakes, nacelles, fans, compressor blading, combustion chambers, turbine blading, turbine cooling systems, mixers and exhausts and wing–engine installations. Its use enables engine design to be undertaken in a shorter time, at reduced cost, and to increasingly demanding specifications in terms of efficiency, component life, pollutant emission levels, noise levels, etc.

In most engine components the fluid flow is complex and either partially or wholly turbulent. In compressors and turbines, in particular, the state of the flow and the location of transition are of crucial importance to the performance of the component so these must be accounted for in the CFD code. Since the Navier-Stokes equations represent the flow exactly they will, in principal, account for both phenomena but solving them directly is usually impractical for all but the simplest flows. This is because there are very small length and time scales associated with turbulent dissipation which implies the need for a very fine discretisation of the flow field and so is computationally very expensive.

Currently the most popular method of reducing the computational cost of CFD is to time average the Navier–Stokes equations and solve for the mean properties of the turbulence. As these vary more gradually than the instantaneous details, the discretisation can be less fine so fewer calculations are needed. The difficulty, however, is that time averaging introduces unknown second order correlations into the equations so that they no longer form a closed, soluable set. Equations may be derived for these unknowns but they, in turn, contain further unknown higher order correlations. This 'closure' problem is usually dealt with by approximating the unknowns with a number of empirical equations which attempt to model turbulence and sometimes transition.

Many models have been proposed of varying sophistication but those currently in use on a routine day–to–day basis are still fairly simple. This is partly due to the speed and cost of computer time and partly because of the limited level of knowledge and understanding of the physical processes involved. As increasing computer power allows more complex models to be used, their development requires detailed experimental data both to provide an insight into the physics involved and to test their performance. The aim of the current work is to provide such suitable data and to carry out some comparisons with existing models.

In general, the data used for validating CFD models should be representative of the type of flows that the code will be used to predict. The current work is directed towards external blading flows, so the experiments have been carried out in a linear cascade of High Pressure (HP) turbine rotor blades. This is a particularly suitable geometry for this task because it has a complex and highly three–dimensional flow with significant laminar, turbulent and transitional regions. Though simplified compared with engine compressors and turbines, the flow in a cascade still exhibits most of the important features and provides a severe test of CFD capabilities.

Whilst this type of flow has been the subject of much previous research, most has been aimed at understanding its nature rather than being suitable for the validation of CFD codes so the experimental results presented here will be unique. Rather than taking measurements over the whole of the flow, as has been done previously (e.g. Cleak [1989]), the current work concentrates on the boundary layer and secondary flow regions since these are the most difficult to predict. Secondary flows are large scale vortices generated by the turning of an initially sheared flow and are found in the endwall regions of the blade row. They are responsible for a significant proportion of the generated loss and also produce a non–uniform exit flow angle which, in a real machine, must be taken into account when designing subsequent blade rows.

The boundary layers also generate loss, the amount of which depends largely on their state (laminar or turbulent). This also has a considerable effect on the rate of heat transfer to the blades and endwalls, so is of particular interest to engine designers. Unfortunately one of the weaknesses of the simpler turbulence models currently used in CFD codes is that they are not capable of predicting transition.

It is, however, possible to specify its location and the effect this has on the results of a calculation using such a model has been examined. More sophisticated turbulence models are theoretically able to predict transition and one, the low Reynolds number k–ϵ model, has been tested. A variety of other calculations have also been made, the aim being to understand the effect of individual aspects of existing turbulence and transition models rather than to develop new models or, indeed, produce accurate results.

The structure of the remainder of this thesis is then as follows. First a general description of the flow in turbines is presented in Chapter 2 along with a review of the measurement techniques that may be used. This chapter also covers the flow prediction methods used in the design process and the data requirements for their validation. Chapter 3 gives a detailed description of the experimental apparatus and techniques. Chapter 4 then describes the measurements that have been taken and presents the experimental results. Next Chapters 5 & 6 describes the computational work and compares the results with the experimental ones. These are then discussed in Chapter 7 and finally some conclusions and recommendations for further work are given in Chapter 8.

Chapter II

Review of secondary flows and computational techniques

2.1 Introduction

This chapter reviews experimental investigations of the flow through a turbine blade row and the methods used to calculate such flows. The first section describes the main flow features, the mechanisms of loss generation and its distribution. This discussion is restricted mainly to the simplified flow found in linear cascades, though the differences between this and that found in a real turbine are also briefly covered. The intention is to highlight which areas of the flow are important with respect to loss production, and which require investigation in more detail.

The next two sections discuss the merits of various measurement techniques and the methods of calculating such flows. This latter section starts with a description of the traditional techniques used the initial design of blades before moving on to the various full, three–dimensional flow solvers used for the final design. Particular emphasis is given to the turbulence and transition models used within these codes since they have a big effect on their accuracy. Finally the data requirements for the validation of these models are discussed.

2.2 Description of secondary flows

2.2.1 Flow features in a turbine cascade

The flow through a turbine blade row is complicated and highly three–dimensional due to the presence of large regions of secondary flow. These are transverse velocity components which are produced when a non–uniform velocity profile is turned. They are of interest because of the variations they cause in the outlet flow angle and the losses they generate within the blade row (which may account for as much as half the total loss in a low aspect ratio cascade without a tip gap).

Over the last twenty years there have been many experimental investigations of the flow in turbine blade rows, for example: Marchal and Sieverding [1977], Langston, Nice, Hooper [1977], Gregory–Smith and Graves [1983] and Zunino, Ubaldi, Satta [1987]. In 1985 Sieverding [1985] summarised the results of previous studies and presented a detailed description of the secondary flow structure and its effect on boundary layers and loss growth. This structure is shown in *Figure 2.1* and the main features are briefly described below.

The passage vortex

The most dominant flow feature within the blade row is the passage vortex. It is generated by the cross–passage pressure gradient that is produced as the flow is turned by the blades. The pressure gradient produced by the 'freestream' flow is greater than that which would be produced by the slower moving fluid in the endwall boundary layer. To maintain this pressure gradient this boundary layer fluid must turn on a tighter radius and so migrates towards the blade suction surface. Since the fluid cannot collect in the corner, it then flows along the suction surface, away from the endwall, before returning back across the passage and to the endwall so setting up a circulation.

As it progresses through the cascade, the passage vortex grows in size and migrates towards the suction surface. It is initially centered close to the endwall but in the latter part of the cascade it begins to move up the suction surface away from the endwall (e.g. Gregory–Smith and Cleak [1990], Harrison [1989]). This movement then continues for some way downstream of the trailing edge as the vortex begins to decay (Kawai et al. [1985], Perdichizzi et al. [1992]).

The horseshoe vortex

Where the endwall boundary layer meets the leading edge of each blade a horseshoe vortex is formed with a leg that runs down each side of the blade. The pressure side leg rotates in the same sense as the passage vortex and crosses the blade passage to merge with it. Though the fluid in the pressure side leg of the horseshoe vortex has been shown to emerge from the blade row at the core of the passage vortex (e.g. Moore and Smith [1984], Sieverding and Van den Bosche [1983]) it is not believed that the horseshoe vortex initiates the passage vortex. Indeed, Turner

[1957] showed that the passage vortex develops even in the absence of an inlet boundary layer and Boyle et al. [1989] modified a turbine blade passage into a duct and found little change in the passage vortex. In both cases the horseshoe vortex does not form.

The suction side leg of the horseshoe vortex rotates in the opposite sense to the passage vortex and appears to be convected around it (e.g. the coloured smoke visualisations of Sieverding and Van den Bosche [1983]). Langston et al [1977] thought it remained in the suction surface/endwall corner whilst Marchal and Sieverding [1977] and Moore and Smith [1984] found it on the mid–span side of the passage vortex. Hence, the final location of this vortex is thought to depend on the strength of the passage vortex which, in turn, depends on the blading design and flow conditions.

Corner vortices

A further vortex may also be found in the corner between the endwall and blade suction surface. It exists between the endwall separation and suction surface reattachment lines due to the passage vortex and rotates in the opposite sense (see for example, Gregory–Smith and Graves [1983] who found it produces a reduction in overturning near the endwall). Endwall visualisation by Belik [1975] show the vortex to originate where the endwall crossflow is nearly perpendicular to the blade surface possibly implying that it is formed by a stagnation process similar to that which forms the horseshoe vortex. He also comments that a similar vortex may form in the endwall/pressure surface corner due to the downwash of the pressure surface boundary layer. This is not often reported, however, possibly due to its probable small size.

Shed vortices

Downstream of the cascade a final vortex is evident in the blade wake to the midspan side of the passage vortex. This shed vortex rotates in the opposite sense to the passage vortex and can crudely be thought of as resulting from the large radial component of velocity in the flow shed from the suction surface reacting with the much smaller (and opposite) component from the pressure surface. More formally it results from the trailing filament and trailing shed vorticity predicted by classical secondary flow theory (e.g. Hawthorn [1955], Came and Marsh [1974], Marsh [1976]). This theory gives an expression for the streamwise component of vorticity for a steady, inviscid flow which, downstream of a cascade, has three components.

The first of these is a distributed secondary circulation which is due to the turning of a non–uniform flow and, in turbomachinery, is generally called the passage vortex. The second is the trailing shed circulation, which arises from the spanwise variation of circulation around the blade, and the third is the trailing filament circulation. This is due to the stretching of the vortex filaments in the blade wake as those passing over the suction surface arrive at the trailing edge before the corresponding filaments that pass over the pressure surface. These latter two components then form a vortex sheet which rolls up to form the vortex that is visible in the blade wake.

Boundary layers

The effect these secondary flows have on the boundary layers is considerable, particularly on the endwall and blade suction surface. On the end wall the initial, relatively thick boundary layer is completely stripped away by the passage vortex and rolled up to form a loss core (Langston et al [1977]). Behind the separation line of the pressure side leg of the horseshoe vortex a new, thin and highly skewed boundary layer forms. Though most workers have found this too thin to determine its state, measurements by Harrison [1989] using hot–film gauges have shown it to be initially laminar except close to the blade suction surface where it is indistinguishable from the loss core. Transition of this new laminar boundary layer was found to occur near the trailing edge plane.

Measurements of the blade suction surface boundary layer have also been carried out by various researchers. Halstead, Okiishi and Wisler [1990] used a single hot–film sensor mounted on a mylar strip that was wrapped around the blade, thus allowing the sensor to be moved over the surface, to take detailed measurements of the boundary layer state. For a low level of inlet turbulence (Tu $< 1\%$) they found the boundary layer to be laminar until shortly after the point of maximum freestream velocity where separation occurred followed by a turbulent reattachment. Similar results were reported by Gregory–Smith, Graves and Walsh [1987] and Walsh and Gregory–Smith [1987] for two slightly different blade profiles using surface flow visualisation.

The low level of inlet turbulence used in these experiments is not, however, typical of a real turbine where turbulence would be much higher (Tu 4–7%). Halstead et al [1990] also reported results at these higher levels and found the same initially laminar boundary layer but this time followed by a region of natural transition rather than a separation bubble, as did Gregory–Smith and Cleak [1990]. Measurements of suction surface boundary layer profiles by Mee, Baines and Oldfield [1990] (using a pitot probe mounted on a traverse buried within the blade) again show similar results but with some indication of a small unsteady separation bubble.

A study of the importance of boundary layers and transition in gas turbine engines has been presented by Mayle [1991] and has been further discussed by Walker [1992]. Both highlight the importance of transition, particularly its effect on heat transfer and loss generation, and recommend further research into boundary layer flows. Cleak, Gregory–Smith and Birch [1991] have also shown that the assumed location of transition has a large effect on the results of computational predictions, so further demonstrating the importance of the boundary layer flows. Despite this there is still relatively little detailed data on the state of the boundary layers within blade rows (particularly velocity profiles) with which to compare the results of CFD calculations.

2.2.2 Loss generation and distribution

Classically losses in turbines are split into 'profile losses', 'secondary losses' and 'leakage losses'. Profile loss is the loss that would be generated by the blade profile in a purely two–dimensional flow such as is found well away from the endwalls. Secondary loss is that which arise from the secondary flows and leakage losses are those due to flow through any clearance gap between the blades and the endwall. Whilst the latter exists in real machines, cascades do not necessarily have tip gaps so it is often not present. The relative magnitudes of each of these three losses depends on the blading design but, in his review of loss mechanisms in turbomachines, Denton [1993] states that in many machines they are often approximately equal.

Profile loss

Profile loss is taken to be the loss away from the secondary flow regions so is an essentially two–dimensional feature. It is partly caused by the viscous dissipation of energy within the blade boundary layers and is very dependent on the boundary layer state. Denton [1993] shows that, at transitional Reynolds numbers, the dissipation in a turbulent boundary layer is between 2 and 5 times as large as in a laminar one and so concludes that boundary layer loss is dominated by the location of transition. Furthermore, he shows that the suction surface boundary layer is the dominant producer of loss.

There are two other sources of loss generation included in the profile loss, separation and trailing edge loss. Separation, if it occurs, causes losses to increase by an amount depending on the extent of the detached region (Schlicting [1978] p773). The larger the separation bubble the greater the loss. The trailing edge loss is due to turbulent mixing of the blade wake. For subsonic flow over a blade with a thick trailing edge it can contribute typically 1/3 of the total profile loss and for a supersonic flow this proportion can rise to about 50 percent (Mee et al. [1992]).

Secondary losses

Secondary losses are usually taken to include all the losses in the endwall region of a blade row and as such are sometimes called endwall losses. Upstream of the cascade the only loss is due to the endwall boundary layer which is generally turbulent and relatively thick. Downstream of the cascade the new endwall boundary layer is much thinner, though still containing loss, and there are three further loss cores due to the secondary flows (e.g. Langston et al. [1977], Gregory–Smith et al. [1988]), Gregory–Smith and Cleak [1990] and Zunino et al. [1987]). These loss cores are particularly evident in high turning cascades as these produce the strongest secondary flows.

The first loss core is located on the endwall and is due to the corner vortex that develops in the endwall/suction surface corner. The second loss core is associated with the passage vortex and is located away from the endwall and to the suction surface side of the blade wake. This is composed of fluid from the inlet endwall boundary layer and pressure side leg of the horseshoe vortex (Langston et al [1977] and Moore and Smith [1984]) along with extra loss from the passage walls within the blade row. The third loss core is found close to the blade wake on the midspan side of the passage vortex and is associated with the shed vortex.

All three loss regions also exhibit a high level of turbulence. Moore et al. [1987] studied the flow downstream of a replica of the UTRC cascade (Langston et al. [1977]) and discovered a peak level of turbulence of 25% of inlet velocity. Zunino et al. [1987] found 12% turbulence close to the throat of their rotor blade passage and a peak of 15% downstream of the cascade. Gregory–Smith et al. [1988]) found turbulence levels of 29% in the passage vortex core and Cleak [1989] found levels of 22% in a slightly different HP turbine rotor cascade. In each case, however, the turbulence level only accounts directly for a small proportion of the total loss (10–25%) but this is largely because its rate of dissipation is generally of the same order of magnitude as production (Tennekes and Lumley [1978]).

All the above measurements imply that the action of the secondary flows in rolling up the endwall boundary layer causes significant turbulence generation. Moore et al. [1987] used their measured Reynolds stresses to calculate the rate of production of turbulent kinetic energy and showed that this accounted for the majority of the secondary loss. Gregory–Smith and Cleak [1990] and Gregory–Smith and Biesinger [1992] carried out similar calculations (though they could not include all the terms) and found broad agreement. Both also found a considerable contribution from the normal stresses as well as the shear stresses and showed the effect of laminar viscosity to be minor.

Gregory–Smith and Cleak [1990] and Gregory–Smith and Biesinger [1992] also calculated the eddy viscosity for their two measured shear stresses ($\overline{vw}$ was not measured). Whilst Gregory–Smith and Cleak [1990] concluded that the eddy viscosity was fairly isotropic downstream of the blades, the more extensive measurements of Gregory–Smith and Biesinger [1992] showed that this was not the case within the blade passage and, indeed, found regions of negative eddy viscosity. This and the contribution of normal stresses have considerable implications for the prediction of turbulence, and hence losses, since neither are allowed for by the Boussinesq eddy viscosity concept used in many turbulence models.

2.2.3 Real turbines

The above discussion has been restricted mainly to the simplified flow in low-speed, linear cascades. The flow in real turbines is significantly different as there are several other flow phenomena present. Probably the most obvious is that the blades are arranged radially in an annulus and that alternate rows rotate. This leads to a radial pressure gradient which causes low momentum fluid to migrate from casing to hub in fixed blade rows (and vice versa in rotating rows). Boletis [1984] investigated this effect in an annular cascade with the same blade profile as used by Marchal and Sieverding [1977] and found significant changes to the secondary flows and increased losses at the hub.

The relative motion between rotor and stator blades also means that annulus wall boundary layers will be skewed, relative to the mainstream flow, when crossing between them. In a turbine the direction of this skew is such as to reinforce the secondary flows and increase losses (e.g. Boletis [1984], Walsh and Gregory–Smith [1987]). The latter took took their measurements in a linear cascade with the skew produced by a moving endwall. They also investigated the effect of skewing in the opposite direction and found a significant reduction in the secondary flows and losses.

Another consequence of rotating blades is that they require a clearance gap between their tip and the endwall. Even if the blades are shrouded there is some flow through this gap which distorts the flow and increases losses (e.g. Bindon [1989]). Modern turbines may also be transonic and so will contain shocks with their associated losses. However, in turbines, these are usually oblique and weak (Denton and Cumpsty [1987]) so the losses will be small. More significant is their interaction with boundary layers where they can cause separation and induce transition.

Also, with the exception of the first blade row, the flow in a real turbine is unsteady due to the periodic shedding of wakes from upstream stages. In addition to this HP blades are often cooled due to the high temperature of the exhaust gasses from the combustor. This is achieved by circulating cooler air, bled from the compressor, through the engine core and blades. Some is also injected through holes in the blade and endwall surfaces to reduce heat transfer. Whilst all these phenomena can be modelled to some extent in a cascade, the effect they have on the flow is beyond the scope of the current work.

2.3 Measurement techniques

2.3.1 Pressure measurement

The most common type of measurement made in a flow is probably that of pressure. Single or multi–hole pitot probes provide a simple and accurate method of finding the flow velocity and are the only method of measuring losses. One of their main limitations, however, is they are larger than most other measuring devices so have lower resolution and can disturb the flow more. Distortion of the flow, however, is generally only significant close to walls, typically within 2 head diameters, (Treaster and Yocum [1979]) but does restrict their use to some extent. A second potential problem with pitot probes is that turbulence produces an over–reading of the total pressure (Dominy and Hodson [1992]) but the effect is only significant at high turbulence levels.

Whilst standard pitot probes are not suitable for unsteady measurements due to the damping effect of the column of air between the probe head and transducer, this can be achieved using miniature surface mounted transducers (e.g. Kulite transducers). An arrangement of several transducers on a traversable probe allows Reynolds stress measurements to be made with a comparable accuracy to more conventional hot–wire techniques (e.g. Ruck [1988]). The main drawbacks of the technique are poor spatial resolution and flow blockage due to the size of the probe which make it unsuitable for complex, rapidly varying flows. The probes are, however, considerably more robust than hot–wires so do have some applications.

2.3.2 Hot–wire anemometry

The hot–wire anemometer is probably still the instrument most widely used for unsteady flow measurement. Its design and principle of operation are described in, for example, Bradshaw [1975] and will not be repeated here (though see Appendix A which describes the technique used in this work). The hot–wire probes themselves, may have a variety of configurations with one, two or three sensors arranged at various angles or as surface mounted films. Their suitability for turbulence measurement is due to the small size of the sensing element (typically $5\mu m$ dia. and $1mm$ long) which gives the required features of rapid response, fine resolution and slight disturbance of the flow. The disadvantages are that the probes are fragile and prone to contamination by airborne particles and that complex analysis of the anemometer output is required.

This analysis usually follows a technique developed by Jørgensen [1971] who related the three components of velocity to an effective cooling velocity and hence to the wire voltage. For triple sensor probe this equation may be solved for the instantaneous velocity components (e.g. Lekakis, Adrian and Jones [1989]). For single sensor probes several readings must be taken with the wire at different angles and, since readings are taken at different times, the equations must be time averaged. This makes them harder to solve (usually requiring some assumptions to be made) and allows the use of a variety of different methods, e.g. Perdichizzi, Ubaldi and Zunino [1990] and Rodi [1975].

An alternative to using the Jørgensen equation is to carry out a direct calibration of the wire by recording its response at points over the whole range of flow velocities and angles. This produces a 'look–up' table which may then be used to find the mean flow velocity (and the Reynolds stresses for a triple wire probe). The advantage of the direct calibration methods are that they require no assumptions to be made about the response of the wire. Their disadvantage is that they usually require a large amount of data to be stored since first and second derivatives are often needed to interpolate between data points (though there are methods that do not require this e.g. Browne, Antonia and Chua [1989]). A combination of the two techniques (direct calibration and equation solving) may also be used to provide both mean flow and Reynolds stresses.

2.3.3 Other techniques

The first aerodynamic flow measurements can be traced back to Dr. Ludwig Mach who, in 1893, observed and photographed flows using silk threads, cigarette smoke and glowing iron particles. These techniques are all still in use today, smoke injection, in particular, is widely used (e.g. Mueller [1983]) and is now often combined with laser light sheets to show only the flow on a particular plane (Véret

[1983]). For boundary layer studies, surface flow visualisation, using tufts (Crowder [1982]), oil/dye mixtures (e.g. Stark and Bross [1995]) or liquid crystals (e.g. Mee et al [1991]) may be used. These give an indication of the boundary layer state, the location of transition and, in the latter case, heat transfer or skin friction.

A second category of flow visualisation techniques are those which rely on changes of refractive index due to changes in air density. Examples include interferometry, Schlieren photography and shadowgraphs (e.g Pankhurst and Holder [1968]). Though most suited to high speed flows, they can be applied to low speed flows in conjunction with spark discharges or some other method of changing the refractive index. Examples of the type of results that can be achieved by flow visualisation are given in Van Dyke [1982].

Historically, these methods have given only qualitative results but image processing techniques are beginning to allow some quantitative data to be obtained (Kobayashi et al. [1983], Balint et al. [1983]). Direct quantitative results may also be obtained from liquid crystals (Stinebring [1983]) and from smoke injection (Dominy [1990]). This latter technique is in many ways similar to tracer gas measurements (e.g. Moore and Smith [1984]) where the concentration of an injected gas is measured at points on a downstream plane. Whilst all these methods have their applications, better quantitative results are usually obtained from pressure measurement, hot–wire anemometry or various optical techniques.

Pressure measurement and hot–wire anemometry have been described in previous sections. One disadvantage of both techniques is that they are intrusive so disturb the flow to some extent. They are also unsuited to harsh conditions, such as combustion, which could damage the probes. Optical techniques, such as laser doppler anemometry, LDA, (Drain [1980]), laser two focus, LTF, (Schodl [1980]) and particle image velocimitry, PIV, (Adrian [1986] & [1991]) avoid these problems. They do, however, have disadvantages including the cost and complexity of the equipment, the need for a clear optical path and, sometimes, the need for seeding of the flow. For three–dimensional Reynolds stress measurements within a blade passage these can often outweigh the advantages, so making hot–wire anemometry the better choice.

2.4 Prediction of flow and losses

2.4.1 Theoretical and empirical methods

Early attempts at predicting the flow and losses in turbomachinery blading were based on empirical correlations derived from experimental data. Ainley and Mathieson [1951], for example, produced a correlation for the deviation of exit yaw angle in an axial turbine. They and many others have also proposed loss correlations, a number of which have been reviewed by Dunham [1970]. They all, however, only give a single, averaged value rather than any indication of the distribution and are of limited applicability due to the range of data from which they were derived.

Theoretical calculations of secondary flows have also been developed (Squire and Winter [1951], Hawthorn [1955]). These derive expressions for vorticity assuming an incompressible, inviscid flow with zero inlet vorticity and low turning. Hawthorn and Armstrong [1955] extended the theory slightly to calculate the spanwise variation of lift and circulation in a linear cascade of turbine blades and found fair agreement with experimental measurements. Since then the work has been considerably extended by a number of researchers and a good review has been given by Horlock and Lakshminarayana [1973]. More recently an alternative approach, based on Kelvin's Circulation Theroem, has been proposed (Came and Marsh [1974]) and extended to annular cascades (Glynn and Marsh [1980]).

Unlike the empirical correlations these calculations allow the spanwise distribution of exit yaw angle to be approximated but do not give the loss. Gregory–Smith [1982] added a loss model to the secondary flow calculation of Glynn and Marsh [1980] and obtained reasonable agreement with experimental results. This was further improved by modifying the calculation of vorticity to allow for convection of the Bernoulli (constant stagnation pressure) surfaces (Gregory–Smith and Okan [1991]) to give a technique suitable for use in the preliminary design of blading (Okan and Gregory–Smith [1992]). Alternative loss prediction methods have been described by Sharma and Butler [1986] and Harrison [1989].

2.4.2 Computational fluid dynamics

Computational fluid dynamics (CFD) deals with the numerical solution of the governing equations of fluid motion. To solve these equations (the unsteady Navier–Stokes equations) directly (direct numerical simulation, DNS) is usually impractical, due to the need for a very fine discretisation of the flow in both space and time, but has been achieved for simple flows (e.g. Rai and Moin [1991], Spalart [1988]). Large–eddy simulations similarly solve the unsteady Navier–Stokes equations but employ a low–level model for the small–scale turbulence (e.g. Yang and Voke [1993]). Excellent results may be obtained with these techniques, Yang and Voke [1993] for example, present results for a flat plate boundary layer that closely match measurements by Roach and Brierley [1992]. At present, however, their usefulness is restricted to providing a better understanding of the physics of turbulence and transition.

Practical CFD requires some approximations to be made to the Navier–Stokes equations in order to obtain solutions at acceptable cost. These approximations relate to the physics of the flow rather than those made in the discretisation of the equations and their subsequent numerical solution. Whilst these latter approximations can affect the stability, speed and accuracy of calculations, they will not be considered in any detail. A good introduction to the mathematics of CFD is given by Anderson [1986] and a comprehensive review of numerical techniques can be found in Hirsch [1990]. The remainder of this discussion will be restricted to the physical modelling of the flow since this clearly has a considerable effect on the performance of CFD calculations.

Approximations to the unsteady Navier–Stokes equations may be made at various levels. Increasing the number of approximations generally decreases the accuracy or applicability of the solution but increases its speed. Some common approximations are Reynolds averaging, where the equations are time averaged, thin layer Navier–Stokes, which neglect streamwise diffusion, the inviscid (Euler) equations, which neglect all viscous terms and potential flow models. Details of each are given by Lakshminarayana [1991] along with an assessment of various solution techniques. Reynolds averaging is currently the approach used for the detailed design of engine components, the other techniques though may be used in the earlier stages. Inviscid calculations, in particular, are often used as part of quasi–3D systems (e.g. Hirsch and Warzee [1979], Wang et al [1985]) which combine blade–to–blade and throughflow calculations to approximate the three–dimensional flow.

Turbulence modelling

The process of time averaging the Navier–Stokes equations introduces unknown second order correlations, the Reynolds stresses. Transport expressions may be derived for these stresses (e.g. Bradshaw et al [1981]) but they in turn contain triple correlations and equations for these contain higher orders still. This leads to the problem of 'closure' which is solved by approximating, or modelling, the unknown terms with a series of algebraic or partial differential equations. This turbulence modelling is a large and rapidly developing subject so no attempt will be made here to describe all the various types. Reviews of existing models may be found in Lakshminarayana [1986] (eddy viscosity models), Patel et al [1984] (low Reynolds number k–ϵ), Sieger et al [1992] (low Reynolds number k–ϵ) and So et al [1991] (second order closure).

Most of the more complex models are still computationally too expensive to be used on a day–to–day basis. In turbomachinery design most 3D calculations still use an algebraic mixing–length model such as Baldwin–Lomax [1978] (Coupland and Stow [1993], Dunham [1995]). The limitations of such models are well known (e.g. Lakshminarayana [1986]) but it is by no means clear that more sophisticated, higher order models produce better overall results (Dawes [1990], Gregory–Smith [1995]). Further evaluation of such models is required, as is the validation of new models, but these are hampered by the lack of suitable experimental data (Coupland and Stow [1993]). Whilst some data is available for two–dimensional flow (e.g Roach and Brierley [1992], Elazar and Shreeve [1989]) there is still a need for complex three–dimensional flow data typical of turbomachines (Lakshminarayana [1991]).

Transition modelling

The importance of transition on the flow in aeroengines has been described by Mayle [1991] and further discussed by Walker [1992]. Its location and extent has a significant effect both on aerodynamic loss and heat transfer so must be accounted for within CFD calculations. This is made difficult by the number of factors that affect transition. These include Reynolds number, freestream turbulence, pressure gradient, flow unsteadiness, surface curvature and surface roughness. Attempts have been made to produce empirical correlations for transition, such as that of

Abu–Ghannam and Shaw [1980], but these are limited by their range of applicability. A systematic evaluation of transitional models for turbomachinery flows is being carried out under the ERCOFTAC SIG (European Research Community On Flow Turbulence And Combustion; Special Interest Group) on Transition (see Savill [1994]).

The simpler turbulence models, such as mixing length, cannot predict transition so its location and extent must be prescribed. More sophisticated models however can, the most commonly used being the low Reynolds number k–ϵ formulations. Sieger et al [1993] evaluated a number of these models for their ability to predict transition and found the best results were obtained using the Lam–Bremhorst [1981] model and its PTM extension (Schmidt and Patankar [1988]). Other studies (Patel et al [1984], Savill [1993]) have found the Launder–Sharma [1974] model to give the best overall results. Transition has also been predicted with varying success using one–equation and Reynolds stress transport models, large eddy simulation and direct numerical simulation (Savill [1993]). The latter, in particular, is often taken as producing better results than experimental measurements.

CFD codes

The governing equations of CFD may be formulated in two distinct ways by considering either a finite volume of the fluid or an infinitesimal fluid element. The former leads to the integral form of the equations and the latter to the differential form (e.g. Anderson [1986]). Discretisation of the integral form of these equations leads to finite volume techniques (such as Hah [1984]) whilst the differential form leads to finite difference methods (e.g. Chima [1985]). There is also a third approach, finite element (e.g. Laskaris [1975]), though this is not as widely used as the other two.

The discretised equations are usually solved by one of two main methods, time marching or pressure correction. In time marching techniques (e.g. Denton [1975], Dawes [1991]) the unsteady terms in the Navier–Stokes equations are retained, even if only the steady solution is required, so the equations are hyperbolic for all types of flow. An initial guess is then made and the calculation is marched forwards in time until the boundary conditions cause the solution to settle to a steady state. Many schemes have been developed to do this, such as MacCormack

& Crank–Nicolson (e.g. Anderson [1986]) and may be classed as explicit or implicit depending on the type of discretisation used.

Explicit solvers (such as Denton [1975]) are relatively simple (since any value at time n depends only values at time $n-1$) but must use small time steps in order to remain stable and so may be slow to converge. Implicit methods allow larger time steps but are more complicated (any value at time n depends on other values at time n so the whole flowfield must be solved for at once) and so need to make more calculations per step. If only the steady state solution is required, convergence of explicit techniques may be accelerated by the use of different time steps for each control volume. Alternatively a multigrid technique (e.g. Denton [1982]) may be used where calculations are initially carried out on a 'coarse grid' before moving to more refined grids after the initial large transients have been removed.

One limitation of either time marching technique, however, is that they are not suitable for incompressible flows (Lakshminarayana [1991]). This is because they solve for density which remains virtually constant at low Mach numbers. This problem is most commonly overcome by running low speed calculations at an elevated Mach number (typically $\sim$ 0.3). Alternatively the problem may be coped with by making modifications to the algorithm such as in the pseudo–compressibility technique of Chorin [1967].

In pressure correction methods (such as Hah [1984] & Moore and Moore [1985]) the pressure field is first assumed and then updated using an auxiliary equation. At each step the velocity field is found by solving the momentum equation but does not initially satisfy continuity so a correction is made to the pressure by solving the auxiliary equation. The velocity field is then re–calculated and the process is repeated until the pressure correction is sufficiently small. There are many variations on this basic method some of which are reviewed by Lakshminarayana [1991]. Unlike the time marching techniques, pressure correction codes are suited to low speed, incompressible flows and so are more suitable for the current work.

2.5 Code validation

Before any new CFD code or turbulence model can be used with confidence its performance must be validated against detailed experimental data. Development and initial testing is usually carried out against simple two–dimensional flows such as that over flat plates (e.g. Roach and Brierley [1992]). The results of direct numerical simulations and large eddy simulations may also be used to refine the turbulence and transition models, for example, Yang et al [1994]. For complete testing, however, complex three–dimensional flows must be modelled. Ideally these tests would cover the range of conditions, Reynolds number, freestream turbulence level, etc., found in the types of flow the code will eventually be used to predict.

For turbomachinery flows much of the data needed can be obtained from large–scale cascade tests, though rotating rig measurements would be needed for centrifugal effects. Whilst many studies of this type of flow have been made (see section 2.2), most are incomplete in terms of the information needed for code validation. Most commonly the inlet conditions are not sufficiently well defined or there is a lack of detail of the flow within the boundary layers. The need for further measurements of this type of flow, specifically for validation purposes, has been identified by Lakshminarayana [1991] and Coupland and Stow [1993] amongst others.

The data requirements for steady three–dimensional blading flows can be summarised as follows (Coupland [1992]). At inlet (which must be defined well upstream of the leading edge) the freestream velocity, turbulent stresses and length scale must be provided along with the boundary layer velocity and turbulence profiles. On the blade surfaces the static pressure distribution, skin friction and/or heat transfer are required. Within the blade passage, particularly within the boundary layers and secondary flow region, the normal and shear stress are needed along with the velocity and pressure distributions. Downstream of the blades area traverses are required of total and static pressure, velocity and turbulent stresses. Whilst not exhaustive, this list does give an indication of the amount of detail required for full code validation.

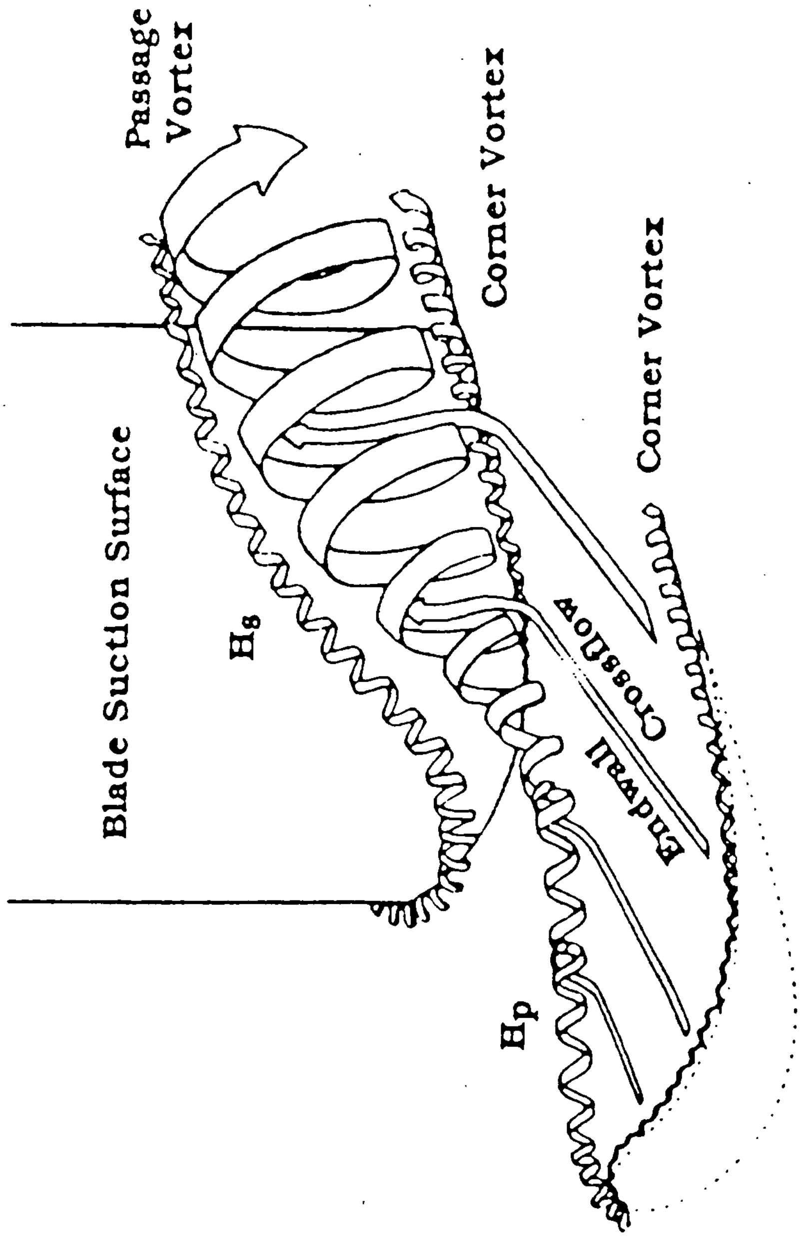

Figure 2.1 — Secondary flow structure (from Kawai et al [1989]).

Chapter III

Experimental apparatus and methods

3.1 Introduction

This chapter describes the apparatus, instrumentation and methods used to obtain the experimental data presented in this thesis. Since the current work forms part of a continuing program of turbomachinery flows at Durham University much of the apparatus has been used and described by previous workers. Graves [1985] started the work with a study of secondary flows and losses in a turbine cascade. This was followed by Walsh [1987] who studied the effect of inlet skew in the endwall boundary layer on the development of secondary flows. The boundary layer skew was created by replacing part of the working section endwall with a moving belt. He also replaced the entire cascade and changed the blade profile.

Cleak [1989] then took a series of measurements through the cascade and used them to validate various three–dimensional viscous calculations. He also added a turbulence grid to make the inlet turbulence more representative of that found in an actual high pressure turbine. Next Beisinger [1993] investigated methods of reducing secondary flows and experimented with injecting air tangentially into the endwall boundary layer. In order to do this he, again modified the cascade, this time to include an injection slot just upstream of the blade leading edge.

The present author has also made several modifications to the apparatus but rather than just describing these changes, as previous authors have, a full description of the equipment will be given here. This is done in the interest of clarity and to avoid any confusion as to the current state of the apparatus.

3.2 The Durham low speed wind tunnel

Air supply

The main piece of apparatus consists of a cascade of blades mounted on the exit of a large, low–speed, blowing wind tunnel. The air is supplied by a double entry centrifugal fan (Keith Blackman Series 28) driven by a variable speed motor (Fuller KB25). The fan and motor are enclosed in a housing, three of whose walls each contain six 457mm square Vokes general purpose filters. These remove dirt and dust from the air which might otherwise contaminate instrumentation, particularly hot–wires. Air from the fan first passes down a short parallel walled section and then enters a large settling chamber through a diffuser containing 5 gauze screens. The flow is then accelerated through a contraction, to produce a uniform, high speed flow, before entering the rectangular, parallel walled working section via a honeycomb flow straightener.

The working section

The working section is shown diagramatically in *Figure 3.1*. It is initially 700mm high by 460mm wide but is reduced to 400mm wide by a false endwall which allows the existing tunnel boundary layer to be bled off. When used by Walsh [1987], this endwall consisted mainly of the moving belt he used to provide inlet skew. This had been taped down by more recent workers but was removed by the author and replaced by a smooth wall because it was thought that the edges of the belt, which 'flap' slightly, could significantly affect the endwall boundary layer.

Only one side of the wind tunnel has a false endwall to bleed off the boundary layer so the working section is slightly asymmetric. Accordingly, measurements are only taken in one half of the cascade, the other side providing access for the instrumentation. The boundary layer bleed is located close to the start of the working section, (1250mm upstream of the blade leading edge) its position originally being determined by the width of the belt. The false endwall has an elliptical leading edge with two static pressure tappings, one located on either surface, just behind it. An adjustable baffle partly covers the bleed slot and is positioned so that the pressure at both tappings is equal. This ensures that the boundary layer is removed cleanly without any separation on either surface.

The turbulence grid

Just upstream of the bleed there is a grid of bars designed (by Cleak [1989]) to raise the freestream turbulence level to a value more representative of that found in actual gas turbines. Its position was, again, fixed by the presence of the belt which meant that it could not easily be located any closer to the blades.

The grid is made up of $25mm$ diameter bars spaced at $80mm$ when measured in a plane perpendicular to the flow. There is also an additional $8mm$ diameter bar located $25mm$ from the endwall. This fills in the gap between the grid and endwall just upstream of the bleed and was needed to stop a 'jet' effect in the flow close to the endwall. The grid is set parallel to the leading edge plane, so that it is a constant distance ($1400mm$) from the blades, (as is the boundary layer bleed) which means that it is at an angle to the flow ($42.75°$). One effect of this is that it causes a slight deflection of the flow but this was thought to be better than having an unequal level of turbulence across the blade pitch.

The advantages of locating the turbulence grid so far upstream of the blades are that there should be sufficient time for the jets of flow between the bars to thoroughly mix out and for the turbulence to become isotropic. The large distance should also prevent significant decay of turbulence within the blade passage but does mean that the turbulence generated by the grid must be considerable to avoid it decaying too much by the time it reaches the blades. The predicted turbulence characteristics at the blade leading edge (estimated by the method reported by Roach [1987]) are given in the table below.

	Streamwise direction	Orthogonal directions
Turbulence intensity	4.6%	4.1%
Macro/Integral scale	$38mm$	$19mm$
Micro/Dissipation scale	$4.4mm$	$3.1mm$

Table 3.1 — Predicted inlet turbulence characteristics

Instrumentation

In order to measure the velocity in the working section a pitot–static probe is located at mid–height, $700mm$ upstream of the leading edge. In addition to this, three slots have been added to allow instrumentation upstream of the blades (see *Figure 3.2*). The slots are each $250mm$ long by $12mm$ wide and are aligned parallel to the working section. Their downstream ends are $172mm$ upstream of the blade leading edge plane and each is aligned with a different position relative to the bars of the turbulence grid. Their location was chosen to allow measurements to be taken at one axial chord upstream of the blades which may then be used as the inlet conditions for CFD calculations. Their different alignments relative to the bars of the turbulence grid is to allow the uniformity of the turbulence to be checked.

3.3 The Durham linear cascade

Geometry

The cascade is mounted on the exit of the wind tunnel and exhausts to the atmosphere. It consists of six high pressure rotor blades with a profile (*Figure 3.2*) based on the RT60 model turbine but modified slightly for operation at low speed. The purpose of this was to give a similar aerodynamic behaviour at low speed as the RT60 profile gives at transonic speeds. The blades are cast in epoxy resin from an aluminium master using a technique similar to that of Gregory–Smith and Marsh [1971]. Full details are found in Walsh [1987] but the critical design parameters are reproduced below.

Inlet Dynamic Head	215Pa
Design inlet Flow Angle	42.75°
Blade Exit Angle	−68.7°
Blade Chord	$224mm$
Blade Axial Chord	$181mm$
Blade Pitch	$191mm$
Blade Half-Span	$200mm$
Zweifel loading coefficient	0.97
Reynolds Number (C_{ax} and V_{exit})	4.3×10^5

Table 3.2 — Cascade design data

One endwall of the cascade contains eleven tangential traverse slots, through which various probes may enter the cascade, (*Figure 3.2*) whilst the other consists mainly of a perspex plate. Both the plate and the traverse slots are aligned with the central blade passage where all measurements are taken. Four of the slots are located outside the blade passage and cover slightly more than one pitch, whilst the remainder run from blade to blade. When not in use, the slots are closed off by wooden inserts that fit flush to the inside of the endwall and when in use they are covered by a pair of flexible brushes to reduce leakage whilst still allowing the probe to move.

Blade pressure tappings

Two of the blades are instrumented with static pressure tappings. These take the form of hypodermic tubing laid just below the surface with holes drilled into them at several spanwise locations. When in use all but one set of holes are covered with thin tape. There are 14 tappings on the suction surface and 10 on the pressure surface at each of 6 spanwise locations. Little use has been made of these tappings as the pressure distribution has been measured previously by Cleak [1989].

Operating conditions

To ensure consistent results the cascade is operated at constant Reynolds number taken from a 'standard day' set of atmospheric conditions. Variation from these conditions are corrected for by adjusting the upstream dynamic head and correcting all measurements relative to this. The 'standard day' conditions are given in the table below.

Density of air	1.179 kg/m^3
Ambient temperature	19.0°C
Dynamic viscosity	1.814×10^{-5} Ns/m^2

Table 3.3 — Standard day conditions

3.4 Instrumentation

3.4.1 The traverse

The main instrumentation is mounted on a traverse unit originally constructed by

Graves [1985] but modified several times since. It consists of a pair of linear slides (Time and Precision 'Unislide' series A) one mounted on the other (*Figure 3.3*). The fixed slide is mounted on a back plate which in turn is clamped to two 'T' slotted mounting brackets. These brackets may be bolted onto either the cascade or the wind tunnel working section, allowing the traverse to be used in all the access slots. The fixed slide provides motion along the slots, which is tangentially in the cascade slots and streamwise in the upstream slots, whilst the other slide provides spanwise movement.

Both slides are of the leadscrew type with a $1mm$ pitch and each is driven by a Mclennan HS23 stepper motor. These produce 200 steps per revolution giving a linear step size of $0.005mm$. To hold the probes themselves, either a motorised or a manual rotary stage may be mounted on the spanwise traverse. The motorised stage (Time and Precision A375TSP) is driven by a 200 step per revolution stepper motor with a 90:1 gear ratio giving an angular resolution of 0.02°. The manual (Time and Precision A375TS) stage has a vernier scale which gives a possible resolution of 5/60°.

3.4.2 The probes

Various probes may be mounted on the rotary stages, the most common being hot–wire probes and three and five–hole pitot probes. Three different probes have been used in the current work, two hot–wire probes and a three–hole pitot probe.

The rotatable single wire probe

Most of the measurements have been taken using the hot–wire probe shown in *Figure 3.4*. It consists of a hollow probe support, mounted in the rotary stage, which is usually free to slide and rotate in an outer sleeve. The hot–wire probe is mounted coaxially on the end of the support so can be moved tangentially, radially and be rotated about its axis by the traverse. The outer sleeve may be clamped to the probe support to increase its stiffness and reduce vibration but for measurements close to the endwall a better method is to use the locating pin. This fits to the sleeve and presses against the endwall to provide support at both ends of the probe rather than just one. It is more effective at reducing vibration but does restrict the area over which the wire may be traversed.

One limitation of this probe is that that its diameter restricts how close to the blade surfaces the hot–wires may be located. This is particularly bad close to the trailing edge where the blade surfaces are at an acute angle to the traverse slots. Here, when the probe is as close to the surface as possible, the wire may still be several tens of millimeters away, measured in the tangential direction (though the shortest distance to the surface is much smaller). This results in an apparently large gap between measured data and the blade surface when presenting results on an axial plane. Though this problem is relatively minor, having the hot–wire aligned with the axis of the probe does mean that it can never be held close enough to the surface to take measurements within the blade boundary layers.

The cranked single wire probe

In order to measure close to the blade surfaces a second, cranked, hot–wire probe is used (see *Figure 3.5*). This has a solid probe support, for stiffness, with the probe holder mounted at 45° to the spanwise direction. It is used in conjunction with a slanted wire probe (Dantec 55P02) so that the sensing element is parallel to the blade surface. As with the other hot–wire probe a locating pin is used to reduce vibration but in this case it presses against the blade rather than the endwall. The limitation of this probe is that the hot–wire cannot be rotated so cannot be used to measure the Reynolds stresses. It is only used for the measurement of intermittency in the blade surface boundary layers.

The three–hole pitot probe

A three–hole pitot probe has been used to measure the midspan yaw angle within the cascade. It is a cranked probe with a conical head of 1/4" dia. and an included angle of 60°. The head is aligned with the axis of the probe so that it remains stationary in space when rotated by the traverse. The two outer tappings are connected across an oil filled micro–manometer and the yaw angle is measured by rotating the probe until the pressure difference is zero. An initial calibration showed the pressure difference between the tappings to vary almost linearly with angle at 15.5 Pa (2.0mm) per degree over the range of ±20°.

3.4.3 Control and data acquisition

Traverse control

The traverse is controlled from a 386PC using various add–on circuit boards. Each stepper motor is driven by a 4 phase bipolar driver board (RS 342–051) which are in turn controlled from a 48 channel Input/Output board (Amplicon Liveline PC14AT) installed in the computer. The motors are driven in half step mode and are accelerated and decelerated slowly to ensure accuracy of movement. A typical traverse will return the probe to within 2 steps ($0.01mm$) of its original start point.

The I/O board is also used to control a servo–valve (RS 723–674) which links the upstream pitot–static probe to a pressure transducer (CMR 200–008) to monitor the inlet dynamic head. The valve switches both sides of the transducer to the same pressure to allow the zero offset to be measured. This is necessary to keep the transducer in calibration during long experiments (for accuracy the transducer is calibrated against a micro–manometer rather than assuming a linear output) since its offset varies slightly with temperature. Depending on the type of traverse the offset is measured at between 5 and 20 minute intervals. It could be measured before each individual hot–wire measurement but this would considerably increase the traverse time and is much more frequent than necessary.

Data acquisition

Data acquisition is carried out using one of two Analog to Digital (A/D) converters. Both have 12 bit resolution and take a ±5V input. The standard one (PC–LabCard PCL–812PG) will sample 16 channels at speeds of up to 30kHz. Normally only two channels are used, one to monitor the inlet dynamic head and the other to take readings from a single hot–wire. The second A/D converter (Strawberry Tree Inc. Flash–12) is used where higher sampling rates are required and operates at speeds of up to 1MHz. Its main use is for measurements of intermittency within boundary layers.

The hot–wire equipment itself consists of a TSI IFA–100 control unit used in conjunction with Dantec gold plated hot–wires. The control unit contains three channels each consisting of a MODEL 150 constant temperature anemometer and a MODEL 157 signal conditioner, though only one channel is used. In addition to normal probe operation, the anemometer allows the cable and probe resistances to be measured, the operating resistance to be set and the frequency response to be optimised. The signal conditioner applies an offset and gain to the output signal to amplify it to a level suitable for input to the A/D converter. The offset approximately subtracts a voltage half way between the minimum and maximum to allow a large gain to be used (since only the fluctuating component is then amplified) and so improve the resolution of the signal.

Traversing and data acquisition have been automated as far as possible to speed up the taking of measurements. The only operation that still has to be carried out by hand is releasing the endwall locating pin, if it is used, to allow tangential movement of the probe. During a traverse, sampled data is only processed as far as is necessary to reduce storage requirements. This usually involves converting a set of A/D readings to a pressure or effective velocity (see next section) and calculating the mean and r.m.s. (root mean squared). These values are then saved to disk and transferred to a workstation for further processing. A typical traverse, however, will still take between three and seven hours to complete depending on the number of measurements it contains.

3.5 Hot–wire techniques

Two types of hot–wire measurements have been carried out, the first to give the full set of velocities and Reynolds stresses at a point and the second to measure intermittency. The former requires two traverses, each with a single rotatable wire and the latter a single measurement with a fixed wire. Both techniques are described below.

3.5.1 Reynolds stress measurement

Governing equations

Reynolds stress measurements are carried out using the rotatable single wire probe (*Figure 3.4*). If a hot–wire is held at a point in the flow and rotated about its axis the amount it is cooled varies with its angle to the flow. Taking several measurements at different angles then allows the flow velocity and Reynolds stresses to be determined. Though in theory enough information to do this can be gained from measurements with a single wire, the equations this produces are very ill conditioned and so, in practice, readings are taken from two separate probes with different wire configurations.

For the probe shown in *Figure 3.6* in a flow defined by the velocity vectors U_1, U_2 & U_3 the following equations may be derived by inserting exressions for these velocity components into the Jørgensen [1971] equation and expanding the various terms:

$$\overline{U}^2_{eff} = \overline{X}^2 + \overline{z^2} - \frac{1}{4\overline{X}^2}\overline{\left(\overline{Y}y\right)^2} \tag{3.1}$$

$$\overline{u^2_{eff}} = \frac{1}{\overline{X}^2}\left(B_1^2\overline{u_1^2} + B_2^2\overline{u_2^2} + B_3^2\overline{u_3^2} + 2B_1B_2\overline{u_1u_2} + 2B_1B_3\overline{u_1u_3} + 2B_2B_3\overline{u_2u_3}\right) \tag{3.2}$$

Where:

$$\overline{X}^2 = A_{11}\overline{U}_1^2 + A_{22}\overline{U}_2^2 + A_{33}\overline{U}_3^2 + A_{12}\overline{U}_1\overline{U}_2 + A_{13}\overline{U}_1\overline{U}_3 + A_{23}\overline{U}_2\overline{U}_3 \tag{3.3}$$

$$\begin{aligned}\overline{Y}y =& 2A_{11}\overline{U}_1u_1 + 2A_{22}\overline{U}_2u_2 + 2A_{33}\overline{U}_3u_3 + \\ & A_{12}(\overline{U}_1u_2 + \overline{U}_2u_1) + A_{13}(\overline{U}_1u_3 + \overline{U}_3u_1) + A_{23}(\overline{U}_2u_3 + \overline{U}_3u_2)\end{aligned} \tag{3.4}$$

$$\overline{z^2} = A_{11}\overline{u_1^2} + A_{22}\overline{u_2^2} + A_{33}\overline{u_3^2} + A_{12}\overline{u_1u_2} + A_{13}\overline{u_1u_3} + A_{23}\overline{u_2u_3} \tag{3.5}$$

And:

$$\begin{aligned}
A_{11} &= \cos^2\alpha + k^2\sin^2\alpha \\
A_{22} &= \cos^2\theta(\sin^2\alpha + k^2\cos^2\alpha) + h^2\sin^2\theta \\
A_{33} &= \sin^2\theta(\sin^2\alpha + k^2\cos^2\alpha) + h^2\cos^2\theta \\
A_{12} &= (1 - k^2)\sin 2\alpha\cos\theta \\
A_{13} &= (k^2 - 1)\sin 2\alpha\sin\theta \\
A_{23} &= \sin 2\theta(-\sin^2\alpha - k^2\cos^2\alpha + h^2)
\end{aligned} \tag{3.6}$$

$$\begin{aligned} B_1 &= A_{11}\overline{U}_1 + \frac{1}{2}A_{12}\overline{U}_2 + \frac{1}{2}A_{13}\overline{U}_3 \\ B_2 &= \frac{1}{2}A_{12}\overline{U}_1 + A_{22}\overline{U}_2 + \frac{1}{2}A_{23}\overline{U}_3 \\ B_3 &= \frac{1}{2}A_{13}\overline{U}_1 + \frac{1}{2}A_{23}\overline{U}_2 + A_{33}\overline{U}_3 \end{aligned} \tag{3.7}$$

Here $\overline{U}$ and u are the mean and fluctuating components of velocity such that the instantaneous velocity, $U = \overline{U} + u$. The suffixes $_{1,2}$ & $_3$ refer to three mutually perpendicular directions and the suffix $_{eff}$ refers to the effective cooling velocity. This is the velocity which, if applied normal to the wire, would cause the same amount of cooling as the actual velocity. The angle of the wire normal to the probe stem is α (and is different for the two hot–wire probes) and its orientation relative to the U_2 direction is θ. Finally k^2 and h^2 are 'constants' from the Jørgensen equation. The full derivation of these equations is given in *Appendix A.1* and they have been derived previously by Perdichizzi et al [1990].

Calibration

When using the equations above two problems are encountered. The first is what values to take for the 'constants' k^2 & h^2. For an ideal, infinitely long wire $k = 0$ and $h = 1$ but taking these values produces poor results. Also, neither is truly constant but vary with the magnitude and direction of the flow relative to the wire. The second problem is to convert the measured wire voltage, E, to the effective velocity, U_{eff}, used in the equations. The relationship is sometimes described by Kings heat transfer law, $E^2 = A + BU_{eff}^n$ where A, B & n are constants. If this is used, the constants must be determined (King gave $n = 0.5$ but $n = 0.45$ is often considered better) but even so the relationship is not truly accurate. A better method is to determine this relationship and the 'constants' by calibration of each individual hot–wire probe.

To do this the wire is held in a flow of variable velocity and its response is measured at a series of different orientations to the flow. Knowing the velocity and the angle of the wire to the flow and making some assumptions about the variation of k^2 & h^2 the approprate realtionships can be determined. Since these take the form of values at discrete velocities and angles, splines are fitted to the data to allow interpolation at any flow condition. Full details of the calibration technique are presented in *Appendix A.2* but the results are three relationships, one that converts E to U_{eff} and one each that gives k^2 & h^2 for any flow velocity.

Practical technique

The two types of probes used are a slanted wire (Dantec 55P02) which has a wire angle, α, of 45° (*Figure 3.6*) and a normal wire (Dantec 55P01) with $\alpha = 0°$. Seven readings are taken with the slanted wire at 25° intervals (of θ in *Figure 3.6*) and five are taken with the normal wire, again at 25° intervals. To ensure that the wires are not rotated into the wake of one of their prongs they are initially aligned close to the flow direction and are rotated to angles either side of this. At each point readings are taken both from the hot–wire and from the pressure transducer connected to the upstream pitot–static probe. Sampling is carried out at 10kHz for a period of 1 second.

The output of the pressure transducer is converted to a pressure via a calibration against a micro–manometer. The mean and 99% confidence limit are then calculated and if these exceed preset limits the measurement is repeated. The individual voltage readings from the hot–wire are each then converted to effective velocities, using the E to U_{eff} calibration, before the mean, $\overline{U}_{eff}$, and mean squared (of the fluctuating component), $\overline{u^2_{eff}}$, are calculated. The effective velocities are then corrected for variations in the inlet dynamic head by multiplying by the ratio of required to actual velocity. This is done to improve the accuracy of the solution but is only valid for small variations in velocity and temperature.

For each point in the flow this produces 12 values of $\overline{U}_{eff}$ and $\overline{u^2_{eff}}$ which may be inserted into equations (3.1) and (3.2) to give 2 sets of overdetermined simultaneous equations. Solution of these equations is not straightforward but is achieved using an iterative method based on the following steps.

Step 1. To start the iteration a guess is made for U_1, U_2 & U_3. These are used to find k^2 and h^2 from their calibrations and initial values of the 'A' coefficients (eqn. (3.6)) are calculated. The initial guess does not have to be good, it is usually taken as $U_1 = U_3 = 0$ & $U_2 = 10$ m/s (since the hot–wires are initially aligned close to the flow, U_2 is almost the streamwise velocity).

Step 2. The equation $\overline{U^2_{eff}} = \overline{\mathrm{X}}^2$ is solved to give a first approximation for U_1, U_2 & U_3. This is a simplified version of eqn. (3.1) which is only, strictly, valid for low levels of turbulence where z^2 & $\overline{Y}y$ tend to zero. However, since turbulent fluctuations are generally small compared to the mean flow, it does give a reasonable solution for U_1, U_2 & U_3.

Step 3. For this solution k^2 & h^2 (from their calibrations) and the 'A' coefficients (from eqn. (3.6)) are recalculated along with $\overline{\mathrm{X}}^2$ (from eqn. (3.3)) and the 'B' coefficients (from eqn. (3.7)).

Step 4. Equation (3.2) is solved for the Reynolds stresses. $\overline{\mathrm{X}}^2$ and the 'B' coefficients are known from the previous step and $\overline{u^2_{eff}}$ comes from the experimental data.

Step 5. The Reynolds stresses are used to calculate $\overline{\mathrm{Y}}\mathrm{y}$ (3.4) and $\overline{\mathrm{z}^2}$ (3.5) and equation (3.1) is solved for U_1, U_2 & U_3.

Step 6. This process is then repeated from Step 3 until the mean flow and Reynolds stress solutions have converged. In practice this takes in the order of 3–5 iterations.

Equation (3.2) is linear in six unknowns (the Reynolds stresses). Since twelve measurements are taken at each point it is also overdetermined and so a least squares approach may be used. Solution is by a routine from the NAG library (F04AMF) which involves QR factorisation followed by iterative refinement using backsubstitution. The advantage of solving an overdetermined set of equations is that accuracy is improved and the effect of bad experimental data is reduced. It also allows an indication of the likely accuracy of the solution to be obtained by inserting the solution back into the equation and looking at the size of the error.

Equation (3.1) is less easy to solve since it is nonlinear. The approach used is to minimise a sum of squares function derived from the equation using the NAG library routine E04FDF. This minimises F(x) where:

$$\mathrm{F}(x) = \sum_{i=1}^{m} [\mathrm{f}_i(x)]^2 \tag{3.8}$$

by estimating successive points, from an initial guess (of U_1, U_2 & U_3), based on the curvature of $\mathrm{F}(x)$. The values of U_1, U_2 & U_3, at this minimum, are taken to be the mean flow solution. In this case $\mathrm{f}_i(x)$ is the residual found by rearranging eqn. (3.1) as:

$$\mathrm{f}_i(x) = \overline{\mathrm{X}}^2 + \overline{\mathrm{z}^2} - \frac{1}{4\overline{\mathrm{X}}^2}\overline{\left(\overline{\mathrm{Y}}\mathrm{y}\right)^2} - \overline{U}_{eff}^2 \tag{3.9}$$

Ideally $\mathrm{f}_i(x) = 0$ but in practice it will have a small value. The equations are again overdetermined, with all the advantages that implies, and an estimate of the accuracy is provided by the value of $\mathrm{F}(x)$ at the solution.

The velocity components and Reynolds stresses calculated by this method are based on a coordinate system defined by the initial alignment of the hot–wire probes (i.e. close to the local flow direction). This is not usually the coordinate system in which the results are presented but since all the stresses are present the coordinate set may be rotated to whatever is required. In practice the Reynolds stresses are presented in a streamwise coordinate system where the streamwise direction is defined as that found at midspan at each particular pitchwise position. This involves a rotation of the stresses about the spanwise direction which is achieved using the equations given in *Appendix A.3*.

3.5.2 Intermittency measurement

Intermittency measurements have been carried out in the cascade close to the endwall and blade surfaces using a single wire probe. Measurements close to the endwall used a normal hot–wire (Dantec 55P01) mounted in the rotatable probe holder, whilst those close to the blades used a slanted wire (Dantec 55P02) mounted in the cranked probe holder. When using the rotatable probe, the wire was held at 90° to the flow to maximise its response. This was not possible for the cranked wire probe, since it does not rotate, though at most locations at which it was used it would not have been far from perpendicular.

The principle of intermittency measurement is then straightforward, the signal from the hot–wire is sampled for a period of time and the portion for which the flow is turbulent, characterised by large fluctuations, is calculated. In practice, however, it can be difficult to distinguish between the laminar and turbulent portions of the raw signal so some processing is often required. The technique used here is based on the TERA (Turbulent Energy Recognition Algorithm) method of Falco and Gendrich [1990] which has been found to work well even in regions of adverse pressure gradient and high freestream turbulence (Walker and Solomon [1992]).

The sampled wire voltage is first converted to effective velocity and then the function $\left|u\frac{\mathrm{d}u}{\mathrm{d}t}/\overline{U}\right|$ is calculated where $\overline{U}$ is the mean effective velocity and u is the fluctuating component. A rolling average is then used to smooth the data and a threshold is chosen above which the flow is taken to be turbulent. The intermittency is then calculated as the fraction of time for which the function is greater than this threshold. This differs slightly from the TERA method which uses $(u\mathrm{d}u/\mathrm{d}t)_{\mathrm{rms}}$ over a small window. The divide by $\overline{U}$ was added because it was found to give a more constant threshold and the arithmetic mean was used because taking the rms was found to give too much bias to single large values.

Data is logged at 50kHz with 8192 samples being taken at each point. To take more samples than this in one go is not possible due to PC memory limitations but testing showed that this is sufficient to give repeatable results. Calculation of the derivative in the function was by achieved by forward differencing and the rolling average was carried out over 20 samples (400μs). An example of the effect of this processing is given in *Figure 3.7* which shows a typical raw trace, the result of applying the function and the effect of the rolling average. Whilst it is difficult to distinguish anything from the raw trace the rolling average clearly shows the laminar and turbulent portions. The choice of the threshold value is then made by inspection of this trace (*Figure 3.7c*). This is not ideal but the various attempts to devise a more formal method have not been successful.

An investigation of the effect of varying both the threshold and window size showed results similar to those found by Walker and Solomon [1992]. Beyond a certain level the averaging window size had a fairly small effect, unless taken to an excessively large size, but with threshold the intermittency varies continuously with no plateau or break to indicate a suitable value. Other functions, such as $\mathrm{d}u/\mathrm{d}t$ and $\mathrm{d}^2u/\mathrm{d}t^2$, were tried but produced results that were either similar or worse. In consequence there is a certain margin of error associated with these results but if the same criteria is always used when choosing the threshold they should be reasonably consistent within themselves.

3.5.3 Experimental accuracy

Positional

All measurements have been carried out using probes mounted on the traverse apparatus. This is driven by stepper motors with a $0.005mm$ or 0.02° step size and is accurate to within ±2 steps over the whole traverse. The initial positioning of the probe has an estimated error of $\pm 0.1mm$ but it is deflected slightly by the flow so the error in the axial and tangential directions could be up to $\pm 0.5mm$. The use of the probe locating pins does reduce this deflection particularly for measurements close to the surfaces.

Data acquisition

Both A/D convertors have an input range of $\pm 5V$ with 12 bit ($2.44mV$) resolution. The PCL–812PG card has a stated accuracy of ±1 bit and a linearity also of ±1 bit. The Flash–12 card self–calibrates against an internal voltage source and has an overall accuracy of ±0.05%. In order to reduce noise, all electrical components have mains filters and coaxial cable was used wherever possible.

Upstream velocity

Accuracy of the upstream pressure measurements was ensured by calibrating the pressure transducer against a micro–manometer and measuring its zero offset at regular intervals. The individual measurements were estimated to have an accuracy of $\pm 0.5Pa$. Multiple samples were taken in sequence with measurements from the hot–wire anemometer and the dynamic head and 99% confidence limit (Kreyszig [1983], pp.947) were calculated. Measurements were repeated if the dynamic head exceeded ±2% of the required value or if the confidence limit was greater than 0.5%.

Pitot probe yaw angle

The pitot probe was used to measure the midspan yaw angle at each traverse slot. Measurements were taken by hand by rotating the probe to zero the reading on a micro–manometer and a resolution of less than ±0.1° was easily obtainable. In addition to this, however, there will be an error due to the initial alignment of the probe which was estimated to be within ±0.5°.

Rotatable Hot–Wire measurements

Errors in the results of hot–wire measurements arise from two sources, uncertainty in measured values when calibrating the wires and the approximations involved in the time averaging technique. Following Yavuzkurt [1984] the errors in the calibration were estimated to be within 1% over the velocity range encountered but decrease with increasing speed. Yavuzkurt [1984] also estimated the uncertainty in Reynolds stress measurements in a 2D flat plate boundary layer, using a technique similar to that used in the present work, as being 5–10%. This agrees well with an indication of the accuracy of the upstream boundary layer measurements (Section 4.2.2) obtained by calculating the residuals of eqn. (3.2) as a fraction of the left hand side.

Within the blade passage this measure of the likely error of the Reynolds stresses gives values of less than 10% over most of the traverse but rising to 20% in the regions of high turbulence. This does not, however, give any indication of the relative size of the errors for the different stresses. An estimate of this can be obtained from Predichizzi et al [1990] who carried out a sensitivity analysis of eqn. (3.2) for a very similar technique. They found the spanwise component to be four times as sensitive to error as the streamwise component with the others ranged between the two. In a later paper (Perdichizzi et al [1992]) they quote the maximum uncertainties as follows;

Mean velocity	±3%
Flow angles	±1.5°
Streamwise and transverse normal components	±10%
Spanwise normal component	±30%
Shear stresses	±20%

Table 3.4 — Uncertainties in hot–wire measurements

The uncertainty in the mean flow measurements may be compared with the value of F(x) in eqn. (3.8). This is generally less than 2000 but again increases in regions of high turbulence. Whilst this value may seem high it corresponds to a mean value of $f_i(x) \approx 13$ (eqn. (3.9)) which is only 1–4% of U_{eff}^2 (which is typically of the order of U^2) so agrees well with the estimate of velocity in the table above (±3%). Thus, it seems reasonable to take these values as the maximum likely error in the hot–wire measurements.

Intermittency measurements

It is virtually impossible to estimate the error in the intermittency measurements due to the difficulty in selecting the threshold value and the unquantifiable effect of the data processing used. However, taking several measurements at a single point in the flow gave results that were within ±4% of the mean value which suggests reasonable repeatibility. Also, the variation of intermittency with threshold is such that ±0.1 should be a reasonable estimate of the accuracy.

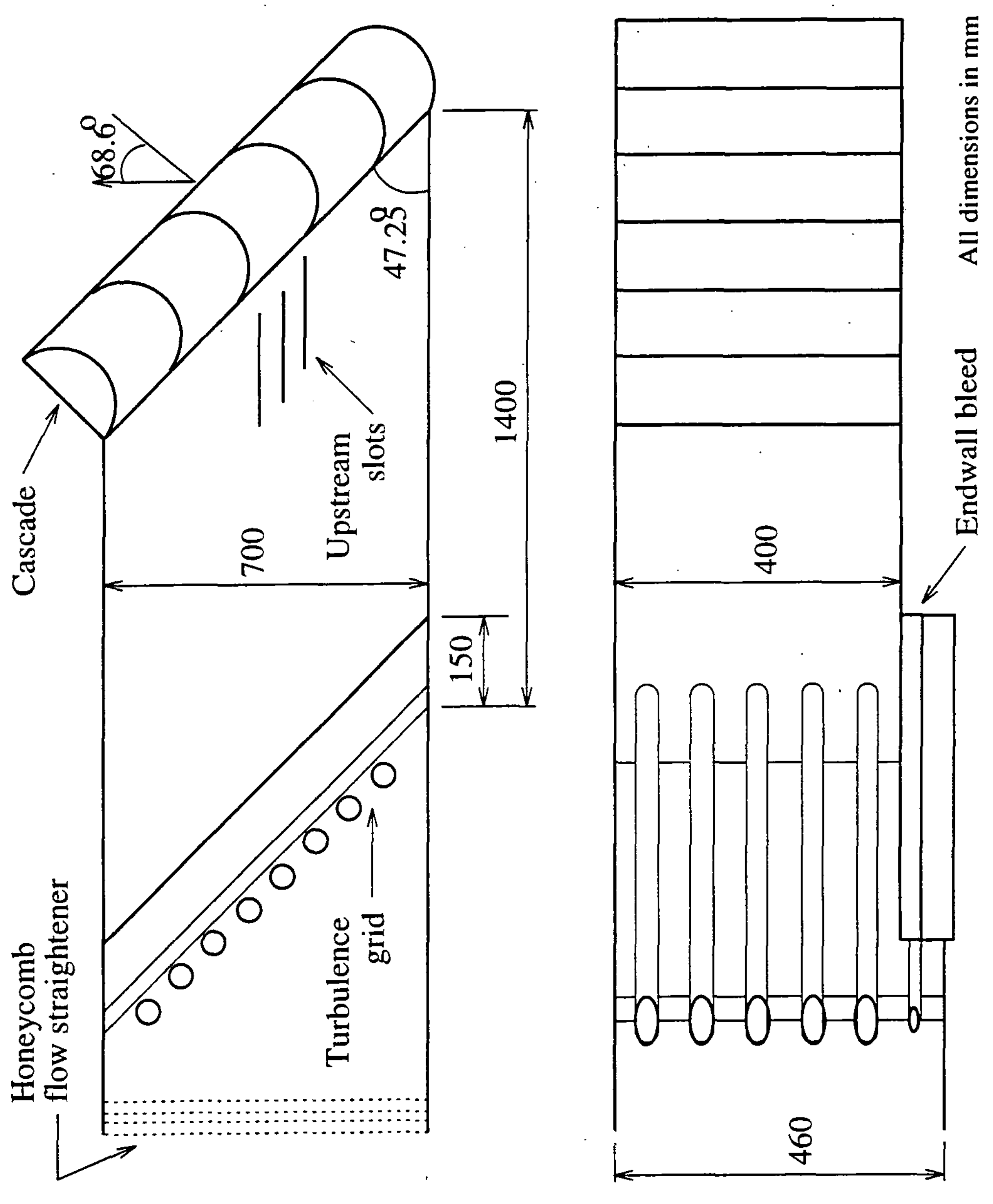

Figure 3.1 — Wind tunnel working section and cascade.

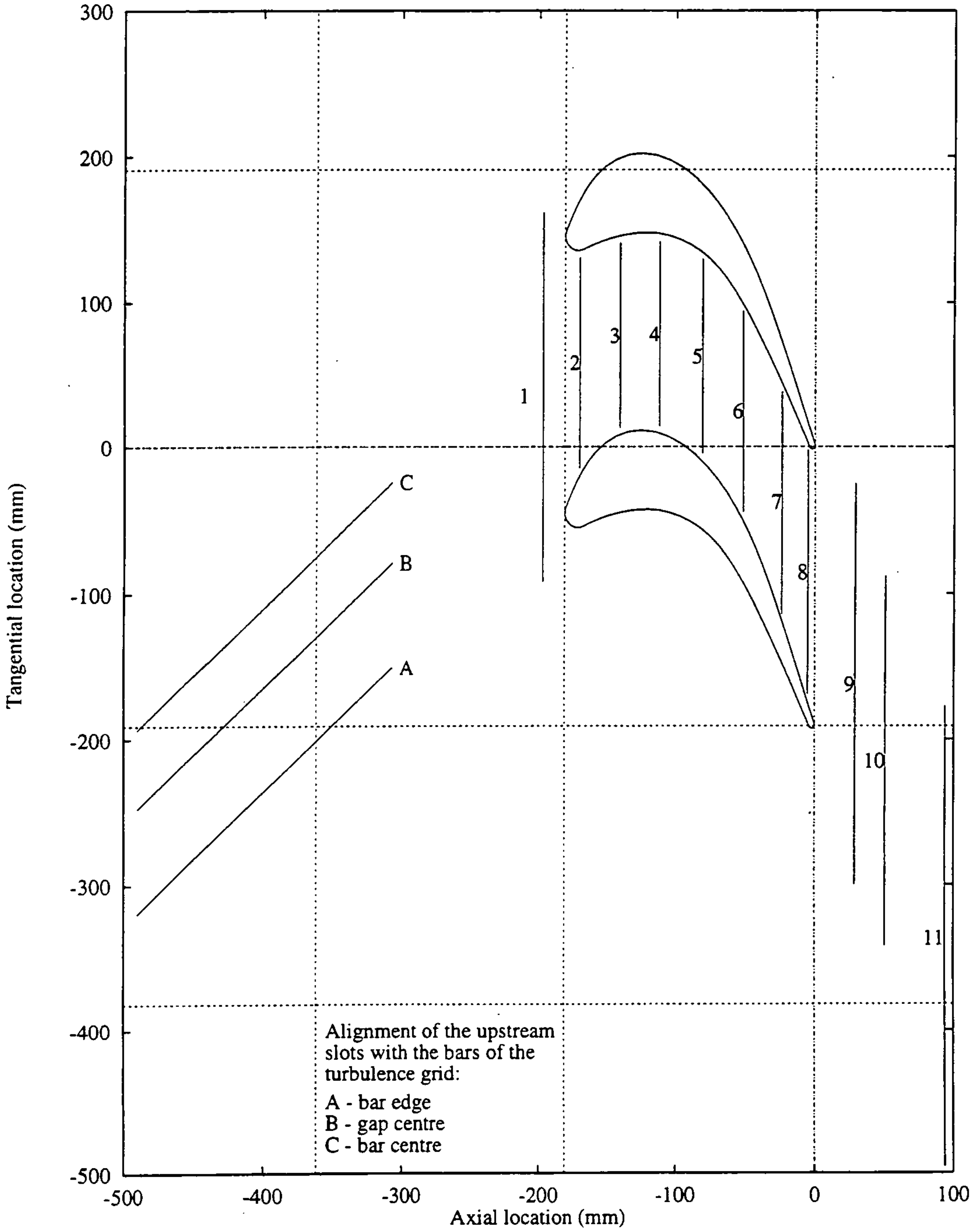

Figure 3.2 — Location of traverse slots.

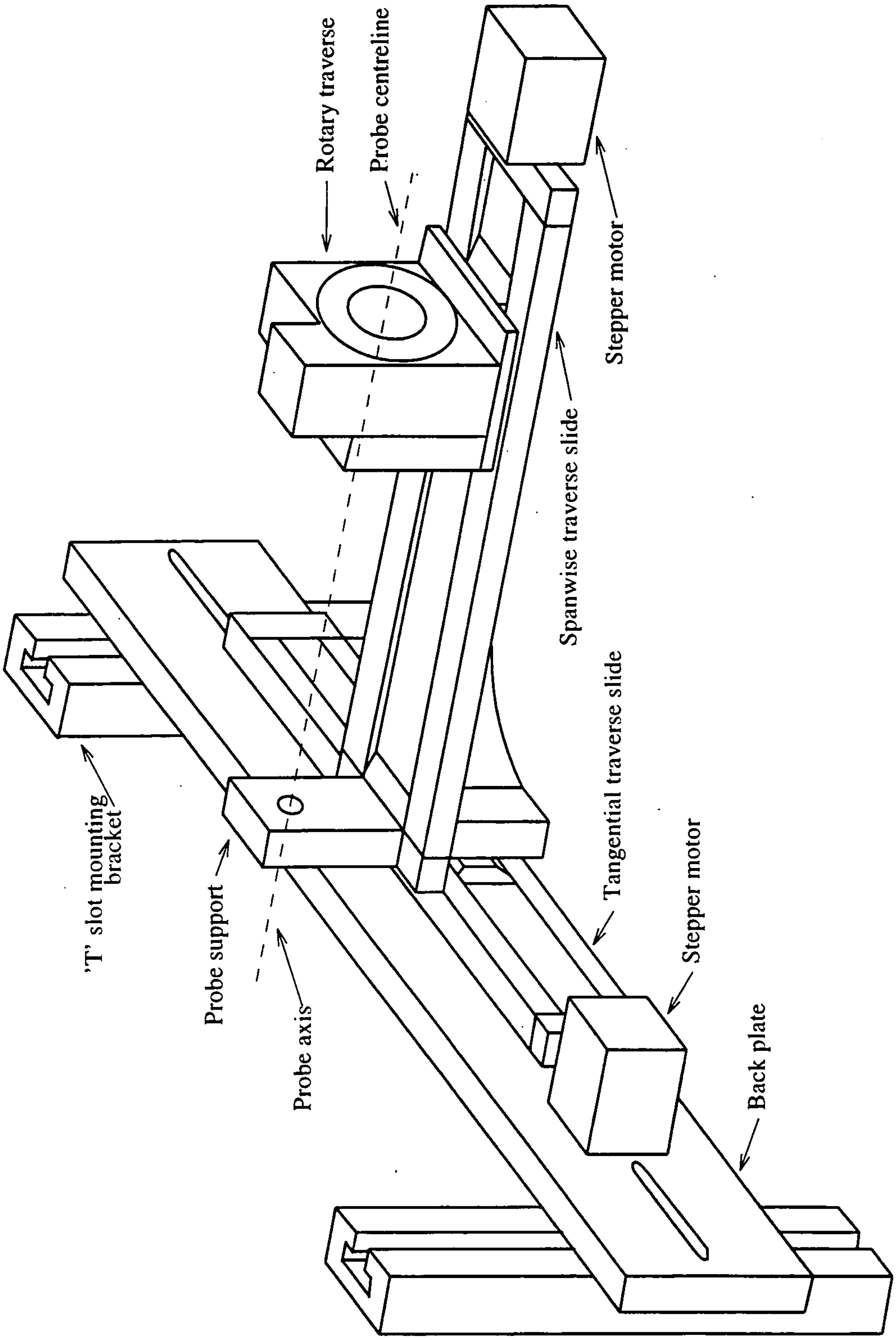

Figure 3.3 — Diagram of the traverse.

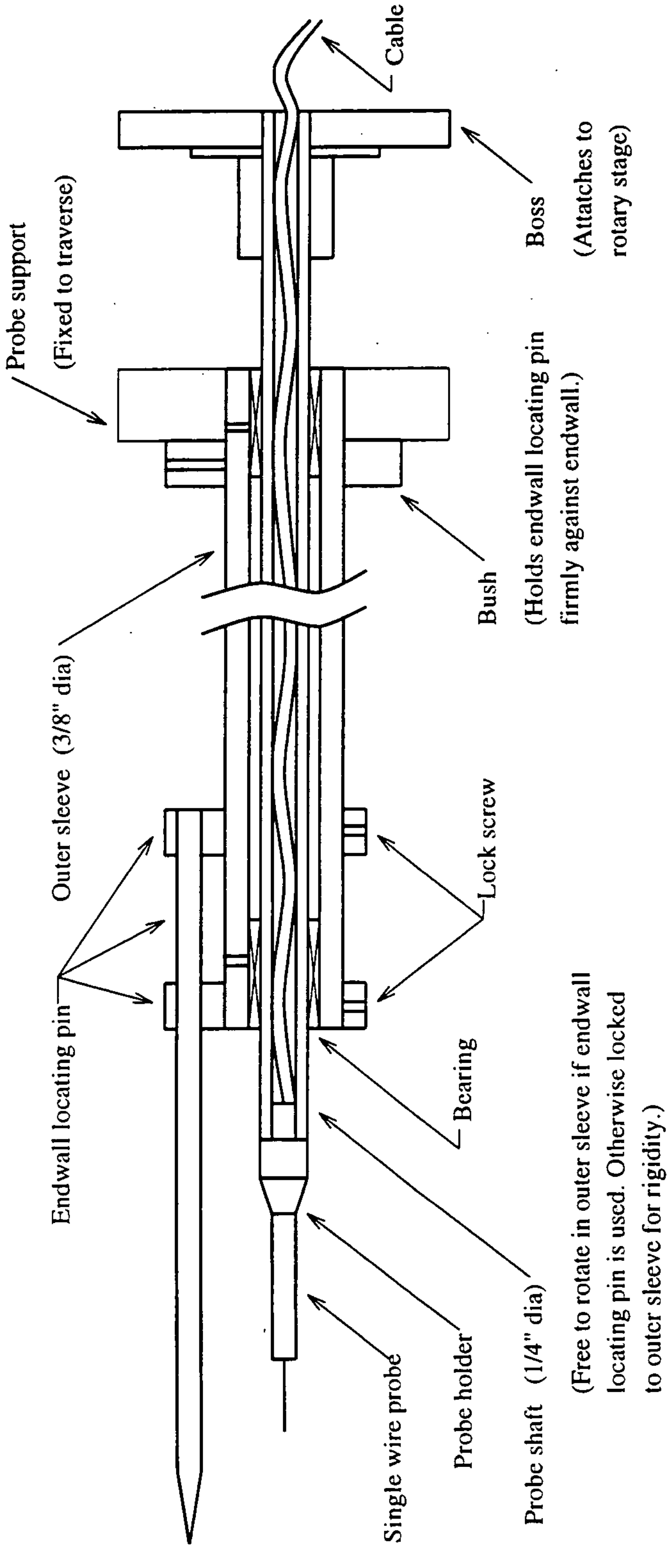

Figure 3.4 — Diagram of the rotatable wire probe.

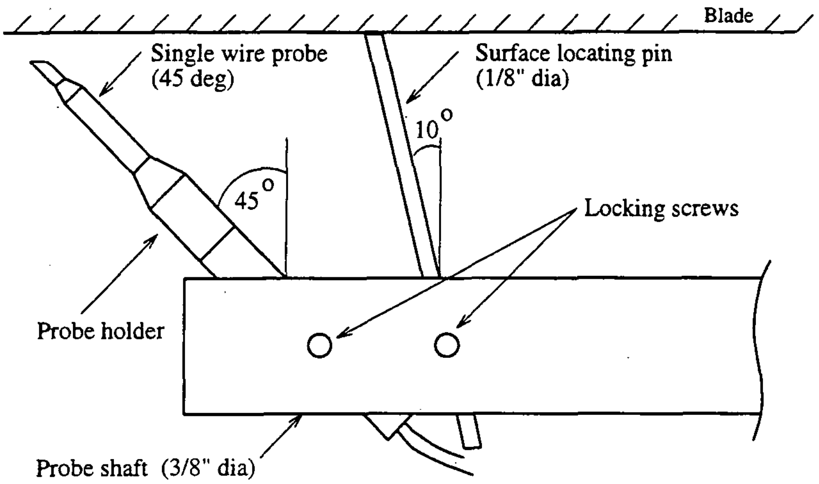

Figure 3.5 — Diagram of the cranked wire probe.

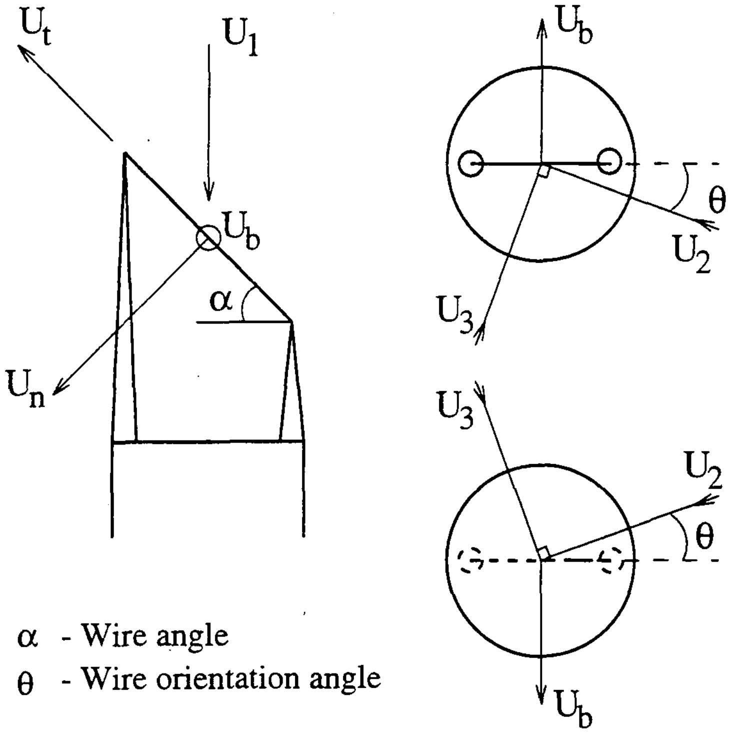

Figure 3.6 — Definition of hot-wire velocity components.

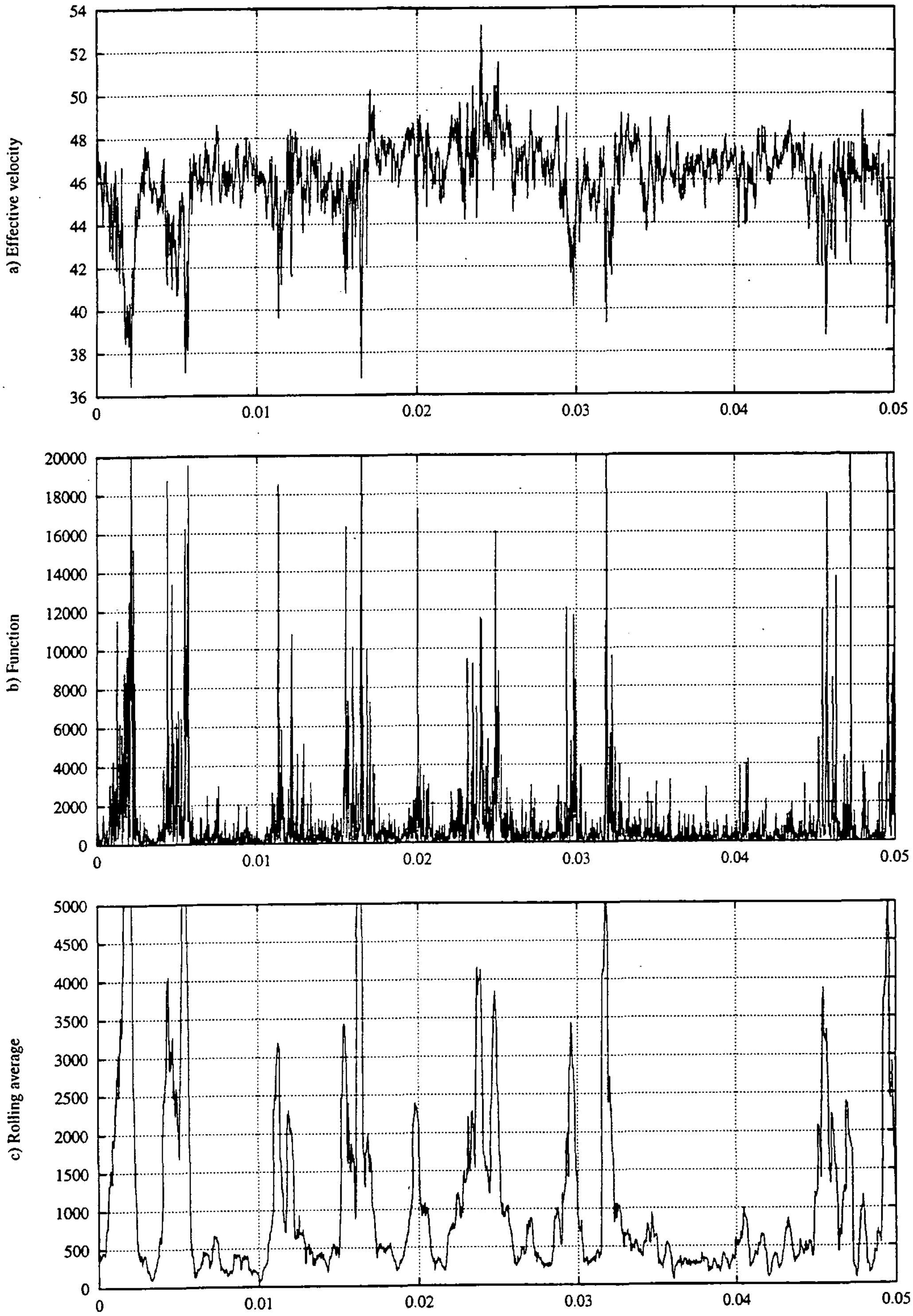

Figure 3.7 — Sample intermittency traces.

Chapter IV

Experimental results

4.1 Presentation of results

Area traverses

Area traverses may be taken on a number of axial planes, called slots, the location of which are given in the table below (see also *Figure 3.2*). The results are presented either as contour or vector plots and, where appropriate, the location of the blade surfaces are shown, the suction surface being on the left and the pressure surface on the right. For the later slots in particular there appears to be a large gap between the data and the suction surface. This, however, is due to the acute angle between the blade surface and the tangential direction, the distance normal to the blade surface is only slightly larger than the diameter of the hot–wire probe.

Slot number	Axial position		Slot number	Axial position	
	mm	%C_{ax}		*mm*	%C_{ax}
1	-197	-9	6	-52	71
2	-170	6	7	-24	87
3	-141	22	8	-5	97
4	-112	38	9	29	116
5	-81	55	10	51	128

Table 4.1 — Location of tangential traverse slots

A total of eleven graphs are plotted at each tangential location – total velocity, yaw angle, pitch angle, secondary velocity vectors, turbulent kinetic energy and the six Reynolds stresses. The secondary velocities are defined as those on a plane perpendicular to the midspan flow direction at that pitchwise position and for plotting this vector is first projected onto the tangential plane. The turbulent kinetic energy and Reynolds stresses are all plotted as non–dimensional values defined in Appendix B.

Boundary layer parameters

Boundary layer shape parameters are obtained by numerical integration of the boundary layer profile using a four point, cubic interpolation scheme due to Gill and Miller [1971]. A problem arises, however, between the wall and the first data point where the profile is not defined. The momentum thickness profile should have a peak where the velocity is half that of the freestream but this occurs well inside the first data point and so is not captured. Unfortunately its location has a considerable effect on the values of both displacement and momentum thickness so it must be defined. This is achieved by extrapolation of the data to the wall assuming a viscous sublayer and log law profile (see *Figure 4.9*).

Pitch and area averaging

Pitch and area mass averaging of data is carried out using the same numerical integration scheme as for the boundary layer integral parameters (Gill and Miller [1971]). Integration is carried out over the range of data across the pitch rather than extrapolating to the surfaces. This is because the distance involved may be relatively large and large gradients may be present (and possibly incorrect due to erroneous data) so extrapolation may introduce significant errors. When area averaging, however, the data is extrapolated to the endwall to make the values more comparable with those from calculations where the data covers the whole flow. This is reasonable because the distance is generally smaller and it is pitch averaged values that are extrapolated which, being averages, are less susceptible to error. Outside the blade row mixed–out parameters may also be calculated if pressure traverse results are available. Definitions of the various parameters are given in Appendix B.

4.2 Upstream measurements

In order to define accurately the cascade inlet conditions, measurements have been made at the three upstream traverse slots (see *Figure 3.2*). These slots cross a plane one axial chord upstream of the blade leading edge which is sufficiently far from the blades for the flow to be undisturbed by their presence. As such it is a suitable location at which to define the inlet conditions for CFD calculations. The three slots, A, B & C, are aligned with the edge, halfway between and with the centre of the bars that make up the turbulence grid to allow the homogenity of the flow to be checked. Two sets of measurements have been taken, one of the freestream flow and the other of the endwall boundary layer.

4.2.1 Freestream

In each upstream slot, freestream measurements have been made with both the 3–hole pitot probe and the hot–wire anemometer. The 3–hole probe was first used to measure the midspan yaw angle at each of 11 axial locations covering $200mm$ in the flow direction. Hot–wire measurements were then taken on a grid consisting of 6 radial points, from $100mm$ to $200mm$ from the endwall, at each of the same 11 axial positions. The hot–wires were initially set parallel to the tunnel axis by first aligning them with the flow (using the routine developed for wire calibrations) and then rotating them by the measured yaw angle. At the point where this was done, therefore, the hot–wire solution for the yaw angle should equal the angle measured by the pitot probe so any difference gives an indication of the likely error.

Measurements were taken as described in section 3.5, using two hot–wires and a total of 12 angles at each point. For presentation, the results have been projected onto a tangential plane and scaled by the blade axial chord (C_{ax}). The zero on the graphs corresponds to 1.0 C_{ax} axially upstream of the leading edge (i.e. the inlet plane for CFD calculations) and the results cover approximately 0.8 C_{ax}. The most upstream measurement location is approximately 40 bar diameters ($1016mm$) downstream of the turbulence grid and the predicted turbulence intensity (Roach [1987]) at -1.0 C_{ax} is 5.7% in the streamwise direction and 5.1% in the orthogonal directions.

Figure 4.1 shows the mean flow results for each slot, along with the yaw angle measured with the pitot probe. The results have been averaged over the spanwise direction to give a single value (an indication of the variation across the span is given in later plots). As can be seen, the total velocity decreases in slot A, stays fairly constant in slot B (and is also too high but this is due to the tunnel being run slightly too fast) and increases in slot C. This implies flow is moving towards the bottom of the tunnel, decreasing the speed at the top and increasing it at the bottom, and this is confirmed by the yaw angle plots (a positive yaw angle is downwards).

The hot–wire yaw angle results at each slot follow the same shape as those measured with the 3–hole probe but are approximately 0.4° higher. This difference is clearly a systematic error introduced either by the calibration or by the solution method but is within the stated accuracy. The positive yaw angle is thought to be due to the flow being deflected by the turbulence grid which is not perpendicular to the axial direction. The pitch angles at slots A & B are in reasonable agreement but those at slot C are approximately 1° higher. Again they are within the expected accuracy of the measurements but may, in part, be due to the non–symmetrical endwall boundary layers in the working section.

The results for the three turbulence intensities and the turbulent k.e. coefficient are given in *Figure 4.2*. All have been non–dimensionalised by the inlet velocity as defined in Appendix B. The streamwise and cross–stream results for each slot agree reasonably well, whilst the radial turbulence intensity shows more scatter. This is probably due to the lower accuracy of the radial measurement rather than a true variation between slots. All 3 intensities, however, seem to decrease in a fairly linear manner with the radial component being largest and the cross–stream component the smallest.

To obtain a single set of results for each parameter the data from all the slots were combined. At each tangential position the data was averaged and the r.m.s. variation was calculated. A best fit (least squares) quadratic was fitted to each set of data and the results are plotted in *Figures 4.3* & *4.4*. The error bars show the r.m.s. variation at each point, rather than the range of values, because this is representative of all the data whereas the total variation simply shows the two extreme points. Typically, the r.m.s. value is about half of the total variation.

The large r.m.s. for the total velocity is due both to the slightly high velocity in slot B and to the fact that the velocity profiles are different in each slot. This means that averaging them all to get a single profile is not particularly relevant and the result is not used. The results for the yaw angle (both hot–wire and pitot) are reasonable and give an indication of the true inlet flow angle. The pitot probe measurement is the more accurate one and gives an angle of 0.72° at 1.0 C_{ax} upstream of the blades i.e. a slight positive incidence. The large scatter on the pitch measurements are due to the slot C results but the angle will be taken to be 0° when defining inlet conditions.

The averages of the turbulence intensities and kinetic energy coefficient give values (at -1.0 C_{ax}) of 5.1%, 4.9%, 5.6% and 0.0083 for the streamwise, cross–stream & radial intensities and the turbulent k.e. coefficient, respectively. These compare reasonably well with the predicted values of 5.7%, 5.1%, 5.1% and 0.0085 (Roach [1987]) though the radial turbulence intensity is higher than predicted and the streamwise value is lower. Cleak [1989] found similar results at -14% C_{ax} (4.1% (streamwise), 3.9% (cross–stream) & 4.7% (radial)) where again the overall agreement was reasonable except that the radial intensity was the highest and the streamwise value the lowest.

The main reason for measuring the freestream flow over a range of streamwise locations was to allow the turbulent dissipation rate, ϵ, and freestream mixing length scale, L_∞, to be calculated. Note, L_∞ is not the same as the micro/dissipation length scale found from Roach [1987] (section 3.2) but is the one used within turbulence models (see Chapter 5). L_∞ and ϵ can be calculated by equating convection and dissipation e.g.

$$V_u \frac{\partial k}{\partial x} = -\epsilon = -\frac{C_\mu^{3/4} k^{3/2}}{L_\infty} \tag{4.1}$$

Where $\partial k/\partial x$ & k are obtained from the curve fit in *Figure 4.4d* and $C_\mu = 0.09$. The results at -1.0 C_{ax} are summarised in Table 4.2 below.

As a comparison with the predictions from Roach [1987] the micro/dissipation length scales may also be calculated from the measured turbulence intensities. At $-1.0C_{ax}$ these are 4.1, 3.7 & 3.1mm in the streamwise, cross–stream and radial directions which agree reasonably well with the predicted values of 4.0mm in the streamwise direction and 2.8mm in the orthogonal directions.

Inlet yaw angle	43.47°
Streamwise turbulence intensity	5.12%
Cross–stream turbulence intensity	4.95%
Radial turbulence intensity	5.62%
Turbulent k.e. coefficient	0.0083
Turbulent k.e. $(\sqrt{k}/V_u)$	6.44%
Freestream mixing length scale	$9.36mm$
Turbulent dissipation rate	32.7 m^2/s^3

Table 4.2 — Freestream flow conditions at -1.0 C_{ax}

4.2.2 Endwall boundary layer

Measurements of the endwall boundary layer profile have been made in each of the three upstream slots at -1.0 C_{ax}. Each traverse consisted of 26 measurements from $1.5mm$ to $60.0mm$ from the endwall. Cleak [1989] measured the boundary layer thickness to be $40.0mm$ at 14% upstream of the leading edge so these traverses were expected to extend well into the freestream. Measurements were taken with the hot–wires initially aligned with the flow direction and the results were then rotated (typically by less than 1.0°) to align them with the tunnel axis (see Appendix A.3). The reason for this was to allow the results from each slot to be presented in the same coordinate system (the flow angle at each slot being slightly different).

The velocity profiles for each slot are presented in *Figure 4.5.* They have been normalised with the freestream velocity (taken as the average of the outer 3 velocity measurements) and, as can be seen are all very similar. The shape of the profile does not, however, correspond to a $1/7^{th}$ power law or to the universal log law, though the inner part of the boundary layer does follow a log relationship. The reason for this is believed to be due to the turbulence grid which is located $150mm$ upstream of the endwall bleed. It is thought that, despite attempts to avoid it, there is a 'jet' effect in the flow between the bars that results in a non–uniform velocity profile at the start of the false endwall and so distorts the boundary layer shape.

The three turbulent kinetic energy profiles are shown in *Figure 4.6.* Though the data shows some scatter, there are no consistent differences between the slots which suggests the flow is essentially uniform and the variations are due to experimental error. This is confirmed by the 6 velocity correlations shown in *Figures 4.7 & 4.8*. These, again, seem to show a large amount of scatter but this is mainly due to the scale of the graphs. As with the freestream measurements, the largest variations are found in the radial $(\overline{w^2})$ components and again this is due to the hot–wire technique.

The results, themselves, are very much as expected, with the streamwise $(\overline{u^2})$ and cross–stream $(\overline{v^2})$ turbulence intensities increasing towards the endwall. This gives the peak in turbulent k.e. that is found in a turbulent boundary layer though, unfortunately, it was not possible to take measurements close enough to the wall to capture the subsequent decrease. Two of the cross–correlations, $\overline{uv}$ and $\overline{vw}$ remain roughly at zero, as expected, whilst the $\overline{uw}$ velocity correlation becomes increasingly negative towards the wall. This corresponds to the positive shear stress which produces the velocity gradient through the boundary layer.

The main reason for taking these upstream measurements is to provide suitable inlet conditions for CFD calculations. In order to do this the boundary layer profiles must be extended to the endwall to allow the velocity and turbulent k.e. to be defined on all calculation planes (a 3D calculation will need several planes closer to the endwall than $1.5mm$). Whilst simple linear interpolation could be used, a better method would be to fit the known profiles for a turbulent boundary layer to the experimental data. In order to do this the wall shear stress, τ_w, is required to determine the width of the viscous sublayer and the extent of the log law region.

The value of τ_w can be estimated by fitting a polynomial to the $\overline{uw}$ velocity correlation and extrapolating to the wall. A quadratic was found to produce the best fit and gave a value of $\tau_w = 1.25\mathrm{N/m^2}$. There is however a considerable amount of scatter of the data which means this value may not be very accurate. A rough check can be made by calculating the the local skin friction factor, C_f', and comparing with an approximation based on a $1/7^{th}$ power law profile (e.g. Schlicting [1978] pp. 638) where;

$$C'_f = \frac{\tau_w}{\frac{1}{2}\rho V_u^2} \tag{4.2}$$

and for a $1/7^{th}$ power law profile;

$$C'_f = 0.0576\,(Re_l)^{-1/5} \tag{4.3}$$

Here the Reynolds number is based on the surface length (1.04m). This gives a value of $C'_f = 0.0058$ for the measured boundary layer which is slightly higher than $C'_f = 0.0035$ for the $1/7^{th}$ power law profile. Using this calculated value of τ_w, y^+ $(= \sqrt{\rho\tau_w}y/\mu)$ and U_τ $(= \sqrt{\tau_w/\rho})$ may be calculated and used to produce a log plot of the velocity profile (*Figure 4.9*).

The profile is then defined in four parts. In the viscous sublayer ($y^+ < 8$) the relationship $U/U_\tau = y^+$ is used. For the log law region ($y^+ > 30$) a log relationship has been fitted to the first 11 data points. This is used up to the first data point ($1.5mm$, $y^+ = 100$) after which a sixth order polynomial is used to the edge of the boundary layer. Finally, in the transitional region ($8 < y^+ > 30$) linear interpolation, in terms of U/U_τ and $\ln(y)$, between the values of U/U_τ at $y^+ = 8$ and $y^+ = 30$ is used. Whilst this does not quite agree with experimental data (which follow a slight curve) the difference is not likely to be significant.

This velocity profile may then be used to calculate the 99% boundary layer thickness, the displacement thickness, δ^*, and the momentum thickness, θ. The latter two are calculated by numerical integration of the experimental data along with an additional point at half the freestream velocity the location of which ($0.45mm$) was found from the velocity profile. The results are shown in the table below along with the shape factor, H $(= \delta^*/\theta)$.

Finally the boundary turbulent k.e. profile was found by fitting a polynomial to the experimental data and extending it from $y^+ = 30$ until k drops to the freestream value. For $y^+ < 30$ k is taken to decrease in proportion to the square of the distance from the wall. These two equations are given in the table below and shown in *Figure 4.10*.

99% thickness	39.9mm
Displacement thickness	2.788mm
Momentum thickness	2.281mm
Shape factor	1.222

Table 4.3 — Boundary layer thicknesses.

Span (mm)	Turbulent k.e. profile (z in mm)
z = 0.00 → 0.45mm	$k/k_{free} = 9.128z^2$
z = 0.45 → 49.33mm	$k/k_{free} = 1.855\text{x}10^0 - 3.288\text{x}10^{-2}z + 3.154\text{x}10^{-4}z^2$

Table 4.4 — Boundary layer turbulent k.e. profile.

4.3 Area traverses

Area traverses have been carried out in 6 slots, 1 upstream of the blade (slot 1 at -9% C_{ax}), 4 within the blade passage (slots 3, 5, 6 & 8 at 22%, 55%, 71% & 97% C_{ax} respectively) and 1 downstream of the trailing edge (slot 10 at 128% C_{ax}). With the exception of the slot 10 traverse all measurements have been taken on 21 radial planes from 1.5mm to 60.0mm from the endwall. By restricting the measurements to this region the endwall and secondary flow features are obtained in considerable detail. Traverses to midspan at some of these slots have been made previously by Cleak [1989] and Biesinger [1993] but do not give sufficient detail near to the endwall.

The traverse at slot 1 consists of the same 17 tangential locations as used by Cleak [1989] (though the slot was moved by Biesinger [1993] to make room for his 'blowing slot' so they are not strictly comparable) and cover approximately 1.3 pitches. The 4 traverses within blade passage each consist of 16 equally spaced tangential locations. The downstream traverse at slot 10 has 27 tangential and 30 radial locations covering just over 1.4 pitches from 5.0mm from the endwall to midspan. This is a repeat of a traverse by Cleak [1989] and was carried out mainly as a check of the hot-wire technique but does add the $\overline{vw}$ velocity correlation that he could not measure.

In addition to these hot–wire measurements, the midspan yaw angles at all but slot 10, were measured with a 3–hole pitot probe. Measurements were taken at each of the tangential traverse locations and the results were used to calculate the secondary velocity vectors and secondary kinetic energy coefficient. At slot 10 the midspan yaw angle was obtained by averaging the hot–wire results from the planes closest to midspan.

4.3.1 Slot 1 (-9% C_{ax})

The results at slot 1 are shown in *Figures 4.11 & 4.12*. *Figures 4.11a–d* shows the mean flow results, *Figures 4.11e–k* the turbulence results and *Figure 4.12* the pitch averaged values. The mean flow results clearly show the upstream potential effect of the blades away from the endwall, while closer in the development of the horseshoe vortex can be seen, causing flow towards the surface. These results agree well with those of Cleak [1989] though the secondary velocities and angles are all larger. This, however, is because the slot position was moved 5%C_{ax} closer to the leading edge by Biesinger [1993] so the effect of the blades will be greater.

Since the flow at slot 1 is still relatively undisturbed the velocity may be pitch averaged to obtain the boundary layer profile. The results are presented in the table below along with those at $-1.0C_{ax}$ and those from Cleak [1989] (labelled JGC). As can be seen the boundary layer has grown slightly but is thinner than found by Cleak [1989]. It would appear then, that replacing the moving belt by a solid wall has slightly reduced the boundary layer growth in the tunnel working section.

	HM		JGC
	-100%	-9%	-14%
99% thickness	40mm	42mm	43mm
Displacement thickness	2.8mm	2.9mm	3.7mm
Momentum thickness	2.3mm	2.4mm	3.1mm
Shape factor	1.22	1.18	1.20

Table 4.5 — End wall boundary layer parameters

Measurements of the turbulence quantities at slot 1 show away from the wall the expected decay in turbulence from the upstream traverse position. At $60mm$ away from the endwall the pitch averaged turbulence intensities are 4.5, 4.3 & 5.1% in the streamwise, tangential and spanwise directions respectively which agrees reasonably well with the design values of 4.6% (streamwise) and 4.1% (orthogonal) and the measurements of Cleak [1989] (4.1, 3.9 & 3.7%). As with the upstream measurements, the spanwise turbulence intensity is the largest. Their behaviour towards the endwall also follows the upstream measurements with the streamwise intensity almost doubling, the tangential intensity increasing slightly and the spanwise intensity remaining virtually constant. The turbulent k.e. coefficient reaches a peak of almost 0.016 close to the endwall and drops to approximately 0.0065 at $60mm$.

Close to the endwall the $\overline{uw}$ velocity correlation is predominately negative (positive shear stress) as expected in a boundary layer. The $\overline{uv}$ and $\overline{vw}$ correlations are generally small other than near to the endwall directly in front of the leading edge where there is a region of negative $\overline{uv}$ correlation associated with the horseshoe vortex. The secondary flow caused by the horseshoe vortex also appears in the pitchwise mass averages (*Figure 4.12*) as an increasing yaw angle and secondary k.e. coefficient. Unlike the rise in the turbulent k.e. coefficient which starts at the edge of the boundary layer, the rise in these two mass averages occurs entirely within $10mm$ of the endwall and is due entirely to the horseshoe vortex.

4.3.2 Slot 3 (22% C_{ax})

The results of the traverse at slot 3 are shown in *Figures 4.13* & *4.14*. The main flow features are shown best by the secondary velocity vectors (*Figure 4.13d*). The passage vortex can be seen towards to the pressure surface while in the suction surface/endwall corner the suction side leg of the horseshoe vortex can be seen. It should be noted here that the vertical scale of the area plots is magnified relative to the horizontal scale so that the vortices are more 'squashed' than they appear. The passage vortex is centered approximately $15mm$ from the endwall and is already much larger than the horseshoe vortex.

The total velocity vectors show a large cross–passage velocity gradient has formed due to the pressure gradient between the blade surfaces. Beneath and behind (i.e.

towards the pressure surface) the passage vortex the contours are distorted by the secondary flows. The yaw angle contours show that the flow here is skewed, towards the suction surface, by up to 60° from the remainder of the flow. The pitch averaged yaw angle plot (*Figure 4.14*a) also shows this overturning, though to a lesser degree, and the effect of this cross–flow can also be seen in the pitch averaged secondary k.e. which rises sharply within $5mm$ of the endwall.

The action of the vortices can also be seen in the turbulent k.e. and turbulence intensity plots (*Figures 4.13e–h*). The more turbulent fluid in the endwall boundary layer has begun to be rolled up into two distinct cores, a large one due to the passage vortex and a smaller one due to the suction side leg of the horseshoe vortex. The peak level of turbulent k.e. has also increased, in both cores, to approximately 14% of the inlet dynamic head. Towards the pressure surface the turbulence decreases to freestream levels (7%) due to the passage vortex convecting mainstream fluid down to the endwall. The pitch averaged turbulent k.e. profile (*Figure 4.14c*) still rises towards the endwall but is also beginning to develop a second peak associated with the turbulent core of the passage vortex.

The $\overline{uv}$ velocity correlation (streamwise/cross–passage) is positive over the whole traverse corresponding to a negative shear stress. Outside the suction surface boundary layer this is consistent with the strong negative velocity gradient across the passage. Within the suction surface boundary layer, however, the shear stress should be positive (though if the boundary layer is laminar the values will be small) but it is probably too thin to extend into the measured region so no negative $\overline{uv}$ values are seen. The $\overline{uw}$ correlation still shows negative values close to the endwall upstream of the passage vortex (i.e. towards the suction surface side). Behind the passage vortex the values are very close to zero which is consistent with the initially thick, turbulent endwall boundary layer having been stripped away. The results do not, however, give any clear indication of the state of the new boundary layer.

4.3.3 Slot 5 (55% C$_{\text{ax}}$)

The results at slot 5 are shown in *Figures 4.15* & *4.16*. Between slots 3 & 5 a large amount of turning of the flow occurs as a result of which the passage vortex crosses the passage to the suction surface and increases in strength (*Figure 4.15d*).

The suction side leg of the horseshoe vortex is no longer visible and the yaw angle contours show that the flow within $15mm$ of the endwall is now all highly skewed towards the suction surface. This is confirmed by the pitch averaged yaw angle (*Figure 4.16a*) which shows a maximum overturning of almost 40°. The total velocity contours show the cross–passage velocity gradient to have increased slightly and give no indication of an endwall boundary layer.

The turbulent k.e. contours (*Figure 4.15e*) show that the endwall boundary layer has now been completely removed and rolled up into a turbulent core close to the suction surface. The peak level of turbulence has also increased to 35% of the inlet dynamic head. The individual turbulence intensities (*Figures 4.15f–h*) all show a similar pattern to the turbulent k.e. with peaks of 20–34% of inlet velocity and are in reasonable agreement with previous measurements by Cleak [1989]. Behind the passage vortex the turbulence close to the endwall remains low at about the level of the mainstream. The pitch averaged turbulent k.e. (*Figure 4.15c*) now has its peak at just under $10mm$ from the endwall and drops by almost two thirds before the surface.

The three velocity correlations (*Figures 4.15i–h*) now also exhibit a significant peak associated with the passage vortex. The $\overline{uv}$ correlation is still entirely positive and has increased considerably in the passage vortex region. The $\overline{uw}$ correlation is mainly negative with a strong peak towards the suction surface side of the passage vortex center. There is also a smaller positive region close to the endwall giving a sign change across the vortex. This is similar to that found by Cleak [1989], though the negative region is larger and more intense. The values on the endwall behind the passage vortex are still close to zero. The $\overline{vw}$ correlation is predominately negative but generally exhibits lower levels than the other two.

4.3.4 Slot 6 (71% C_{ax})

The results at slot 6 are shown in *Figures 4.17 & 4.18*. The passage vortex has now moved slightly closer to the suction surface and is just beginning to move away from the endwall. Most of the turning of the flow has been completed by this point so the cross–passage velocity gradient (*Figure 4.17a*) is beginning to decrease. The velocity contours have become distorted close to the suction surface, particularly in the endwall corner where there is a small region of slower moving fluid. This region is also evident in the angle contours (*Figures 4.17b–c*) where it causes a reduction in overturning and a decrease in pitch angle. It is caused by the formation of a corner vortex which rotates in the opposite direction to the passage vortex and is just visible in the secondary velocity vectors as a reduction in the tangential component in the endwall/suction surface corner.

The peak in turbulent k.e. (*Figure 4.17e*) associated with the passage vortex has continued to grow and now reaches a maximum of 41% of the inlet dynamic head. In addition to this there are two further regions of high turbulent k.e., one in the endwall/suction surface corner and the other spread along the suction surface towards midspan of the passage vortex. The peak close to the endwall is generated by the action of the corner vortex whilst the region on the suction surface may indicate that the boundary layer here has become turbulent. Away from the passage vortex, the level of turbulence close to the endwall still remains low.

The three turbulence intensities (*Figures 4.17f–h*) are all similar to the turbulent k.e. The $\sqrt{\overline{w^2}}$ (spanwise) intensity has the largest peak at 42% of inlet velocity whilst the $\sqrt{\overline{u^2}}$ (streamwise) is smallest at 24%. The three velocity correlations (*Figures 4.17i–k*) still have their largest values associated with the passage vortex, though there are also significant regions associated with the corner vortex and the suction surface boundary layer. The $\overline{uv}$ correlation has decreased considerably in magnitude within the passage vortex region and now has negative values associated with the corner vortex and suction surface boundary layer. In the latter region these negative values are consistent with a turbulent boundary layer and their absence in earlier slots suggests that transition occurs between slots 5 and 6.

The $\overline{uw}$ correlation is still almost entirely negative and shows no significant values other than close to the suction surface. In particular there are no negative values on the endwall that might suggest a turbulent boundary layer, though it is possible that it is still too thin to be detected (e.g. $< 1.5mm$). Finally the $\overline{vw}$ correlation is negative in the passage vortex region and positive in the corner vortex and suction surface boundary layer. In the passage vortex its magnitude lies between the $\overline{uv}$ and $\overline{uw}$ correlations and, as with these, is negligible away from the suction surface.

The pitch average profiles (*Figure 4.18*) show the secondary flows are beginning to decay by this point. The maximum overturning has dropped to approximately 25°, though this is in part due to the passage vortex having moved further away from the endwall. The peak of secondary k.e. coefficient has also decreased, by about 25%, but extends further away from the endwall. The turbulent k.e. coefficient rises to approximately the same level as at slot 5 but the peak has moved out to $13mm$ from the endwall. There is now also a rise in turbulent k.e. close to the endwall due to the turbulence generation in the corner vortex.

4.3.5 Slot 8 (97% C_{ax})

The results at slot 8, just before the trailing edge, are shown in *Figures 4.19 & 4.20*. The total velocity contours show that the cross–passage velocity gradient has almost disappeared and the yaw angle contours show much less skew close to the endwall. The secondary velocity vectors (*Figure 4.19d*) show the passage vortex has moved a considerable distance from the endwall, so much so that it is no longer entirely captured in the traverse. *Figure 4.19d* also shows the passage vortex to have grown in size but the pitch averages secondary k.e. (*Figure 4.20b*) shows it has weakened considerably. Close to the endwall the secondary k.e. coefficient has dropped by almost 65% from slot 6 through there is now a second peak (which unfortunately is not entirely captured) to the midspan side of the vortex center.

The peak turbulent k.e associated with the passage vortex (*Figure 4.19e*) has decreased to 32% of the inlet dynamic head but there may be higher values closer to the suction surface. The turbulence associated with the corner vortex is now clearly separate from the passage vortex and has also decreased in strength. Elsewhere the turbulence levels remain low. The individual turbulence intensities (*Figures 4.19f–h*) all follow the same pattern as the turbulent k.e. and have reduced in proportion. The $\sqrt{\overline{w^2}}$ intensity is still the largest, with a maximum of 32% of inlet velocity, while the other two have a similar peak of 22%.

The $\overline{uv}$ velocity correlation (*Figure 4.19i*) shows a considerable change from slot 6 with the positive peak associated with the passage vortex no longer evident. The values where it was expected to be (i.e. coincident with the peaks of the other stresses) are close to zero which implies the decay seen between slots 5 & 6 has continued. Close to the suction surface there is a negative region, consistent with a turbulent boundary layer (remembering that this slot is at quite an acute angle to the blade surface so the perpendicular distance to the surface is much smaller than it appears), which extends well away from the surface towards midspan. This is in marked contrast to the results of Cleak [1989] which still show a considerable positive peak extending well across the passage and no negative region. The remainder of the $\overline{uv}$ correlation follows the pattern of the previous slots with a negative region associated with the corner vortex and negligible values elsewhere.

The $\overline{uw}$ correlation (*Figure 4.19j*) also follows the pattern of the previous slot with negative values along the entire of the suction surface. As with the other turbulent quantities, the peak associated with the passage vortex is no longer clearly defined because it appears to extend into the region close to the suction surface where measurements could not be taken. However, this again differs from the results of Cleak [1989] which show a positive region around $60mm$ away from the endwall and only a weakly negative region closer in. The $\overline{vw}$ correlation (*Figure 4.19k*) follows the pattern of the $\overline{uv}$ correlation with the negative peak associated with the passage vortex disappearing and the positive region on the suction surface growing.

It is difficult to explain the differences between the present measurements and those of Cleak [1989] particularly as the agreement is much better at slot 5 and slot 10 (see below). The present results, however, do seem to be more consistent, in terms of the development of the velocity correlations through the cascade especially when also taking into account the changes to slot 10. Here Cleak [1989] found a very rapid sign change in the peak of $\overline{uv}$ correlation associated with the passage vortex which he had difficulty explaining. In the present results the change is much more gradual and takes place from slot 5. Zunino et al [1987] also found a similar behaviour, though comparison is not easy as their measurements were taken on planes perpendicular to the blade surfaces rather than on axial planes.

4.3.6 Slot 10 (128% C_{ax})

The results at slot 10 are shown in *Figures 4.21 & 4.22.* Unlike the earlier slots, this traverse consist of 27 tangential and 30 radial locations covering just over 1.4 pitches from $5.0mm$ from the endwall to midspan. It is a repeat of a traverse by Cleak [1989] and was carried out mainly as a check of the hot–wire technique but does also add the $\overline{vw}$ velocity correlation that he could not measure. Due to a leak in the piping from the upstream pitot probe it was also carried out at an inlet velocity 15% lower than intended. The effect this has on the results is difficult to quantify but is not expected to be large. Where values have been scaled by velocity (e.g. all the turbulence quantities) the actual inlet velocity has been used so the results should be comparable with previous slots.

The mean flow results (*Figures 4.21a–d*) show that the passage vortex has moved further away from the endwall and now has its center at a spanwise distance of approximately $65.0mm$. The endwall/suction surface corner vortex is just about visible in the secondary velocity vectors but is more easily seen in the pitch angle and total velocity contours. A third vortex is also visible in the secondary velocity vectors to the midspan side of the passage vortex. This is shed from the trailing edge of the blade and is due to the unequal velocities on the pressure and suction surfaces. The blade wake is clearly visible in the total velocity contours and is approximately $50mm$ thick.

The non–dimensional turbulent k.e. contours (*Figure 4.21e*) show the turbulence associated with the passage and corner vortices to have decreased considerably. The peak value in the passage vortex is now 22% of the inlet dynamic head though is merged with a peak due to the shed vortex that is slightly higher at 26%. There is also a band of increased turbulence associated with the blade wakes. The individual turbulence intensities (*Figures 4.21f–h*) all follow a similar pattern though the $\sqrt{\overline{w^2}}$ intensity is a little messy. They have all dropped by roughly the same proportion from slot 8 to 20% for the streamwise and tangential intensities and 24% for the spanwise intensity.

The velocity correlations (*Figures 4.21i–k*) continue the changes seen over the previous slots. The $\overline{uv}$ correlation is now clearly negative in the passage vortex region though there is now a positive region roughly coincident with the shed vortex. Across the blade wake there is a sign change in the correlation consistent with the shed boundary layer profiles from the two surfaces. The $\overline{uw}$ correlation is still negative in the passage vortex region though has weakened slightly and as with the $\overline{uv}$ correlation there is now a smaller positive region to the pressure surface side of the wake. The negative region due to the corner vortex is still visible but has spread along the endwall possibly indicating the onset of transition in this boundary layer. Finally the $\overline{vw}$ correlation is now positive in the region associated with the passage vortex though is negative in most of the wake.

The pitch averaged yaw angle (*Figure 4.22a*) shows a peak of underturning to the midspan side of the passage vortex as well as the overturning seen close to the endwall. The midspan yaw angle, found as the average of the last three measurements, is slightly more than $-68°$ and is virtually constant from $140mm$. The secondary k.e. coefficient (*Figure 4.22b*) initially falls from the endwall before rising to a peak just before $80mm$. Continuing the trend from slot 5, however, the peak values have decreased considerably. The turbulent k.e. coefficient (*Figure 4.22c*) shows a similar pattern though the peak is further out at $85mm$ and has increased from slot 8. Both these factors appear to be due to the turbulence added by the shed vortex as the rise in k.e. close to the wall has continued to drop.

Despite being taken at a slightly low inlet velocity the area plots generally appear to agree well with those of Cleak [1989]. Though the total velocity contours are slightly low they show a very similar pattern as do the angle contours and the secondary velocity vectors. The turbulence k.e. and the individual turbulence intensities are also in very good agreement. The biggest difference between the results is in the $\overline{uw}$ velocity correlation (*Figure 4.21j*) where the negative region is considerably larger than found by Cleak [1989]. The $\overline{uv}$ correlation, however, is again in good agreement between the two sets of results.

Unlike the previous slots these results extend to midspan so it is possible to area mass–average the various parameters. This has been done and the results are presented in the table below along with hot–wire and 5–hole pitot probe measurements from Cleak [1989] (JGC) and 5–hole pitot probe measurements from Biesinger [1993] (TB). These latter values (JGC & TB) have been re–calculated from the raw data to ensure consistency of method (see section 4.1) with the present results so may differ slightly from previously publications. Pitch averages for the JGC & TB measurements are also presented (see *Figure 4.22*).

The results from Biesinger [1993] agree well with the present ones whilst those of Cleak [1989] are not so close. The cause of the differences is not certain though there is believed to be a systematic error in the JGC yaw angle measurements which are significantly lower than expected. The correlation of Ainley and Mathieson

	HM	JGC	TB
Yaw angle	−68.3°	−67.0°	−68.3°
Midspan yaw angle	−68.4°	−67.4°	−68.3°
Secondary K.E.	0.016	0.029	0.017
Midspan secondary K.E.	0.001	0.001	0.000
Turbulent K.E.	0.023	0.029	–
Midspan turbulent K.E.	0.012	0.016	–
Loss	–	0.180	0.170
Midspan loss	–	0.096	0.097
Mixed out loss	–	0.206	0.189
Midspan mixed out loss	–	0.096	0.098

Table 4.6 — Slot 10 mass averaged results

[1951], for example, gives an exit flow angle of −68.9° which is in reasonable agreement with the HM and TB measurements but is $\sim 1.5°$ away from that of JGC. An incorrect yaw angle will also affect the calculation of mixed–out loss which may explain why the midspan value is no higher than that at slot 10.

One possible cause of the differences in the JGC results is that the endwall belt (Walsh [1987]) was taped down by Biesinger [1993], because he found it affected his measurements, but may not have been by Cleak [1989]. If it flapped slightly, as is likely, it may well be the cause of the thicker inlet boundary layer he found than did either Biesinger [1993] or the present author (see Table 4.5). A thicker inlet boundary layer results in an increased overall loss and greater secondary k.e. (as predicted by classical secondary flow theory, found experimentally by Cleak [1989] and modelled by Moore [1985] & Cleak [1989]) which would explain the differences between JGC and those of TB and HM. Overall, since the agreement between the HM and TB results is good it seems reasonable to assume that these are correct and so will be the values used in the remainder of this work.

4.4 Intermittency measurements

Intermittency measurements have been taken close to both the endwall and the blade surfaces using the technique described in section 3.5.2. On the endwall 17 measurements were taken at slot 1, 16 at slots 2 to 8, 20 at slot 9 and 21 at slot 10. Those at slot 1 were taken at the same tangential positions as the previous measurements whilst the others were all evenly spaced. On the blade surfaces 16 measurements were taken at each slot (slots 2–8) from 1.5mm to 100.0mm from the endwall. All measurements were taken at a distance of 1.0mm from the surface.

4.4.1 Endwall

The results for each slot are shown in the graphs in *Figure 4.23*. For those slots within the blade passage (2–8) the edges of the graph indicate the location of the blade surfaces, with the suction surface on the left. At slot 1 the intermittency is high ($\eta > 0.8$), corresponding to the turbulent inlet boundary layer, with a dip towards the centre of the blade passage away from the horseshoe vortex. At slot 2 (6% C_{ax}, $-170mm$) there is a distinct peak close to the suction surface in the region of separation caused by the suction side leg of the horseshoe vortex and high values ($\eta > 0.9$) towards the pressure surface due to the passage vortex. The drop in intermittency adjacent to the suction surface corresponds to the region of reattachment caused by the horseshoe vortex.

This drop is still evident at slot 3 (22% C_{ax}, $-141mm$) as the passage vortex is only just beginning to cross the passage (see *Figure 4.13d*) by this point. The peak of intermittency now corresponds to the point of separation of both the horseshoe and passage vortices but it remains high under most of the passage vortex. Behind the passage vortex (close to the pressure surface), where the new boundary layer forms, the intermittency decreases. This continues as the passage vortex moves towards the suction surface so that by slot 7 (87% C_{ax}, $-24mm$) the flow over much of the endwall is essentially laminar ($\eta < 0.3$). Close to the pressure surface, however, the intermittency rises rapidly due to the effect of the passage vortex and corner vortex, once the passage vortex has moved away from the endwall.

Downstream of the blades there is high intermittency associated with the turbulent blade wakes and corner vortex. Away from these the intermittency is lower but increases from slot 8 to slot 10 (128% C_{ax}, $51mm$) indicating transition in the new endwall boundary layer. A clearer picture of the boundary layer state is obtained by converting these results to a contour plot on the plane $1.0mm$ from the endwall. This is shown in *Figure 4.24* along with one of the turbulent k.e. at $1.5mm$ from the endwall in *Figure 4.25*. *Figure 4.24* shows clearly the bands of high intermittency associated with the horseshoe and passage vortices and the much lower levels in the new endwall boundary layer. The onset of transition after the trailing edge plane is also visible.

The turbulent k.e. plot (*Figure 4.25*) shows broad agreement with the intermittency contours. High levels of turbulence are found close to the suction surface, due to the passage and corner vortices, but elsewhere the values are low. The main difference between the two plots is there is little evidence of a band of high turbulence crossing the passage from the pressure surface side of the leading edge. This may be because the turbulence measurements were taken further away from the endwall or more simply that, though turbulent, the intensity here is not that great. Overall the results are in broad agreement with the hot–film measurements of Harrison [1989] who also found the new endwall boundary layer to be initially laminar, away from the passage vortex, with transition occurring near the trailing edge plane.

4.4.2 Suction surface

The suction surface intermittencies at slots 2–8 are shown in *Figure 4.26* along with a contour plot in *Figure 4.27*. This latter plot shows the variation of intermittency with axial position, not surface length, starting at 6% of axial chord and ending at 97%. In the spanwise direction measurements extend over one quarter span. The total velocity contours (section 4.3) and surface static pressure distribution (Cleak [1989]) show the flow accelerates rapidly over the first 25% C_{ax} before generally decelerating more slowly to the trailing edge. The spanwise component of velocity caused by the passage vortex does, however, cause a further increase of total velocity over part of the span further down the blade.

The strong initial acceleration ensures the boundary layer remains initially laminar away from the endwall. Close to the endwall first the horseshoe vortex and then the passage vortex keep the flow turbulent and cause the rapid rise in intermittency evident in *Figures 4.26 & 4.27.* This region becomes wider as the passage vortex grows in size and begins to move away from the endwall. From slot 5 (55% C_{ax}, $-81mm$) onwards the corner vortex and passage vortex produce two distinct peaks with a drop in intermittency between them. This is also evident in the turbulent k.e. plots (section 4.3) which show the two vortices becoming separate features from this point. Towards midspan the intermittency begins to rise from slot 6 (71% C_{ax}, $-52mm$) indicating transition in the boundary layer. This agrees reasonably well with both the stress measurements (section 4.3) and the location of the separation bubble that was found with low freestream turbulence (Walsh [1987]).

4.4.3 Pressure surface

Pressure surface intermittency measurements were obtained in the same way as those on the suction surface and are shown in *Figures 4.28 & 4.29.* On this surface the flow initially decelerates slowly to approximately 40% C_{ax} before accelerating at an increasing rate to the trailing edge. A slight initial acceleration around the leading edge causes the boundary layer to maintain some laminar characteristics at slot 2 (6% C_{ax}, $-170mm$) leading to $\eta \approx 0.6$ but this has increased to 0.8 by slot 3 (22% C_{ax}, $-141mm$) due to the adverse pressure gradient. From here to the end of the blade the intermittency drops steadily over most of the surface as relaminarisation occurs in the accelerating flow.

The exceptions to this are in the endwall corner where there is a growing peak and a small rise evident at slots 5 to 7 between 20 & $30mm$ from the endwall. The former is consistent with the formation of a corner vortex by the action of the secondary flow which separates from the pressure surface a short distance from the endwall. That it remains much smaller than the corresponding vortex in the suction surface corner would be due to the strong acceleration of the flow from slot 4 (38% C_{ax}, $-112mm$) onwards. However, the design of the blades is such that there is a small gap ($3.0mm$) between them and the endwall which is filled by a felt pad and it is possible that this is causing some turbulence to be generated.

The other rise in intermittency may be due to experimental error (particularly at slot 7) but the region where it occurs does correspond to the position of maximum negative pitch angle on the pressure surface. This happens where the secondary flow due to the passage vortex just impinges on the pressure surfaces so may disturb the flow sufficiently to cause the intermittency rise. By slot 8 (97% C_{ax}, $-5mm$) the secondary flow extends over the whole of the measured region giving a fairly uniform, slightly skewed, flow so no peak is evident.

4.4.4 Endwall profiles

On the endwall behind the passage vortex, where the new boundary layer is very thin, any growth in its thickness would considerably alter the relative position of the measurements in the boundary layer. Since intermittency varies through the boundary layer this could have an effect on the results. In order to test this, intermittency profiles were taken at slots 5 (55% C_{ax}) and 8 (97% C_{ax}) to see how it varies with distance from the surface. Seventeen measurements were taken at each of 6 tangential locations at slot 5 and 4 at slot 8 from $1.0mm$ to $5.0mm$ from the endwall. The results are shown in *Figures 4.30 & 4.31*, the numbers in the key referring the the tangential position of the profile.

At slot 5 the profiles towards the pressure surface side of the passage (low intermittency) show, if anything, a slight decrease away from the surface, though there is some scatter of the data. The profiles closer to the passage vortex increase away from the wall as they extend into the turbulent core. At slot 8 the intermittency remains virtually constant except for the profile closest to the suction surface which increases fairly rapidly close to the surface. This may reflect the turbulence generated by the corner vortex but it is also possible that there is some error in the results closest to the wall since they are considerably higher than the values found in the endwall traverse (section 4.4.1). Overall, however, it appears that the distance from the surface at which the measurements were taken had little effect on the results.

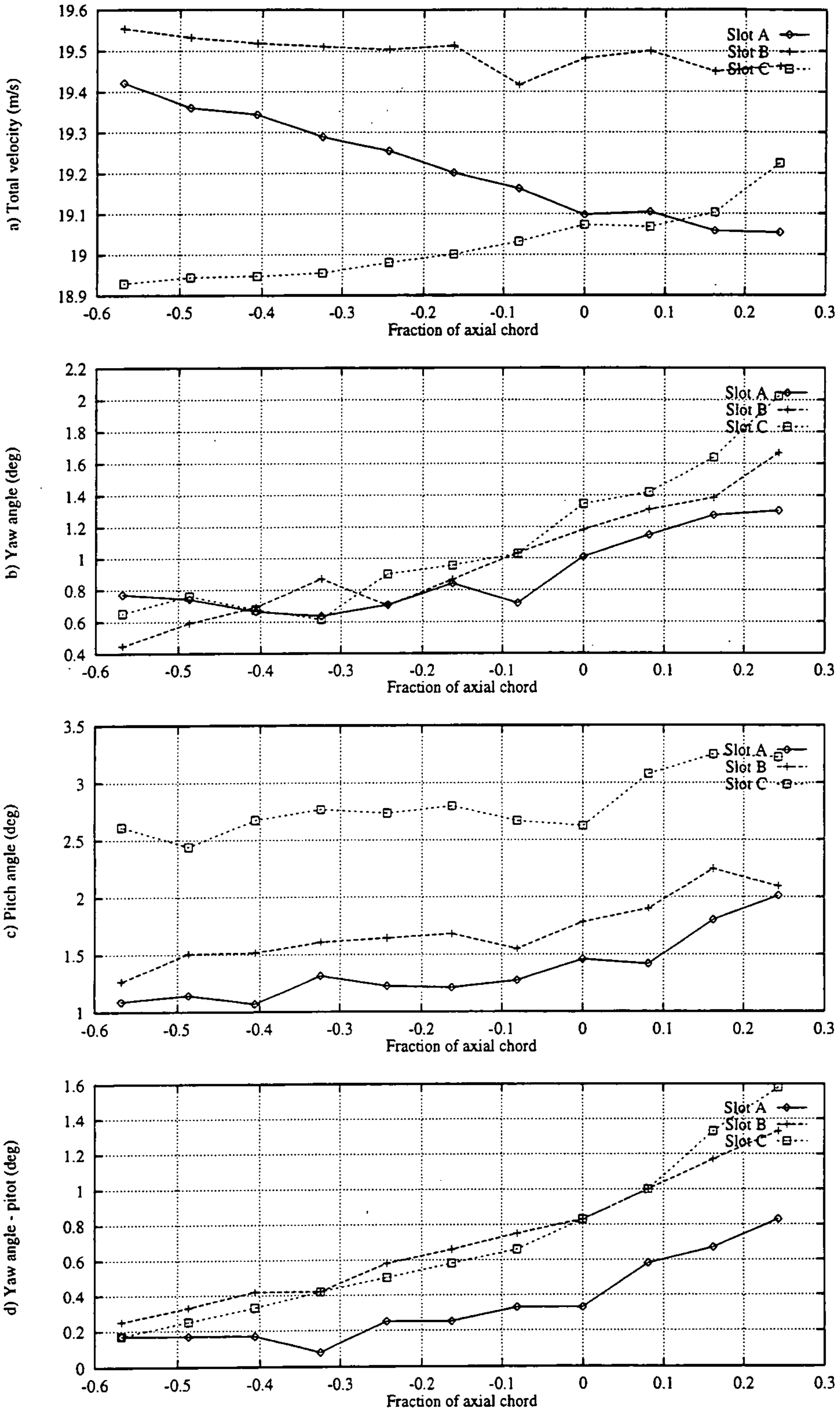

Figure 4.1 — Upstream mean flow conditions.

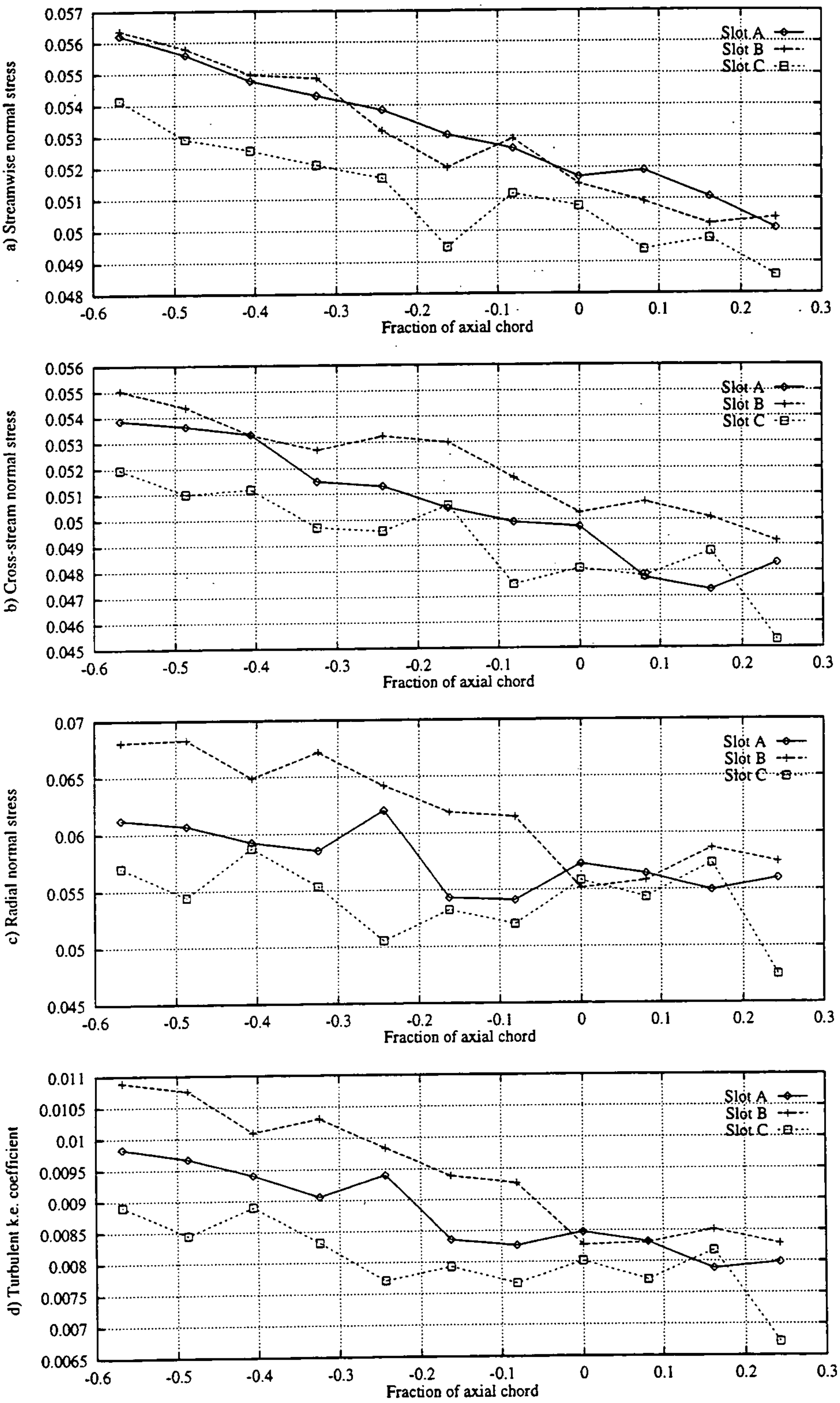

Figure 4.2 — Upstream turbulence quantities.

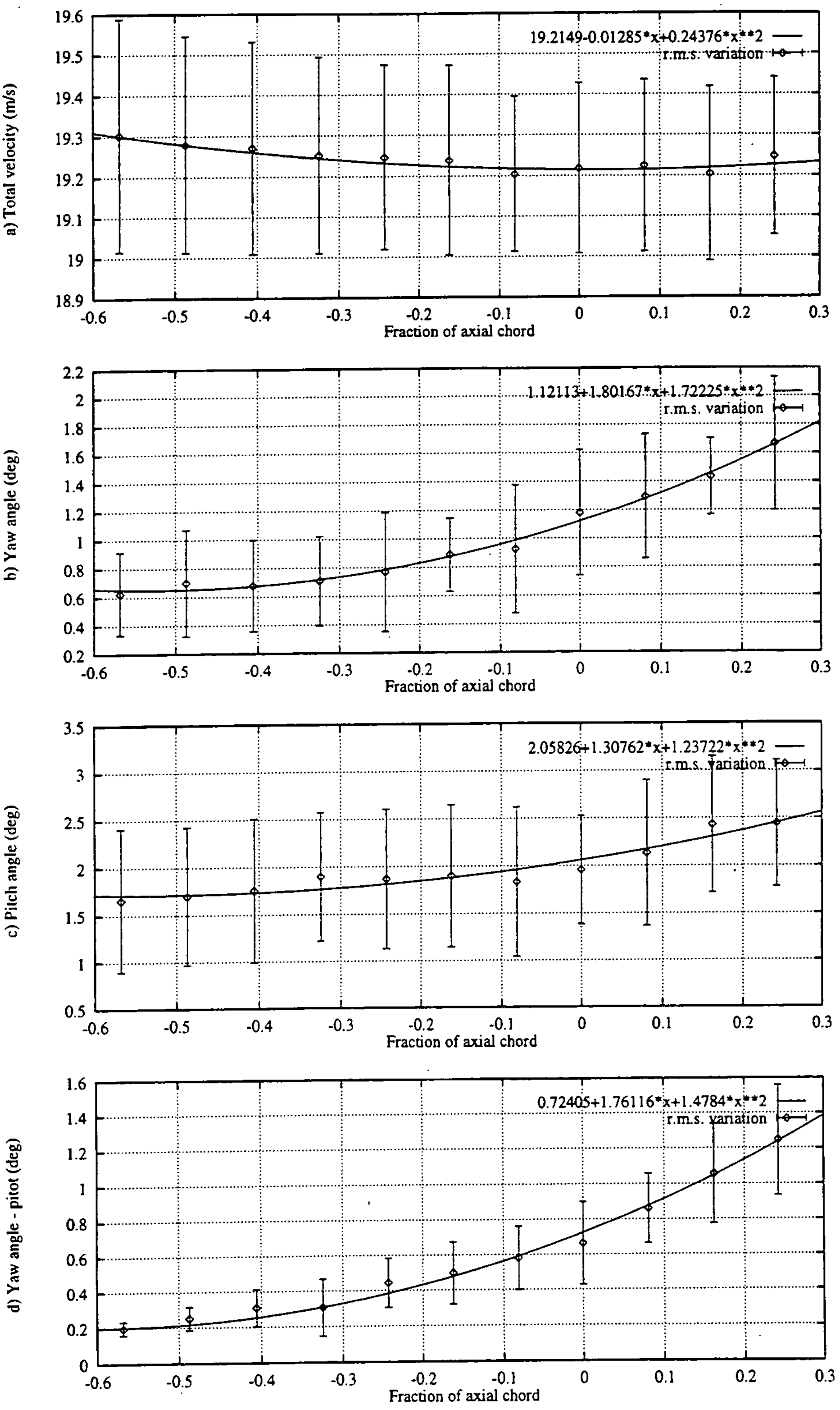

Figure 4.3 — Averaged upstream mean flow conditions.

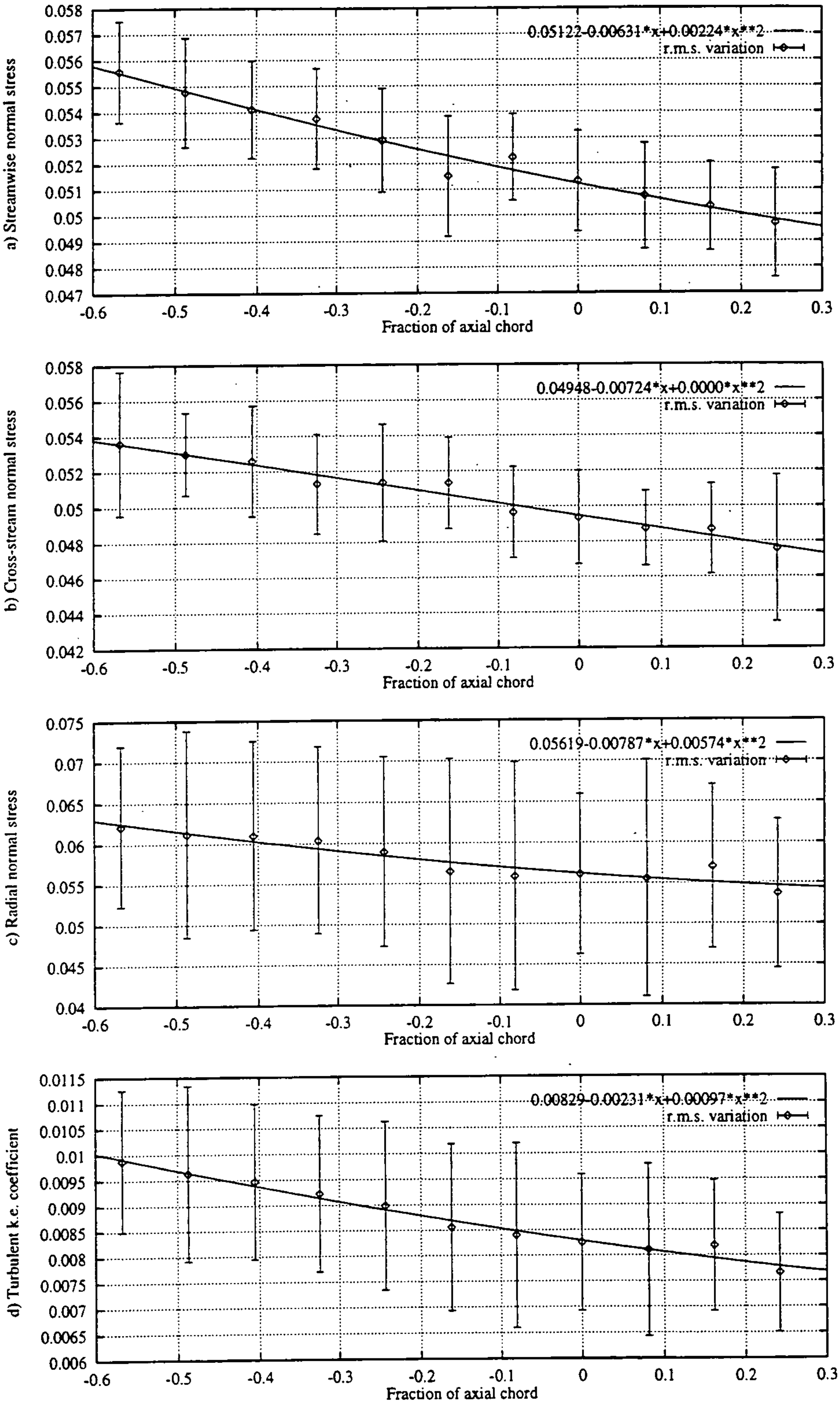

Figure 4.4 — Averaged upstream turbulence quantities.

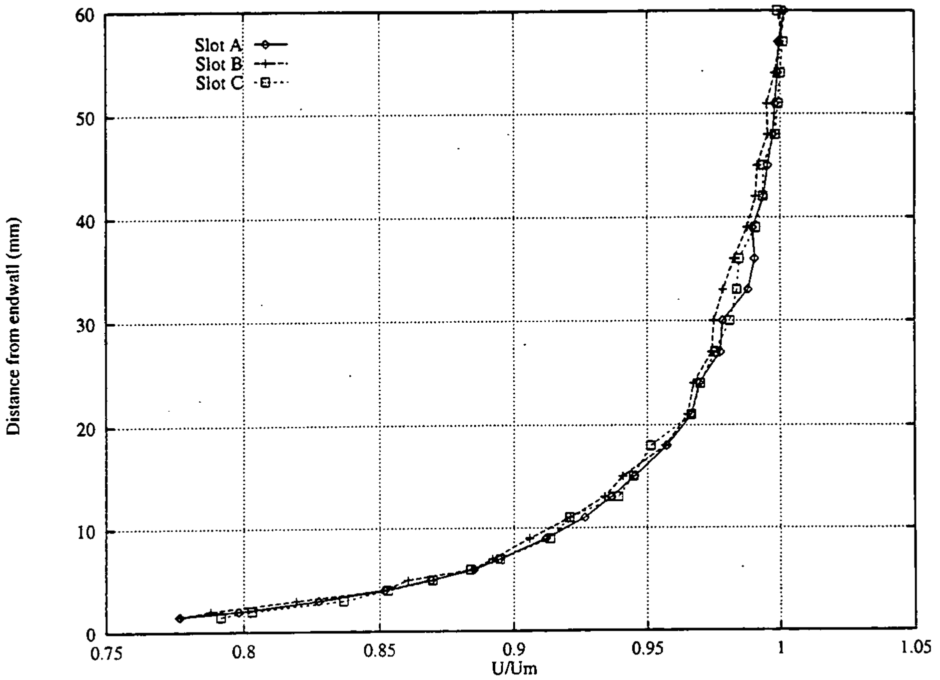

Figure 4.5 — Non–dimensional boundary layer velocity profiles.

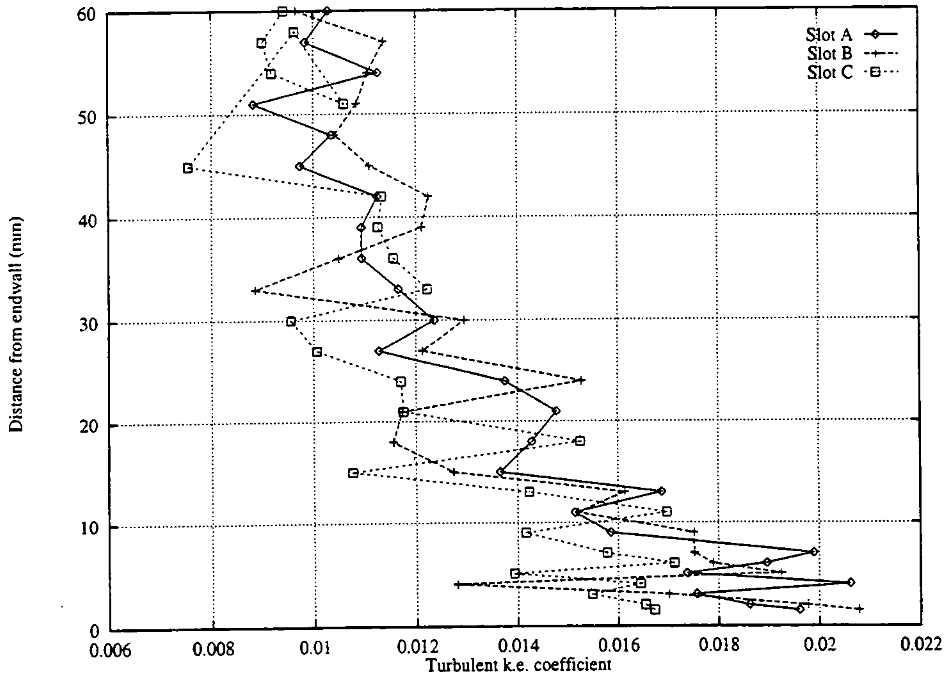

Figure 4.6 — Non–dimensional boundary layer turbulent k.e. profiles.

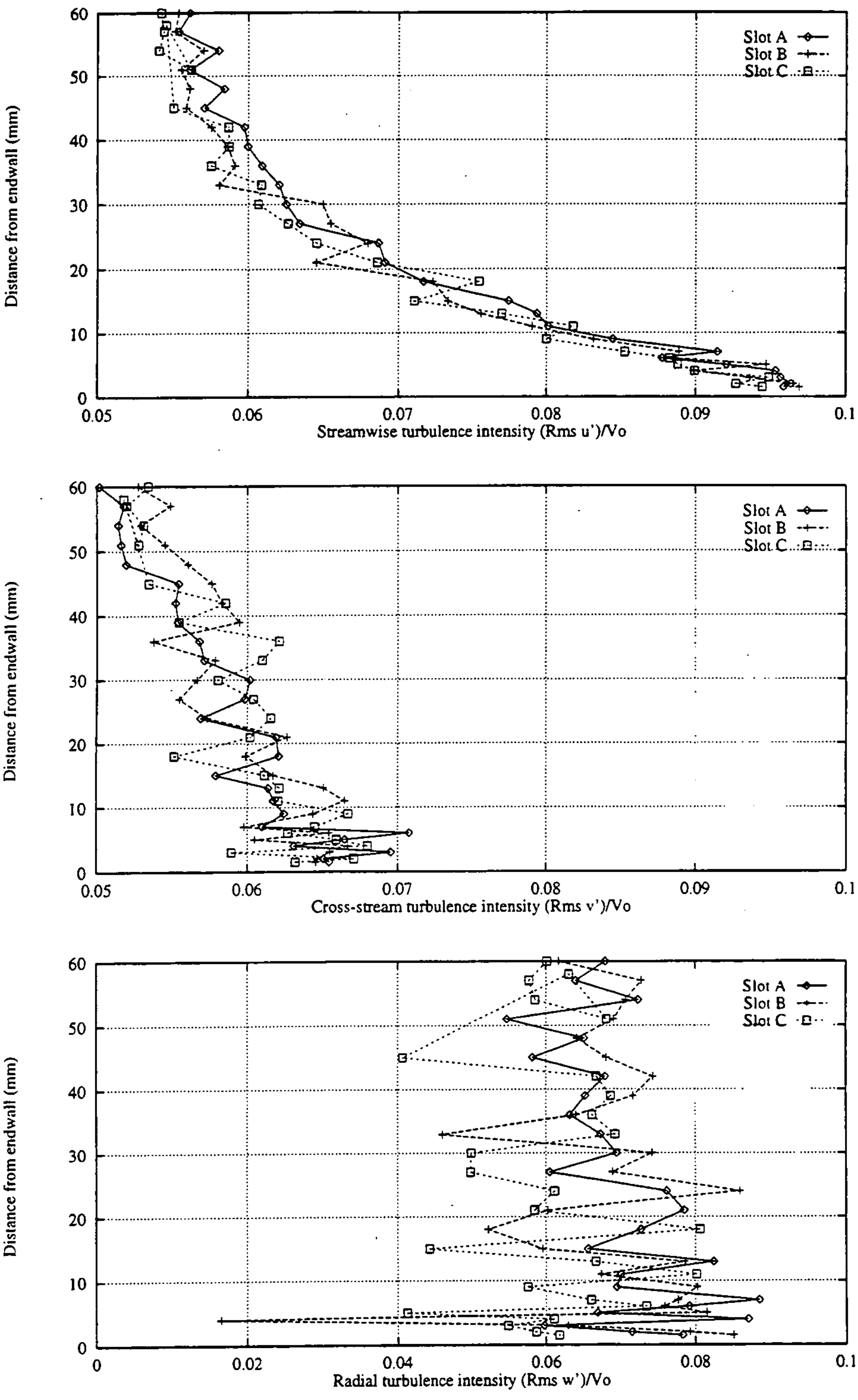

Figure 4.7 — Boundary layer turbulence intensities.

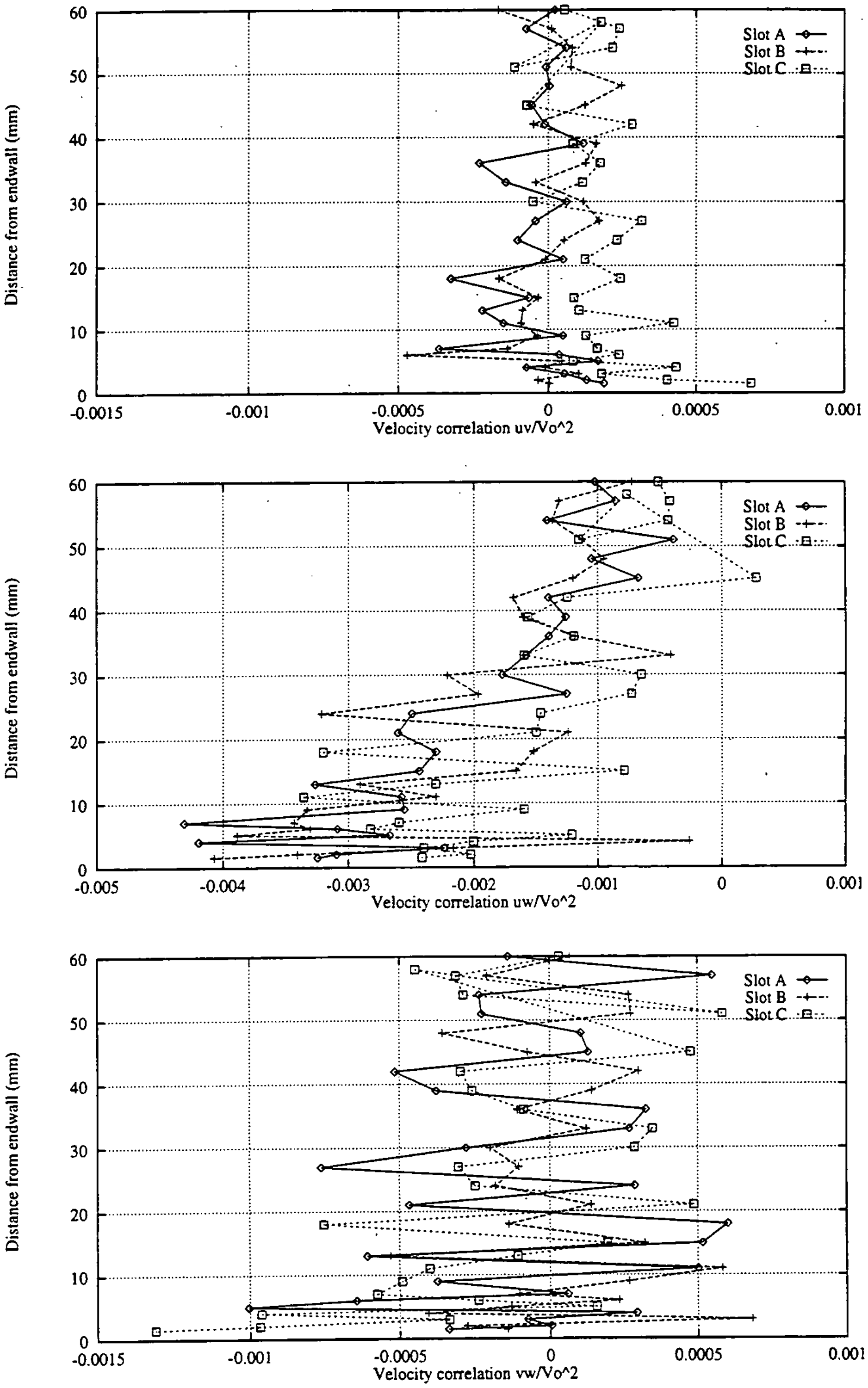

Figure 4.8 — Boundary layer velocity correlations.

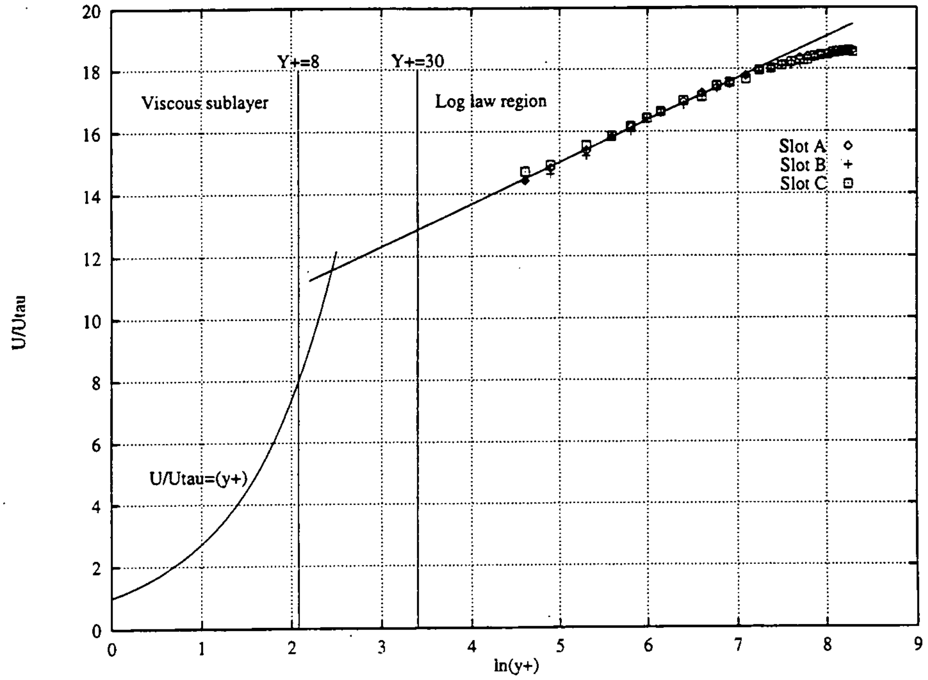

Figure 4.9 — Boundary layer log plot.

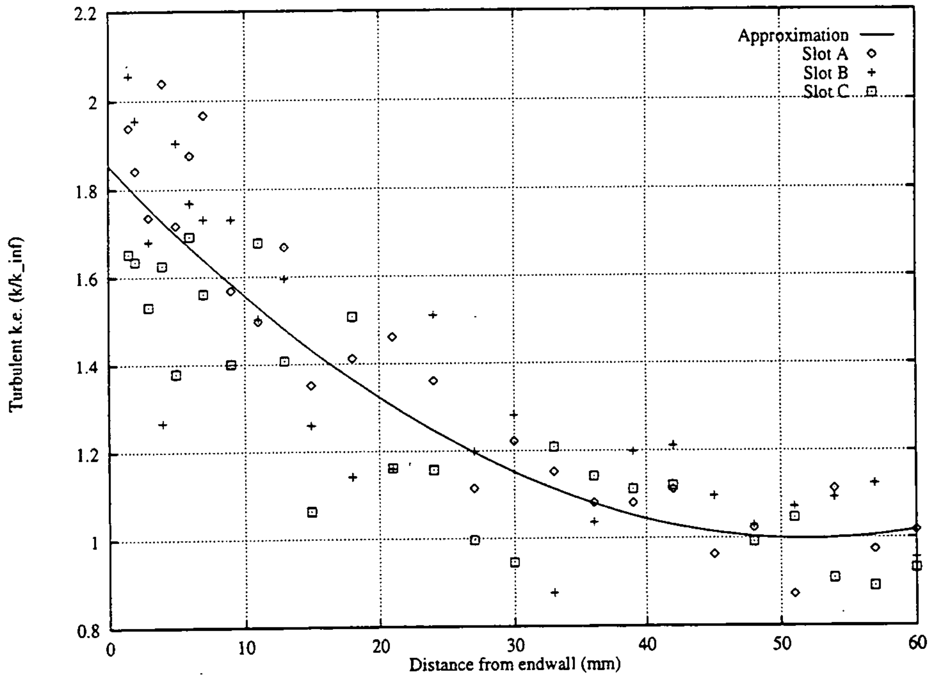

Figure 4.10 — Mean turbulent k.e. profile.

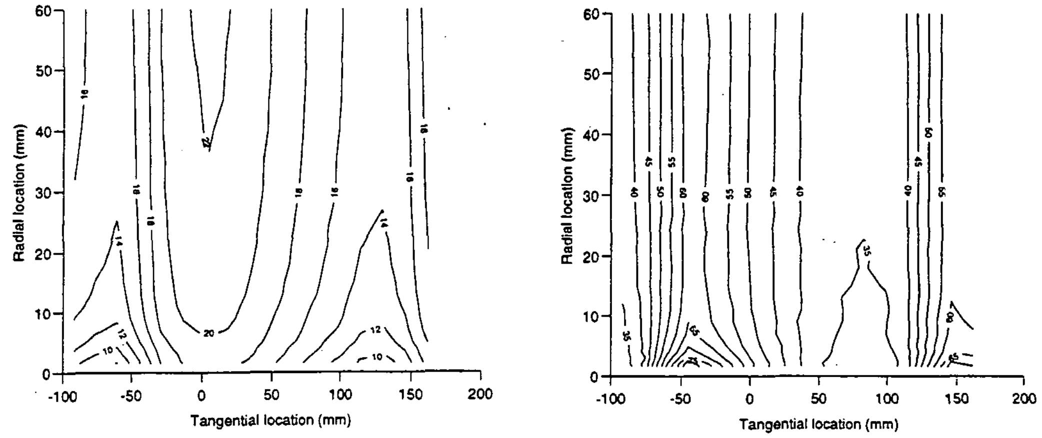

a) Total velocity magnitude (m/s)

b) Yaw angle (deg)

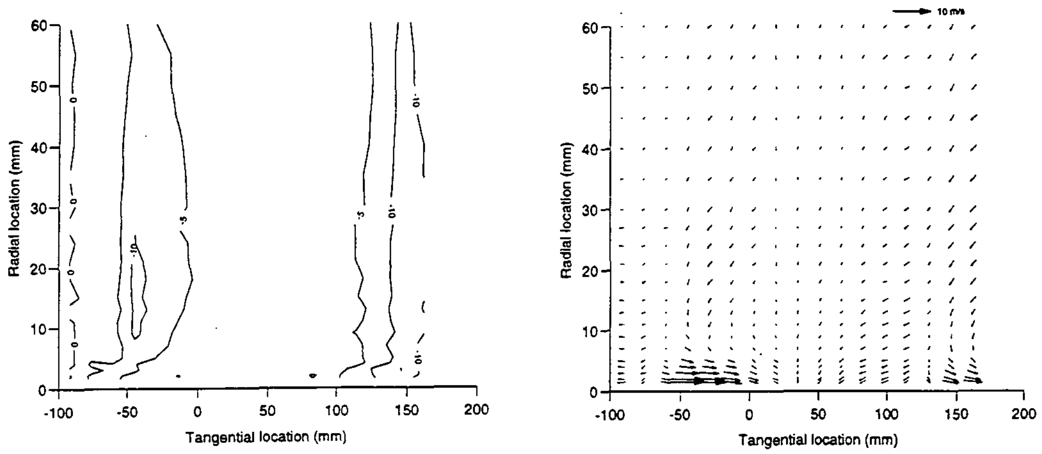

c) Pitch angle (deg)

d) Secondary velocity vectors

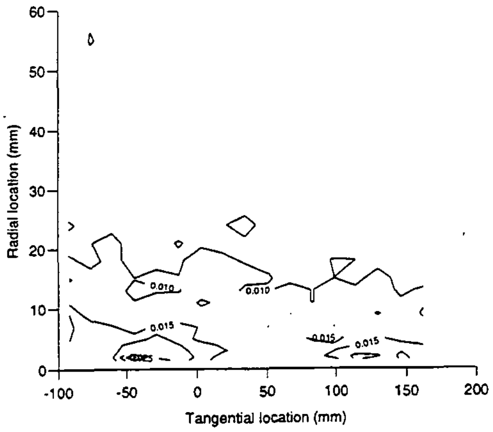

e) Non-dimensional turbulent k.e.

Figure 4.11 — Slot 1 Area traverses (a–e).

f) Turbulence intensity (rms u')/Vo

g) Turbulence intensity (rms v')/Vo

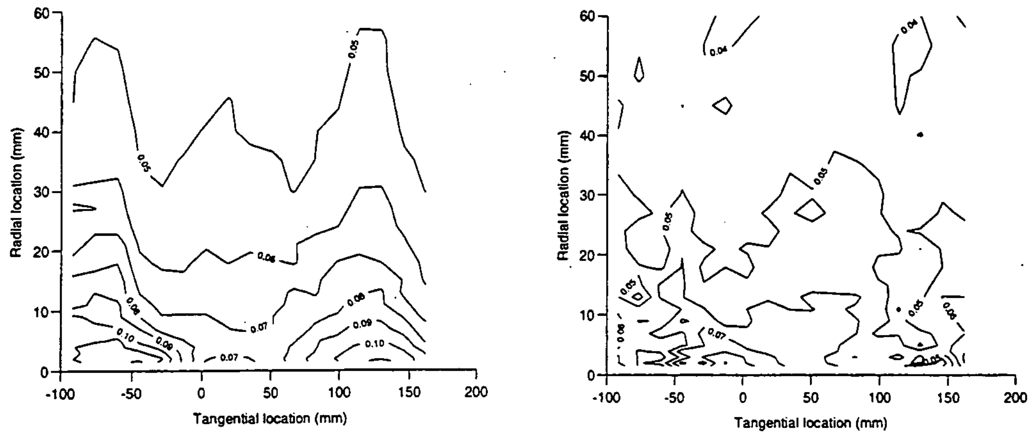

h) Turbulence intensity (rms w')/Vo

i) Velocity correlation uv/Vo^2

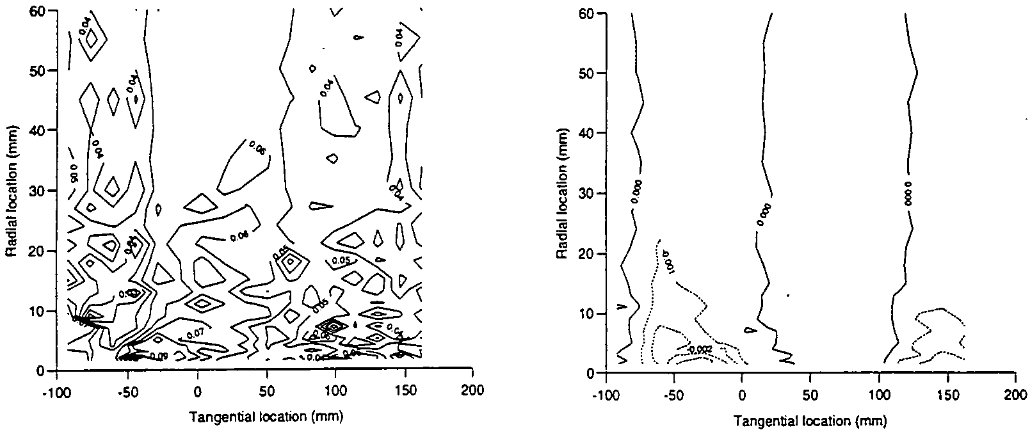

j) Velocity correlation uw/Vo^2

k) Velocity correlation vw/Vo^2

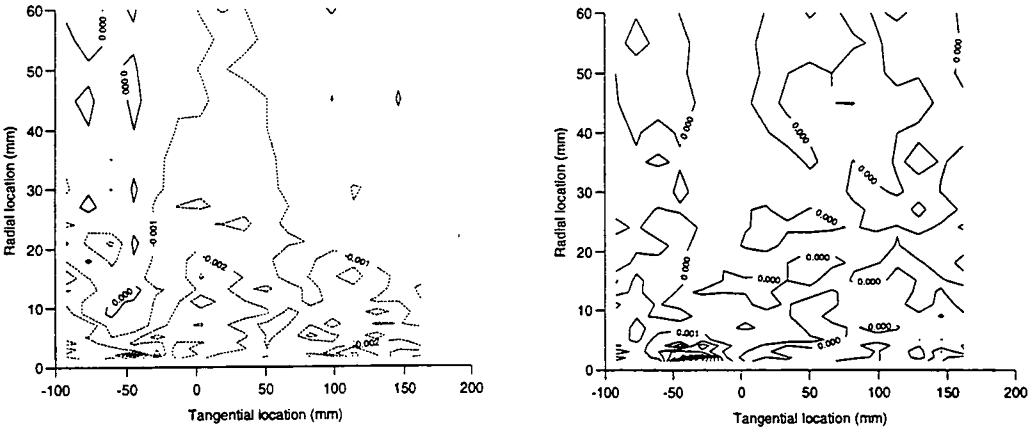

Figure 4.11 — Slot 1 Area traverses (f–k).

a) Yaw angle.

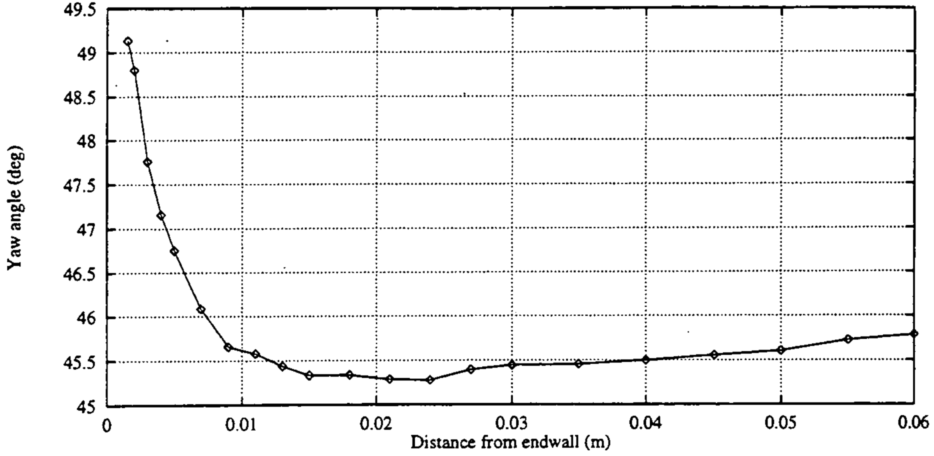

b) Secondary k.e. coefficient.

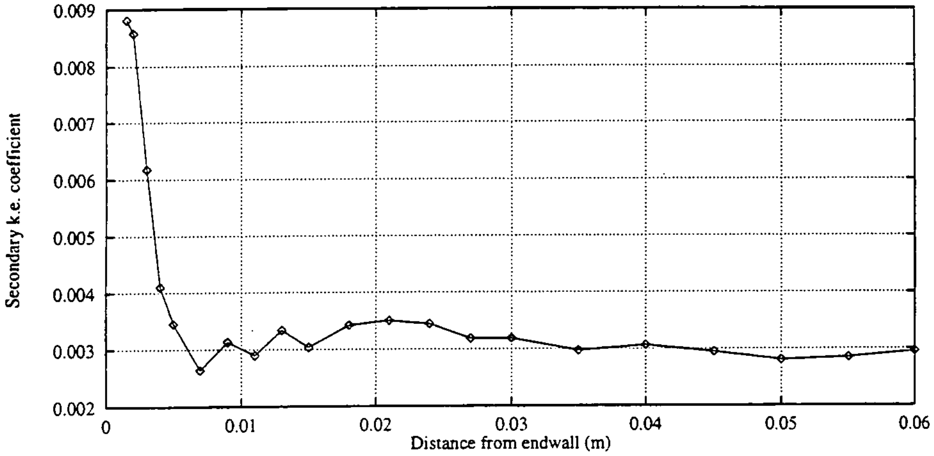

c) Turbulent k.e. coefficient.

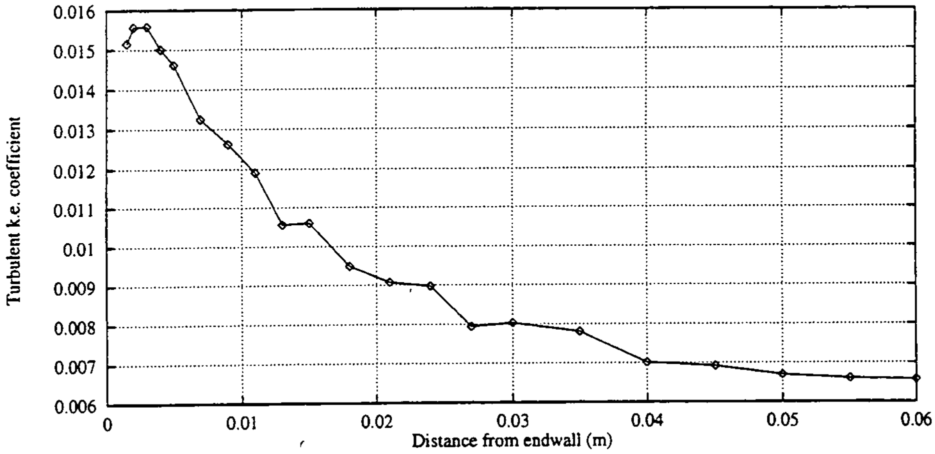

Figure 4.12 — Slot 1 Pitchwise mass averages.

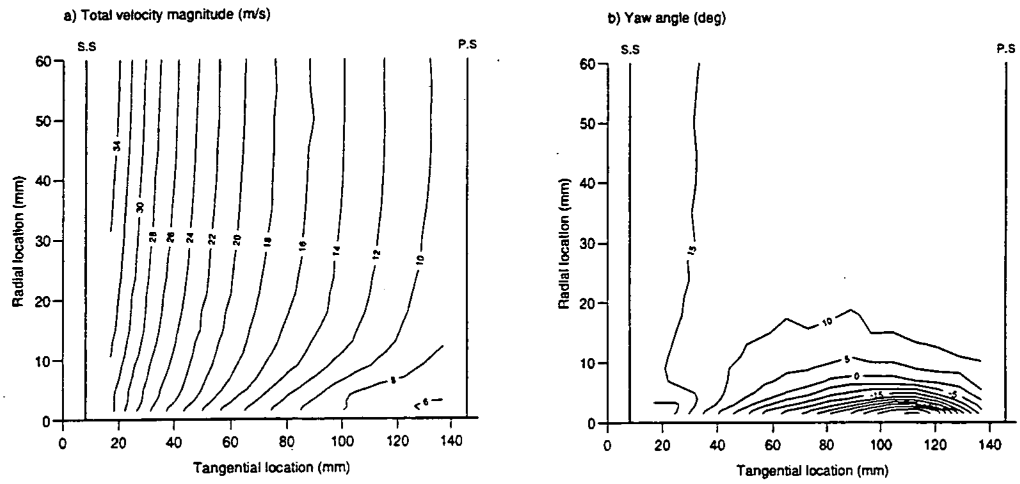

a) Total velocity magnitude (m/s)

b) Yaw angle (deg)

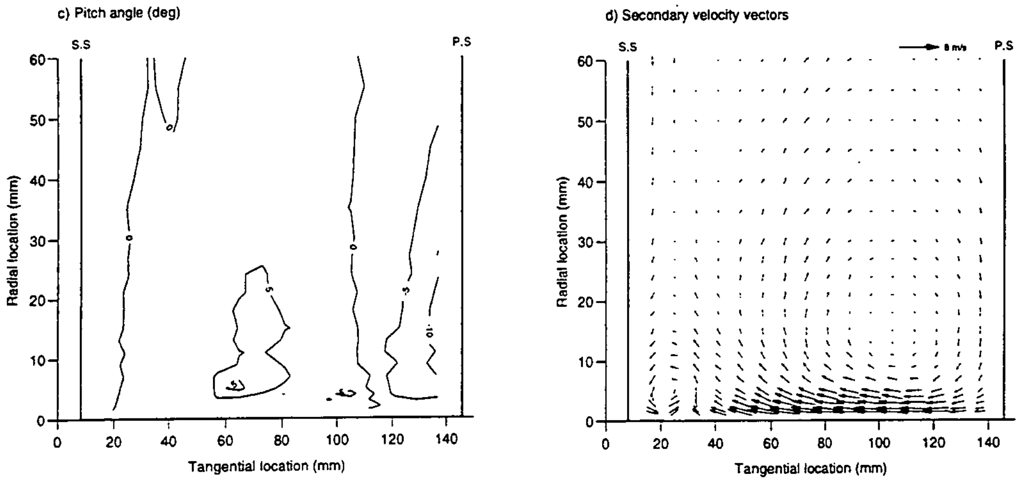

c) Pitch angle (deg)

d) Secondary velocity vectors

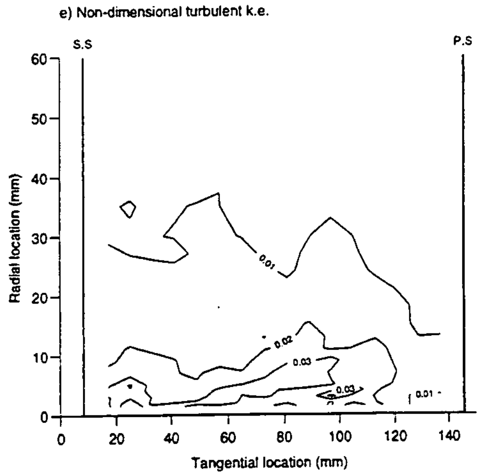

e) Non-dimensional turbulent k.e.

Figure 4.13 — Slot 3 Area traverses (a–e).

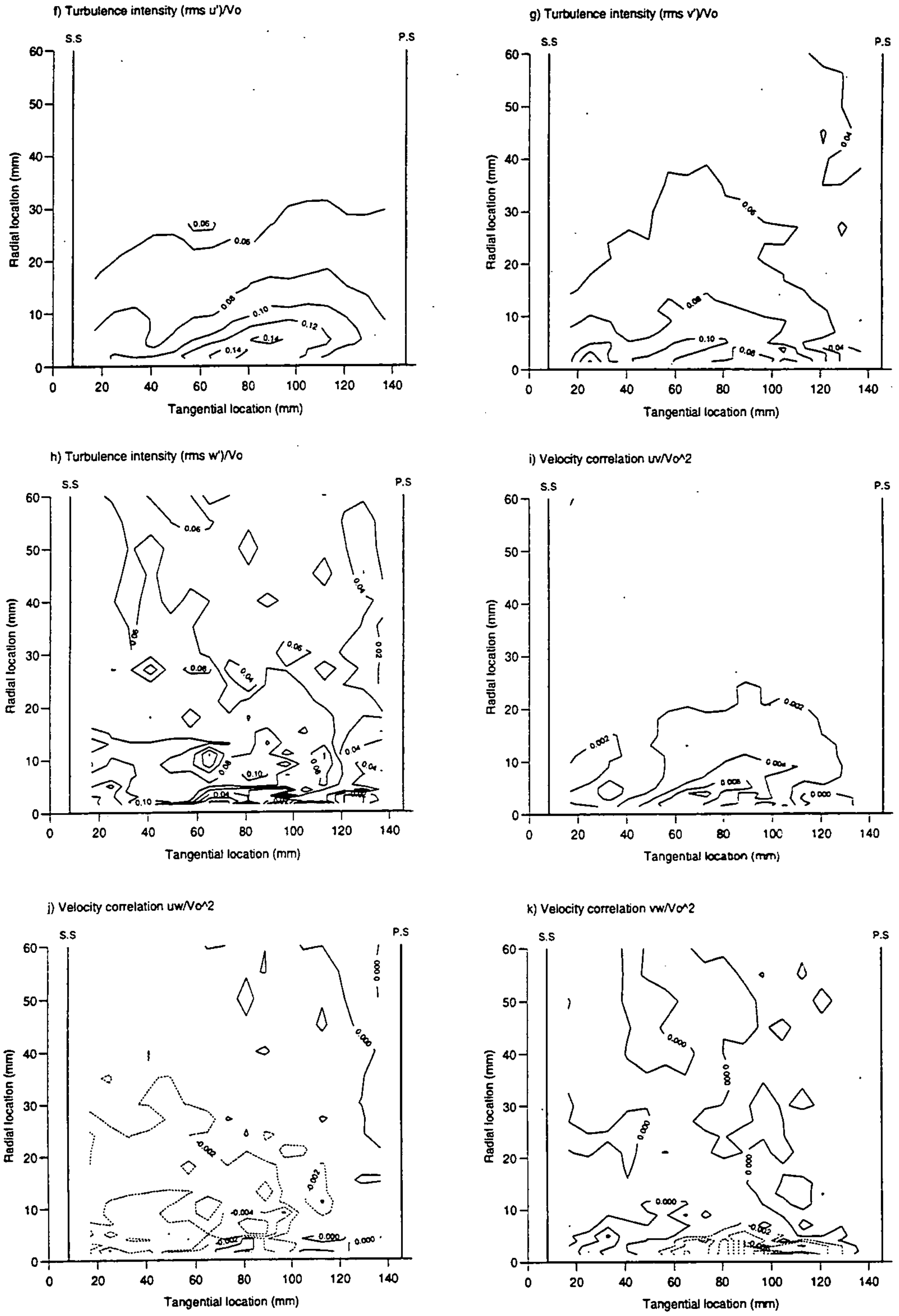

f) Turbulence intensity (rms u')/Vo

g) Turbulence intensity (rms v')/Vo

h) Turbulence intensity (rms w')/Vo

i) Velocity correlation uv/Vo^2

j) Velocity correlation uw/Vo^2

k) Velocity correlation vw/Vo^2

Figure 4.13 — Slot 3 Area traverses (f–k).

a) Yaw angle.

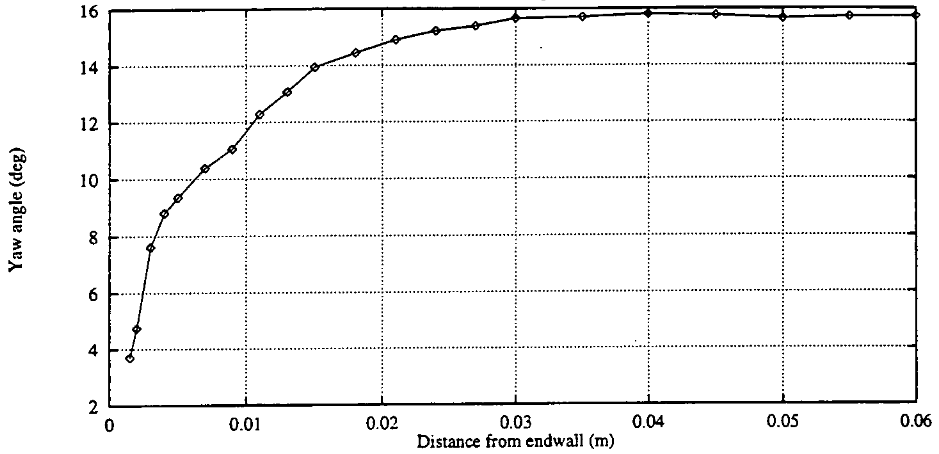

b) Secondary k.e. coefficient.

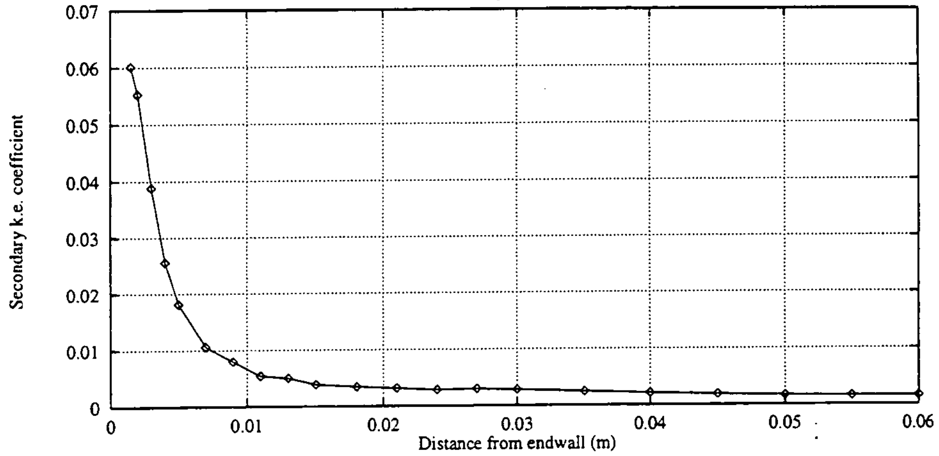

c) Turbulent k.e. coefficient.

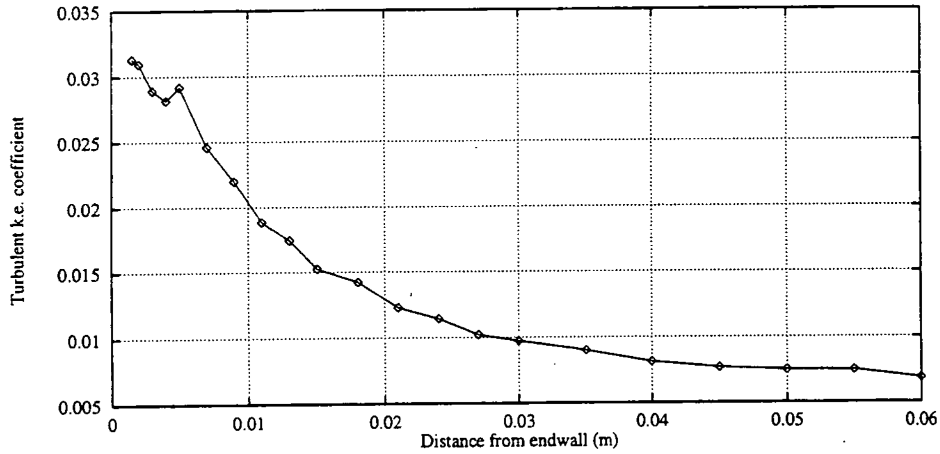

Figure 4.14 — Slot 3 Pitchwise mass averages.

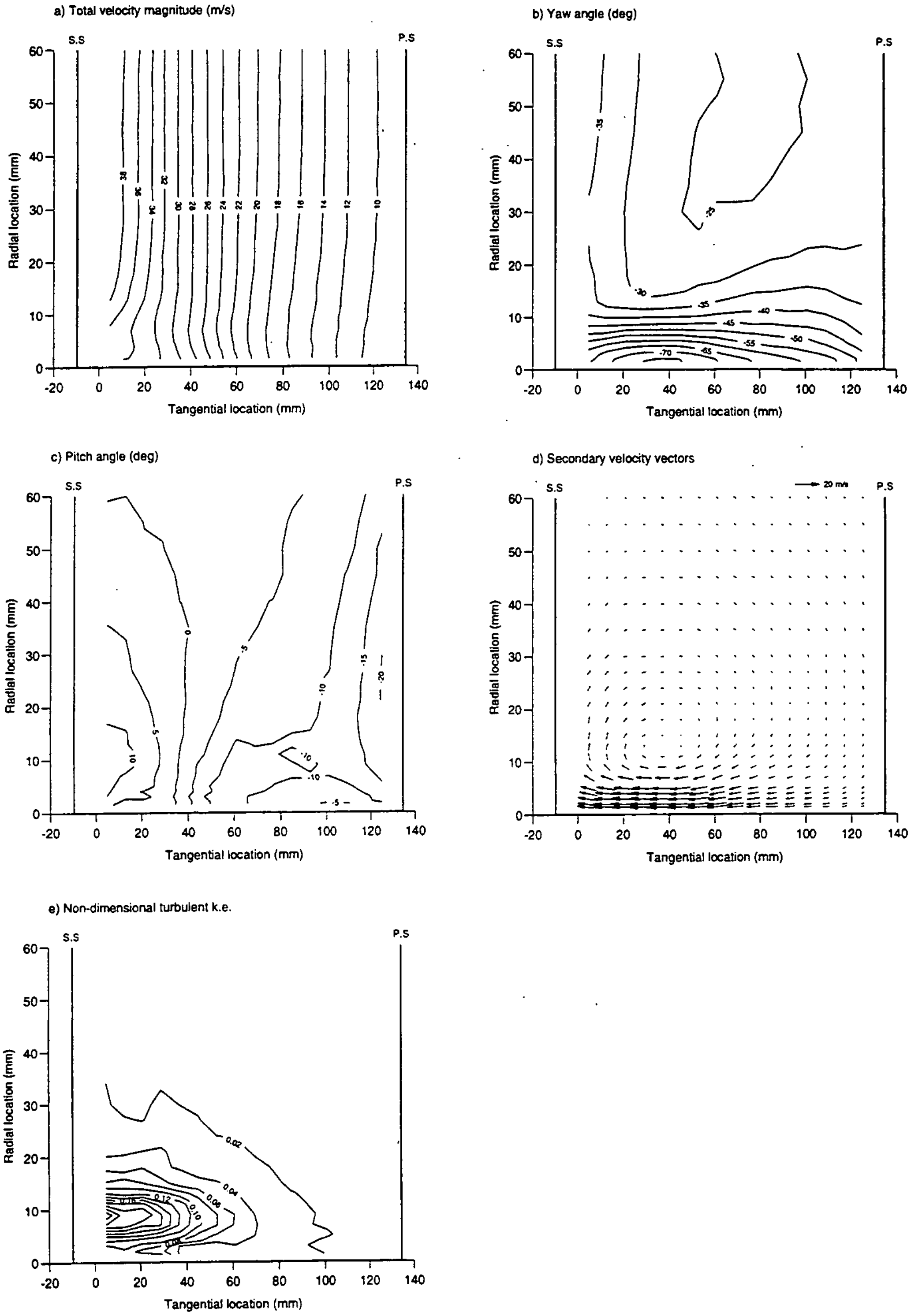

a) Total velocity magnitude (m/s)

b) Yaw angle (deg)

c) Pitch angle (deg)

d) Secondary velocity vectors

e) Non-dimensional turbulent k.e.

Figure 4.15 — Slot 5 Area traverses (a–e).

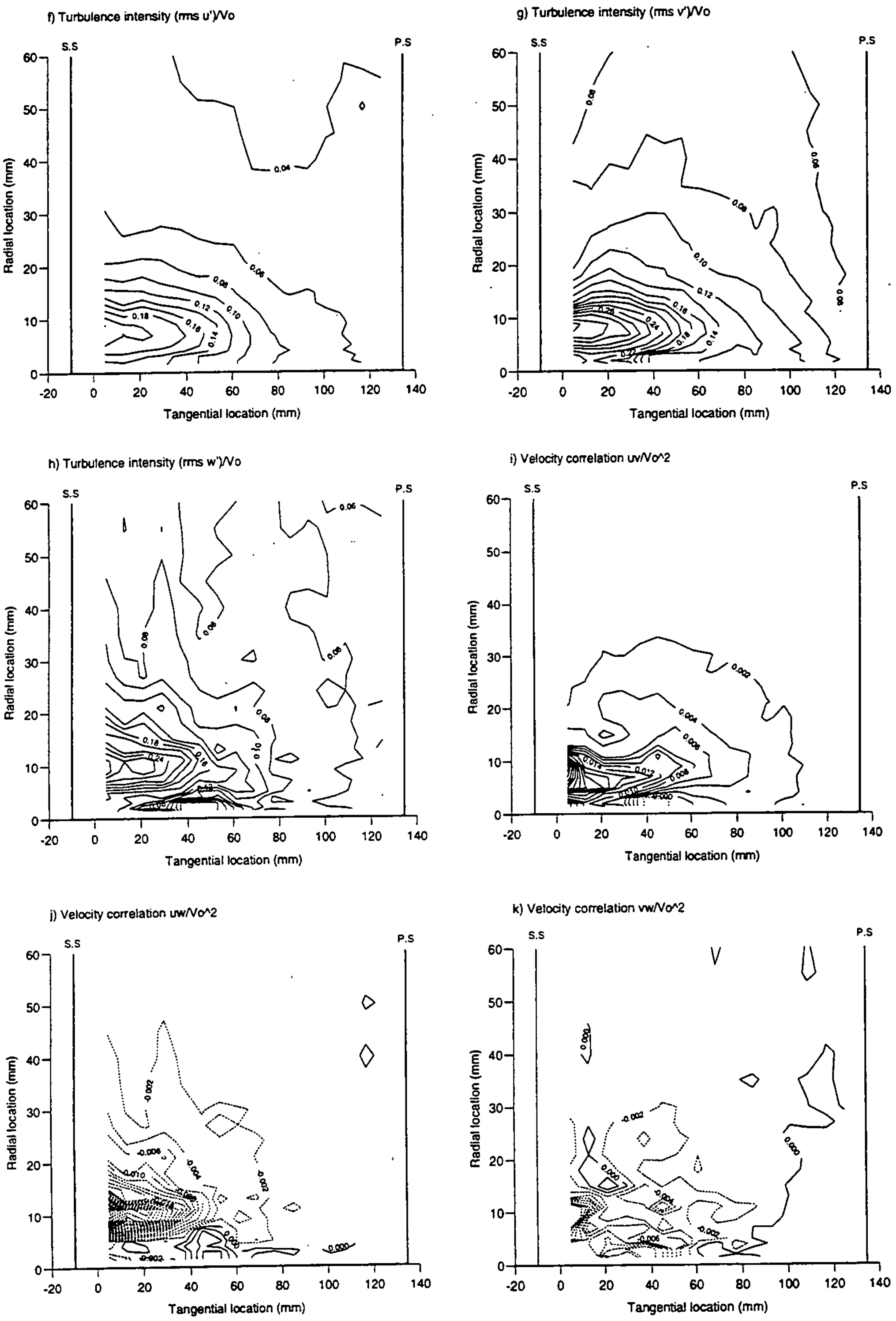

f) Turbulence intensity (rms u')/Vo

g) Turbulence intensity (rms v')/Vo

h) Turbulence intensity (rms w')/Vo

i) Velocity correlation uv/Vo^2

j) Velocity correlation uw/Vo^2

k) Velocity correlation vw/Vo^2

Figure 4.15 — Slot 5 Area traverses (f–k).

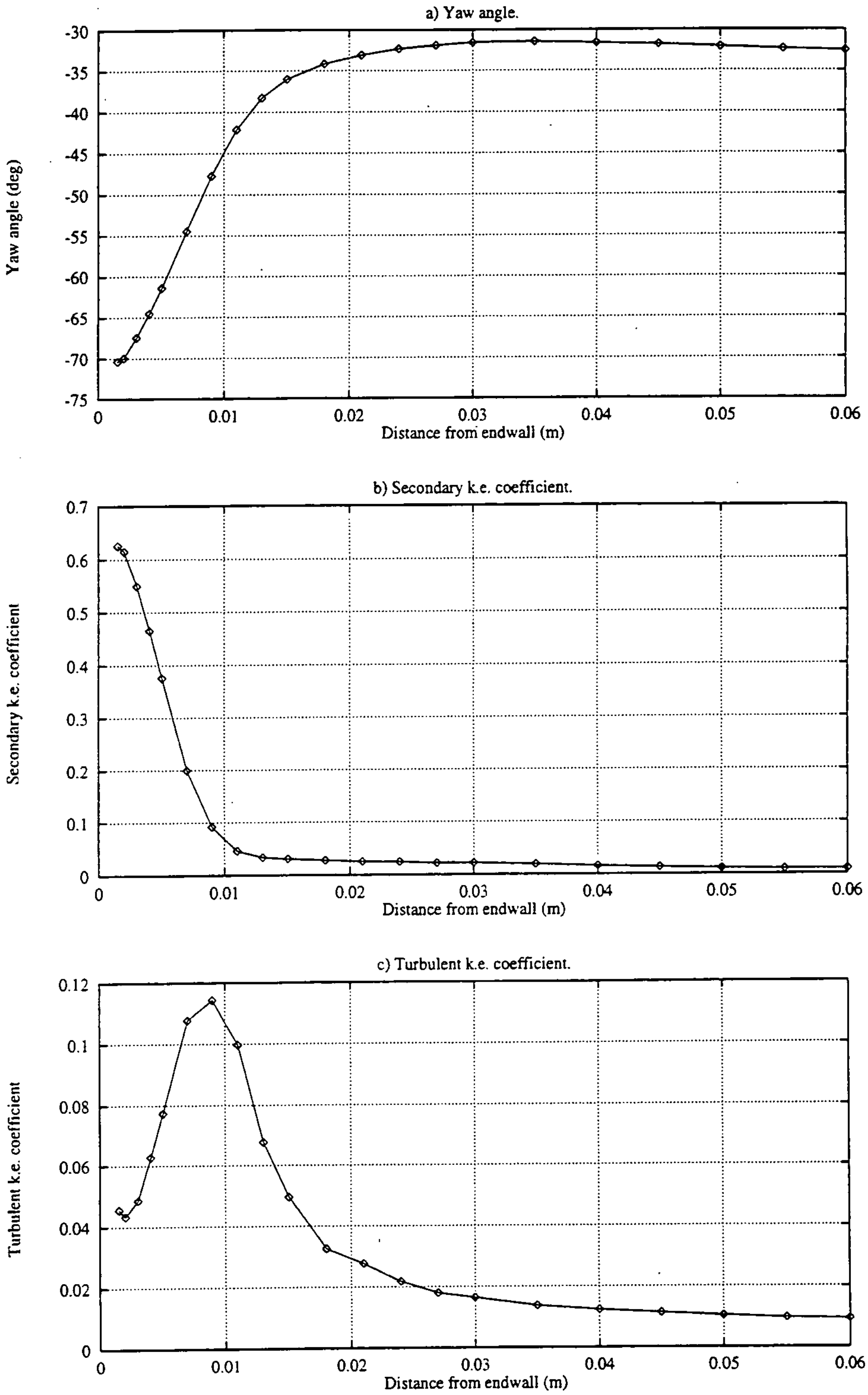

Figure 4.16 — Slot 5 Pitchwise mass averages.

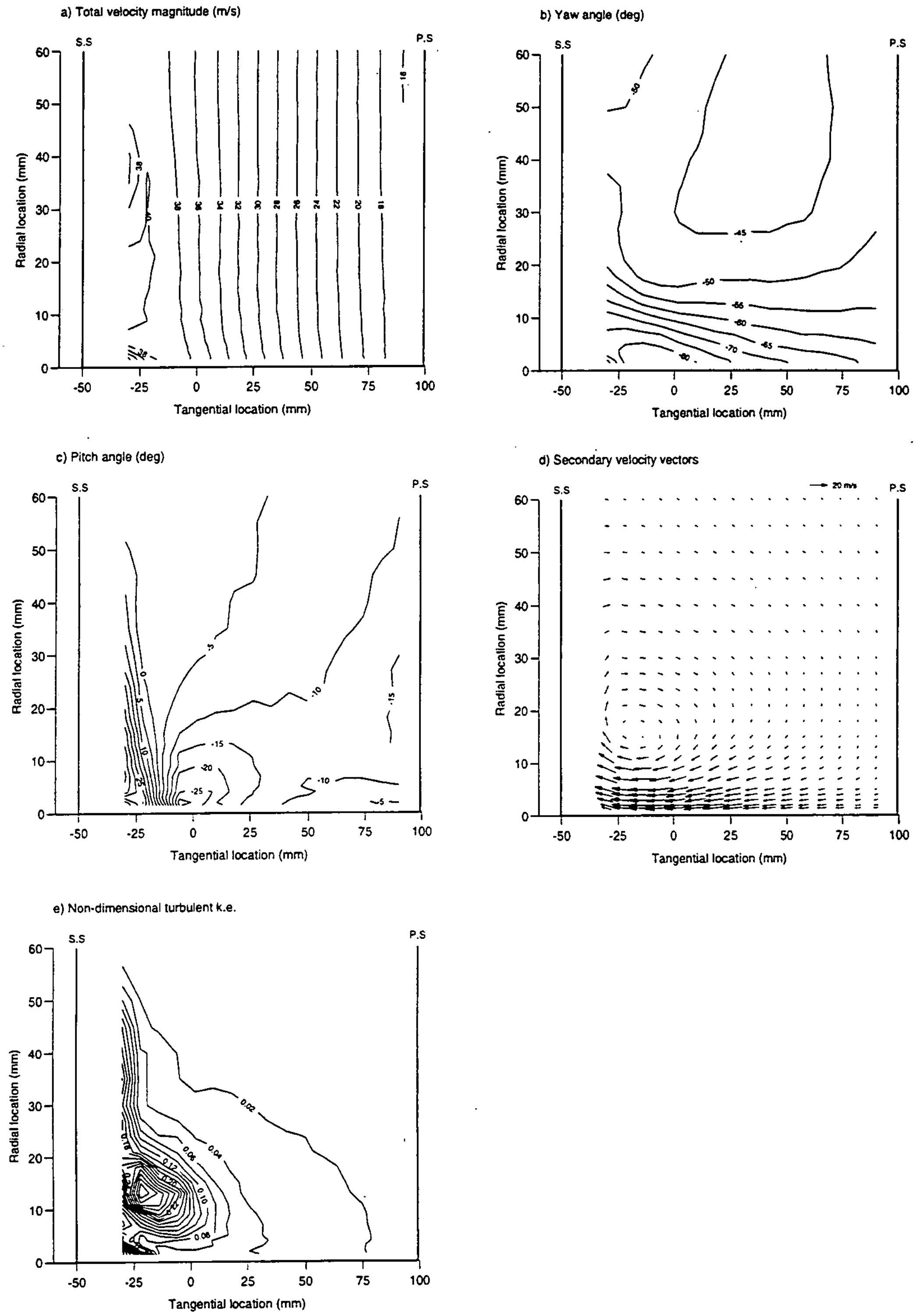
a) Total velocity magnitude (m/s)

b) Yaw angle (deg)

c) Pitch angle (deg)

d) Secondary velocity vectors

e) Non-dimensional turbulent k.e.

Figure 4.17 — Slot 6 Area traverses (a–e).

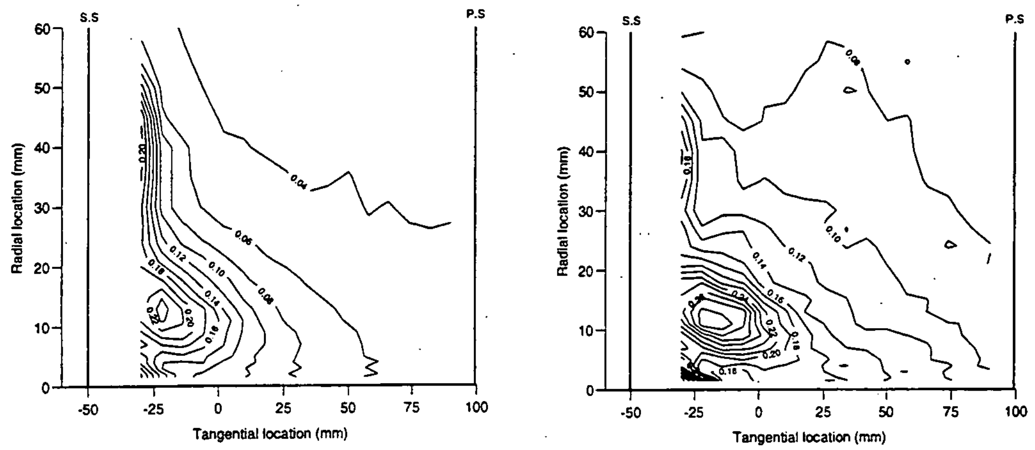

f) Turbulence intensity (rms u')/Vo

g) Turbulence intensity (rms v')/Vo

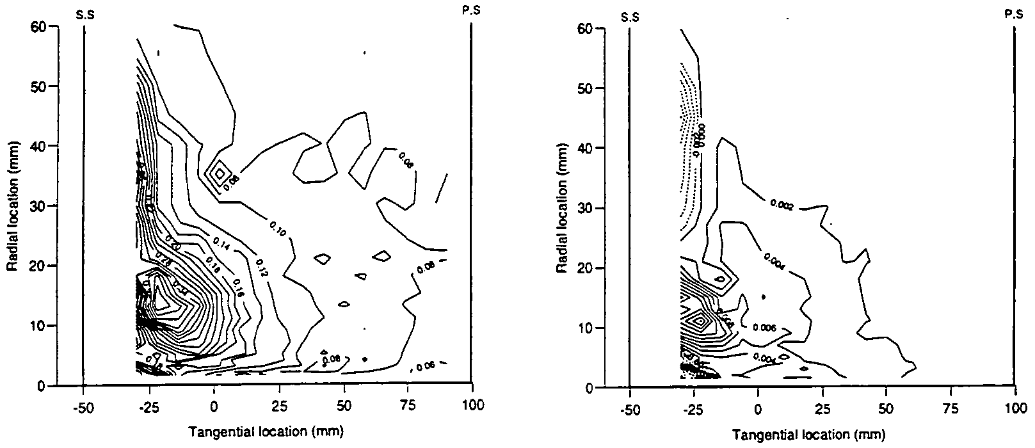

h) Turbulence intensity (rms w')/Vo

i) Velocity correlation uv/Vo^2

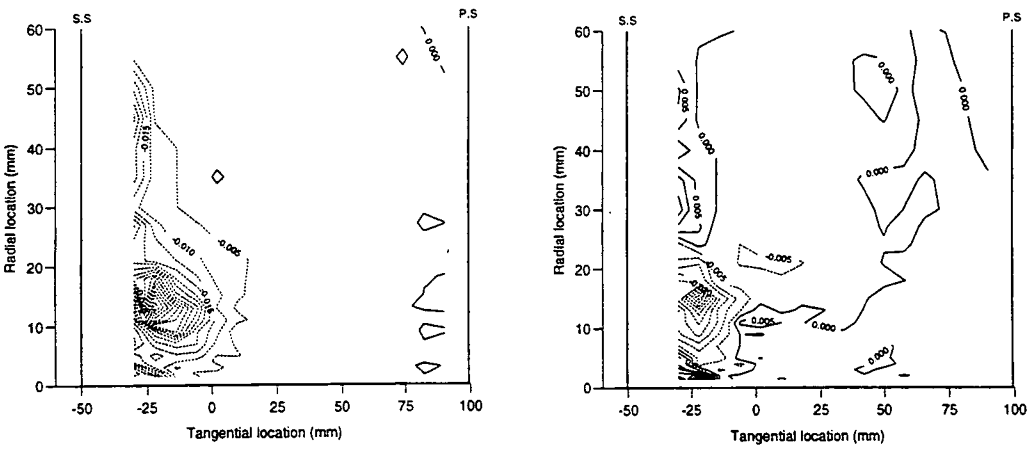

j) Velocity correlation uw/Vo^2

k) Velocity correlation vw/Vo^2

Figure 4.17 — Slot 6 Area traverses (f–k).

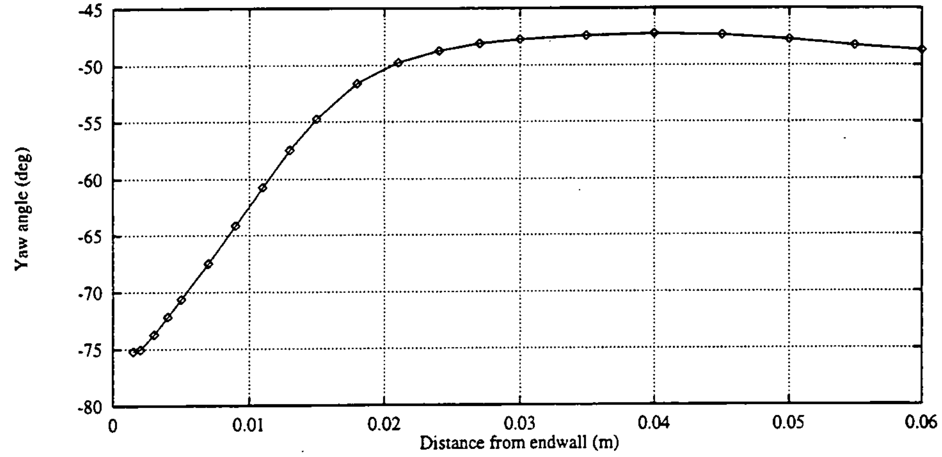

a) Yaw angle.

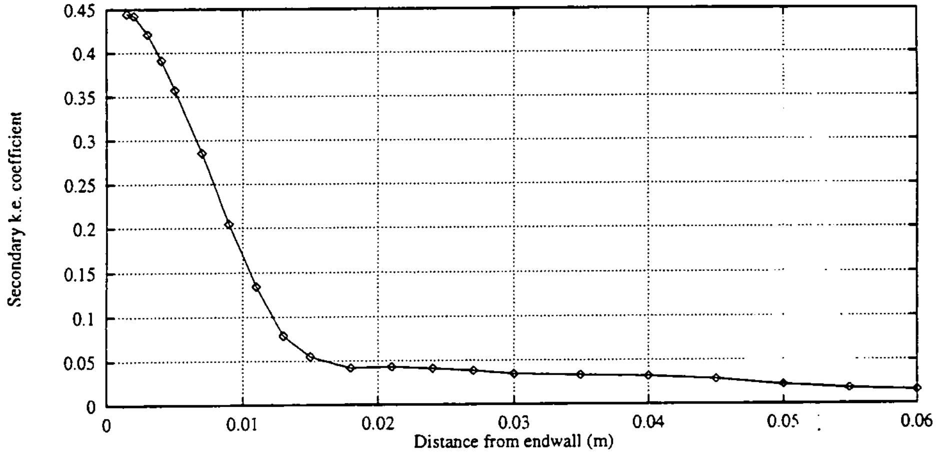

b) Secondary k.e. coefficient.

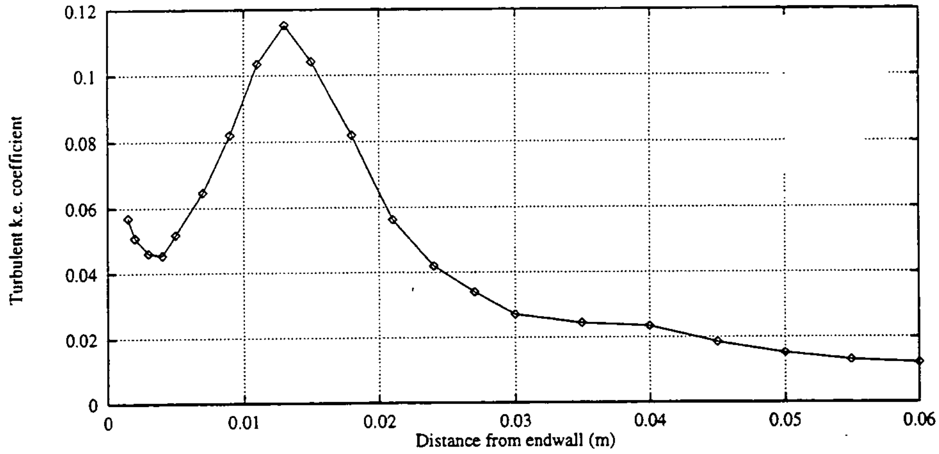

c) Turbulent k.e. coefficient.

Figure 4.18 — Slot 6 Pitchwise mass averages.

a) Total velocity magnitude (m/s)

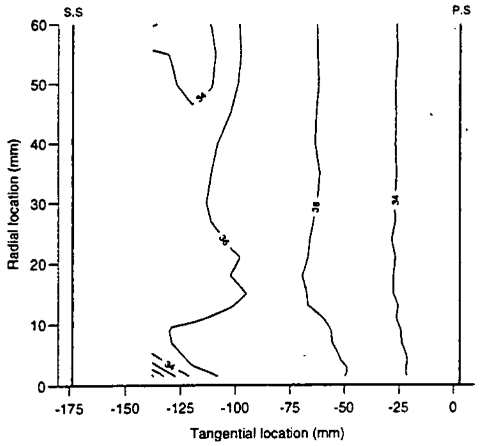

b) Yaw angle (deg)

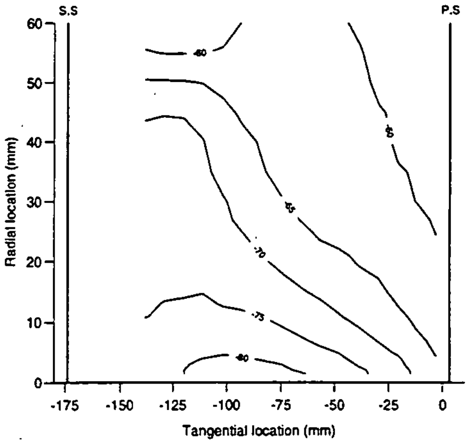

c) Pitch angle (deg)

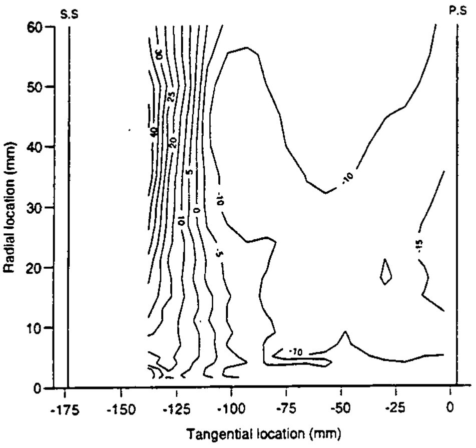

d) Secondary velocity vectors

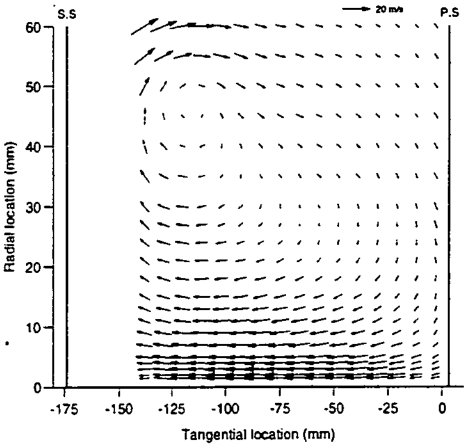

e) Non-dimensional turbulent k.e.

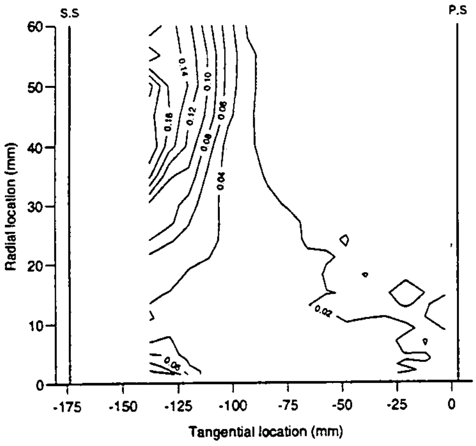

Figure 4.19 — Slot 8 Area traverses (a–e).

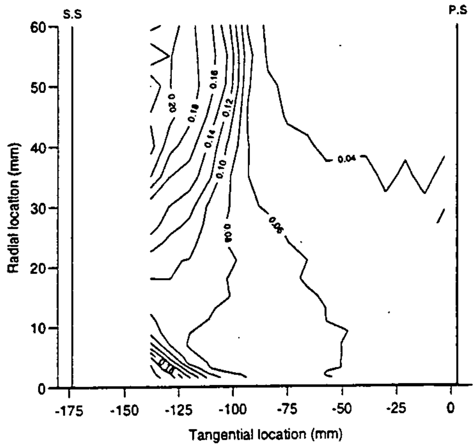
f) Turbulence intensity (rms u')/Vo

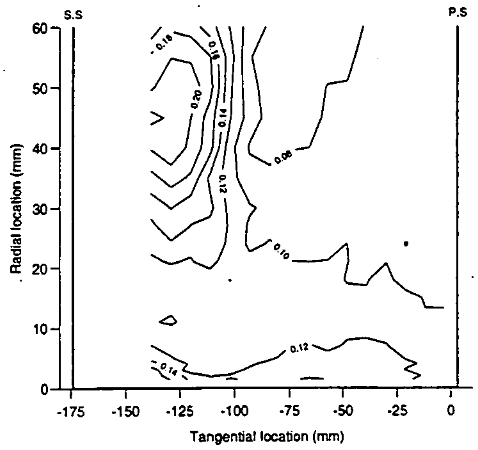
g) Turbulence intensity (rms v')Vo

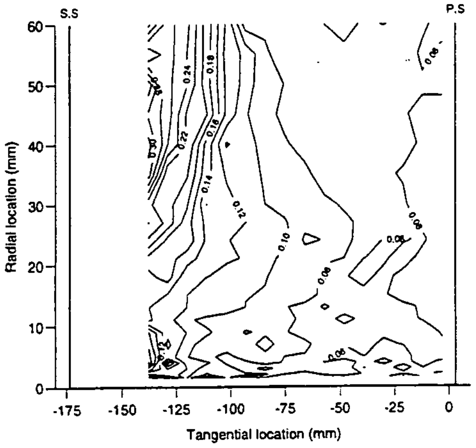
h) Turbulence intensity (rms w')/Vo

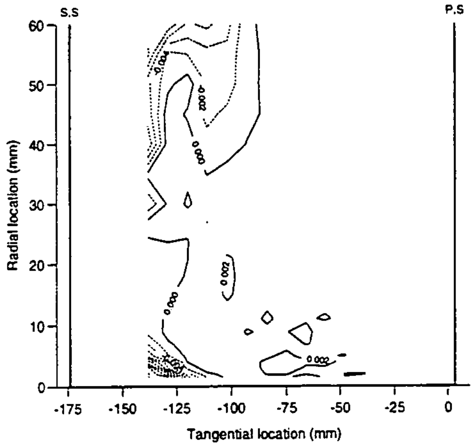
i) Velocity correlation uv/Vo^2

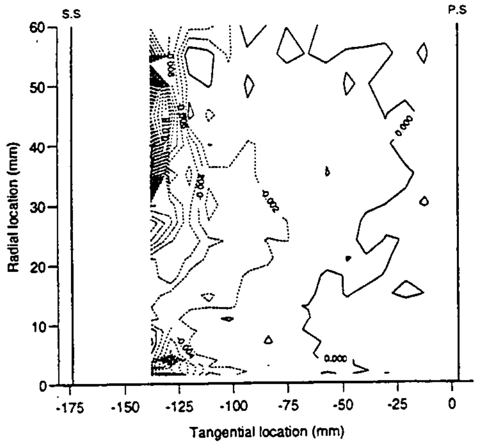
j) Velocity correlation uw/Vo^2

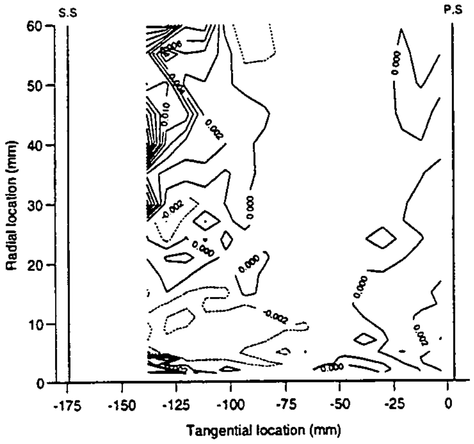
k) Velocity correlation vw/Vo^2

Figure 4.19 — Slot 8 Area traverses (f–k).

a) Yaw angle.

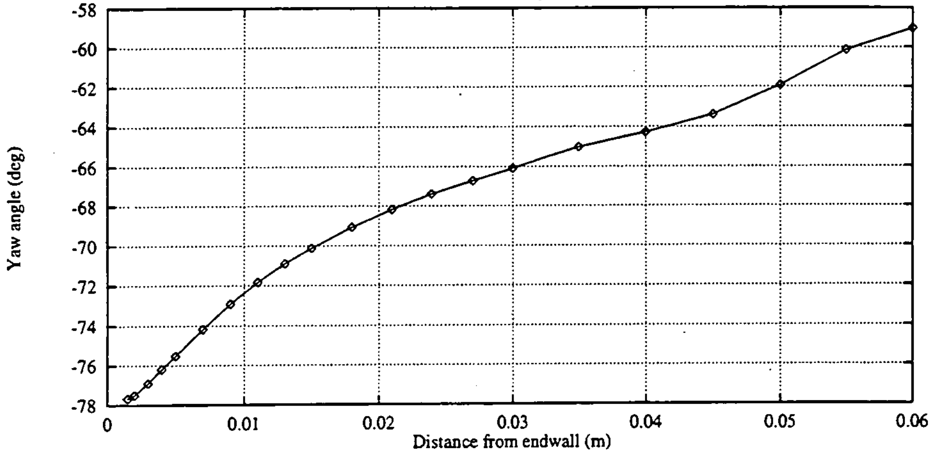

b) Secondary k.e. coefficient.

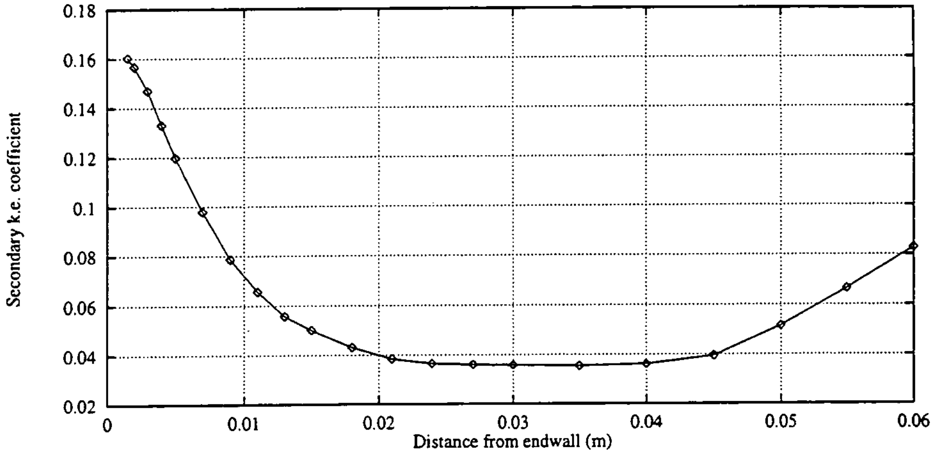

c) Turbulent k.e. coefficient.

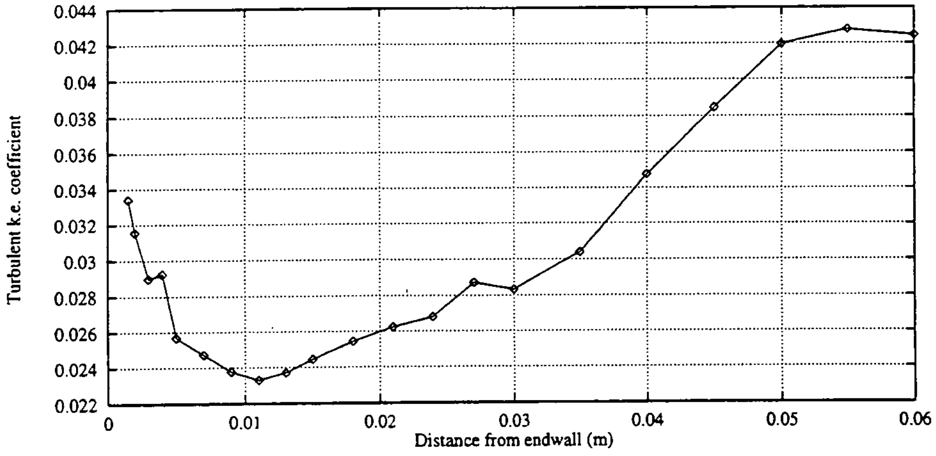

Figure 4.20 — Slot 8 Pitchwise mass averages.

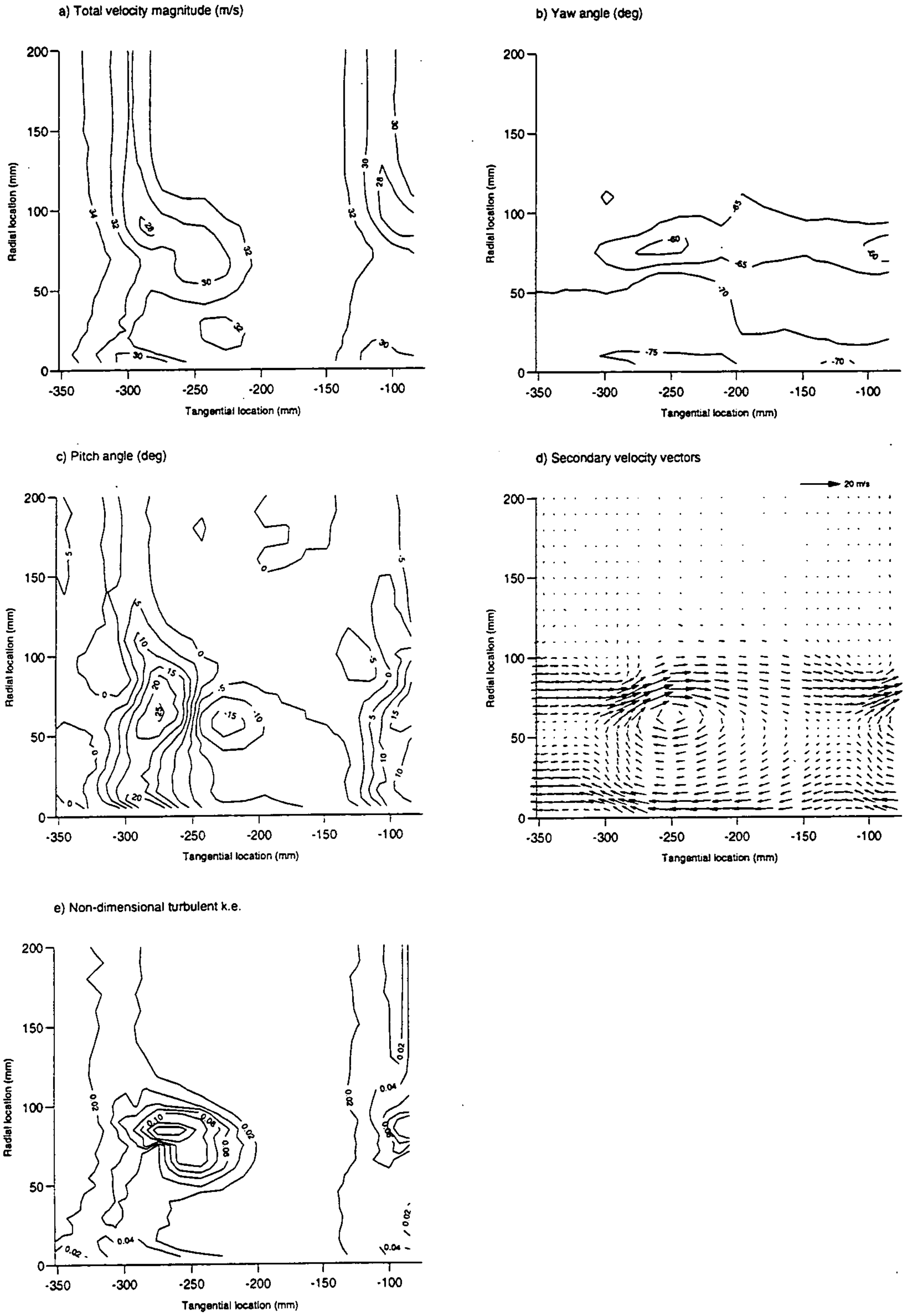

a) Total velocity magnitude (m/s)

b) Yaw angle (deg)

c) Pitch angle (deg)

d) Secondary velocity vectors

e) Non-dimensional turbulent k.e.

Figure 4.21 — Slot 10 Area traverses (a–e).

f) Turbulence intensity (rms u')/Vo

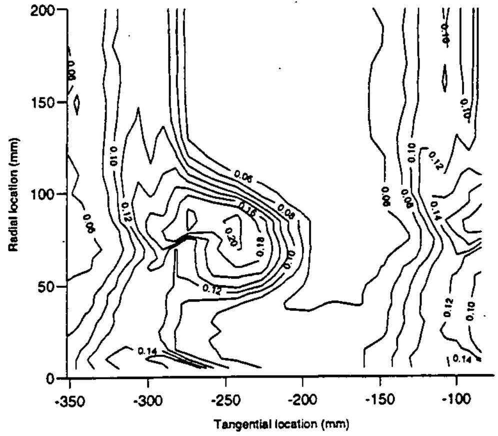

g) Turbulence intensity (rms v')/Vo

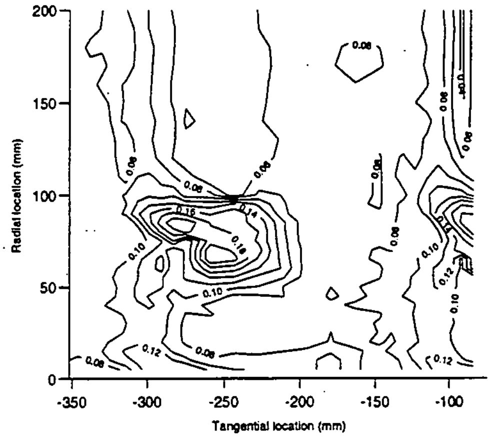

h) Turbulence intensity (rms w')/Vo

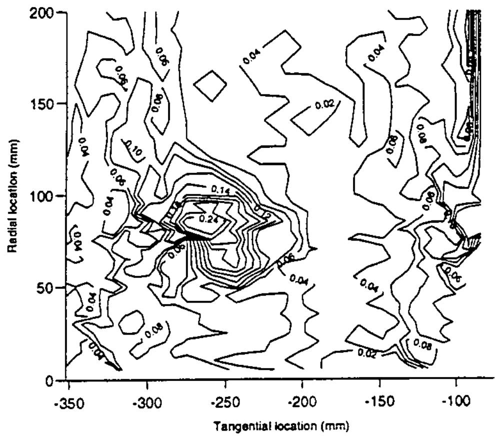

i) Velocity correlation uv/Vo^2

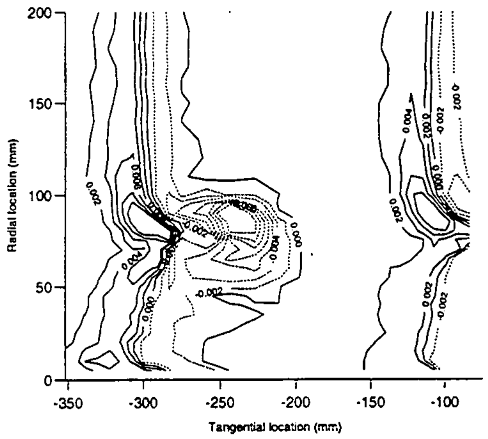

j) Velocity correlation uw/Vo^2

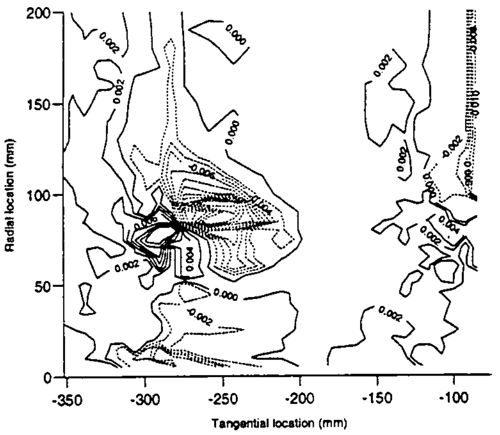

k) Velocity correlation vw/Vo^2

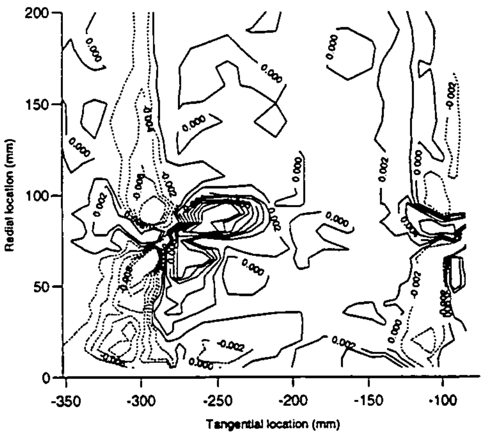

Figure 4.21 — Slot 10 Area traverses (f–k).

a) Yaw angle.

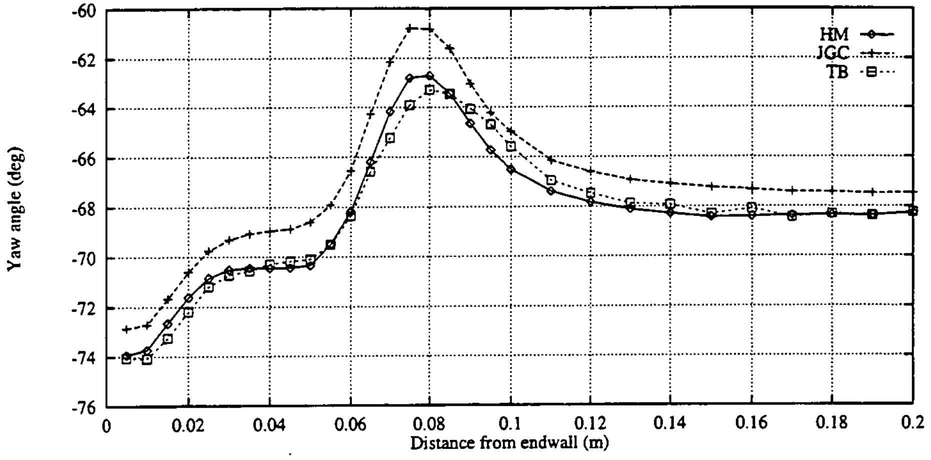

b) Secondary k.e. coefficient.

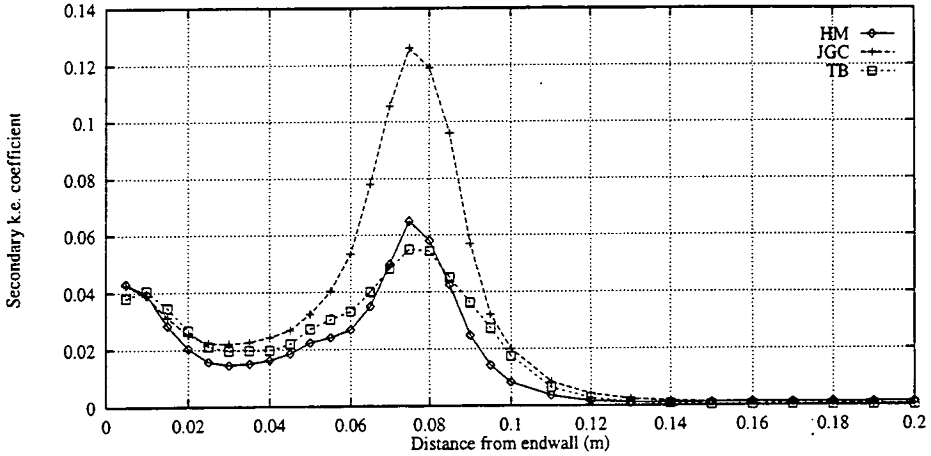

c) Turbulent k.e. coefficient.

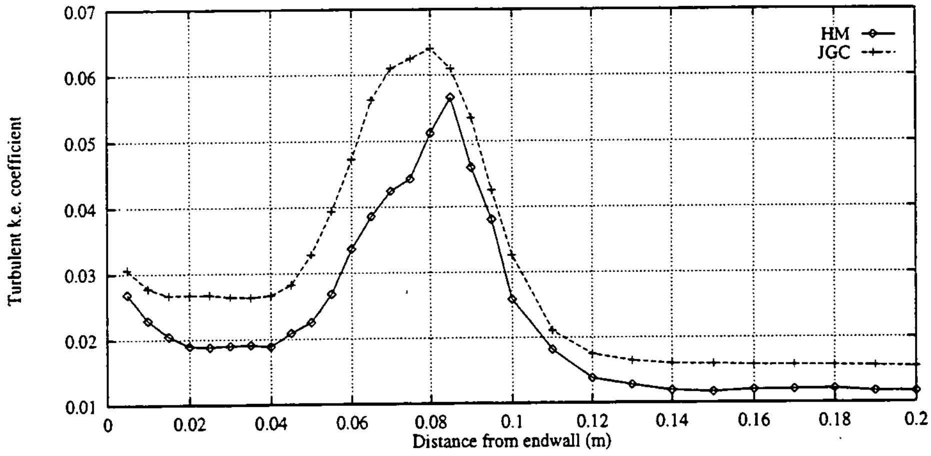

Figure 4.22 — Slot 10 Pitchwise mass averages.

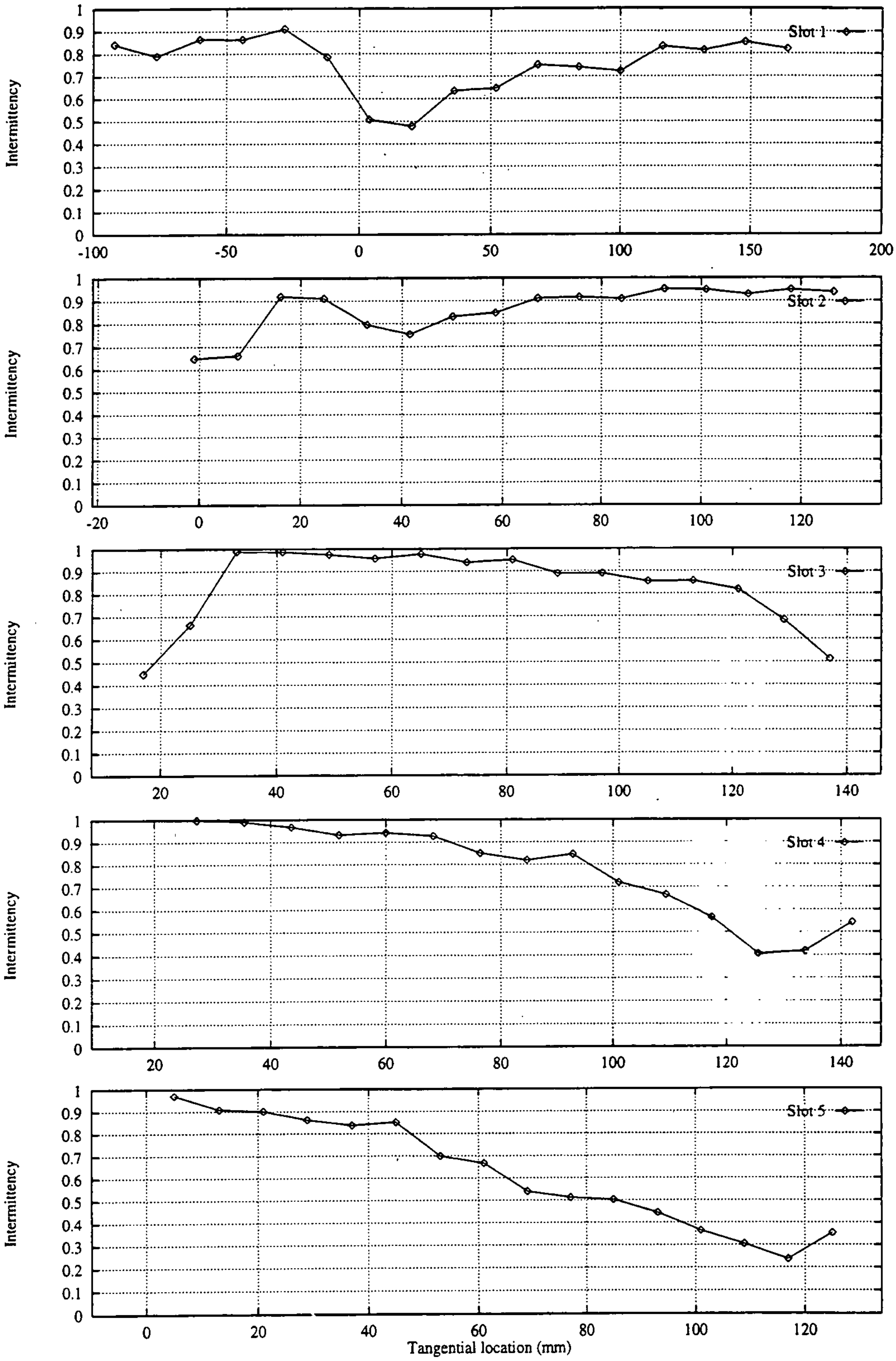

Figure 4.23 — Slots 1–5 endwall intermittencies

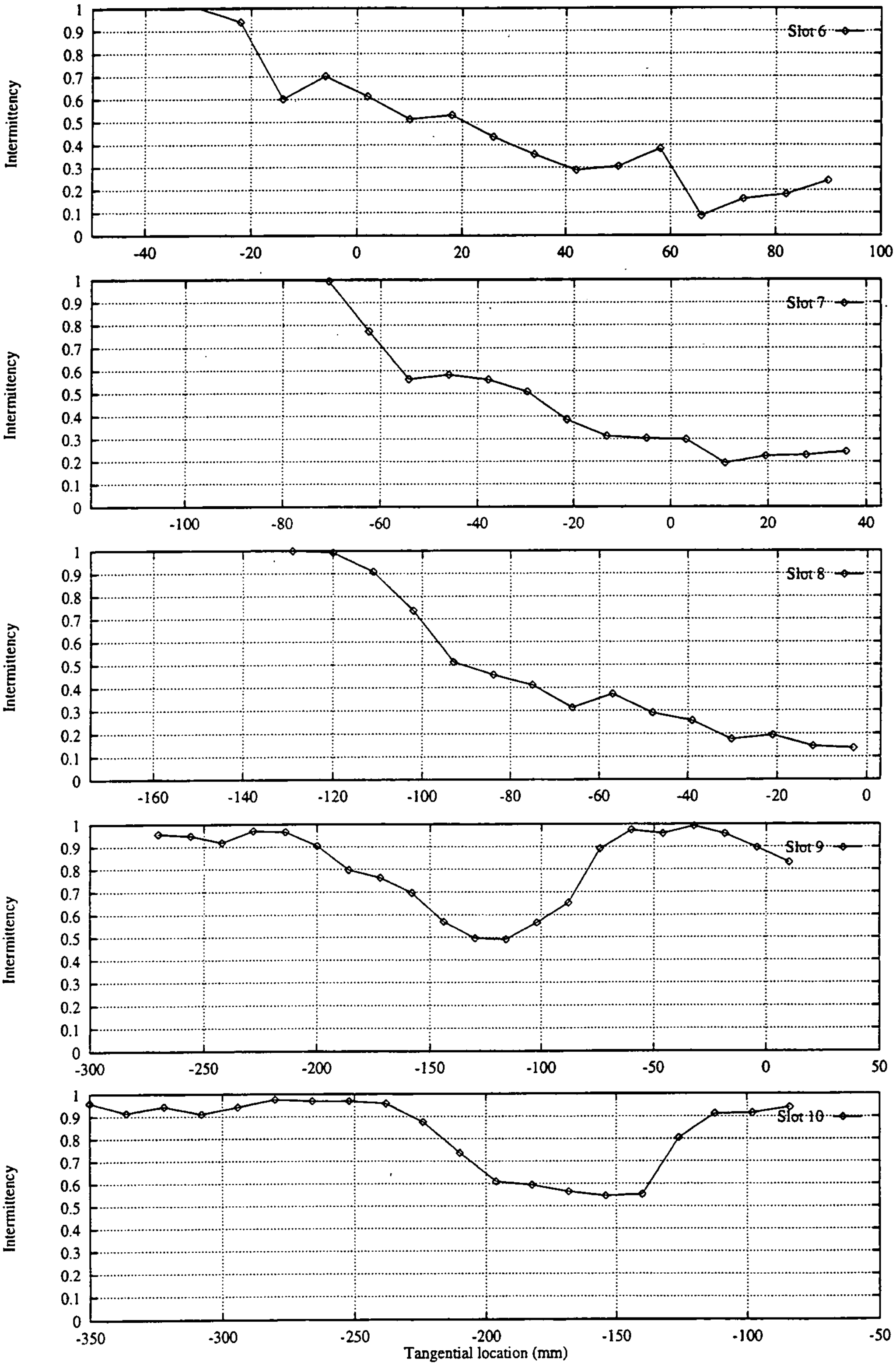

Figure 4.23 — Slots 6–10 endwall intermittencies

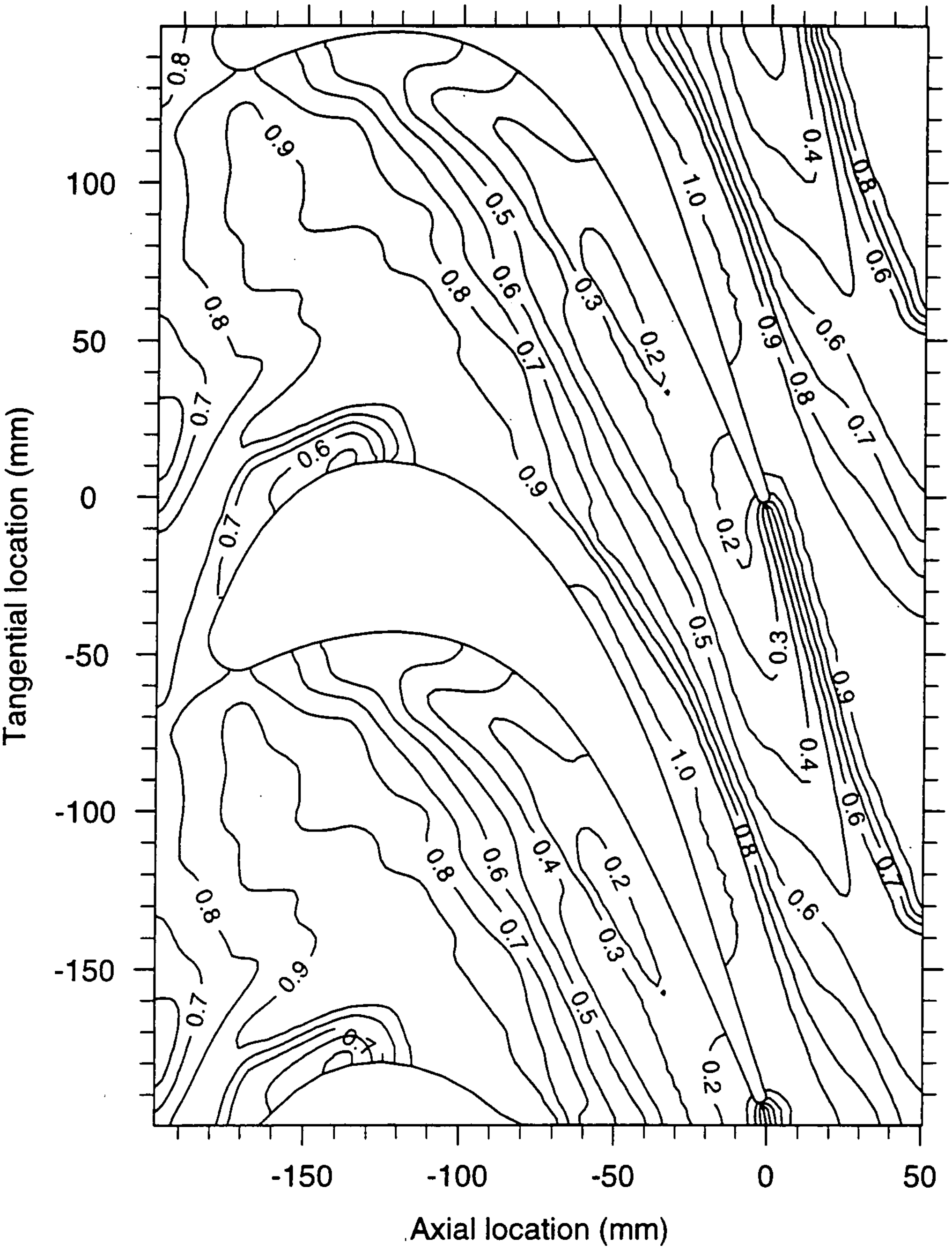

Figure 4.24 — Intermittency (1.0mm from the endwall)

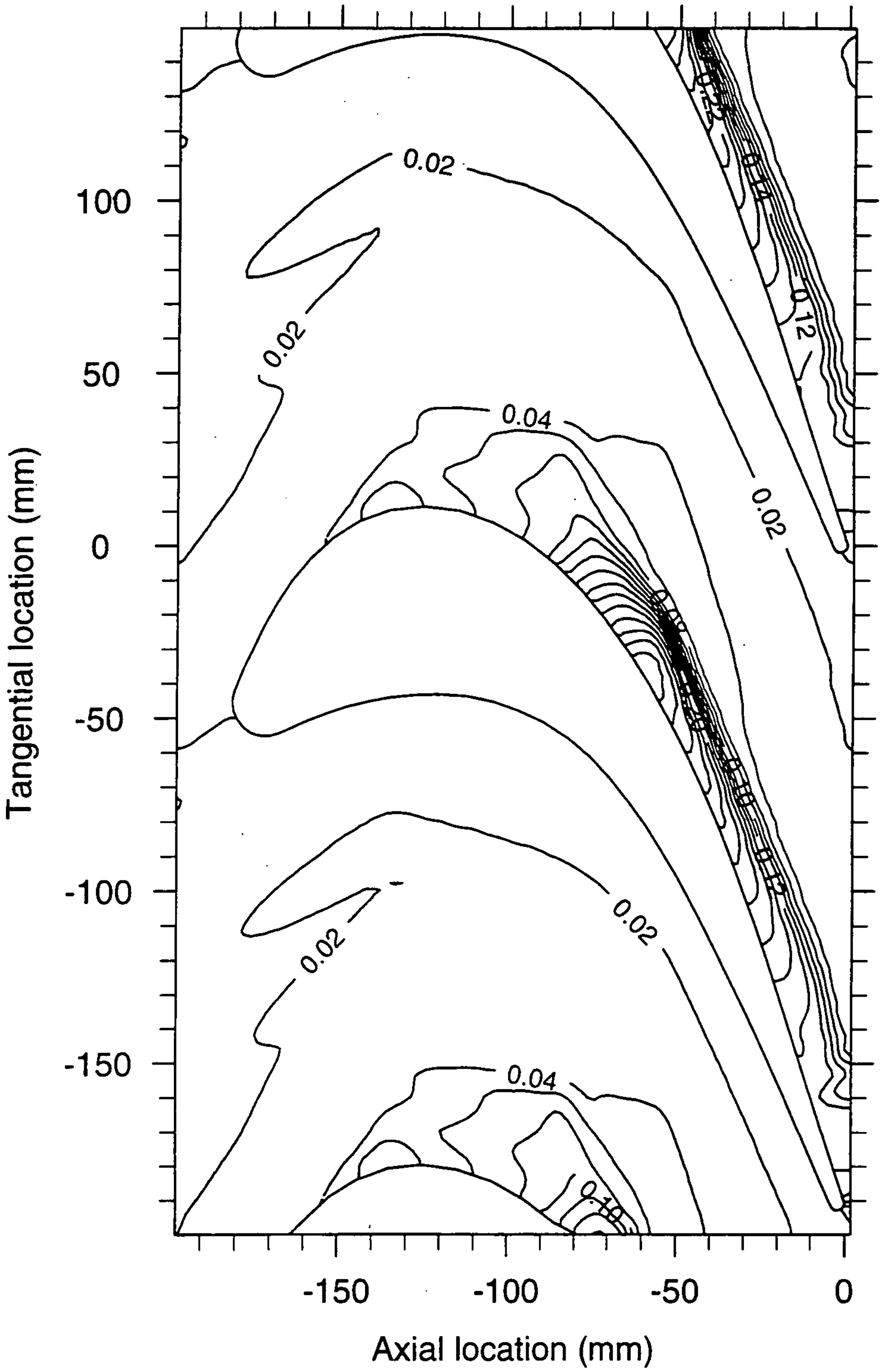

Figure 4.25 — Non–dimensional turbulent k.e. (1.5mm from endwall)

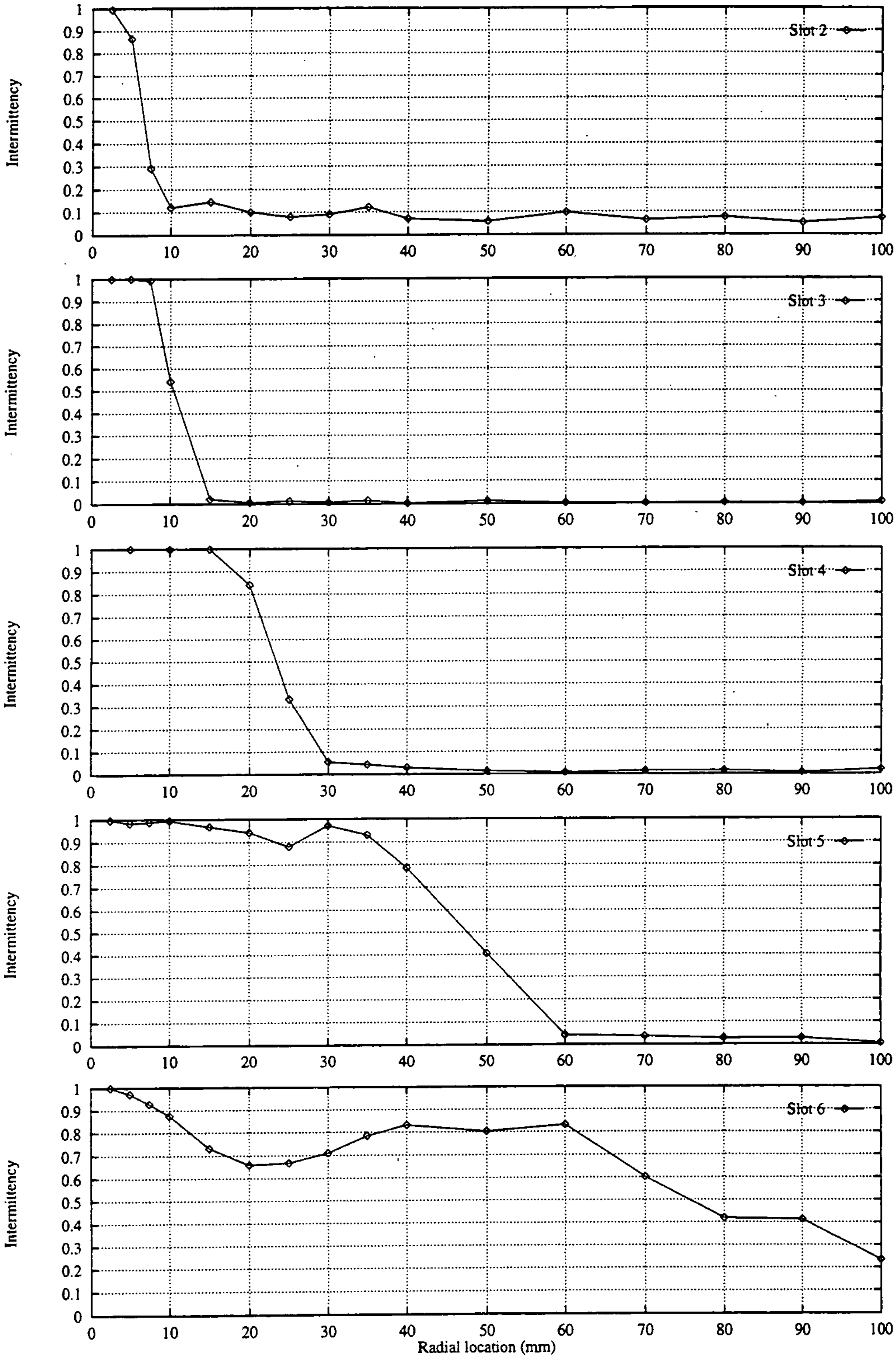

Figure 4.26 — Slots 2–6 suction surface intermittencies

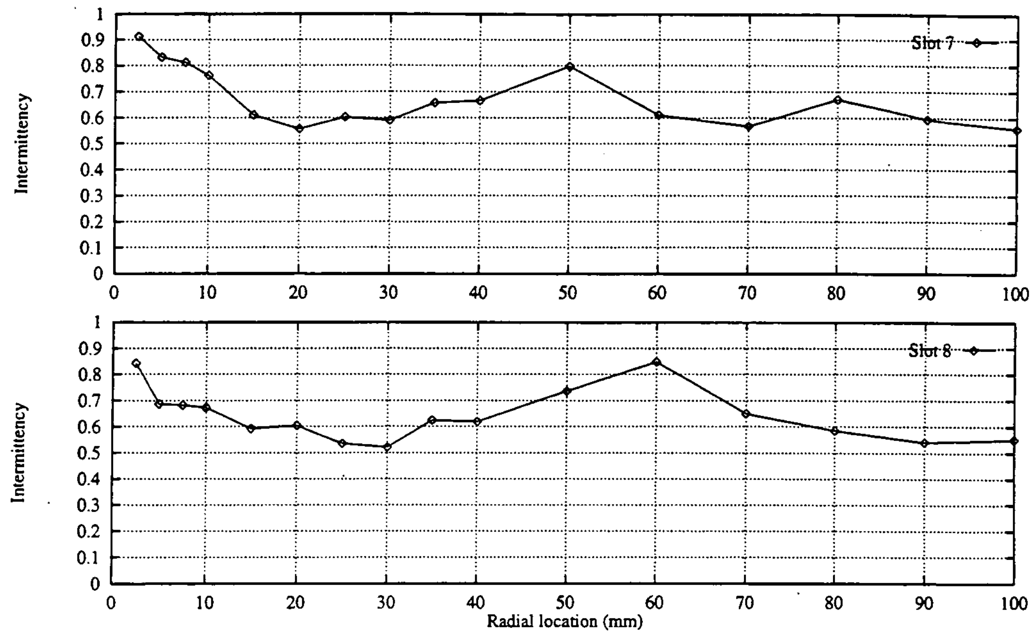

Figure 4.26 — Slots 7–8 suction surface intermittencies

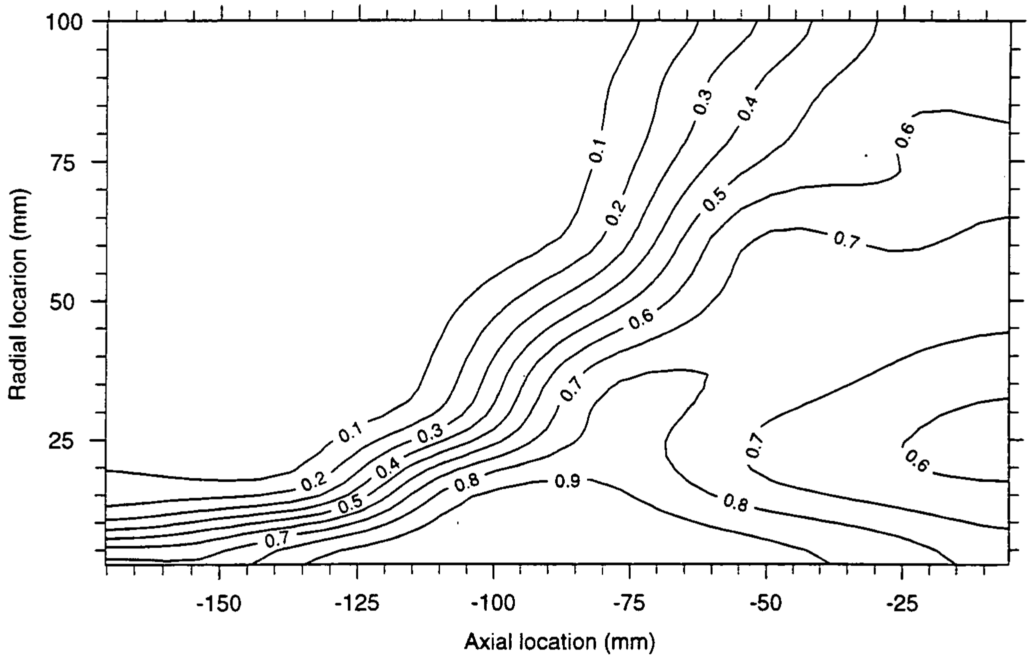

Figure 4.27 — Suction surface intermittency (1.0mm from surface)

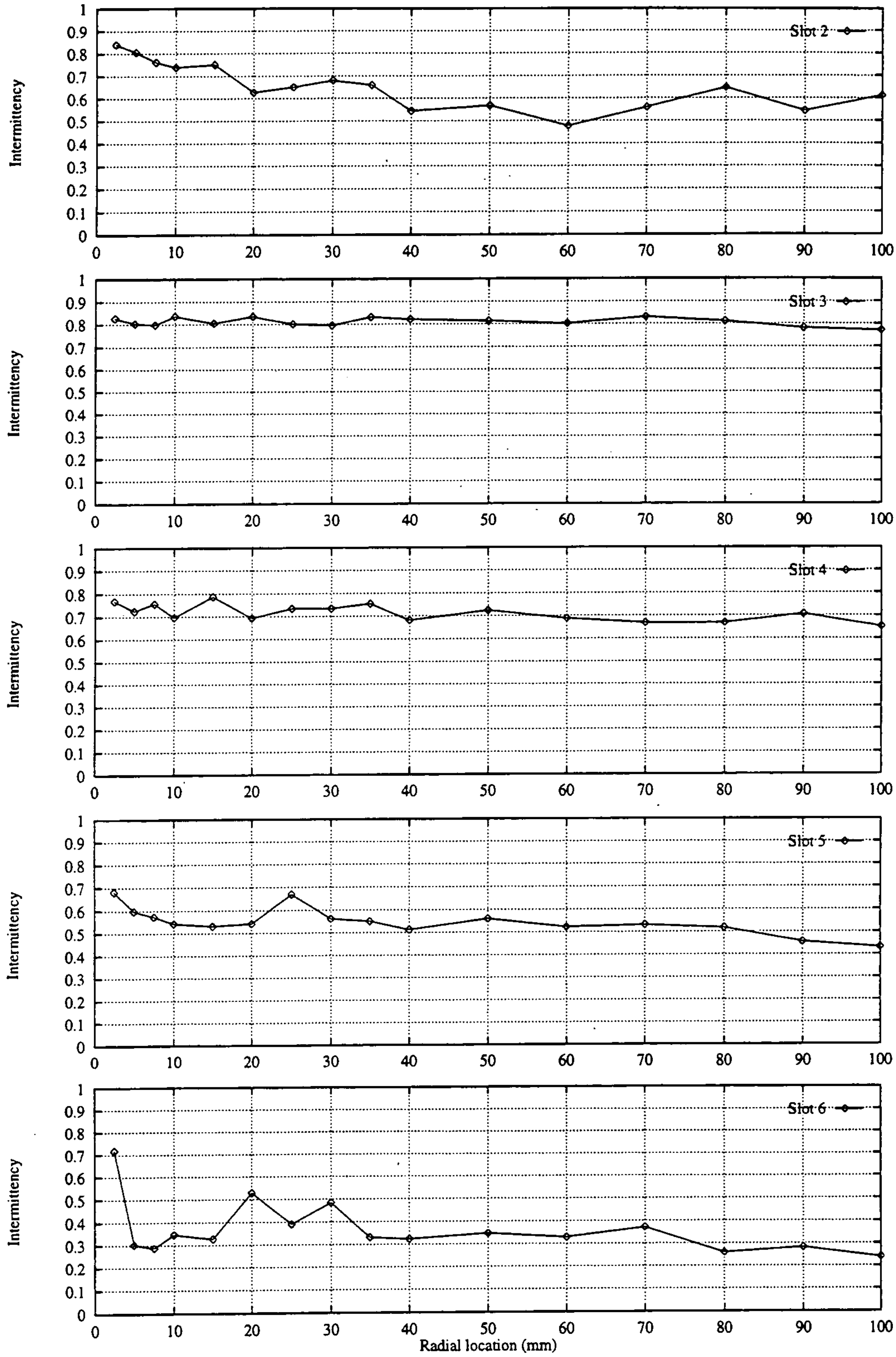

Figure 4.28 — Slots 2–6 pressure surface intermittencies

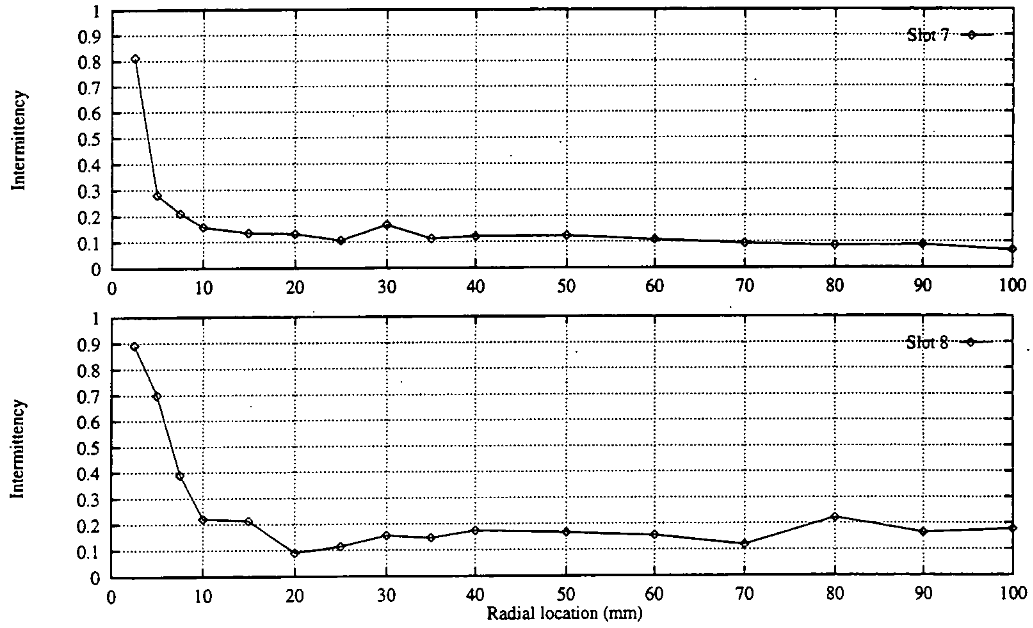

Figure 4.28 — Slots 7–8 pressure surface intermittencies

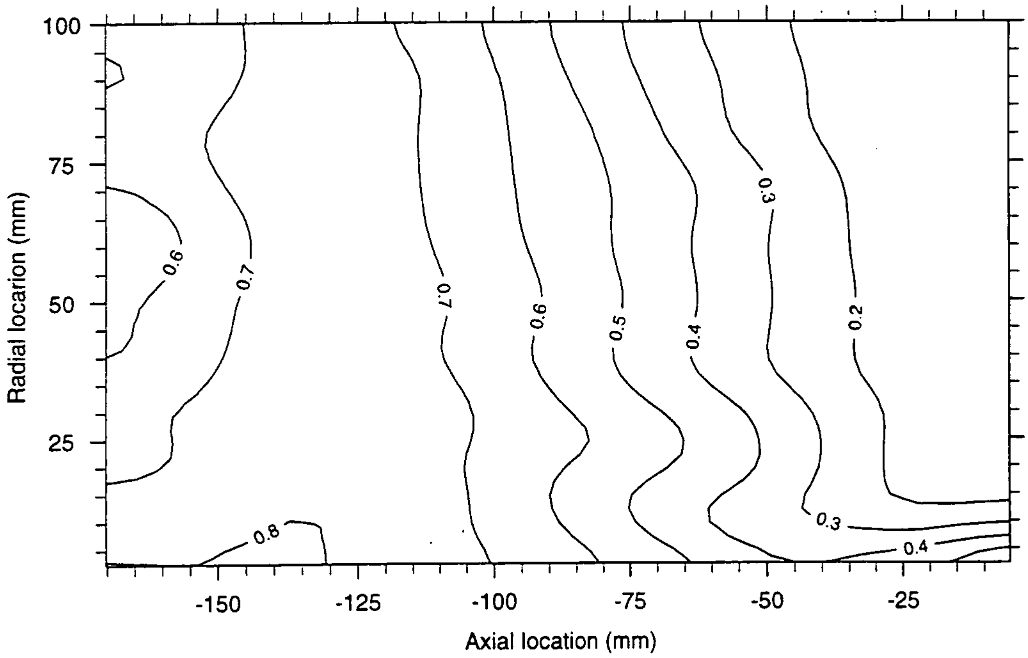

Figure 4.29 — Pressure surface intermittency (1.0mm from surface)

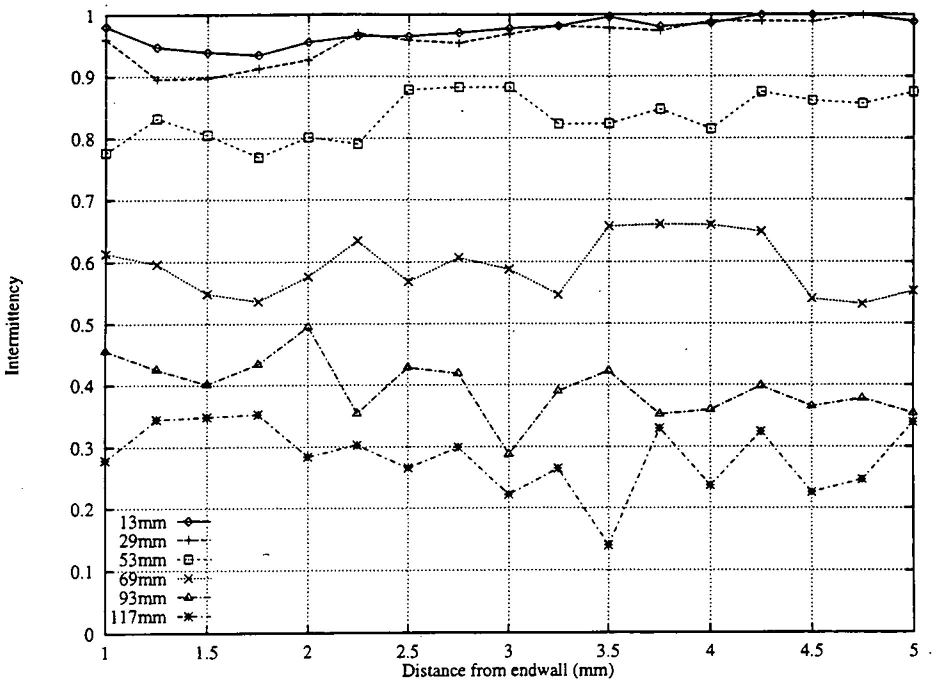

Figure 4.30 — Slot 5 intermittency profiles

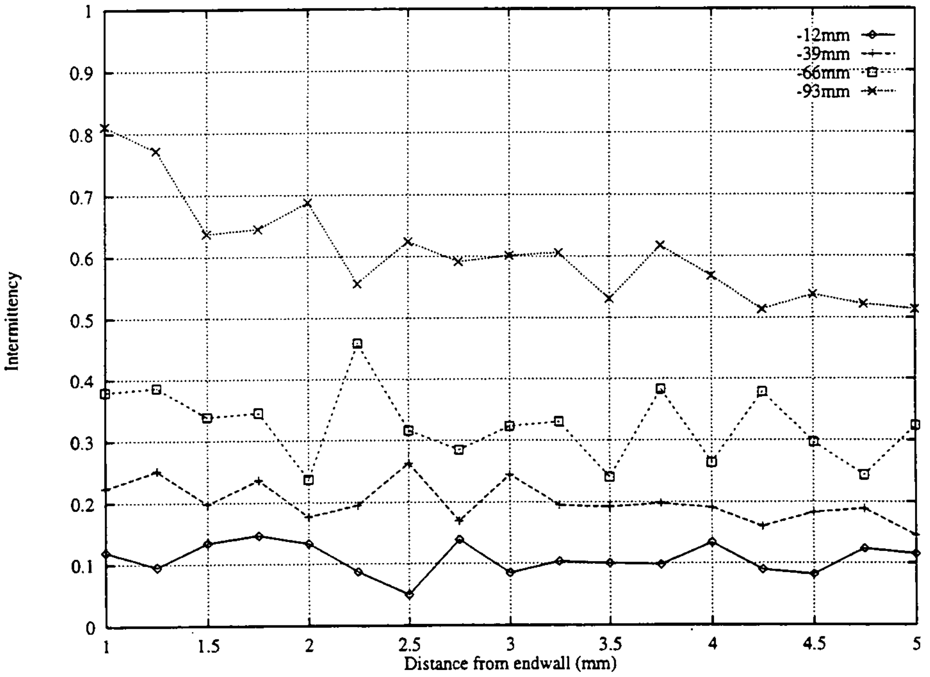

Figure 4.31 — Slot 8 intermittency profiles

Chapter V

Modelling results

5.1 Numerical method

5.1.1 The CFD code

All calculations have been carried out using a code based on the algorithm of Moore and Moore [1985]. This is an elliptic, finite volume pressure correction code based upon Patankar's SIMPLER algorithm and is described in detail in Moore [1985a,b]. In this formulation the continuity equation is integrated over a cell–centered control volume using linear interpolation of the velocity at each corner (grid point) to obtain the mass flux through each side. The momentum equation is integrated over upwinded control volumes and finite difference forms of the convection and pressure terms are then obtained by central differencing of linearly interpolated variables. The use of upwinded control volumes stabilises the finite difference equations without the need for upwind differencing and results in a second order accurate scheme with no numerical mixing (Moore [1985b]). On poorly aligned grids, however, the technique can result in some artificial cross–convection of conserved quantities.

One effect of numerical mixing (viscosity) is that it generally acts to dissipate secondary kinetic energy and hence increases losses (Moore and Moore [1985], Carey et al [1992]). Stow [1985] stresses the importance of eliminating it and comments that before it is possible to validate turbulence models, grid independence from numerical viscosity must be achieved. For any code, the use of a sufficiently fine grid makes this possible but at the cost of increased CPU time and memory requirements. However, a comparison of various calculations of the loss in Langston's cascade (Lakshminarayana [1991]) showed that the Moores' code produced the best results despite using the most coarse grid (28 × 19 × 13 for Moore and Moore [1985], 53 × 31 × 20 for Hah [1984]). At least part, if not most, of the differences may be attributed to numerical mixing (Moore and Moore [1985]).

5.1.2 Turbulence modelling

Three turbulence models have been used in the present work, a mixing length model, a high Reynolds number k–ϵ model and a low Reynolds number k–ϵ model. In addition to this a modification to the k–ϵ models, called here the S–Ω modification, has also been used. Each is described below but only as far as necessary as to describe any non–standard features.

Mixing length model

The mixing length model is based on the Prandtl formulation;

$$L = \min\left(K.y\ ,\ \lambda.\delta\right) \tag{5.1}$$

where $K = 0.41$, $\lambda = 0.08$, y is the distance to the nearest surface and δ is the shear layer thickness which is based on a vorticity test function. Outside a boundary layer or shear layer the length scale varies linearly to the specified freestream length scale, L_∞, at a slope that is no greater than K. From the length scale, the turbulent viscosity is set using;

$$\mu_T = \rho \mathrm{L}^2 S F_{vd}^2 \tag{5.2}$$

where S is the magnitude of the strain rate and F_{vd} is the near wall Van Driest damping function.

For grids where the viscous sub–layer is not resolved a wall function is used to set the near wall viscosity and wall shear stress consistent with the near wall velocity. The function used is;

$$y^+ = U^+ + \frac{1}{E}\left(\exp\left(KU^+\right) - 1 - KU^+ - \frac{1}{2}\left(KU^+\right)^2 - \frac{1}{6}\left(KU^+\right)^3\right) \tag{5.3}$$

where;

$$U^+ = (U - U_w)/U_\tau \qquad y^+ = \rho U_\tau y/\mu \qquad U_\tau = \sqrt{\tau_w/\rho} \tag{5.4}$$

in which U is the velocity at the flow point, U_w is the wall velocity and $E = 8.8$.

In the limit this profile tends to $U^+ = y^+$ for $y^+ < 5$ (e.g. the viscous sub–layer) and $U^+ = \frac{1}{K}\ln\left(Ey^+\right)$ for $y^+ > 40$ (the logarithmic region) and compares well with the measured turbulent profile from the RRASL flat plate experiments (Roach and Brierley [1992]) up to $y^+ \approx 200$. Its advantage over many other wall functions is that it smoothly merges the viscous sub–layer, buffer and logarithmic regions of the boundary layer and so will work with a wide range of grid spacings.

High Reynolds number k–ϵ model

The second turbulence model available is a high Reynolds number k–ϵ formulation. As with the mixing length model it is used in combination with a wall function to describe the boundary layer flows. Away from walls the turbulent viscosity is obtained from;

$$\mu_T = \rho C_\mu k^2/\epsilon \tag{5.5}$$

where $C_\mu = 0.09$ and k & ϵ are the turbulent k.e and dissipation rate which are found by solving two partial differential equations (e.g. Jones and Launder [1972]). Equation 5.5 is only valid where the direct influence of molecular viscosity is negligible so within boundary layers the following wall function is used;

$$\rho C_\mu^{\frac{1}{4}} k^{\frac{1}{2}} \left(U - U_w\right)/\tau_w = \frac{1}{K}\ln\left(ER_y\right) \tag{5.6}$$

where;

$$R_y = \rho C_\mu^{\frac{1}{4}} k^{\frac{1}{2}} y/\mu \tag{5.7}$$

Given the velocity and k at a near wall point, equation 5.6 may be solved for τ_w and the turbulent viscosity is then found from;

$$\tau_w = (\mu + \mu_T)(U - U_w)/y \tag{5.8}$$

Because the wall function used here does not accommodate the buffer region or the viscous sub–layer and because the standard k–ϵ model has no low Reynolds number near wall damping, it is important that the near wall grid points are within the logarithmic region ($12 \leq R_y \leq 200$) for acceptable results to be obtained.

Low Reynolds number k–ϵ model

The low Reynolds number k–ϵ model used is that due to Launder and Sharma [1974]. Whilst there are a number of other low Reynolds number formulations various reviews (Patel et al [1984], Sieger et al [1992], Savill [1993]) have found this to be one of the best. Since it does not use wall functions it requires a very fine calculation grid (typically $y^+ \leq 1$) in order to resolve the boundary layer sufficiently well. This increases the computational time needed to run such calculations but has an advantage over the previous models in that it is, in principle, capable of predicting transition.

Kato–Launder S–Ω modification

One weakness of conventional k–ϵ models is that they can predict excessive levels of turbulence due to the fact that irrotational strain terms in the turbulence energy equation act to generate turbulence irrespective of their sign. This is particularly significant in impingement regions, such as at the leading edge of a blade, where it can trigger early transition. The S–Ω modification of Kato and Launder [1993] provides a method of alleviating this problem by replacing the strain, S^2, in the production term with $S[(1-\alpha)S+\alpha\Omega]$ where Ω is the vorticity and α has a value in the range of $0 \rightarrow 1$.

This modification has been added to both the high and low Reynolds number k–ϵ models described above. If $\alpha = 0$ they revert to the standard form but otherwise setting $0 < \alpha \leq 1$ implements some fraction of the modification. In practice, however, only values of $\alpha = 0$ or 1 have been used. Whilst this modification can be very successful (see later), it is important to remember that it is not physically accurate but introduces an inconsistency between the approximation of the Reynolds stresses in the Reynolds–averaged Navier–Stokes equations and, via the Boussinesq relations, in the turbulence energy equation.

5.2 Computational setup

5.2.1 Grid geometry

All calculations have been carried out on structured 'H' type grids. These were created first in two–dimensions (axial & tangential) and then stacked on parallel spanwise planes to make a full three–dimensional grid. One feature of the grids is that a number of axial grid lines pass through the blade causing some nodes to be located within it. This is done to improve the orthogonality of the cells near the leading and trailing edges where they can otherwise be very highly skewed. Two main grids have been used, a coarse grid and a fine grid, though a third medium grid was used for one two–dimensional calculation.

Coarse grid

The coarse grid is shown in *Figure 5.1.* It consists of 89 axial and 38 tangential nodes and was designed for use with models that employ wall functions. This requires the first cell centres away from the blade to lie within the log–law region of the boundary layer ($y^+ = 30 \rightarrow 100$). This was achieved by testing the grid with a two–dimensional mixing–length model calculation and modifying it as necessary. To convert the grid to three–dimensions it was stacked on 29 spanwise planes giving a total grid size ($89 \times 38 \times 29$) of 98078 points. The first plane is $0.4mm$ from the endwall (chosen to give a suitable y^+) and this expands to a spacing of $10.0mm$ at midspan which is similar to the spacing in the other directions.

Fine grid

The fine grid is shown in *Figure 5.2.* It consists of 99 by 55 nodes and has a much finer near wall spacing ($y^+ < 3$) than the coarse grid. As can be seen this makes it much less smooth and leads to some distorted and high aspect–ratio cells. This is unfortunate but cannot easily be avoided with 'H' type grids unless embedded meshes are used. Alternately 'O' and 'C' grids, particularly as part of multiblock schemes, can also produce better meshes but were not available. To convert to three–dimensions the grid was stacked on 42 spanwise planes with an initial near wall spacing of $0.01mm$ increasing to $8.0mm$ at midspan. This gives a total grid size of 228690 points ($99 \times 55 \times 42$) which is 2.33 times the size of the coarse grid.

5.2.2 Boundary conditions

Inlet plane

The inlet conditions are defined at one axial chord upstream of the leading edge. The velocity, turbulent k.e. and dissipation rate are set to the measured values as defined in Chapter 3. This includes the measured endwall boundary layer profiles for the three–dimensional calculations. Inlet static pressure (which, with the velocity, gives the stagnation pressure and flow angle) and density (which is constant) are also set according the the standard day conditions.

Solid surfaces and edges

The calculation grid covers one pitch and is centered on the blade so that its edges, the mid–passage planes, are defined with repeat conditions (e.g. flow out of one enters the other). For 2D calculations, 2 spanwise planes are defined and are both taken to be planes of symmetry. For 3D calculations the grid runs from the endwall to midspan with the midspan plane again being defined as a plane of symmetry. On the endwall and blade surfaces no slip conditions are enforced.

Exit plane

The calculation exit plane is located one axial chord downstream of the trailing edge and the calculation is run to a constant mass flowrate.

5.2.3 Convergence criteria

A number of criteria are used to test for convergence of a calculation. Firstly the r.m.s. change of parameters (e.g. velocity, pressure, turbulent kinetic energy etc.) between passes is monitored. At a minimum this value is expected to drop by two orders of magnitude and, even if it drops by more, the calculation is run on until it ceases to drop. At regular intervals the integrated total pressure and mass flow on each axial grid plane are also written out. Once the solution has converged the former should not change as more passes are made whilst the latter should have the same value on each axial plane (since mass flow must be conserved).

5.3 2D results

A number of two–dimensional calculations have been carried out in order to test various aspects of the grid design and the effect of altering certain parameters. The inlet conditions to all the calculations are based on the measured freestream flow at one axial chord upstream of the blades (section 4.2.1) so the results may be compared with the measurements at midspan. The calculations, however, do not take into account the effect of the endwall boundary layers on the flow at midspan where the blockage they cause will tend to increase the mass flowrate. This is unlikely to be significant, though, since the pitch averaged slot 10 (128% C_{ax}) results of Cleak [1989] show no significant increase in midspan axial velocity which suggests that the blockage is minimal.

5.3.1 Grid design and independency

In CFD it is important to ensure that the grids on which the calculations are run are suitable. The are two aspects to this, the first is that the grid must be sufficiently fine for the solution to be reasonably independent of it and the second is that the near wall spacing must be suitable for the turbulence model used. This latter constraint is the reason why two main calculation grids have been created, one for turbulence models that use wall functions (the coarse grid) and one for those that do not (the fine grid). The former generally require the first grid points to lie in the log–law region of the boundary layer whilst the latter require a much closer spacing. An exception to this is the mixing length model whose wall function will work with the first grid point at any distance from the surface (up to the outer edge of the log–law region).

To test for grid dependency a mixing length calculation was carried out on three grids, the coarse and fine grids (section 5.2.1) and a third 'medium' grid. This grid consists of 99 × 47 grid points and was an early design that was neither coarse nor fine enough for use with or without wall functions. Since the main difference between the grids lies in their near wall spacing, whilst towards mid–pitch all three are fairly similar, they are not ideal for testing grid dependency but should give some indication. The inlet conditions were taken from the experimental measurements (section 4.2.1) except for the freestream length scale which was reduced by a factor of ten to $0.936mm$ (for reasons that will be discussed later). The calculations were run on a Silicon Graphics 'Indigo 2' workstation for between 400 and 500 passes and in each case convergence was reasonable.

To compare the three calculations the surface static pressure coefficients, C_{ps}, are plotted in *Figure 5.3* and various slot 10 (128% C_{ax}) area averages are given in the table below. The static pressure profiles show very similar results for all three calculations and reasonable agreement with the experimental measurements (from

Cleak [1989]). The main difference is that the two finer grids do not have a smooth profile on the suction surface whilst the coarse grid does. This is probably due to the much higher aspect ratio cells close to the blade surface on the finer grids (compare *Figures 5.1 & 5.2*) which are not ideal for carrying out calculations. Whilst this could be avoided by adding more tangential grid lines, at the cost of increased computational times, the problem is fundamental to 'H' grids because they are very inefficient at dividing up the flow when fine near–wall spacing is needed (see *Figure 5.2*).

	Yaw angle	C_{p0}	$C_{p0\infty}$
Experiment	−68.36°	0.097	0.098
Coarse grid	−69.02°	0.171	0.182
Medium grid	−68.83°	0.192	0.202
Fine grid	−68.89°	0.188	0.192

Table 5.1 — Slot 10. Effect of grid size.

The area (mass) averaged yaw angle, total pressure loss, C_{p0}, and mixed–out total pressure loss, $C_{p0\infty}$, at slot 10 are in reasonable agreement for the three grids. It is interesting that there is no systematic change in any of the parameters with grid size, as would be expected if there were significant grid dependency, but this may be because the medium grid is of a slightly poorer design. It is clear, however, that the differences due to the grids are small compared with those between the calculations and the experimental results, which will be due mainly to the turbulence modelling, so the grids should be satisfactory from this point of view.

The calculations have also been used to plot the near wall y^+ values for the coarse and fine grids (*Figures 5.4a & b*). It varies around the surface because the grid generation program sets the first grid lines at equal and constant distances from both surfaces so y^+ then depends on the wall shear stress. On the coarse grid it is in the range 10 → 80 and so mostly lies within the boundary layer log–law region whilst on the fine grid y^+ is generally less than 2.5. Though ideally this should be lower for models that do not use wall functions, reducing the grid spacing further seriously affected its quality, particularly at the leading and trailing edges, so could not be done. Also plotted in *Figure 5.4a* is the near wall Reynolds number, R_y, from a high Reynolds number k–ϵ calculation on the coarse grid. As can be seen, $R_y > 12$ everywhere which is necessary for this turbulence model (see section 5.1.2).

5.3.2 Effect of freestream length scale

One of the limitations of the mixing length model is that the freestream length scale, L_∞, remains constant whereas, in reality, it should vary. A previous fully turbulent mixing length calculation by Cleak [1989] used a length scale of 3.32mm (which was based on the blade pitch and slot 1 turbulence level) and gave high losses and a poor prediction of the location and shape of the passage vortex. It seems that too much turbulence was being produced which dissipated the the secondary k.e and increased the losses. Since the turbulent viscosity, μ_T, is proportional to L^2 (eqn. 5.2) and the turbulent dissipation rate, ϵ, is inversely proportional to μ_T increasing L_∞ to the measured value of 9.36mm is likely to produce worse results. Conversely, reducing the freestream length scale may improve the results so the effect of varying it has been investigated.

To do this three 2D mixing length calculations have been carried out on the coarse grid with length scales of 9.36mm (the measured value at $-1.0\mathrm{C_{ax}}$), 0.936mm and 0.0936mm. In all cases the remaining inlet conditions were as measured experimentally. Area mass–averaged values at slot 10 are presented in Table 5.2 below along with the experimental results and the results of the calculation by Cleak [1989] (JGC). These are actually midspan results from a three–dimensional calculation on a different grid and with slightly different inlet conditions so are not strictly comparable. They are included because they have a different length scale which is the default value that has been used in all previous calculations carried out at Durham.

As expected reducing the freestream length scale reduces both the turbulent viscosity, μ_T, and the loss. Excluding the JGC result it also increases the yaw angle slightly and increases the difference between the total pressure loss and the mixed out loss. The latter is simply because the amount of mixing is decreased so the flow is further away from its mixed out, uniform, state. The increased yaw angle is likely to be because the wake becomes thinner so, since it is shed more from the suction surface (which has a thicker boundary layer) than the pressure surface, the reduced blockage allows the flow to turn further.

Length scale	Yaw angle	C_{p0}	$C_{p0\infty}$	μ_T/μ
Experiment	$-68.36°$	0.097	0.098	–
$9.36mm$	$-68.94°$	0.494	0.499	700
$3.32mm$ (JGC)	$-69.20°$	0.248	0.264	–
$0.936mm$	$-69.02°$	0.171	0.182	13
$0.0936mm$	$-69.13°$	0.104	0.121	0.24

Table 5.2 — Slot 10. Effect of freestream length scale.

The results show that even the shortest length scale tested gives a higher loss than found experimentally. Whilst reducing the length scale further would appear to improve the agreement (though not by much since μ_T is already small), in reality the calculations should show a higher than measured loss. This is because they assume the flow is fully turbulent whereas the experimental results (section 4.4) show that over much of the blade the flow is either laminar or transitional. Because of this it seems appropriate to use a length scale higher than the lowest value tested but, for reasons discussed earlier, not as high as the measured inlet value. Since there is no justification for any specific value within this range a value of $0.936mm$ will generally be used when running mixing length calculations.

5.3.3 Effect of S–Ω modification

The effect of the Kato and Launder [1993] S–Ω modification has been investigated in 2D by running two high Reynolds number k–ϵ calculations on the coarse grid, one with and one without it. Both calculations used the measured experimental inlet conditions including the correct freestream length scale ($9.36mm$). Unlike the mixing length model the k–ϵ model allows the length scale to change, since it is related to k and ϵ, so there is no real justification for lowering it. The effect of the modification is shown in *Figure 5.5* where turbulent k.e. contours are plotted and in Table 5.3 below which gives area averages at slot 10.

Figure 5.5 shows the modification has a considerable effect on the production of turbulent k.e. Without it k can be seen to rise away from the blade to a peak at mid-pitch and to drop as the blade wake is crossed. These are both clearly unphysical and are due to excessive production around the leading edge. When

	Yaw angle	C_{p0}	C_{tk}	μ_T/μ
Experiment	$-68.36°$	0.088	0.023	–
Standard k–ϵ	$-69.05°$	0.336	0.091	908
S–Ω modification	$-68.98°$	0.208	0.014	283

Table 5.3 — Slot 10. Effect of S–Ω modification.

the modification is applied the results are much more as they should be with the high values of k mainly restricted to the boundary layers and wake regions. The roughness of the contours seen in this figure is due to the interpolation carried out in the contour plotting routine, in reality they are much smoother.

The area averages at slot 10 show that the difference in turbulent k.e. between the two calculations (a factor of 6.5 at slot 10) has a considerable effect on the overall loss. Whilst both calculations produce too much loss, the S–Ω modification gives the lower value since less turbulence leads to less dissipation of energy. As with the previous mixing length calculations, however, these assume a fully turbulent flow, so the losses should be higher than the experimental value. It is also evident from the results that the modification reduces the turbulent k.e. coefficient by too much. This could probably be avoided by only applying a fraction of the modification (see section 5.1.2), as done by Chen et al [1995], but this has not been tried.

5.3.4 Effect of VISMOD

One reason why both the mixing length and high Reynolds number k–ϵ models predict too high a loss is because they assume the flow to be fully turbulent. Within MEFP, however, it is possible to specify laminar and transitional regions in the flow by modifying the turbulent viscosity, μ_T using the VISMOD command. This multiplies μ_T at each calculation point by a factor, FTP, which has a value of between 0 and 1. A value of $FTP = 0$ gives laminar flow, $FTP = 1$ gives turbulent flow and ramping FTP between 0 & 1 gives a transitional like behaviour. In this specifying FTP can be considered to be similar to specifying intermittency. The effect of doing this has been examined previously by Cleak [1989] using very simple laminar blocks with instantaneous transition ($FTP = 0$ or 1) and was found to improve the results. The current work extends this by investigating a number of different schemes initially in 2D and then in 3D (see later).

The first three schemes tested all have a constant value of FTP across the pitch. Whilst this is not physically correct it is easy to implement and follows the approach used by Cleak [1989] at midspan. The first scheme (VA) sets the flow to be laminar ($FTP = 0$) up to 80% $\mathrm{C_{ax}}$ and turbulent ($FTP = 1$) thereafter. This is a repeat of the design used by Cleak [1989] and was based on surface flow visualisation on the suction surface which indicated transition at about this point. The intermittency measurements (section 4.4) show transition on the suction surface occurring from 60% $\mathrm{C_{ax}}$ to the trailing edge so, apart from the suddenness of the transition, this is not unreasonable. The pressure surface, however, was found to be initially turbulent with relaminarisation occurring over the first 80% $\mathrm{C_{ax}}$ so the specification is incorrect here.

Away from the blades it is difficult to decide whether the flow should be defined as laminar or turbulent. The flow at inlet, however, is certainly turbulent (due to the turbulence grid) and the area traverses (section 4.3) do show some turbulence at midspan all through the cascade so turbulent is probably correct. To test the effect of this the second scheme (VB) is the same as the first except that the upstream flow is defined as turbulent with a sudden relaminarisation at the leading edge. The third scheme (VC) is again similar to the first except that gradual transition is defined from 60% $\mathrm{C_{ax}}$ to the trailing edge (as found experimentally on the suction surface) to test the effect of the rate of transition. Contour plots of FTP for these three schemes are shown in *Figure 5.6a–c*. The contours curve because the defined regions follow grid lines and the apparent width of transition in *Figures 5.6a* & *c* is due to interpolation in the contouring software.

The calculations were all carried out on the coarse grid using the mixing length model with a freestream length scale of $0.936mm$. The results for all three are very similar as the slot 10 area averages given in Table 5.4 below show. Whilst the losses are still higher than the experimental values, they have dropped considerably from the fully turbulent case ($C_{p0} = 0.171$, $C_{p0\infty} = 0.181$). They also show that the specified state of the flow away from the blade, or at least upstream of it, and the extent of the transitional region have little effect.

Length scale	Yaw angle	C_{p0}	$C_{p0\infty}$
Experiment	−68.36°	0.097	0.098
VA	−69.15°	0.124	0.130
VB	−69.15°	0.125	0.131
VC	−69.15°	0.123	0.129

Table 5.4 — Slot 10. Pitch–constant implementations of VISMOD.

The above laminar and transitional regions were defined based on the suction surface intermittency profile with no account being taken of that on the pressure surface in order to avoid a pitchwise variation. Three further two–dimensional mixing length calculations have been carried out with regions based on both the suction and pressure surface profiles. The difference between them lies in how far across the pitch the profiles extend. The surface profiles are defined in the table below. They follow approximately the measured intermittency variations and extend upstream and downstream to define the flow in these regions as being turbulent. In the regions where *FTP* varies (e.g. from 1 to 0 between the leading edge and 80% C_{ax} on the pressure surface) linear interpolation is used to set the intermediate values.

Suction surface		Pressure surface	
C_{ax} range	Variation of *FTP*	C_{ax} range	Variation of *FTP*
$-1.0 \rightarrow 0.0$	1	$-1.0 \rightarrow 0.0$	1
$0.0 \rightarrow 0.05$	$1 \rightarrow 0$	$0.0 \rightarrow 0.8$	$1 \rightarrow 0$
$0.05 \rightarrow 0.6$	0	$0.8 \rightarrow 0.99$	0
$0.6 \rightarrow 0.99$	$0 \rightarrow 1$	$0.99 \rightarrow 1.0$	$0 \rightarrow 1$
$0.99 \rightarrow 2.0$	1	$1.0 \rightarrow 2.0$	1

Table 5.5 — Surface variations of *FTP*.

The first calculation (VD) has the suction surface profile extending from the suction surface across 90% of the pitch and the pressure surface profile extending to 5% of the pitch away from the pressure surface. Over the remaining 5% of the pitch the two profiles merge together (see *Figure 5.6d*). The remaining two calculations have the surface profiles ramping to fully turbulent ($FTP = 1$) at 10% (VE) and 5% (VF) of the pitch away from the surfaces (see *Figures 5.6e & f*). The area averaged results at slot 10 for the three calculations are given in the table below.

Length scale	Yaw angle	C_{p0}	$C_{p0\infty}$
Experiment	−68.38°	0.097	0.098
VD	−68.99°	0.092	0.098
VE	−68.97°	0.095	0.101
VF	−68.95°	0.114	0.120

Table 5.6 — Slot 10. Pitch–varying implementations of VISMOD.

The calculations VD & VE give very similar results which tends to confirm the conclusion from the first two (VA & VB) that the specified state of the flow away from the blades has little effect on the results. This is reasonable since the majority of the loss for the 2D profile is due to the boundary layers either directly (as the loss within them) or indirectly (in terms of their effect on the size of the wake and hence its loss). The results from VF suggest that in this case the flow has been allowed to become fully turbulent too close to the blade and so has increased the loss.

Another interesting comparison is between the calculations VC and VD which differ only in the specification of the flow close to the pressure surface. VC has the flow being initially laminar with transition starting at 60% C_{ax} whilst VD correctly has relaminarisation of the flow occurring over the first 80% C_{ax}. The lower losses in the VD calculation are due to the strong acceleration of the flow over the latter part of the blade. In VC the flow here is specified as being turbulent so the loss is high whereas in VD it is the flow over the front part of the blade that is turbulent. Here, however, the velocity is much lower so less loss is generated. Overall the VE specification appears to be the best (since it seems most reasonable to restrict the surface profiles to close to the surfaces) and certainly gives very good results. Of course the loss also depends on the freestream length scale and since this was chosen arbitrarily the good agreement is not that significant.

5.4 3D results

A number of three–dimensional calculations have been carried out on both the coarse and fine grids (section 5.2.1). Results have been obtained using all three turbulence models described in section 5.1 and, in the case of the high Reynolds number k–ϵ model, with and without the Kato–Launder S–Ω modification. The suitability of the three–dimensional grids, in terms of their endwall spacing, is demonstrated in *Figure 5.7* which shows y^+ for both grids and R_y for the coarse grid. The values are similar to those on the blade surfaces (*Figure 5.4*), though on the fine grid y^+ is generally lower. Most importantly the value of R_y for the coarse grid is always greater than 12 so it is suitable for the wall function in the high Reynolds number k–ϵ model (section 5.1.2).

5.4.1 Mixing length model calculations

Four, three–dimensional mixing length calculations have been made, three on the coarse grid and one on the fine grid. The first three calculations assume the flow is fully turbulent and test the effect of the freestream length scale (MLA & MLB) and the grid (MLF). The fourth calculation (MLV) used the VISMOD command to set regions of the flow to be laminar, transitional and turbulent based on the measured intermittency values (section 4.4). These specifications are summarised in the table below. Other than the freestream length scale, the inlet conditions for all the calculations were taken from the measured values.

	MLA	MLB	MLF	MLV
Grid	coarse	coarse	fine	coarse
Length scale, L_∞	$9.36mm$	$0.936mm$	$0.936mm$	$0.936mm$
Fully turbulent	yes	yes	yes	no

Table 5.7 — The mixing length calculations.

The regions for the MLV calculation are defined based on the conclusions from the 2D calculations (section 5.3.4) that the flow should be taken to be fully turbulent away from the walls ($FTP = 1$) with FTP tending towards the measured intermittency value at the surfaces. A reasonable approximation to this has been achieved. Contours of FTP on the endwall and blade surfaces are shown in *Figure 5.8* In the tangential direction $FTP \rightarrow 1$ over 10% of the pitch which at midspan gives a similar variation as for the VE calculation (see *Figure 5.8*). The endwall profile becomes fully turbulent over $15mm$ which makes it slightly thinner than on the blade surfaces but the only region of low intermittency corresponds to the new, thin, skewed boundary layer so this was thought to be reasonable.

Area plots of secondary velocity vectors and total pressure loss coefficient are presented at slot 8 (97% C_{ax}) in *Figures 5.9 & 5.10* and at slot 10 (128% C_{ax}) in *Figures 5.12 & 5.13*. At slot 8 the results are only presented up to $120mm$ from the endwall, except for the experimental secondary velocities which were only taken over $60mm$, since they remain constant over the midspan region ($100 \rightarrow 200mm$). At slot 10 the results are presented up to midspan. Pitch averages of yaw angle, secondary k.e. and loss coefficient at the two slots are presented in *Figures 5.11 & 5.14* and area averages at slot 10 are given in the table below.

	Exp.	MLA	MLB	MLF	MLV
Yaw angle	−68.33°	−68.88°	−68.91°	−68.57°	−68.88°
Midspan yaw angle	−68.36°	−68.93°	−68.83°	−68.43°	−68.89°
C_{sk}	0.016	0.005	0.027	0.026	0.028
C_{p0}	0.170	0.534	0.218	0.250	0.193
Midspan C_{p0}	0.097	0.482	0.148	0.185	0.120
Secondary C_{p0}	0.073	0.052	0.070	0.065	0.073
$C_{p0\infty}$	0.189	0.545	0.259	0.291	0.231
Midspan $C_{p0\infty}$	0.098	0.487	0.159	0.195	0.126

Table 5.8 — Slot 10: Area mass–averaged values.

For both experimental and calculated results pitch averaging is carried out over the range of the data. Within the blade passage the calculated data extends from surface to surface whilst the experimental data does not so the results are not strictly comparable. The effect of this can be quite considerable as can be seen from *Figure 5.9*, for example, where the velocity vectors close to the suction surface in the calculations indicate high secondary k.e. which is not included in the experimental pitch average. Averaging the calculated data over the experimental data range improves the agreement considerably but there is some doubt as to whether the experimental and calculation tangential coordinates correspond exactly (the tangential position of the suction surface, for example, varies by $30mm$ over the width of slot 8). Since small variations in the data range can have a big effect on the pitch average this may give misleading results. Pitch averaging from blade to blade does at least ensure consistency from slot to slot.

Effect of freestream length scale

The effect of the freestream length scale can be seen by comparing the experimental results with the coarse grid calculations MLA ($L_\infty = 9.36mm$) and MLB ($L_\infty = 0.936mm$). The secondary velocities show that the lower length scale calculation predicts the location and extent of the passage vortex reasonably well whilst the higher length scale prediction places the vortex too close to the wall, completely the wrong shape and apparantly too weak. The loss contours are also significantly different for the MLA calculation with too much loss extending over most of the pitch. Neither result is too surprising since the two–dimensional investigation of the effect of L_∞ showed that the higher value leads to a very high turbulent viscosity which would act to dissipate secondary flows and increase losses. The MLB calculation also shows too high losses within the loss core and endwall regions but the shape of the contours are otherwise very similar to those from the experimental results.

These results are largely confirmed by the pitch and area averages (*Figure 5.11*). At both slots the MLA calculation has its peak of underturning too low and too close to the endwall whilst the MLB calculation is much better. The MLA secondary k.e. is also too low and fails to show the peak associated with the passage vortex. The MLB calculation has a peak that is considerably higher than the experimental value at both slots but at slot 8 this is largely due to the averaging range. If, for example, the data is averaged over the experimental range, the secondary k.e. peak becomes slightly lower than the experimental value and the yaw angle is in much closer agreement.

A similar pattern is seen in the pitch averaged loss which is considerably too high for the MLA calculation and only slightly so for MLB. In both cases, however, part of the difference close to the endwall and at midspan is because the calculations assume the boundary layers are fully turbulent when in reality they are not. The slot 10 area averages confirm these results with the MLA calculation giving approximately one third of the secondary k.e. and three times the loss whilst MLB gives about 70% too much secondary k.e. and 50% too much loss. In the MLB calculation much of this extra loss appears to be profile loss since the secondary loss (taken as the difference between the full area and midspan loss) is approximately correct.

Effect of grid

The effect of grid size on a full three-dimensional solution may be examined by comparing the MLB (coarse grid) and MLF (fine grid) calculations. The secondary velocities at both slots are very similar and seem to agree well with the experimental results though the different number of vectors make them difficult to compare. In the total pressure contours, the fine grid has a marginally higher peak loss in the loss core than the coarse grid and the wake appears to be very slightly wider. The differences are, however, considerably smaller than between either calculation and the experimental results. The pitch averages show similar results with relatively good agreement for the yaw angle, secondary k.e. and loss close to the endwall. One exception is the secondary k.e. at slot 8 where the coarse grid peak is considerably higher but only because of a single point.

Away from the endwall region, the loss for the fine grid is substantially higher than for the coarse grid. From the loss contours this appears to be due to a thicker suction surface boundary layer at slot 8 which leads to a thicker wake at slot 10. This is reflected in the area averages where the thicker boundary layer reduces the midspan yaw angle and increases the losses. Comparing the midspan area averages with the equivalent 2D calculations (section 5.3.1) shows that the fine grid results agree reasonably well (as do the high freestream length scale results) whilst the 3D coarse grid results give significantly lower losses. The reason for this is unknown but may be that the 3D calculations had not been run for sufficiently long (the 2D calculations were run for much longer than was necessary). However, the convergence histories and results at earlier passes showed no significant changes were occuring when the runs were terminated.

Effect of VISMOD

The final mixing length calculation (MLV) used modifications to the turbulent viscosity, μ_T, (by a factor FTP) to simulate laminar and transitional regions. In 2D (section 5.3.4) this significantly reduced the profile loss to a value close to that found experimentally. The results may be compared with both the experimental data and the fully turbulent coarse grid calculation (MLB). The secondary velocities are virtually identical to the MLB results so also agree well with the experimental data. However, this should be expected since the flow away from the surfaces is still taken to be turbulent so the VISMOD modifications should not greatly affect the flow here. A similar conclusion may also be drawn from the pitch and area averaged yaw angle and secondary k.e. which are very similar for the MLB and MLV solutions.

The VISMOD modification does, however, have a considerable effect on the total pressure loss close to the surfaces. At slot 8 it virtually halves the width of the high loss region close to the suction surface, implying a much reduced boundary layer thickness. On the endwall it appears to have a similar effect though it is hard to tell since the boundary layer here is much thinner. The peak loss in the loss core, however, remains virtually unchanged. Similar results may be seen at slot 10 where the wake is much thinner and has a reduced loss than for the fully turbulent calculation. The width is approximately the same as measured experimentally but the loss at the wake centre is still greater. As with slot 8 the loss core associated with the passage vortex is virtually unchanged but the second core due to the shed vorticity has become weaker.

The effect on the pitch averaged loss is restricted mainly to the midspan region where the inclusion of laminar and transitional regions has the desired effect of reducing the losses. Closer to the endwall the loss profile changes very little. This can also be seen in the area averaged loss where the total loss decreases but the secondary loss (total - midspan) increases very slightly. In comparison with the experimental value the pitch averaged loss is still slightly high and it is surprising that, at midspan, the reduction in loss is not as great as for the equivalent 2D case (VE). There are some slight differences between the two cases around the trailing edge (compare *Figures 5.6e & 5.8*), made necessary by the extension to three–dimensions, but it is unlikely that this could have such a large effect.

Flow development

The development of the flow in terms of loss and secondary k.e. generation may be shown by plotting area averaged values against axial position for the experimental data and each of the calculations. Experimental loss results are available from Biesinger [1993] who carried out total pressure traverses at slots 1, 5, 8 & 10 whilst secondary k.e. results may be taken from the present measurements. To obtain full area averages from these it is necessary to assume that the pitch averaged value remained constant from the edge of the traverse area ($60mm$) to midspan (except at slot 10 where the data extends to midspan). At slots 1, 3, 5 & 6 this is reasonable since the pitch averages have all become virtually constant well before the edge of the traverse (see Chapter 4). At slot 8, however, the pitch averages are still varying so it was not possible to obtain an area average here.

The results are plotted in *Figure 5.15*. To make them more easilly comparable with the experiment, the results from the calculations have only been plotted at the slots 1, 3, 5, 6, 8 & 10 rather tham more frequently so the distributions do not appear as smooth as they should. From the loss plot (*Figure 5.15a*) it can be seen that the high freestream length scale calculation (MLA) produces far too much loss from slot 1 (-9% C_{ax}) onwards. This leads to too much dissipation of secondary k.e. resulting in the low values seen in *Figure 5.15b*. The remaining calculations follow the experimental results much more closely though still generate too much loss through the blade passage. The agreement in the development of secondary k.e. up to slot 6 (71% C_{ax}) is good. The lack of an experimental result for slot 8 makes the remainder difficult to compare though it does seem that the calculations predict insufficient decay downstream of the trailing edge.

5.4.2 High & low Reynolds number k–ϵ calculations

Three k–ϵ calculations have been carried out, two using the high Reynolds number version and one using the low Reynolds number model. The high Reynolds number calculations were both carried out on the coarse grid and differ in that one uses the standard model (KSS) and the other included the Kato–Launder [1993] S–Ω

modification (KSO). As such these are repeats of previous 2D calculations (section 5.3.3) but in three–dimensions. The low Reynolds number calculation (LSO) was carried out on the fine grid and again used the S–Ω modification. All calculations were carried out using the measured experimental inlet conditions (including the correct freestream length scale).

As with the mixing length model calculations, results are presented at slots 8 and 10. Area plots of secondary velocity vectors, turbulent k.e. and total pressure loss are presented in *Figures 5.16–18* for slot 8 and *Figures 5.20–22* for slot 10. Pitch averages of these parameters (and yaw angles) are presented in *Figures 5.19 & 23* and area averaged values for slot 10 are given in the table below. The comment made about the different averaging ranges at slot 8, in the discussion of the mixing length calculations also applies here. Pitchwise averaging is again taken from blade to blade so these calculations may be compared with the mixing length model results.

	Exp.	KSS	KSO	LSO
Yaw angle	−68.33°	−68.96°	−68.92°	−69.15°
Midspan yaw angle	−68.36°	−69.08°	−68.94°	−69.18°
C_{sk}	0.016	0.009	0.018	0.017
C_{tk}	0.023	0.079	0.016	0.014
Midspan C_{tk}	0.012	0.086	0.013	0.012
C_{p0}	0.170	0.379	0.267	0.298
Midspan C_{p0}	0.097	0.337	0.208	0.234
Secondary C_{p0}	0.073	0.042	0.059	0.064
$C_{p0\infty}$	0.189	0.398	0.297	0.328
Midspan $C_{p0\infty}$	0.098	0.344	0.218	0.244

Table 5.9 — Slot 10: Area mass–averaged values.

The secondary velocity vectors at both slots 8 & 10 show that the standard high Reynolds number calculation (KSS) fails to predict the passage vortex at all well whilst the two calculations incorporating the S–Ω modification are much better. Even for these, however, the passage vortex is centered too close to the endwall and appears to be slightly too weak. The results from the better mixing length calculations (e.g. excluding MLA) are slightly better both in location and strength of the vortex. An indication of the reason for the poor performance of the KSS calculation is given in the contours of turbulent k.e. which show an excessive amount of turbulence at midspan. This was also found in the two–dimensional calculations (section 5.3.3) where it resulted in increased loss due to excessive dissipation of energy from the mean flow. In three–dimensions it clearly also causes a similar dissipation of the secondary flows and hence results in the poor prediction of the passage vortex.

The predicted turbulent k.e. from the S–Ω calculations, both high (KSO) and low (LSO) Reynolds number, are much better. As with the secondary velocities they are both quite similar and are in reasonable agreement with the experiment. The major differences are that the peak level of turbulence in the passage vortex is considerably underpredicted at both slots and the turbulence in the wake is overpredicted, particularly in the low Reynolds number calculation. The distribution of loss for all the calculations is qualitatively similar to the experiment though less so for the high Reynolds number calculation than the other two. Comparisons at slot 8 are difficult since much of the calculated loss, found in the suction surface boundary layer, is not captured by the experimental traverse. It does appear, however, that the loss associated with the passage vortex is slightly overpredicted.

At slot 10 (*Figures 5.20–22*) comparisons are easier as the traverses cover the same area. The KSO and LSO calculations both again slightly overpredict the loss associated with the passage vortex and also overpredict the losses due to the shed vortex and the wake. The KSS calculation is less good with only a single loss core away from the endwall and excessive loss at midspan across the whole passage. The pitch averages show similar results with the failings of the KSS calculation most evident in the secondary and turbulent k.e. plots. The secondary k.e. fails to rise to anything like the expected peak associated with the passage vortex whilst the turbulent k.e. continues to rise to midspan. As expected the losses are also grossly overpredicted over the whole of the span (though at slot 8 some of the difference will be due to the different pitch averaging ranges).

The remaining two calculations are qualitatively in better agreement with the experimental results and are generally very similar to each other. All the plots have their peak too close to the endwall due to the poor prediction of the position of the passage vortex. Whilst the secondary velocity vectors and the pitch averaged yaw angle suggest that the passage vortex is too weak the calculated secondary k.e. is actually slightly greater than the experimental value. The turbulent k.e., however, fails to reach anything like the correct value particularly at slot 10. The losses follow roughly the correct shape but are too high towards midspan. In comparison with the mixing length results the predict yaw angle and losses are slightly worse but the secondary k.e. is better.

The area averages at slot 10 (Table 5.9) confirm these results. Excluding the KSS calculation the secondary k.e. is very similar to the experiment. The turbulent k.e. values are some 35% low which is due entirely to the low values within the passage vortex since the agreement at midspan is good. The losses are overpredicted both overall and at midspan which seems to be due mainly to an overprediction of the thickness and loss within the blade boundary layers (particularly on the suctin surface). This in turn leads to a wake which is slightly too thick and contains too much loss. For the high Reynolds number calculation (KSO) this is expected since the flow is assumed to be fully turbulent. The low Reynolds number model (LSO) however can, in theory, predict transition so should do better. That it does suggests that it has not predicted transition at all well. The secondary loss (full area – midspan) for both calculations is slightly low which may be explained by the low level of turbulence within the passage vortex.

Flow development

As for the mixing length calculations, the development of the flow may be shown in terms of the area averaged loss, secondary k.e. and, additionally, turbulent k.e. (*Figure 5.24*). From the loss plot it can be seen that the extra loss in the calculations is generated in the blade passage with slightly too little being generated at the trailing edge and downstream. The standard high Reynolds number k–ϵ model (KSS) is clearly the worst having generated almost six times the correct loss by slot 8 (97% C_{ax}). The two S–Ω models are better, though not as good as the low length scale mixing length calculations (*Figure 5.15*), with the low Reynolds number version (LSO) producing a slightly higher loss from slot 1 onwards. The difference at slot 1 may be due to the different treatment of the boundary layer or the different grids but, excluding it, the two results are very similar.

The effect of the S–Ω modification is shown most dramatically in the development of turbulent k.e. (*Figure 5.24c*) where, without it (KSS), the irrotational strain caused by the turning of the flow leads excessive generation up to slot 6 (71% $\mathrm{C_{ax}}$). Beyond this point the flow is no longer being turned so the turbulence begins to decay. Implementation of the S–Ω modification (KSO & LSO) eliminates this production but appears to have too great an effect as the turbulence now increases too slowly. There is almost no difference between the development of turbulent k.e. between these two models.

The development of secondary k.e. shows that all three calculations produce too little secondary flow within the blade passage though by slot 10 (128% $\mathrm{C_{ax}}$) the KSO and LSO calculations are approximately correct. The low secondary k.e. in the KSS calculation is largely due to the high production of turbulence taking energy from the secondary flows. Once this production has ceased, beyond slot 6, the secondary k.e. decays at approximately the correct rate. The low secondary k.e. in the other two calculations cannot be due to the same reason but suggests that its gereration is inherently too slow. The decay from slot 6 is also too low but this could be due to the low turbulence. As with the turbulent k.e. the results from the KSO and LSO calculations are very similar.

Prediction of transition

The similarity between the results from the KSO and LSO calculations seems to suggest that the low Reynolds number model finds the boundary layers to be fully turbulent, or almost so, thus behaving in a very similar manner as the high Reynolds number version. To test this hypothesis the boundary layer states need to be identified and there are a number of ways that this may be attempted. Perhaps the most direct is to look at the turbulent viscosity, μ_T, since this should be low if the boundary layer is laminar and high if it is turbulent. However, very close to the surface it should be zero, because of the laminar sublayer, so should be looked at at some point within the log–law region of the boundary layer.

A second parameter that could be looked at is the wall shear stress, τ_w, or skin friction factor, C'_f, since this should also increase rapidly through transition. Calculating it also allows y^+ to be found which would be useful in obtaining a suitable distance from the wall at which to look at μ_T. Though not explicitly calculated during the calculations, the wall shear stress may be obtained from the values at the first grid line from a surface as follows;

$$\tau_w = \mu \frac{\partial u}{\partial y} \approx \mu \frac{U_{t1}}{y_1} \tag{5.9}$$

Where $\partial u / \partial y$ is the velocity gradient perpendicular to the surface which may be approximated by the velocity at the first grid line, U_{t1}, divided by the perpendicular distance to the surface, y_1. This assumes that U_{t1} has no component perpendicular to the surface which is reasonable so long as y_1 is small. The skin friction factor is then obtained from τ_w by dividing by $\frac{1}{2}\rho V_{is}^2$ where V_{is} the isentropic velocity calculated from the surface static pressure. Strictly, the freestream velocity at the edge of the boundary layer should be used but this is difficult to obtain.

The resulting skin friction factor and y^+ at midspan are plotted in *Figures 5.25 & 5.26* respectively. Unfortunately the high aspect ratio of the near wall cells here lead to oscillations of the velocity which, in turn, cause oscillations of these parameters. For plotting a two point rolling average has been used to smooth out these oscillations but the results are still not ideal. Also plotted, in *Figure 5.27* is the turbulent viscosity at the 6th and 8th grid line away from the surface. These lie at approximately 27 and 67 times the distance from the surface as the first grid line (for which y^+ is given in *Figure 5.26* so have y^+ values roughly in the range $20 \rightarrow 200$. For comparison the turbulent viscosity from the KSO (high Reynolds number) calculation is also plotted (*Figure 5.28*) for two grid lines at approximately the same distance (though slightly further away) from the blade.

On the suction surface the initial sharp rise in C_f and the rise in μ_T/μ both suggest almost immediate transition of the boundary layer. Over the latter part of the blade, however, the two seem to contradict each other with C_f decreasing sharply from 60% C$_{\text{ax}}$ whilst the turbulent viscosity remains high. The graph of C_f, however, is slightly misleading since it is plotted against axial chord rather than surface length. This means that, towards the trailing edge, the graph is effectively compressed since here a small axial distance corresponds to a large surface length. As a result the decay of C'_f is not as steep as it appears and may simply be due to the adverse pressure gradient which thickens the turbulent boundary layer and would eventually lead to separation. The graph of μ_T supports this conclusion since, in comparison with the KSS calculation, it is initially lower but rapidly increases to similar values. By comparison the experimental measurements found an initially laminar boundary layer with transition over the last 40% of the surface.

On the pressure surface the skin friction factor is much lower over most of the blade. The initial high values are due to stagnation of the flow, which leads to an almost zero V_{is}, and the remainder generally increase slowly. This may be due to thinning of the boundary layer in the accelerating flow but does not appear to give any indication of transition. The turbulent viscosity suggests that the flow is initially turbulent with some relaminarisation (decreasing μ_T) occuring between 50% & 80% C_{ax}. By comparison the KSO results show no drop in μ_T in this region (the drop near the trailing edge is thought to be a feature of the grid rather than the flow). The experimental results show relaminarisation occuring over the first 80% of the surface so, as for the suction surface, the prediction seems to be for the boundary layer to be more turbulent than it should be.

The turbulent viscosity $1.0mm$ from the endwall is shown in *Figure 5.29* for both the low (LSO) and high (KSO) Reynolds number calculations. The value of y^+ at this plane is in the region of 50 → 150 which is reasonable but the distance was chosen mainly to allow comparison with the intermittency measurements (*Figure 4.24*). As with the viscosity at midspan the two calculations are fairly similar and their shape is quite comparable with the intermittency variation. Both have a band of high viscosity running from the leading edge to the suction surface following approximately the path of the passage vortex. Behind this the viscosity drops, more so in the low Reynolds number calculation, but is beginning to increase again by slot 10 (the edge of the plots). Whilst the differences are not great, the low Reynolds number model does seem to be predicting some laminarisation of the flow behind the passage vortex.

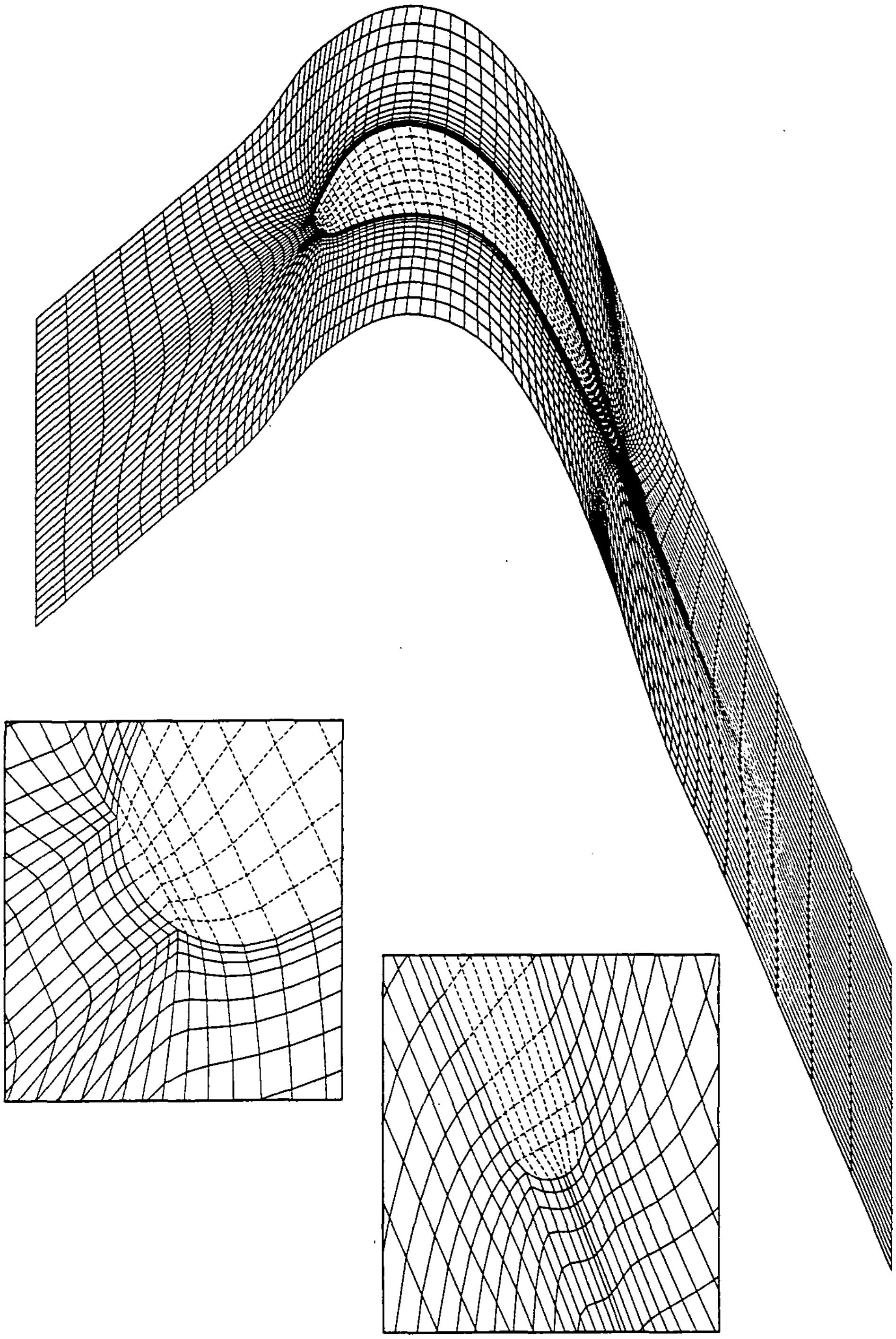

Figure 5.1 — Coarse grid (89 × 38).

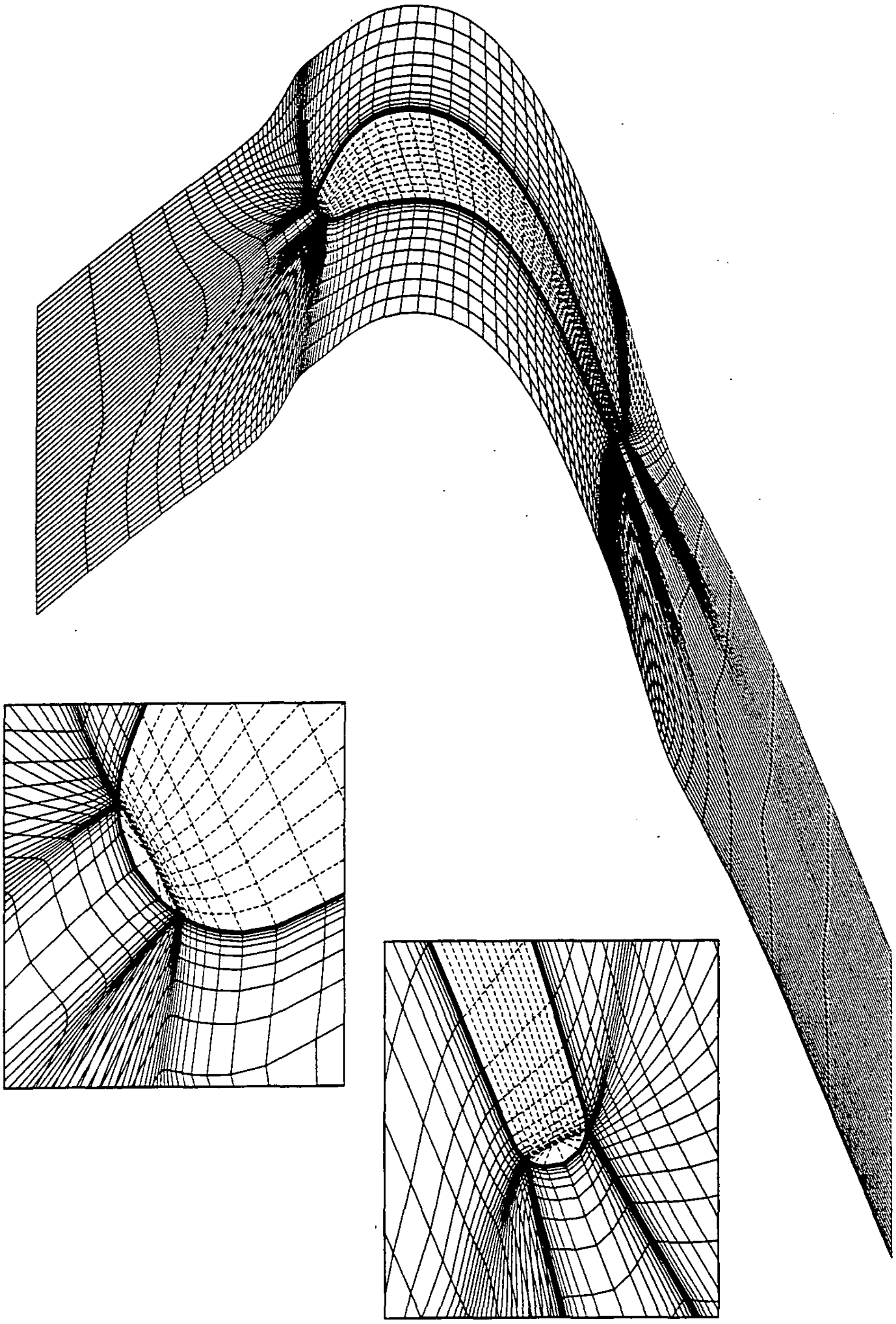

Figure 5.2 — Fine grid (99×55).

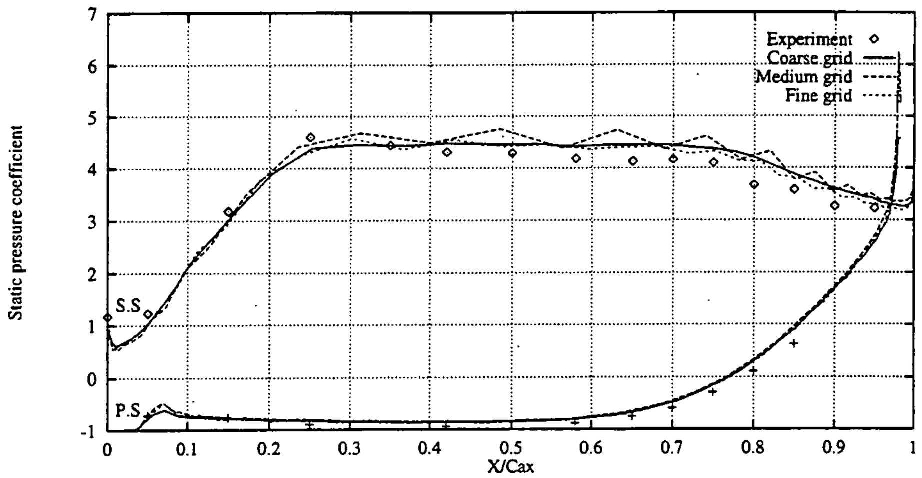

Figure 5.3 — Blade static pressure distributions.

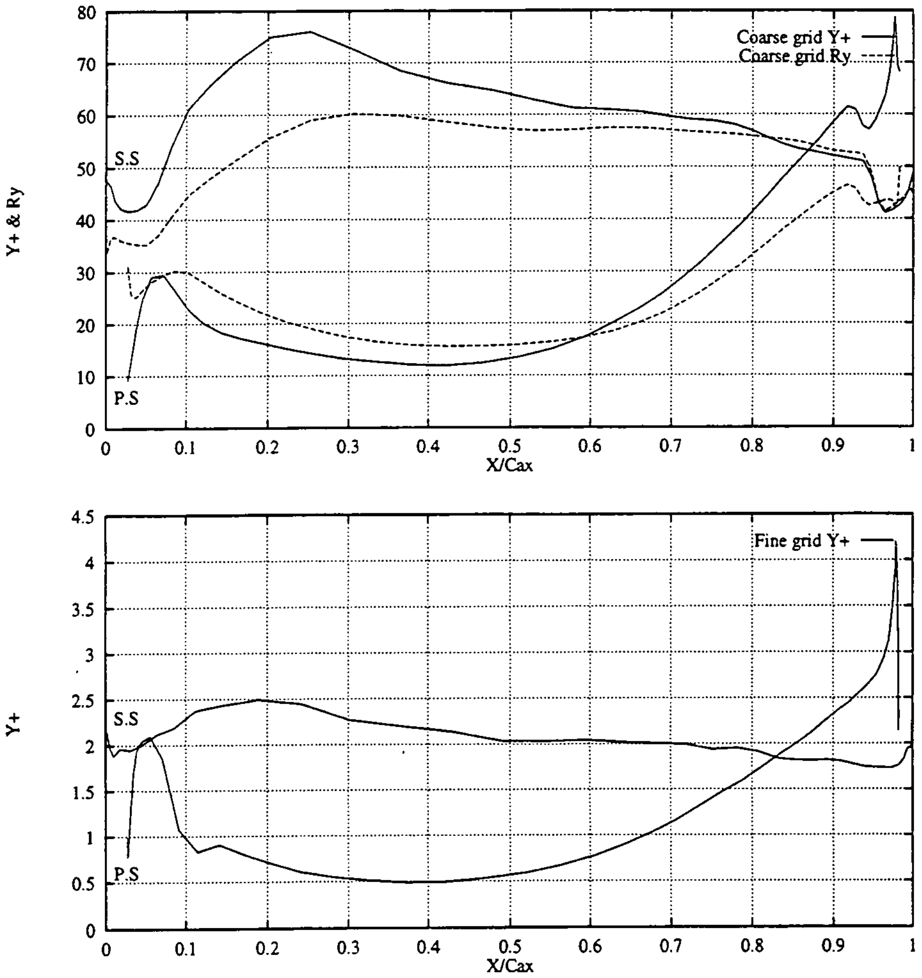

Figure 5.4 — Blade surface y^+ and R_y values.

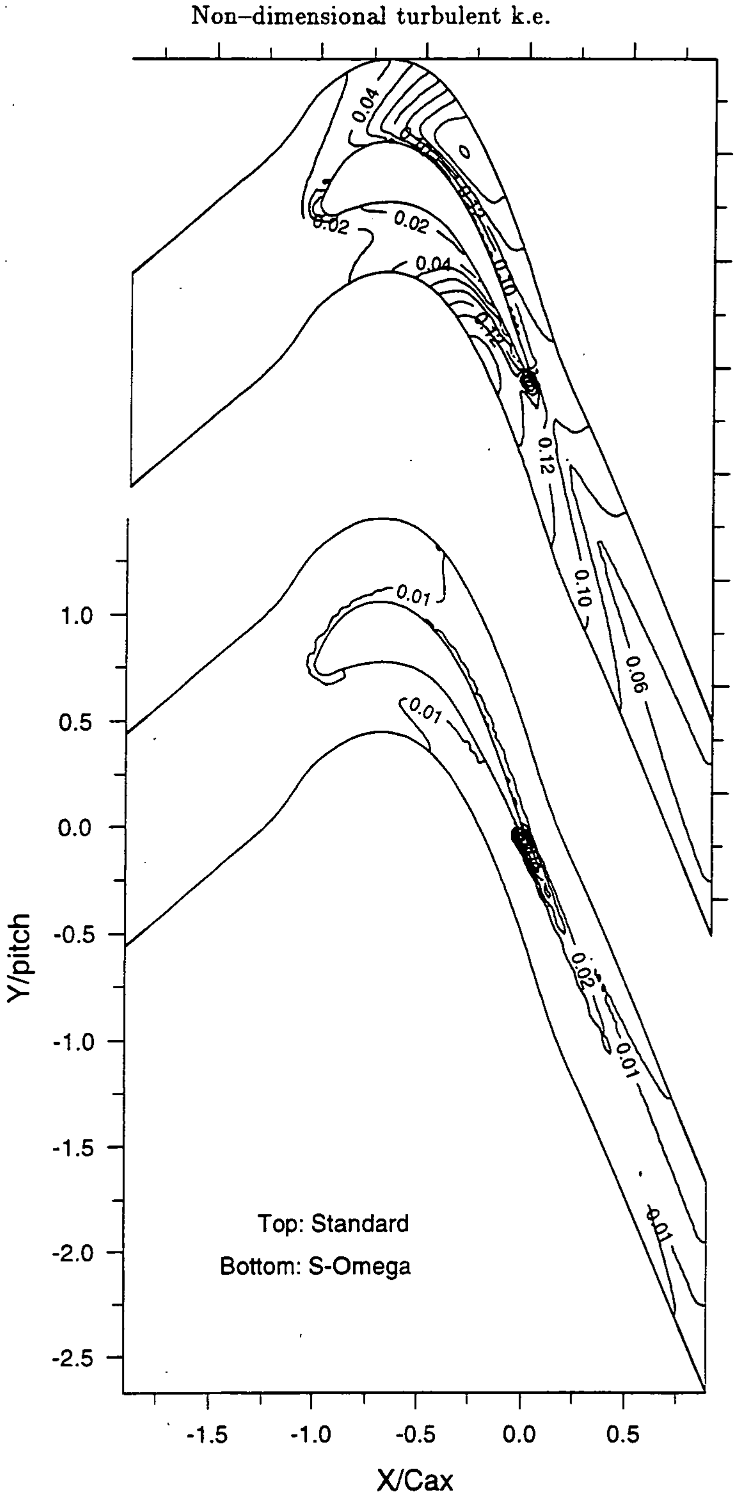

Figure 5.5 — Effect of S–Ω modification.

Contours of FTP (μ_T multiplier)

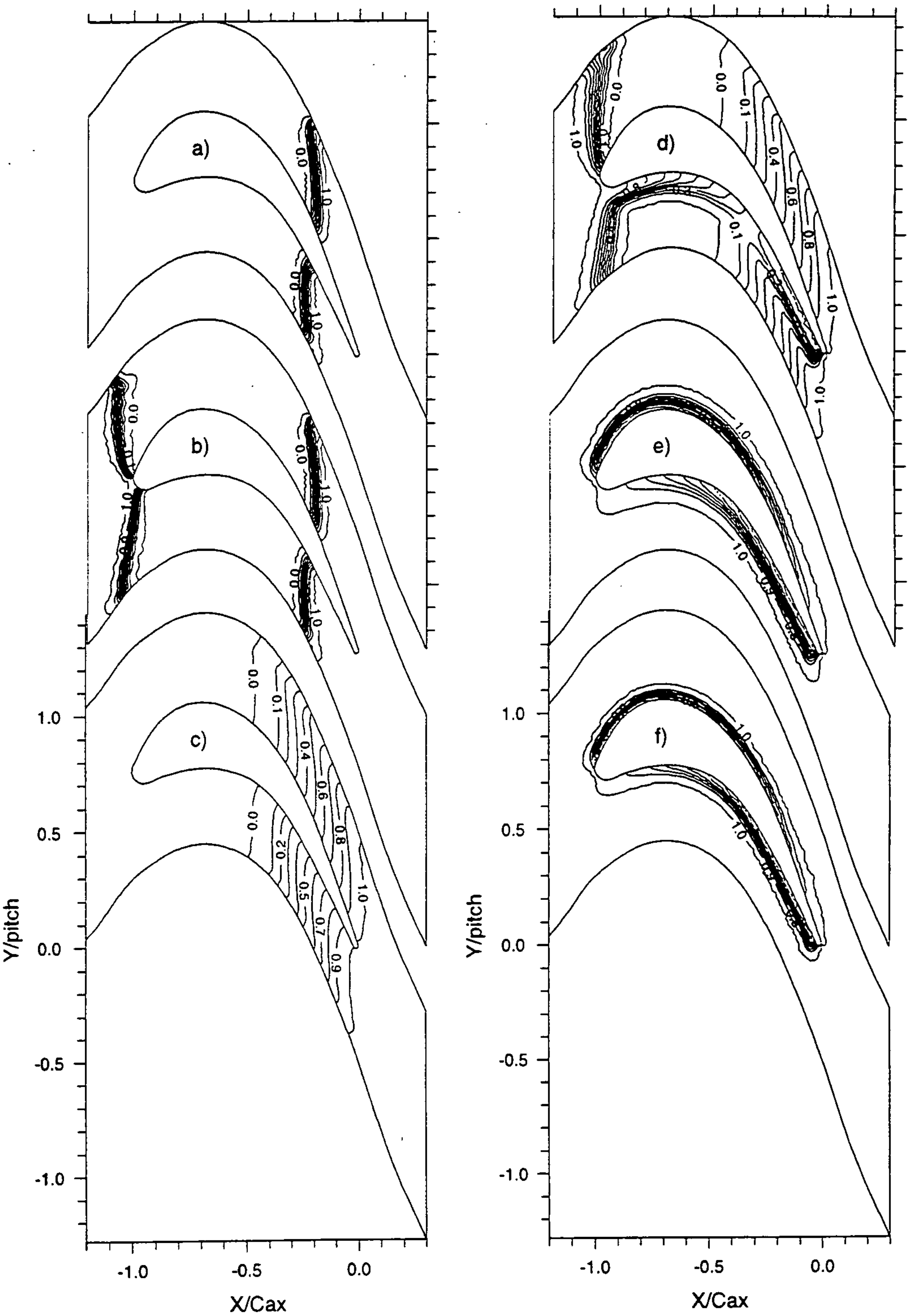

Figure 5.6 — Specified laminar, turbulent & transitional regions

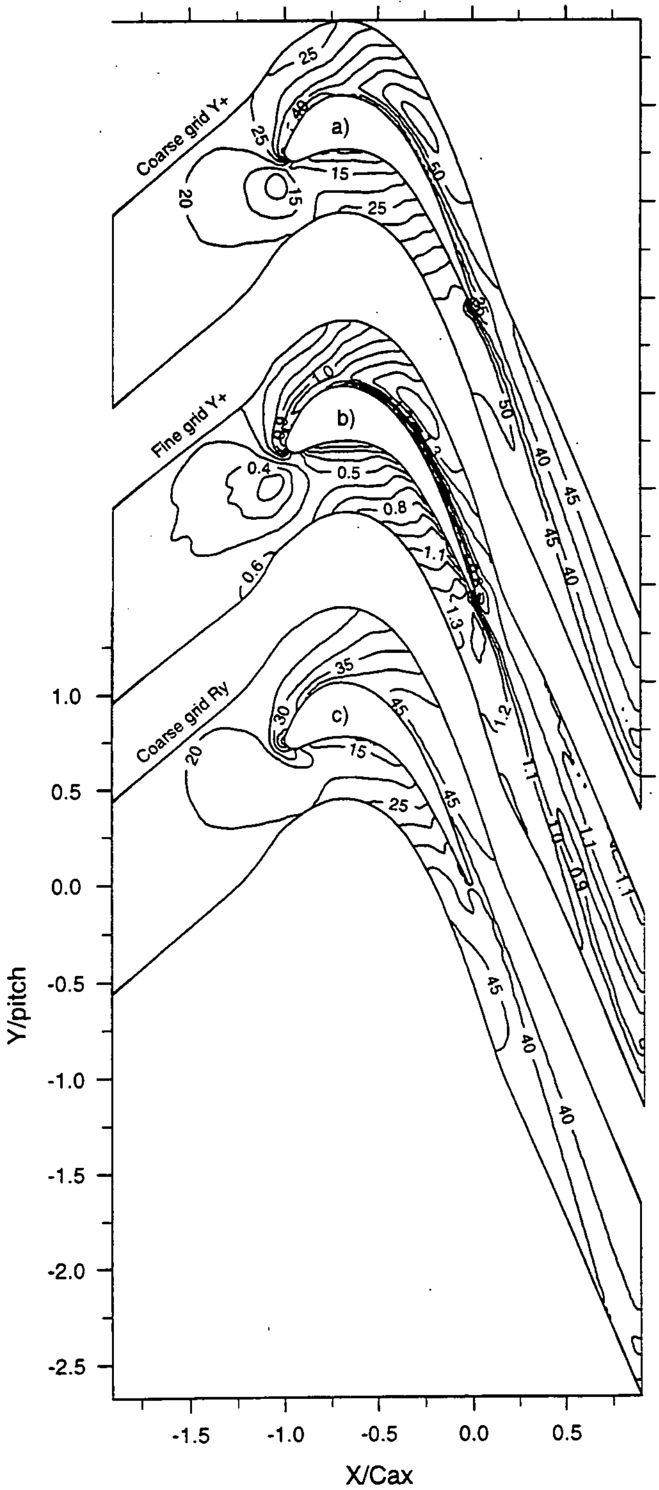

Figure 5.7 — Endwall y^+ and R_y values

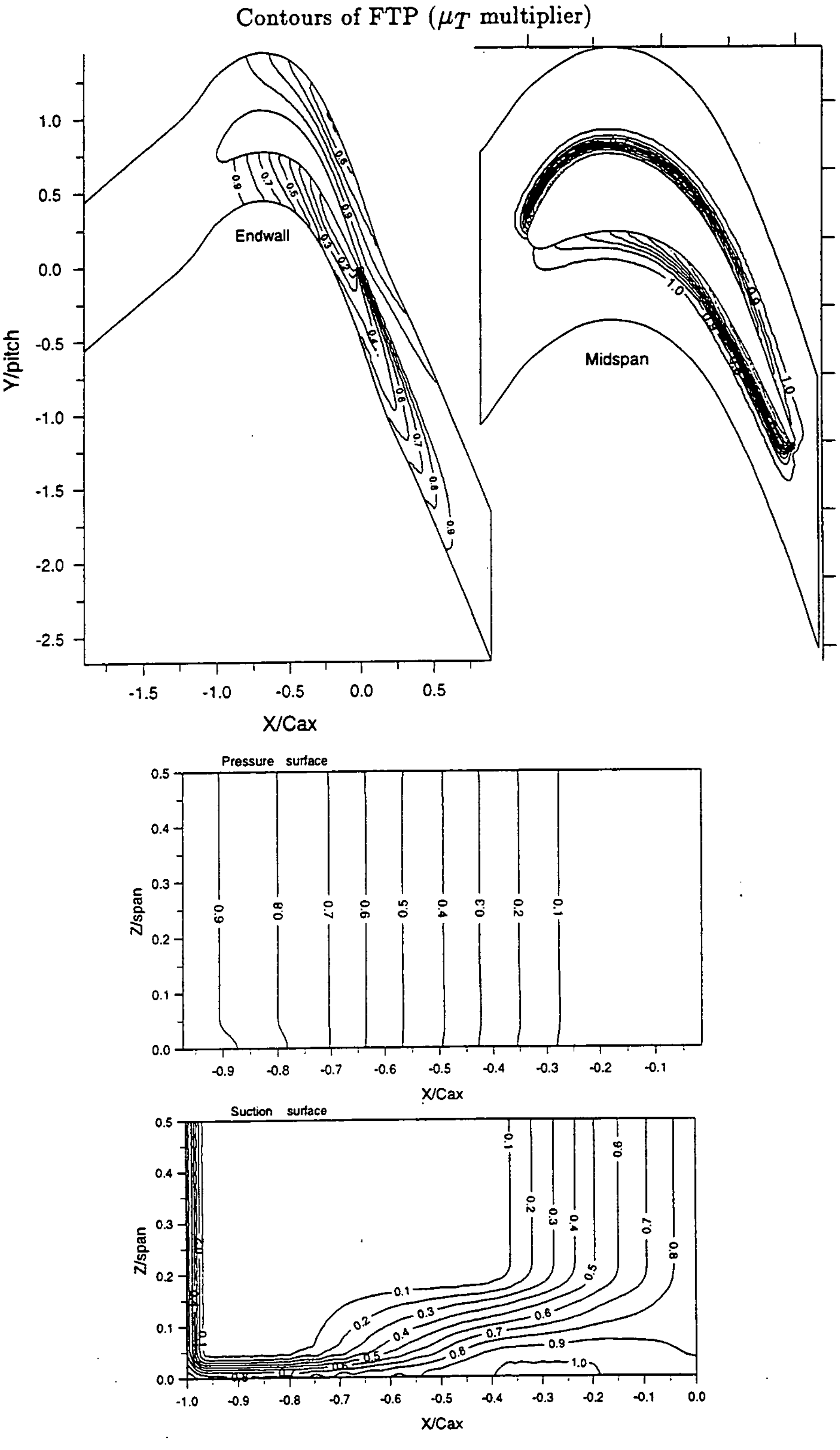

Figure 5.8 — 3D application of VISMOD

mixing length solutions

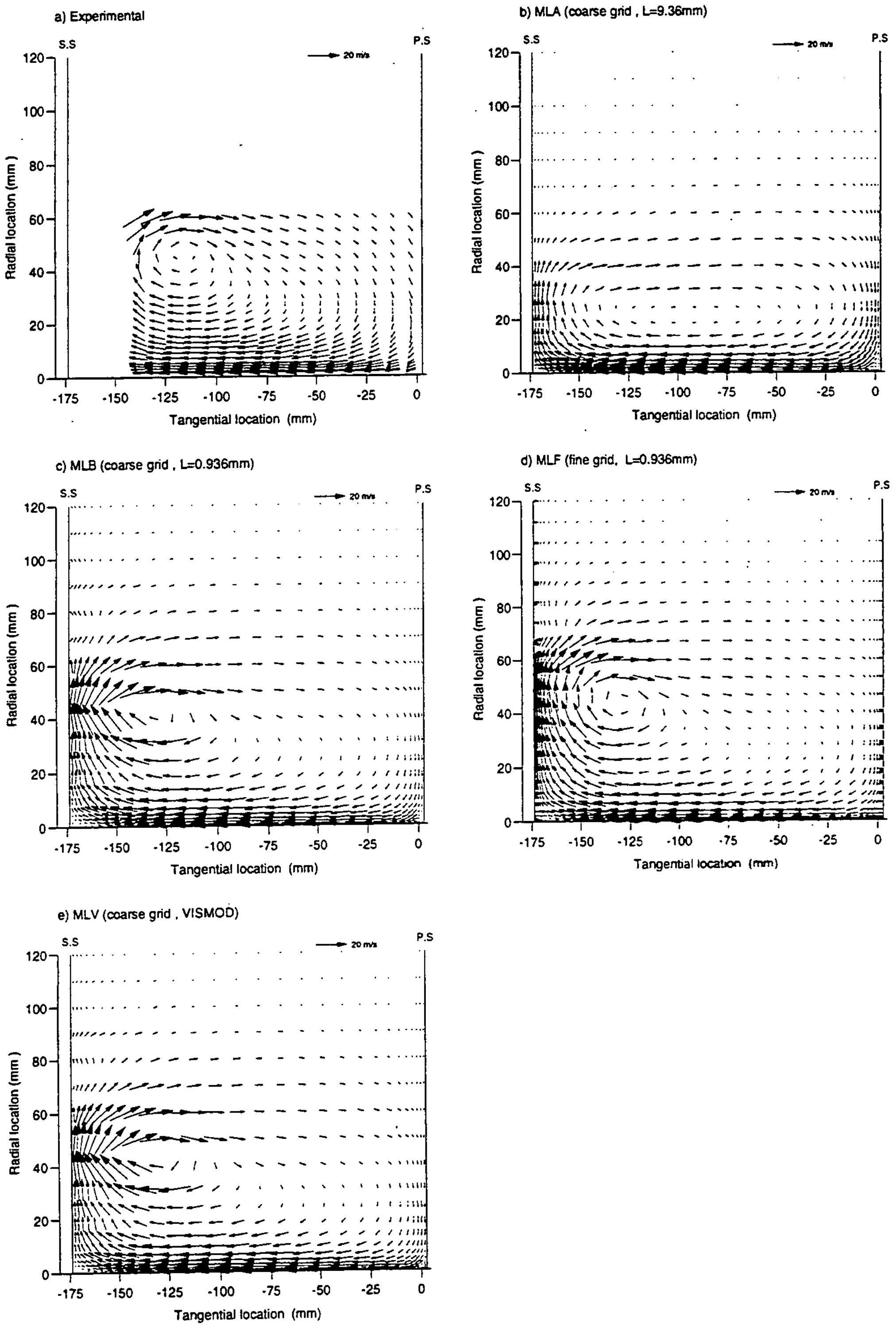

Figure 5.9 — Slot 8: Secondary velocity vectors

mixing length solutions

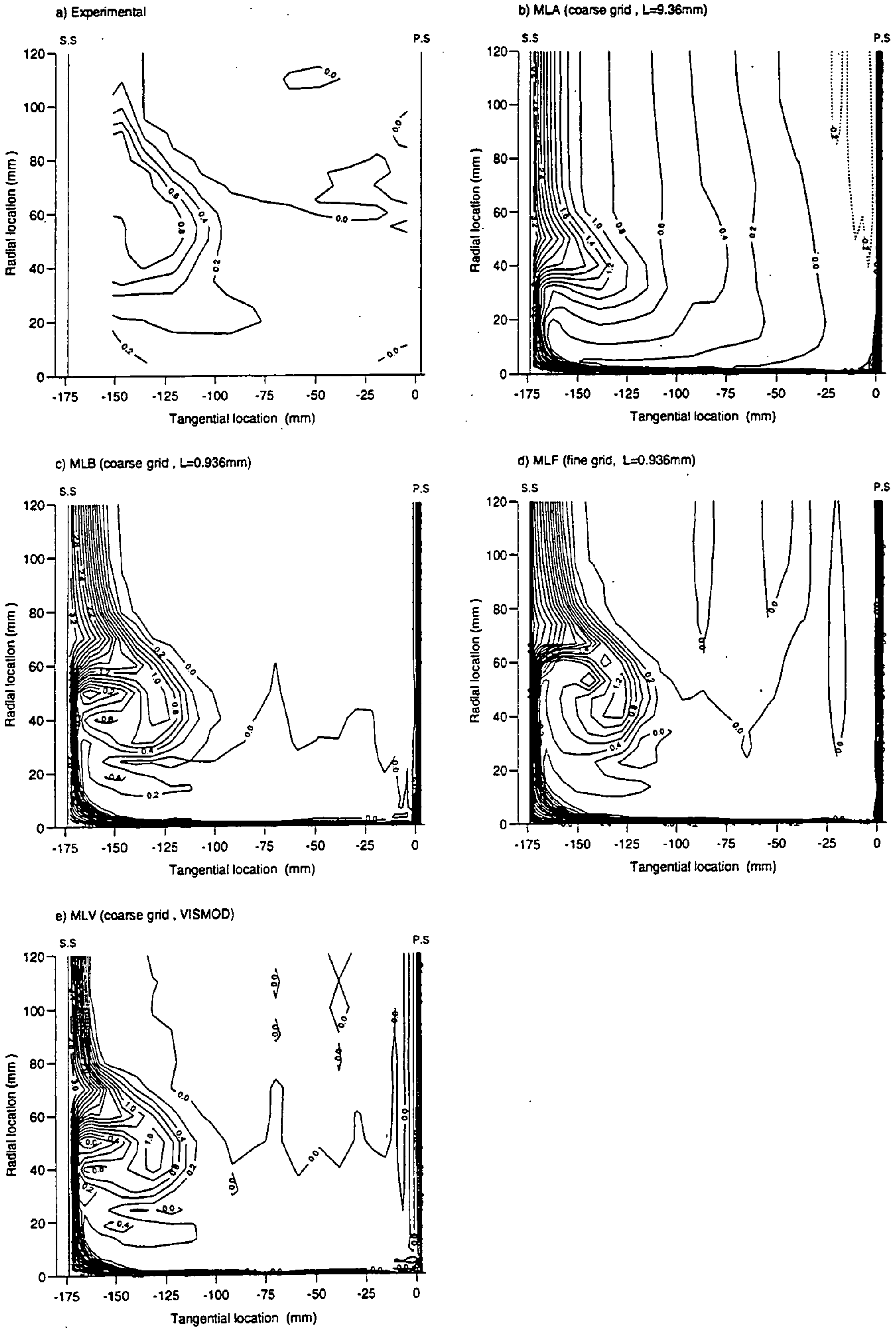

Figure 5.10 — Slot 8: Total pressure loss coefficient

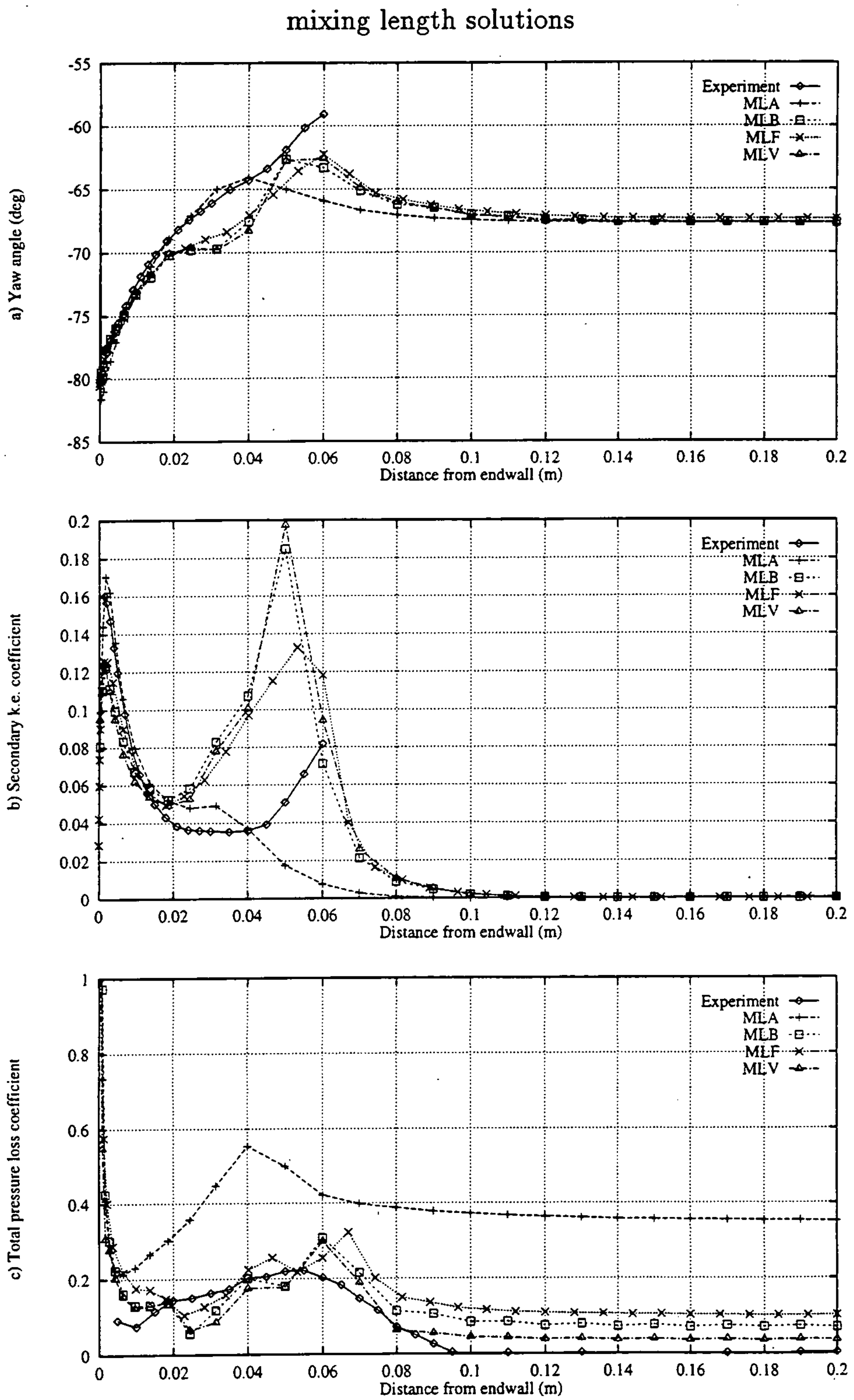

Figure 5.11 — Slot 8: Pitch averaged values

mixing length solutions

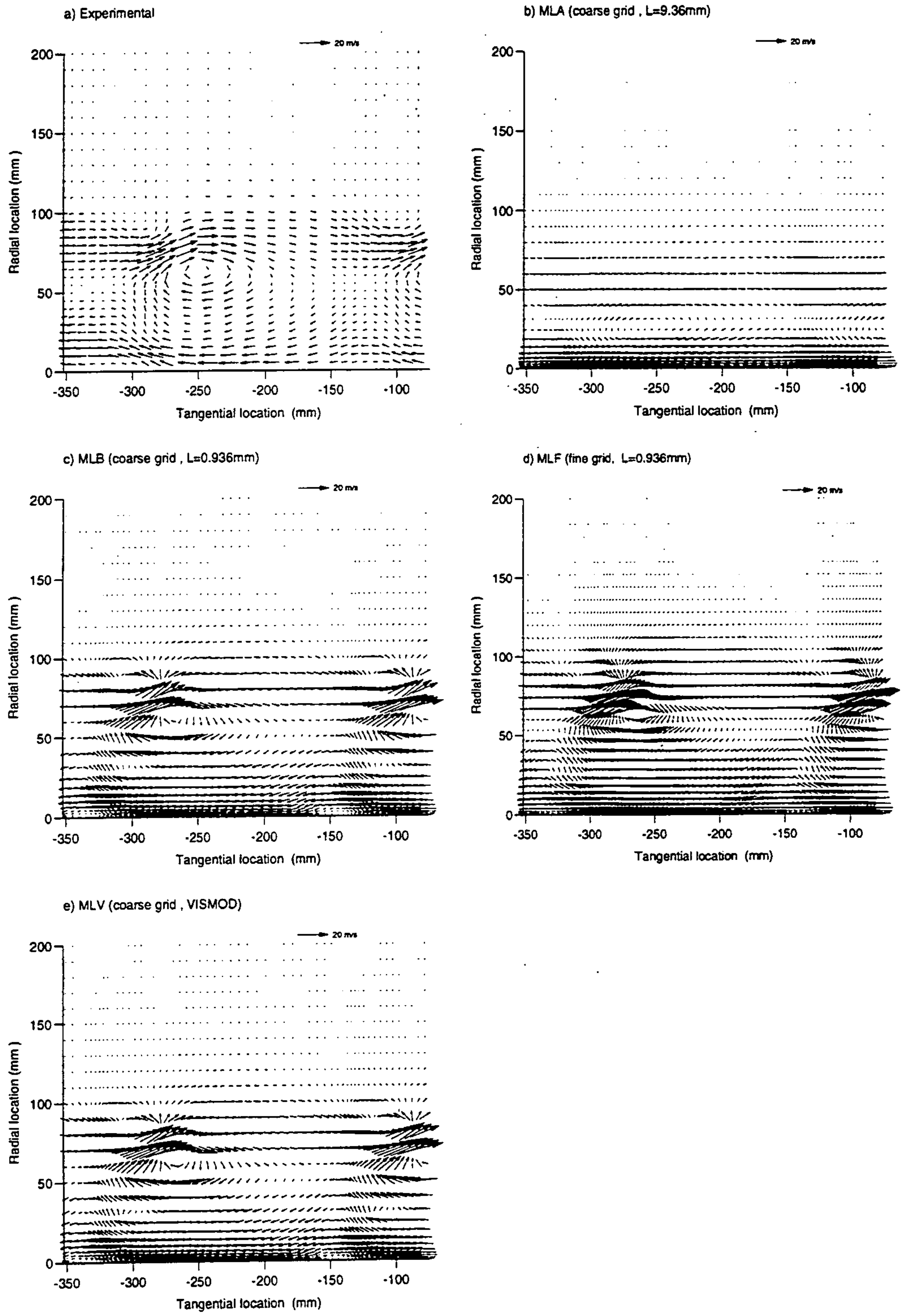

Figure 5.12 — Slot 10: Secondary velocity vectors

mixing length solutions

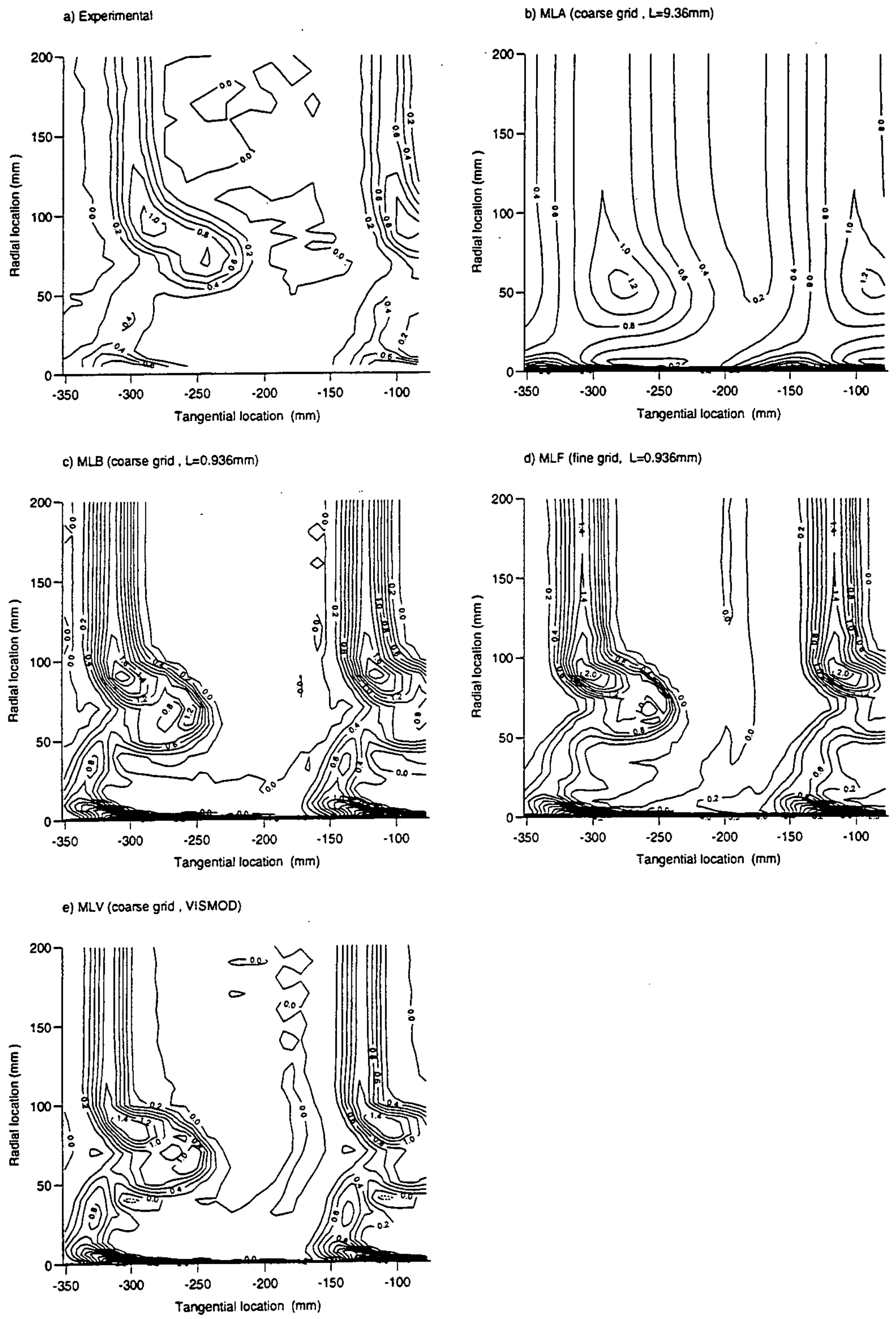
a) Experimental

b) MLA (coarse grid, L=9.36mm)

c) MLB (coarse grid, L=0.936mm)

d) MLF (fine grid, L=0.936mm)

e) MLV (coarse grid, VISMOD)

Figure 5.13 — Slot 10: Total pressure loss coefficient

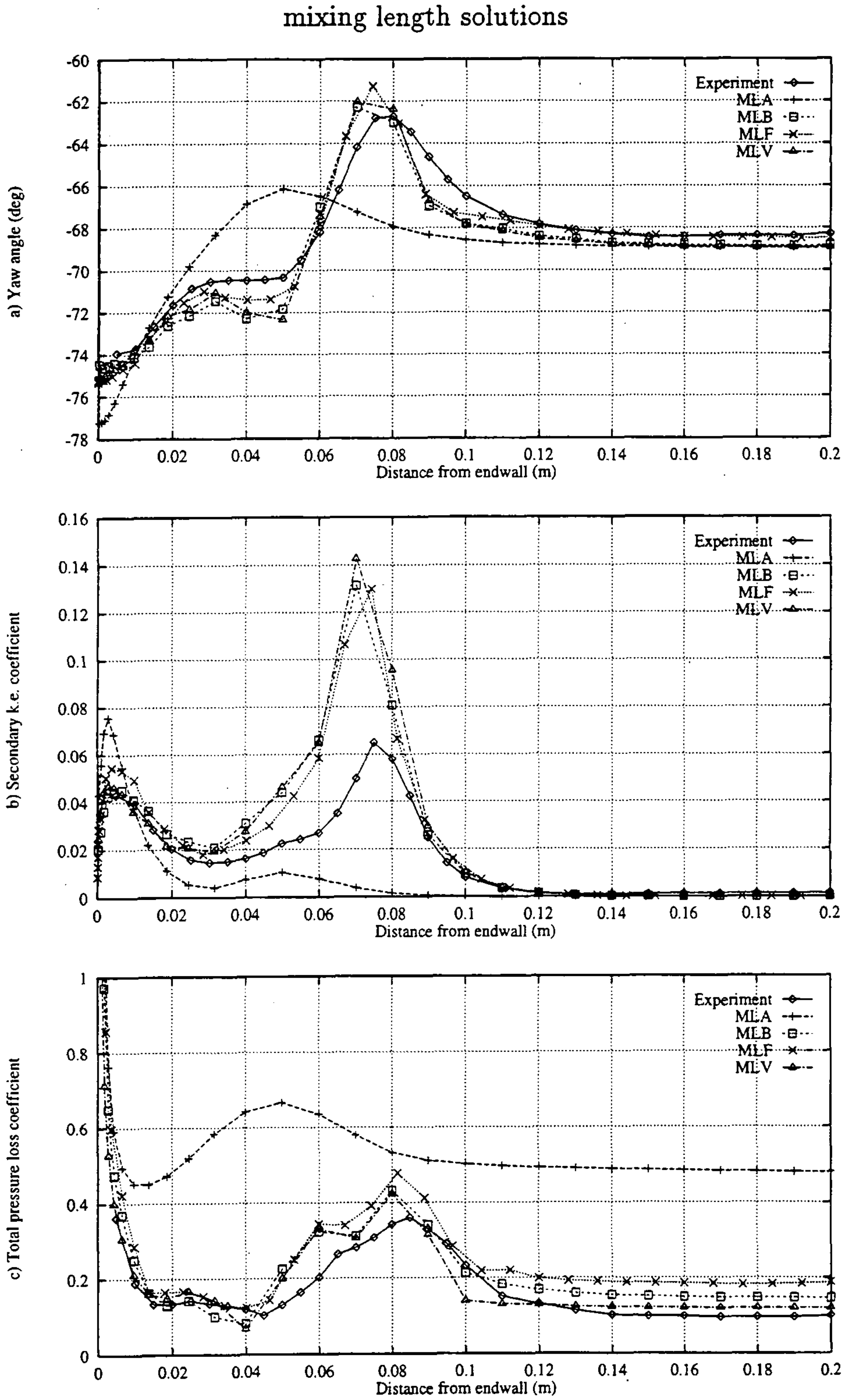

Figure 5.14 — Slot 10: Pitch averaged values

k–ϵ solutions

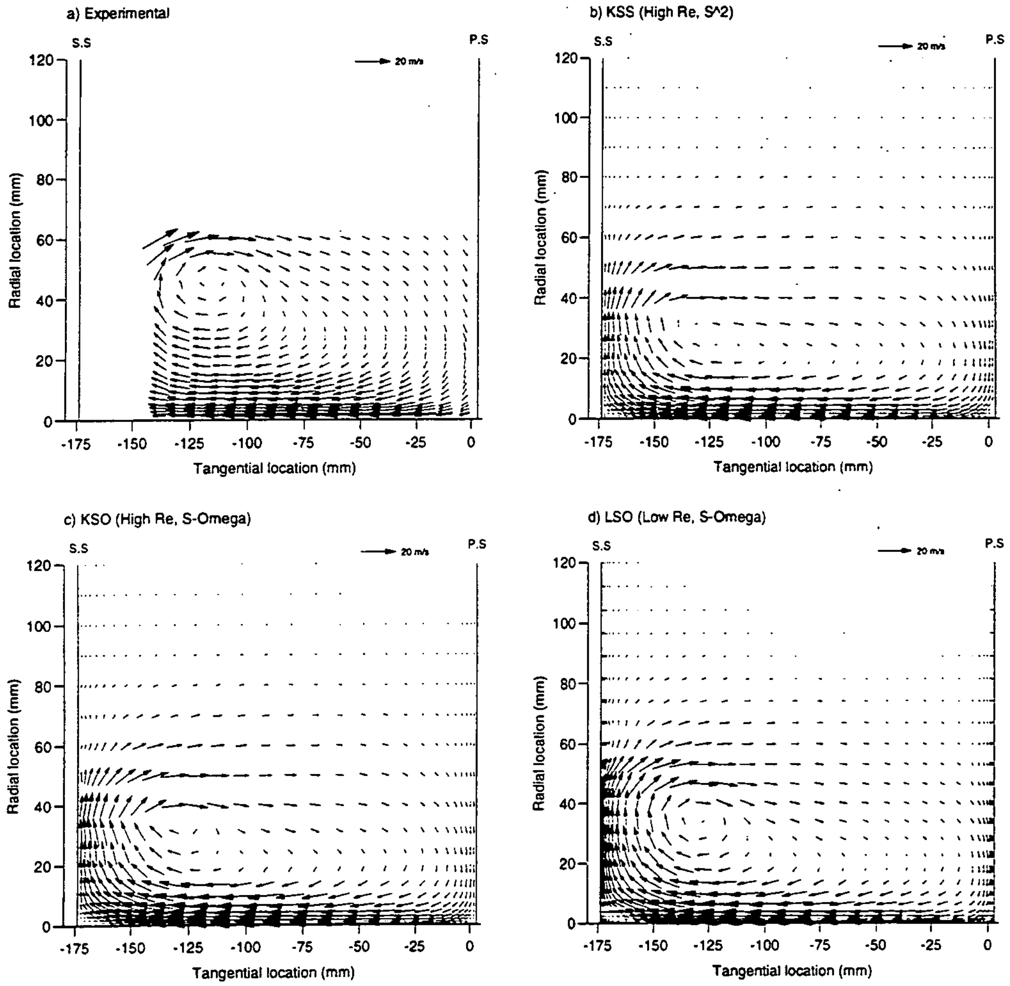

Figure 5.16 — Slot 8: Secondary velocity vectors

k–ϵ solutions

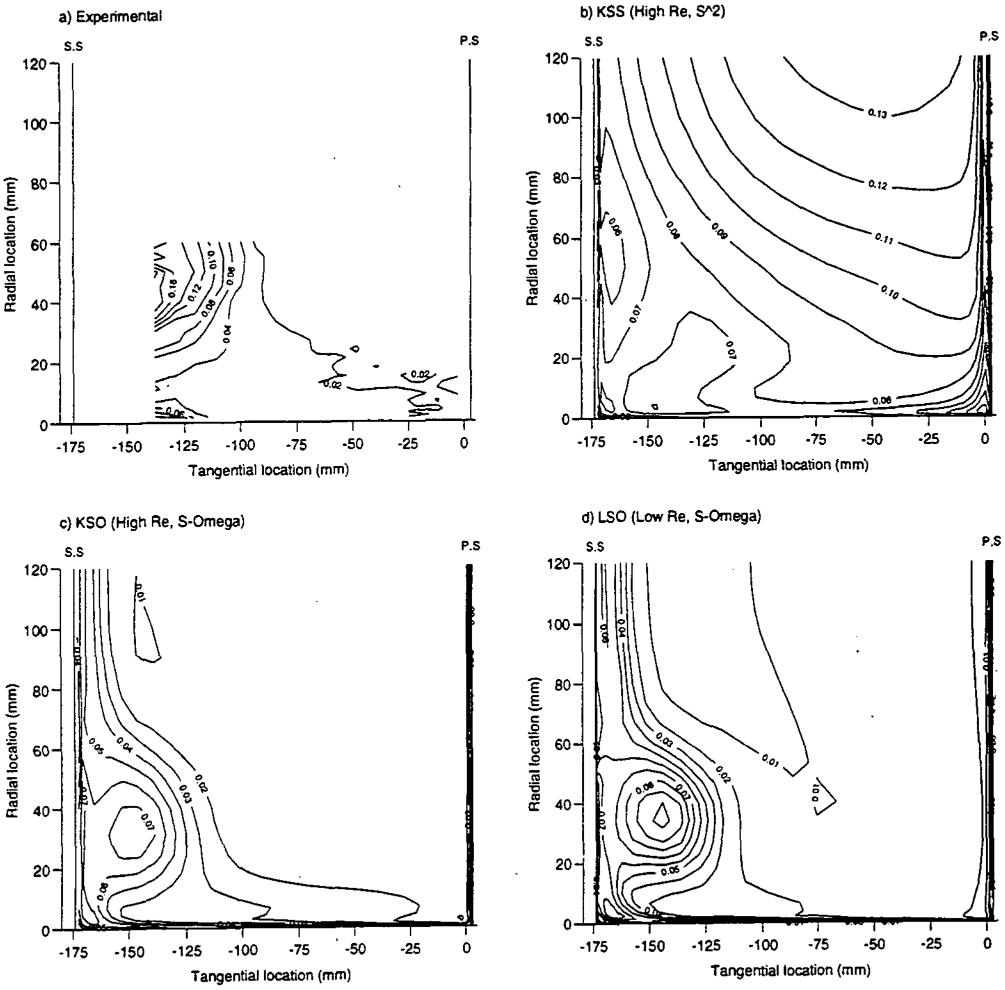

Figure 5.17 — Slot 8: Non–dimensional turbulent k.e.

k–ϵ solutions

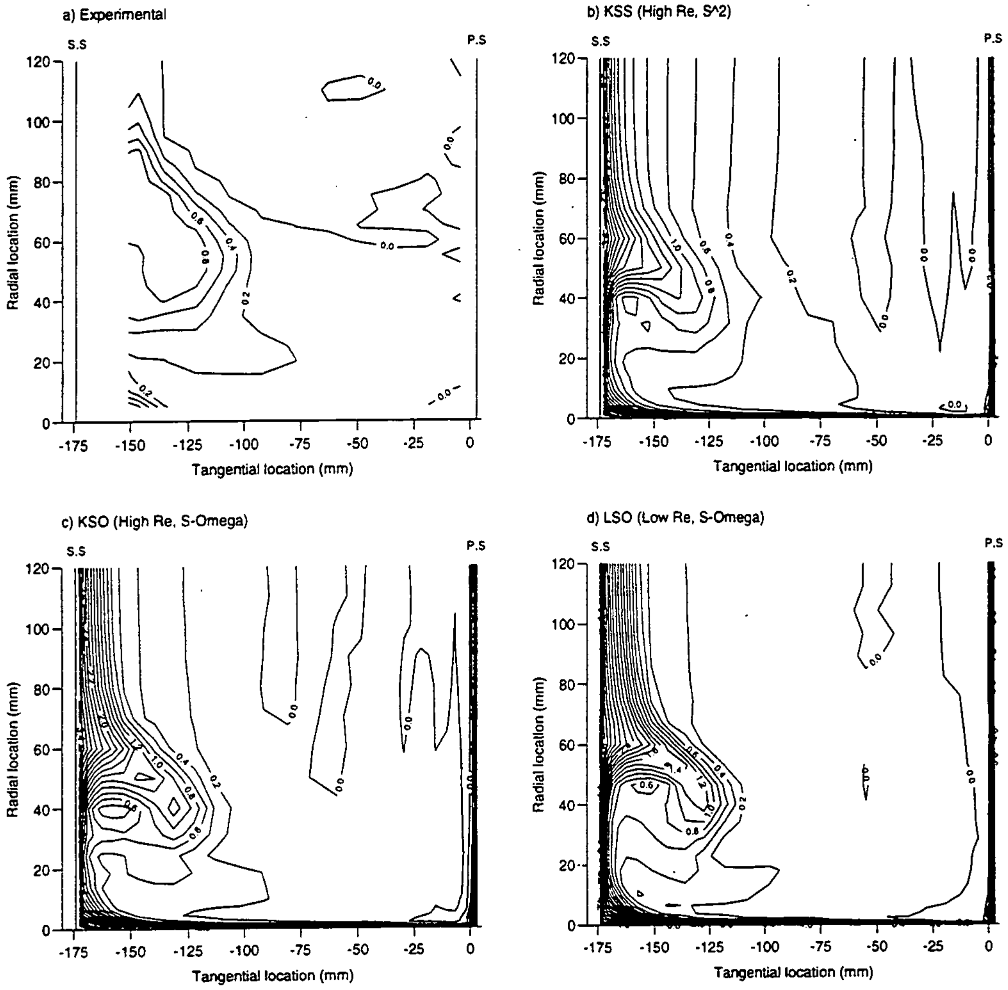

Figure 5.18 — Slot 8: Total pressure loss coefficient

k–ϵ solutions

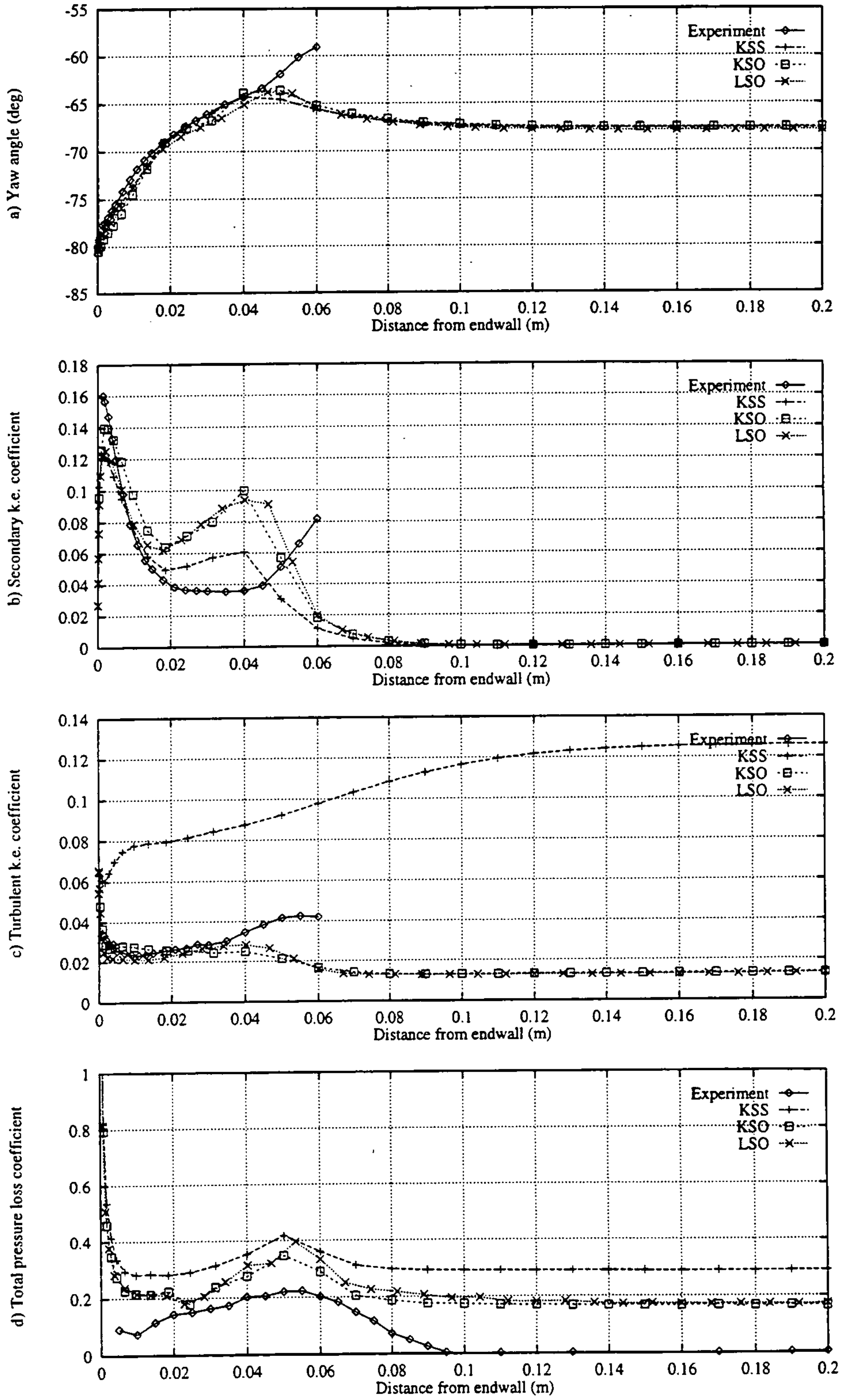

Figure 5.19 — Slot 8: Pitch averaged values

k–ϵ solutions

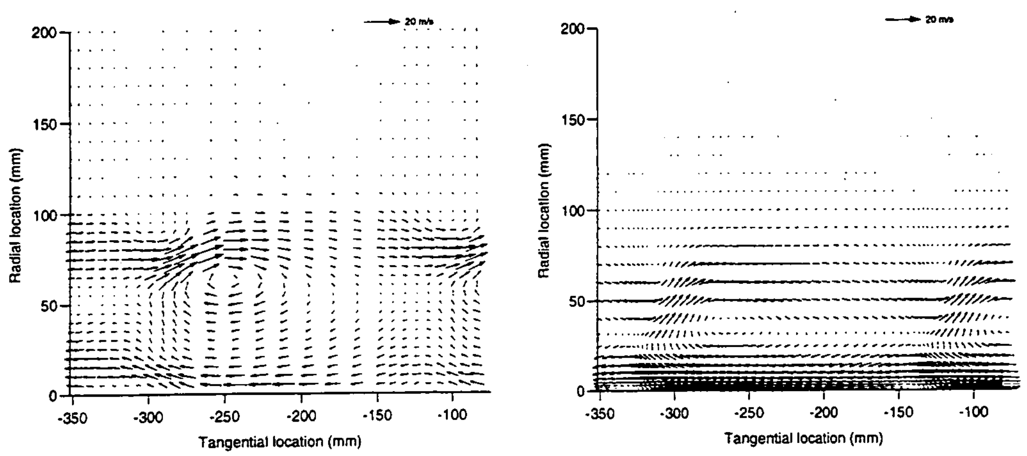
a) Experimental

b) KSS (High Re, S^2)

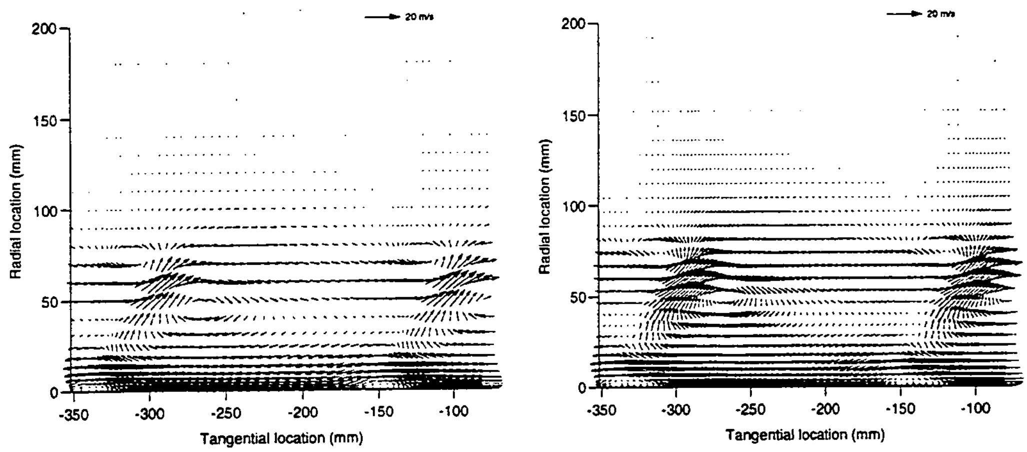
c) KSO (High Re, S-Omega)

d) LSO (Low Re, S-Omega)

Figure 5.20 — Slot 10: Secondary velocity vectors

k–ϵ solutions

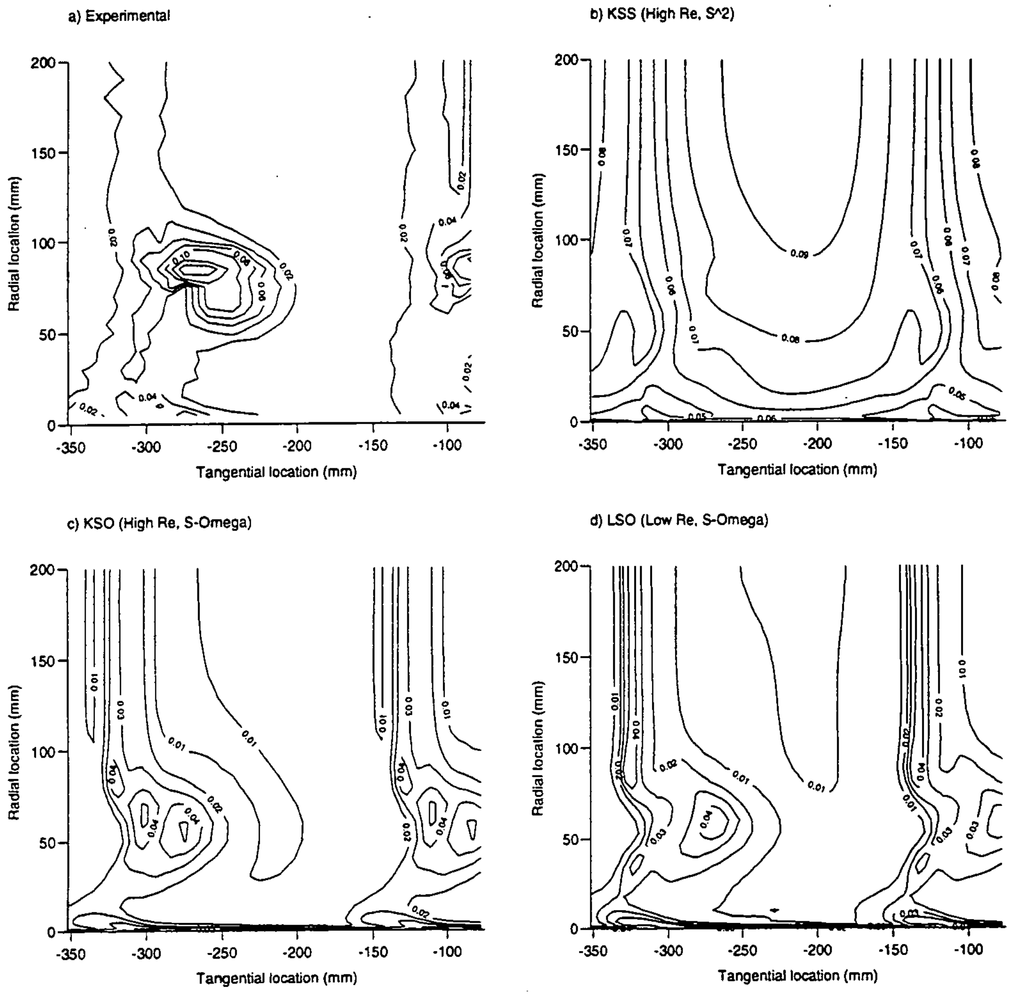

Figure 5.21 — Slot 10: Non–dimensional turbulent k.e.

k–ϵ solutions

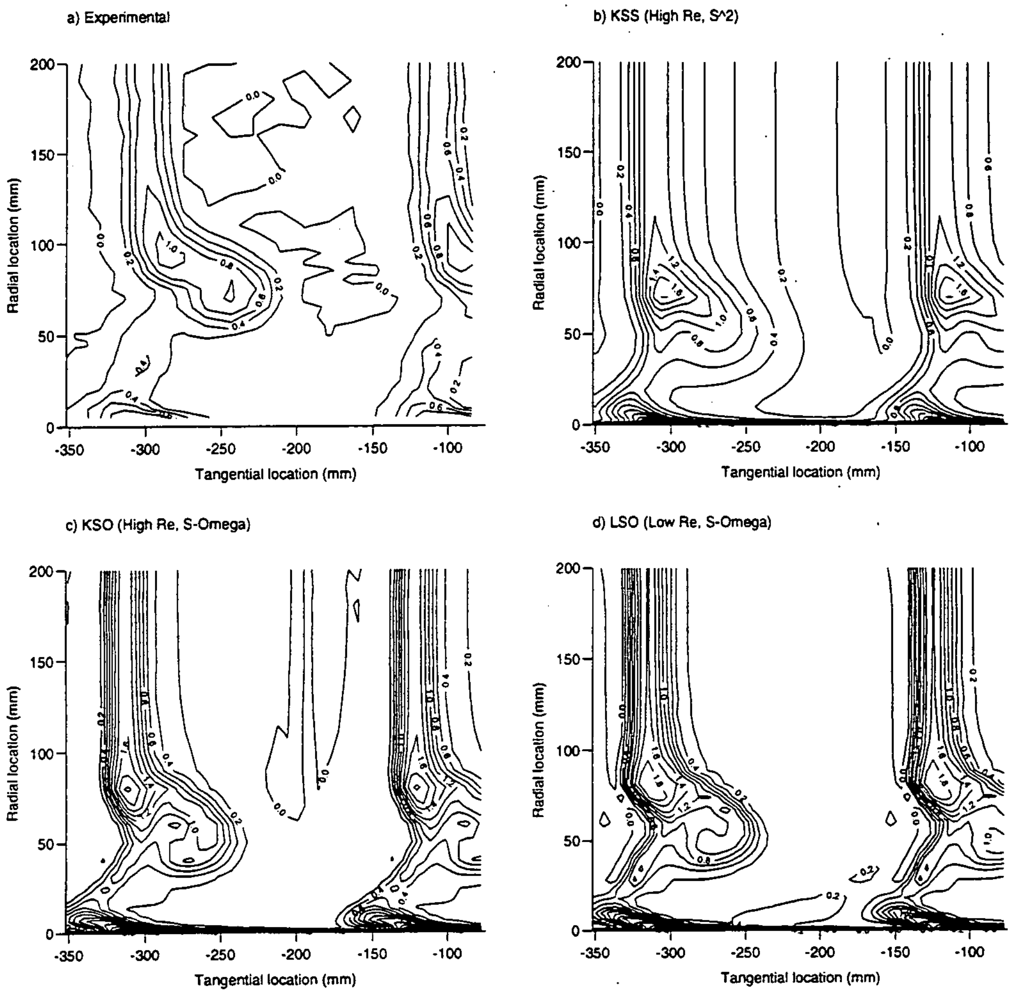

Figure 5.22 — Slot 10: Total pressure loss coefficient

k–ϵ solutions

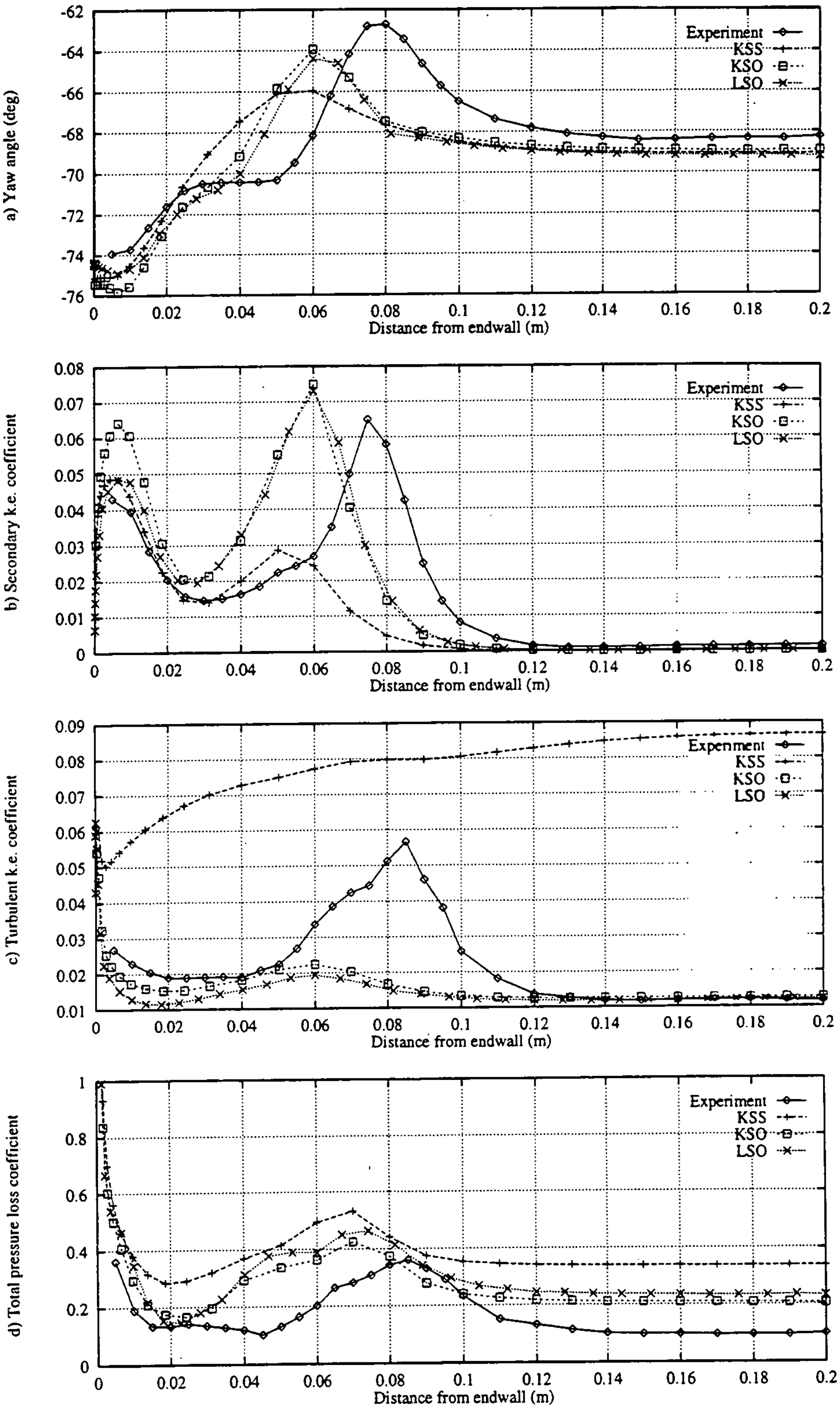

Figure 5.23 — Slot 10: Pitch averaged values

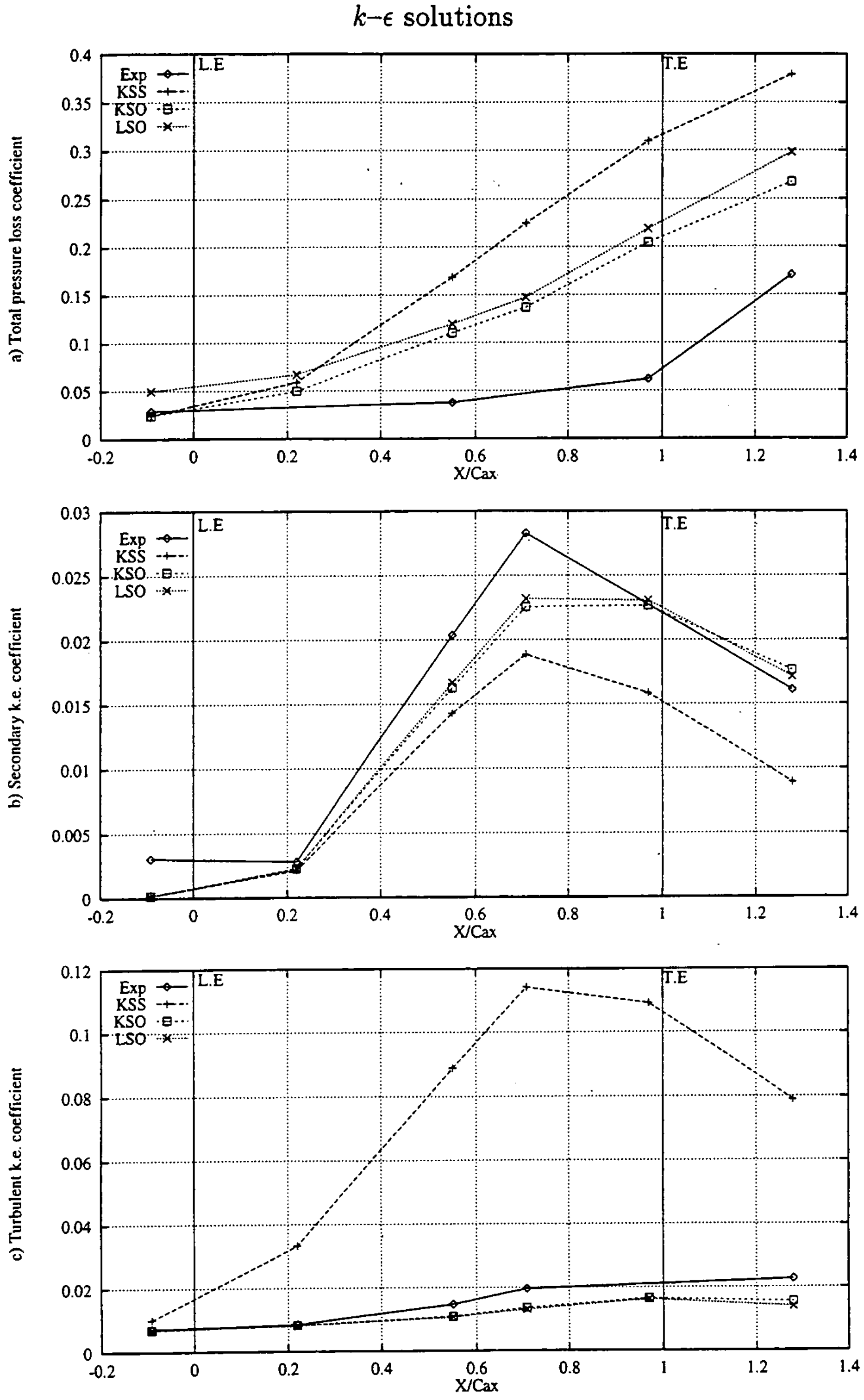
k–ε solutions

Figure 5.24 — Development of loss and kinetic energies

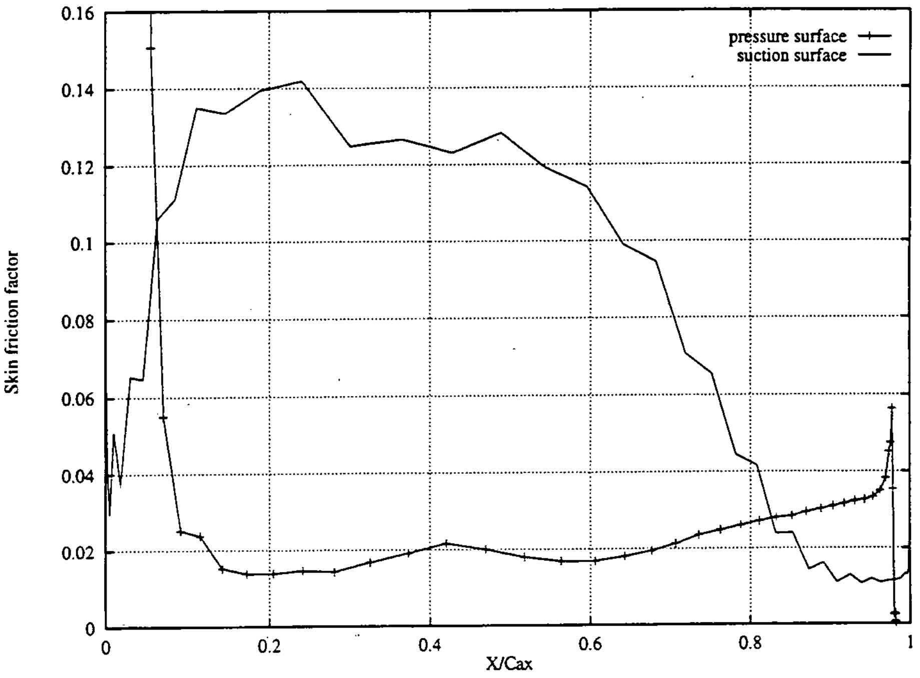

Figure 5.25 — Midspan skin friction factor (LSO)

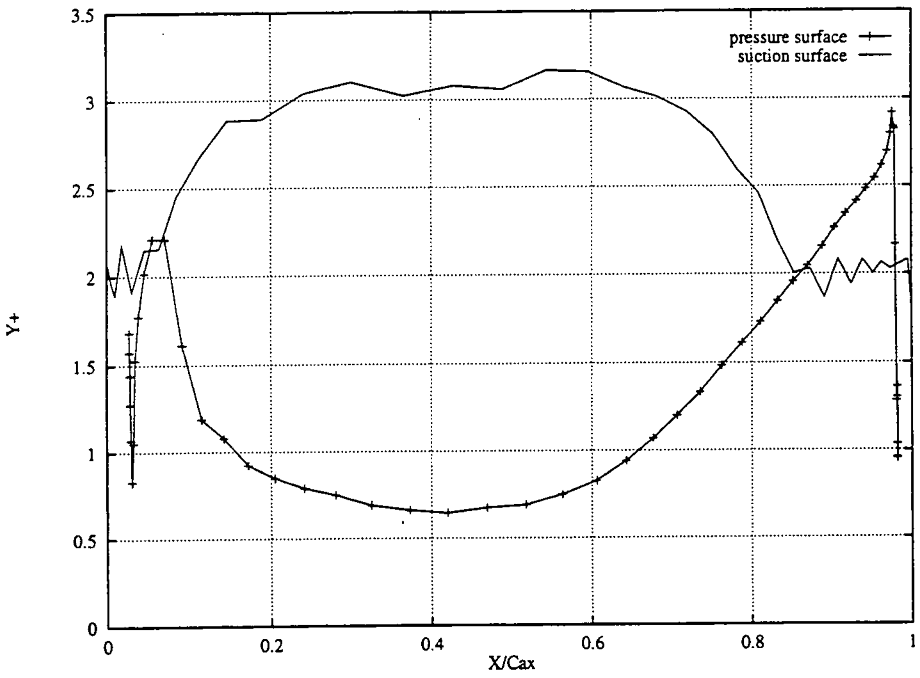

Figure 5.26 — Midspan y^+ (LSO)

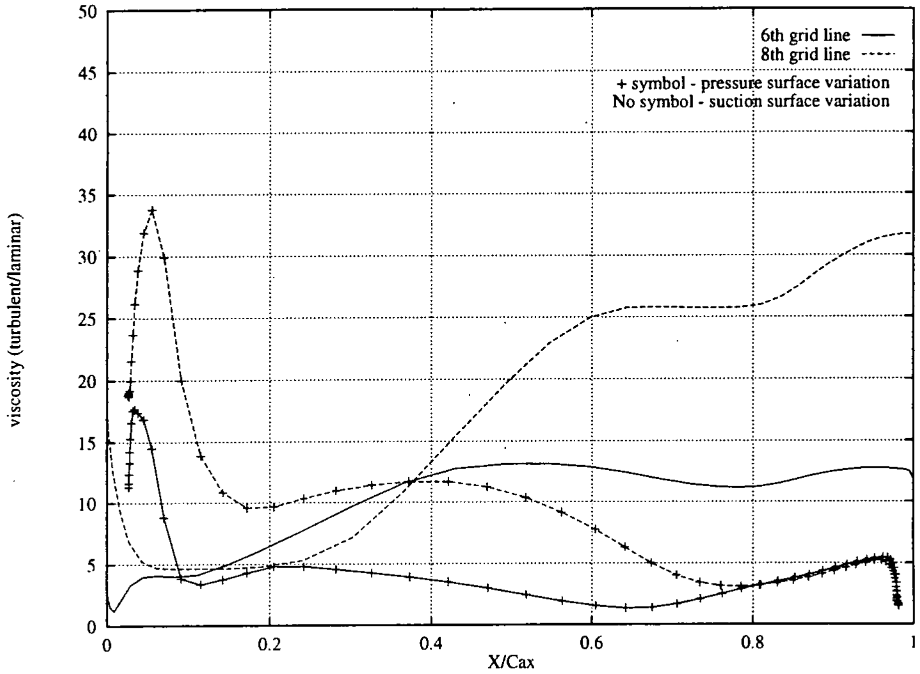

Figure 5.27 — Midspan μ_T/μ (LSO)

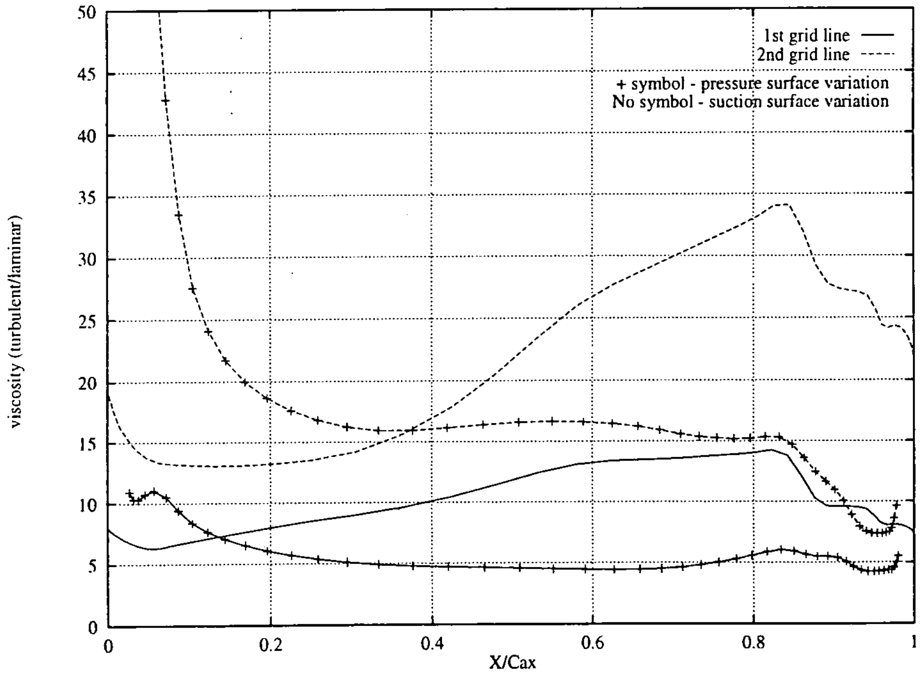

Figure 5.28 — Midspan μ_T/μ (KSO)

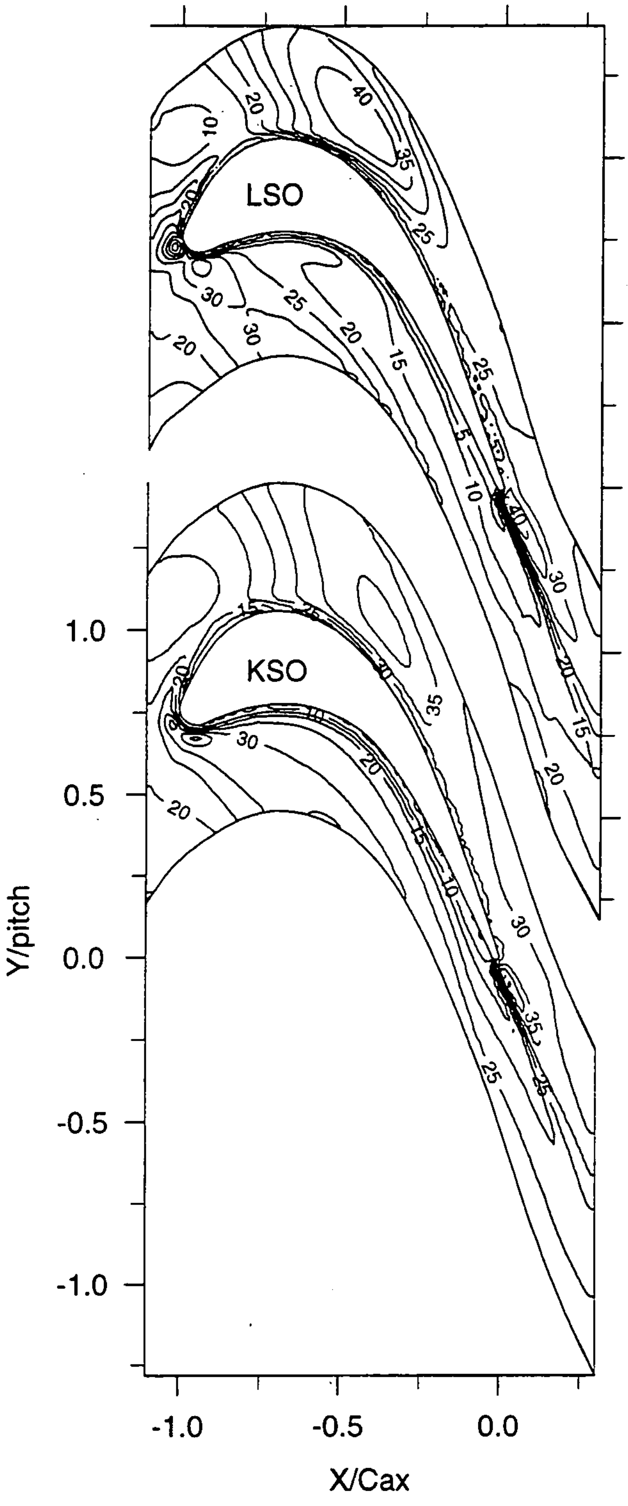

Figure 5.29 — Viscosity (μ_T/μ) 1.0mm from endwall

Chapter VI

Turbulence evaluation

6.1 Introduction

The previous chapter compared the results of the various calculations mainly in terms of their mean flow conditions, though the turbulent k.e. was also compared for the k–ϵ models. Further comparison of the turbulence structure may be made by comparing either individual shear stresses or the turbulent viscosity. The former are available from the experimental measurements whilst it is the latter that is obtained from the calculations. The viscosity is, however, derived from the stresses so conversion between the two is relatively straightforward. The equation relating the two (via the Boussinesq eddy viscosity concept) is as follows;

$$\overline{u_i u_j} = -\frac{\mu_T}{\rho}\left(\frac{\partial U_i}{\partial X_j} + \frac{\partial U_j}{\partial X_i}\right) \tag{6.1}$$

Given the velocity gradients, therefore, either the experimental stresses may be converted to turbulent viscosities (one for each stress, though all should be equal if the eddy viscosity concept is valid) or the calculated viscosity to individual stress components.

There is a problem, however, in calculating the axial velocity gradients from the experimental data since measurements in this direction are very sparse. A technique to obtain them has been described by Gregory–Smith et al [1988a] using the incompressible Helmholtz equation but this requires pressure measurements as well as the velocities and these are not available for the current work. It has been applied, however, at slot 10 by Cleak [1989] (using his own hot–wire and pressure measurements) and at slots 5 & 8 by Biesinger [1993] (using his own pressure measurements and hot–wire results from Cleak [1989]) so some results are available. The hot–wire technique used for these measurements only gave two cross–correlations ($\overline{uv}$ & $\overline{uw}$)

so only two viscosities could be calculated. Cleak [1989] also comments that, due to the various assumptions made, the results should be treated with some caution.

To calculate the shear stresses from the calculations is more straightforward and is the approach used here (though comparisons may still be made with the experimental viscosities calculated by Cleak [1989] & Biesinger [1993]). The calculation grids are sufficiently fine for the velocity gradients to be obtained directly from the velocity components. They are calculated in the streamwise coordinate system used for presentation of the experimental data (Chapter 4) to give the appropriate velocity correlations. In the axial/tangential plane the gradients at each grid node are calculated using the Gauss divergence theorem since subsequent points along grid lines do not necessarily lie in suitable directions to allow the gradients to be calculated directly. In the spanwise direction however, they do, so simple central differencing is used. As with the experimental data the velocity correlations are non–dimensionalised by the square of the inlet velocity.

6.2 Results

The three velocity correlations and the turbulent viscosity (presented as μ_T/μ) are presented at slots 8 (97% C_{ax}) and 10 (128% C_{ax}) for four of the three–dimensional calculations. The high freestream length scale mixing length calculation (MLA) and the standard k–ϵ model (KSS) have not been included since the previous results have shown them to be very poor. The fine grid mixing length calculation (MLF) has also not been included since it was very similar to the coarse grid solution (MLB) and this provides a more direct comparison with the VISMOD calculation (MLV). The results for the MLB, MLV, KSO & LSO calculations are presented in *Figures 6.1 – 6.8* and the equivalent experimental results are given in *Figures 4.19 & 4.21.*

Mixing length model results

The results of the two mixing length calculations show clearly the effect of the inclusion of laminar and transitional regions. At slot 8 (*Figures 6.1 & 6.3*) the $\overline{uv}$ velocity correlation shows a negative region close to the suction surface, indicating a turbulent boundary, that is considerably wider in the MLB calculation than in MLV. This is consistent with the thinner boundary that would be expected when the flow is made laminar over the first 60% of the blade. The pressure surface also shows much less indication of a boundary layer in the MLV calculation since the flow here has been set to be laminar. The MLB calculation, though, has a thin region of negative correlation close to the pressure surface which corresponds to a region of increased turbulent viscosity. Both results are also similar to the experimental values (Biesinger [1993]) but the lack of measurements close to the surfaces and the uncertainty in the tangential positioning makes them difficult to compare.

The $\overline{uw}$ correlations both have a negative region on the endwall and low values elsewhere. In the MLV calculation this region is thinner and stops before the pressure surface due to the laminar specification of the flow here. The experimental results do not go close enough to the endwall to capture this region except close to the suction surface where it is thickened by the corner vortex. The intermittency measurements do, however, show the endwall boundary layer becoming increasingly laminar towards the pressure surface. Neither calculation captures the strong negative region close to the suction surface between 30 & $60mm$ from the endwall that is associated with the passage vortex.

The final correlation ($\overline{vw}$) is very similar for both calculations but, though qualitatively similar to the experimental results, the positive region associated with the passage vortex is far too weak. The negative region close to the suction surface is too thin to be captured by the experimental traverse. The weakness of the $\overline{uw}$ & $\overline{vw}$ correlations in the passage vortex region seems to be due to the relatively low turbulent viscosities predicted in both calculations. Results from Biesinger [1993] give peak values of μ_T/μ of $-6000 \rightarrow 1500$ from the $\overline{uv}$ correlation and $-4000 \rightarrow 3000$ from the $\overline{uw}$ correlation and are also strongly hetrogeneous (as they are also at slot 5). None of the calculations can, of course, produce negative values, nor do they give separate values for each stress and so seem to stand little chance of correctly predicting the stresses in the passage vortex region.

At slot 10 (*Figures 6.2 & 6.4*) similar results are observed. The differences between the calculations are essentially restricted to the $\overline{uv}$ correlation in the wake and the $\overline{uw}$ correlation close to the endwall. The thinner boundary layers in the MLV calculation lead to a less distinct wake and a marginally thinner negative endwall region. Qualitatively the results are similar to the experimental values

(*Figure 4.21*) except in the passage vortex region where the strong positive and negative cores associated with the passage and shed vortices are almost entirely missing. Again the problem appears to be due to the very low turbulent viscosity which peaks at between 2000 & 3000 from the experimental results (Cleak [1989]) but less than 100 in the calculations. Unlike the results at slot 8, the experimental viscosity here is all positive and fairly homogeneous so there is at least the possibility that the flow here could be calculated reasonably well.

k–ϵ model results

The k–ϵ results at slot 8 (*Figures 6.5* & *6.7*) are generally similar to the mixing length model results. The $\overline{uv}$ velocity correlation for both calculations has a negative region close to the suction surface. Whilst very similar to each other, they differ from the MLB calculation in that this region remains wide even level with the passage vortex rather than thinning considerably. The reason seems to be due to the passage vortex which is less strong and has not moved as far as for the mixing length calculations, so does not have the same effect on this part of the boundary layer. The similarity of the k–ϵ calculations close to this surface is a reflection of the lack of any laminar or transitional regions in the low Reynolds number prediction. On the pressure surface there is a slight diffference with lower positive values being found in the LSO calculation. This may well be attributable to the slight relaminarisation (or at least reduction in μ_T) found in the LSO calculation (compare *Figures 5.27* & *5.28*).

The $\overline{uw}$ correlations show the expected negative region associated with the endwall boundary layer and suction surface corner vortex. It may be that there is some very slight thinning of this region towards the pressure surface in the LSO calculation, due to the reduced turbulent viscosity here but even so it is not as significant as found in the MLV calculation. Away from the endwall region this correlation again shows only small values with no sign of the strong negative region associated with the passage vortex that is found in the experimental measurements. The shape of the $\overline{vw}$ correlation is again similar to the mixing length calculations but the strength of the peak associated with the passage vortex has approximately doubled. There is also a distinct, though weak, negative region close to the endwall and towards the pressure surface side of the passage. This brings the calculation into slightly better agreement with the experimental results though the positioning of the regions are slightly different due to the different locations of the passage vortex.

The cause of the stronger $\overline{vw}$ correlations can be seen in the turbulent viscosity plots which show peak values in this region of 200 (KSO) and 250 (LSO) which are 4–5 times as high as either mixing length calculation. However μ_T increases to even higher values towards midspan and close to the pressure surface, more so for the KSO calculation than LSO. Whilst this variation appears to be wrong, the experimental values in this region cannot be relied on as they are calculated as the ratio of two small numbers (both the stresses and the velocity gradients are almost zero) so they cannot reliably be compared with anything. Also, the turbulent viscosity at inlet is approximately 400 times the laminar viscosity so these values are not really high but could simply have been convected from upstream.

At slot 10 (*Figures 6.6 & 6.8*) the k–ϵ results show some slight improvement over the mixing length results. The $\overline{uv}$ correlation, in particular, shows the wake and vortex region more clearly, though the values in this latter region are still much too low. The negative $\overline{uw}$ region on the endwall is still clearly visible in both calculations but, as with slot 8, the positive and negative regions associated with the passage vortex are entirely missing. Both calculations do, however, show the positive and negative regions in the $\overline{vw}$ correlation but at only about half the correct strength. The LSO calculation now shows the weaker values here which is a change from slot 8 where they were stronger.

The peak turbulent viscosity has also decayed in the passage vortex region and now only reaches approximately 150 times the laminar viscosity compared with 2000–2600 for the experimental values (Cleak [1989]). The rise in μ_T towards midspan is still evident but this has also decayed slightly from slot 8. By comparison, the experimental values are much lower but, again, cannot be relied on in this region. The more important difference is around the passage vortex where the low calculated values lead to the low turbulent k.e. and velocity correlations. These, in turn, reduce the dissipation of the secondary velocities and result in the higher secondary k.e. found in the calculations.

mixing length model (coarse grid, $L = 0.936mm$)

a) Velocity correlation uv/Vo^2

b) Velocity correlation uw/Vo^2

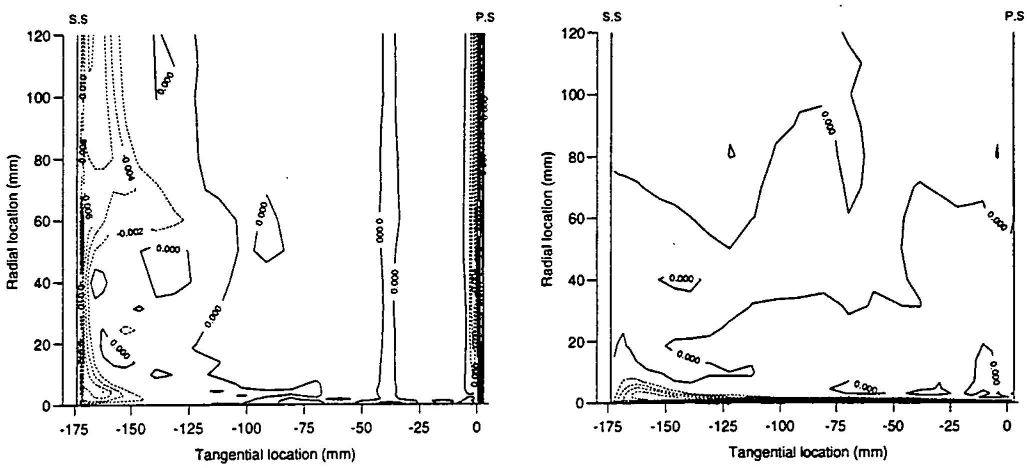

c) Velocity correlation vw/Vo^2

d) Viscosity turbulent/laminar

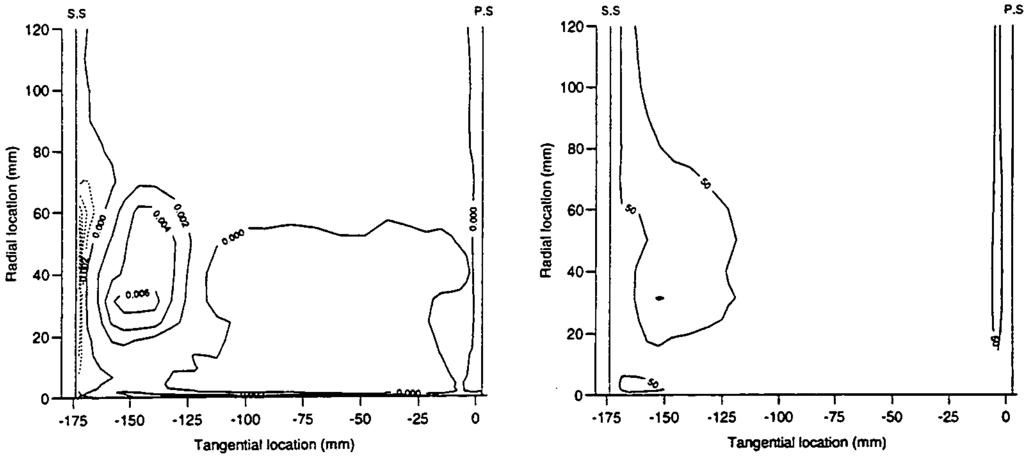

Figure 6.1 — Slot 8: Turbulence quantities (MLB)

mixing length model (coarse grid, $L = 0.936mm$)

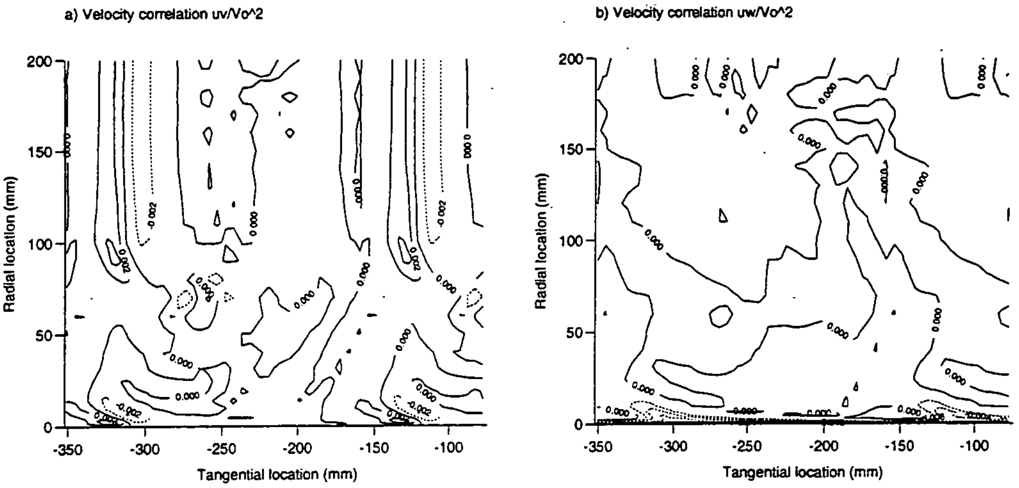
a) Velocity correlation uv/Vo^2

b) Velocity correlation uw/Vo^2

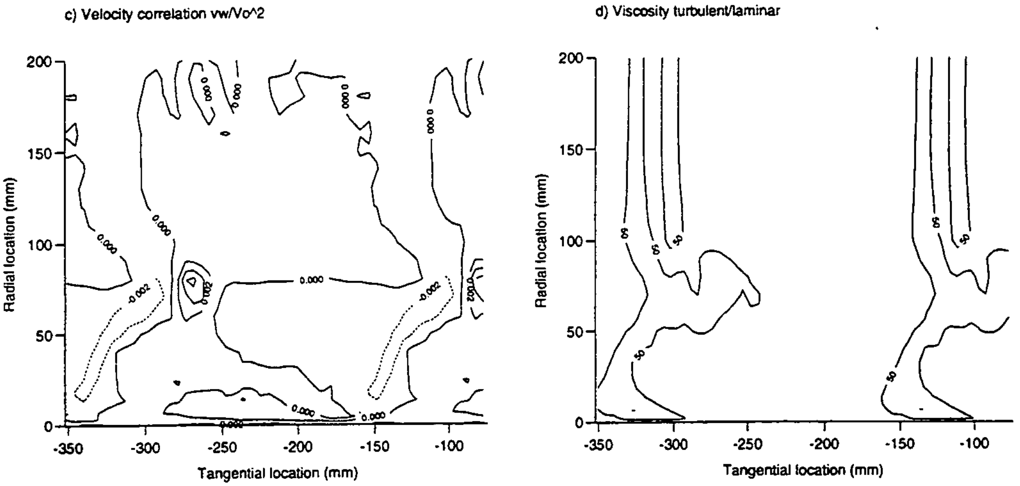
c) Velocity correlation vw/Vo^2

d) Viscosity turbulent/laminar

Figure 6.2 — Slot 10: Turbulence quantities (MLB)

mixing length model (coarse grid, VISMOD)

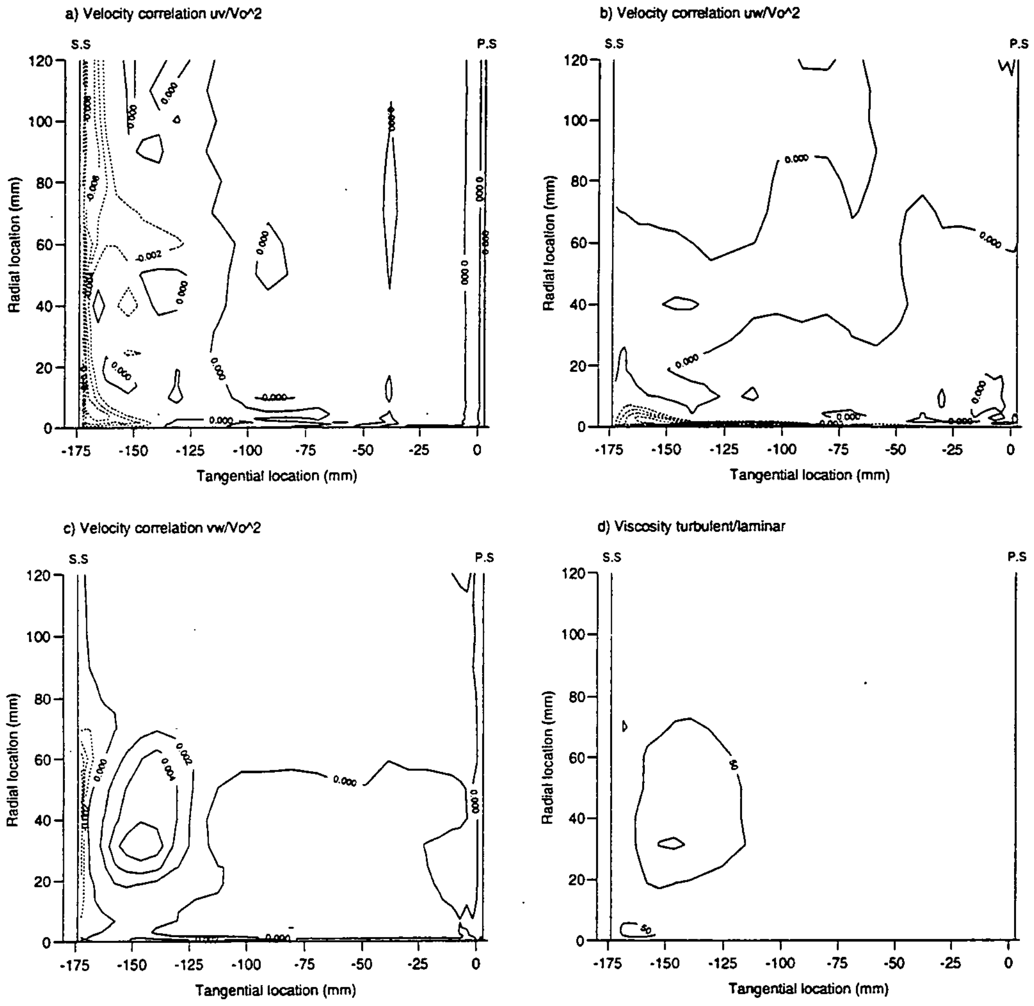

Figure 6.3 — Slot 8: Turbulence quantities (MLV)

mixing length model (coarse grid, VISMOD)

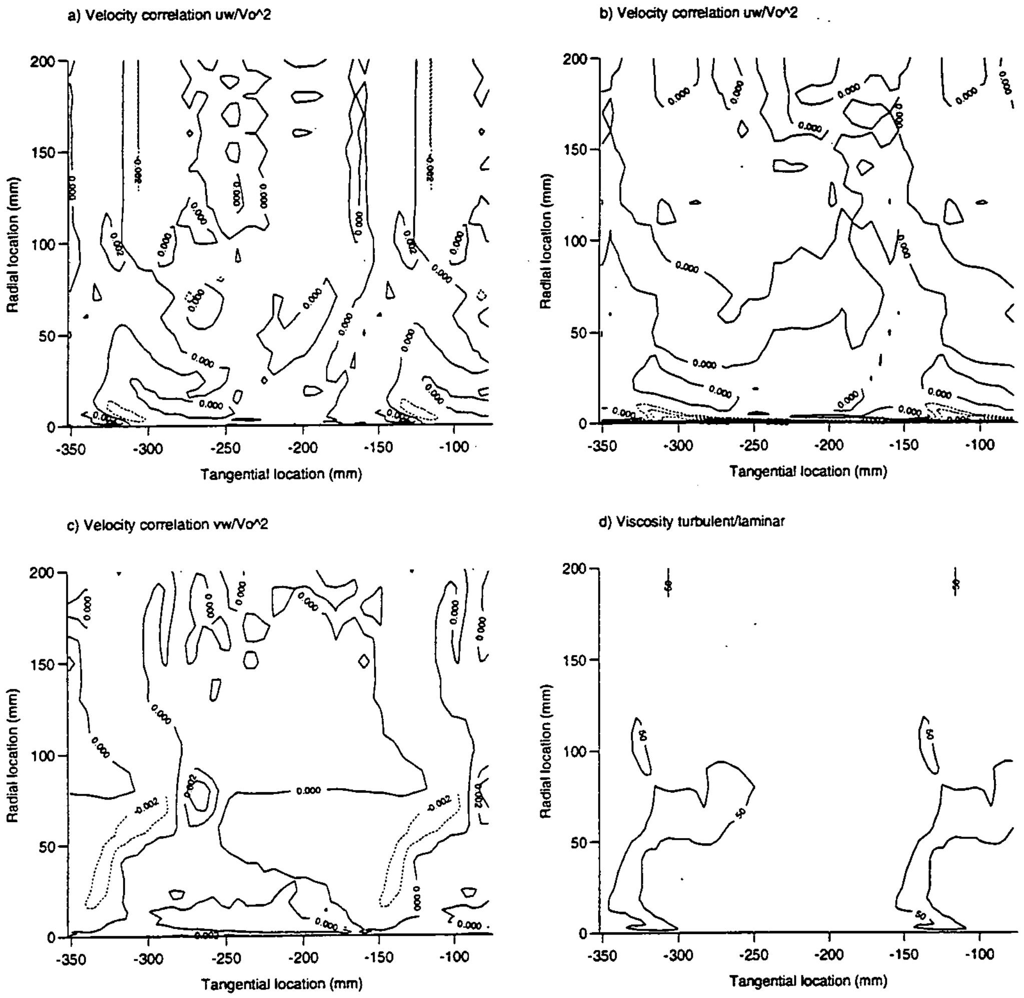

Figure 6.4 — Slot 10: Turbulence quantities (MLV)

k–ϵ model (high Re, S–Ω)

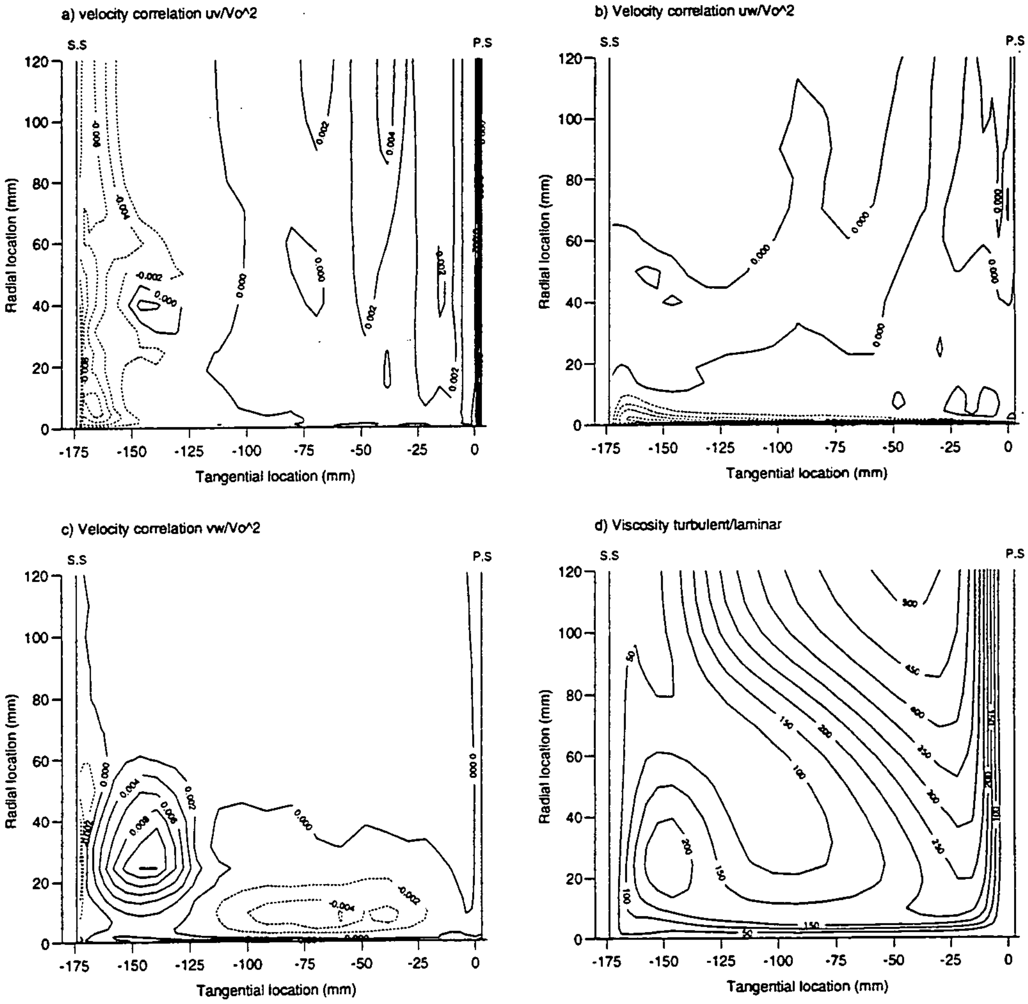

Figure 6.5 — Slot 8: Turbulence quantities (KSO)

k–ϵ model (high Re, S–Ω)

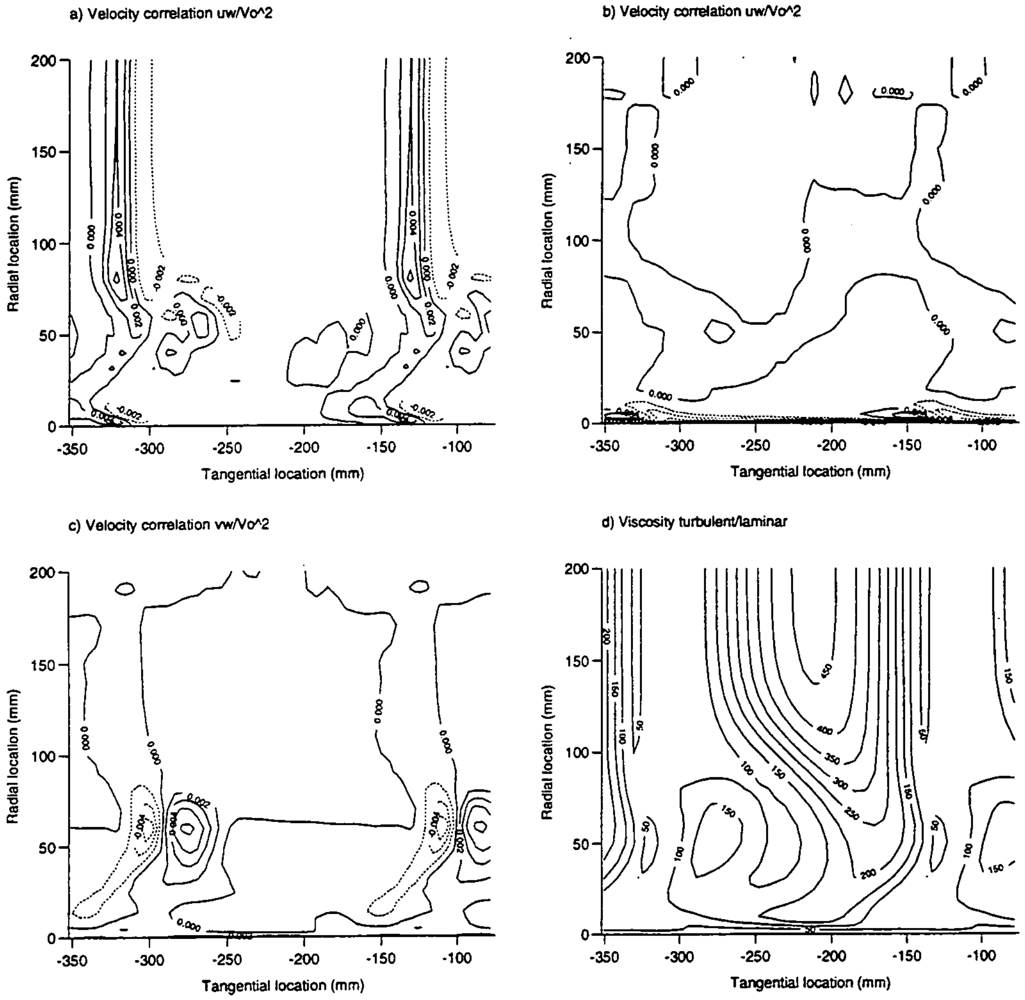

Figure 6.6 — Slot 10: Turbulence quantities (KSO)

k–ϵ model (low Re, S–Ω)

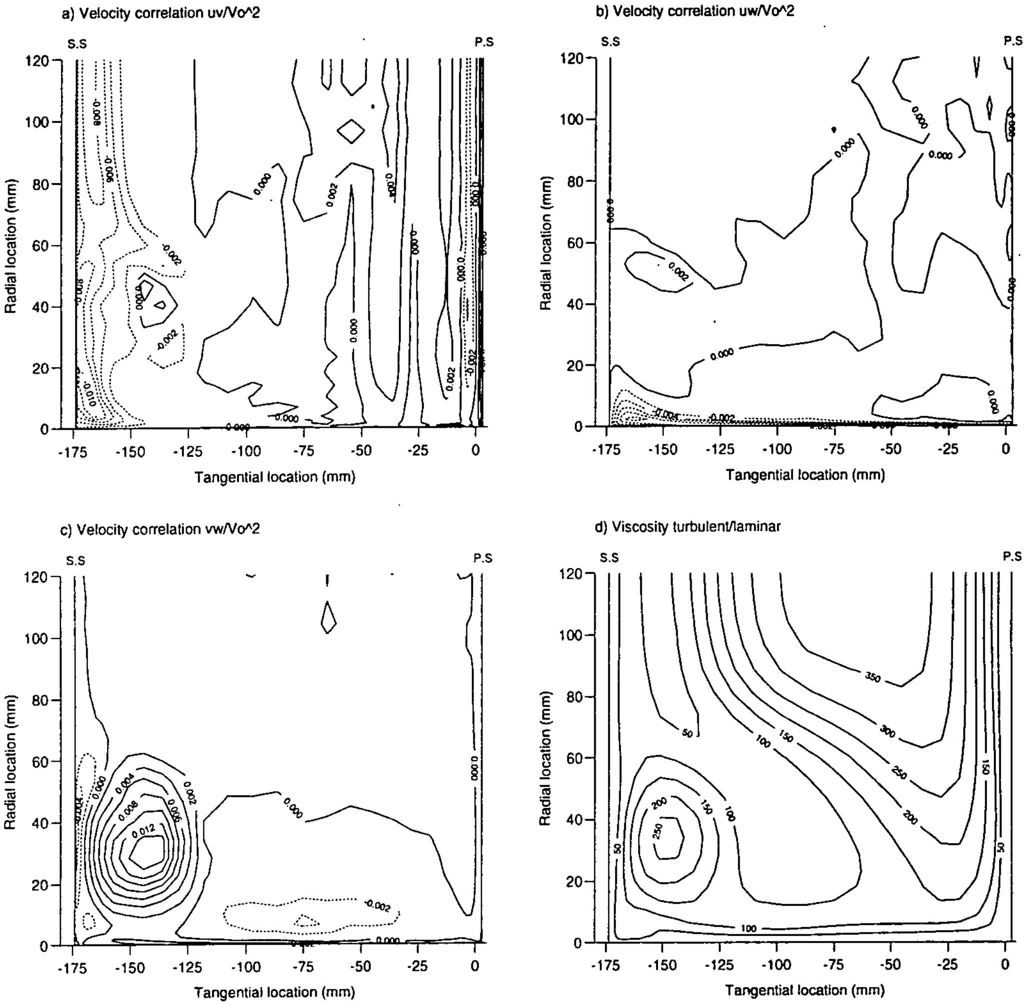

Figure 6.7 — Slot 8: Turbulence quantities (LSO)

k–ϵ model (low Re, S–Ω)

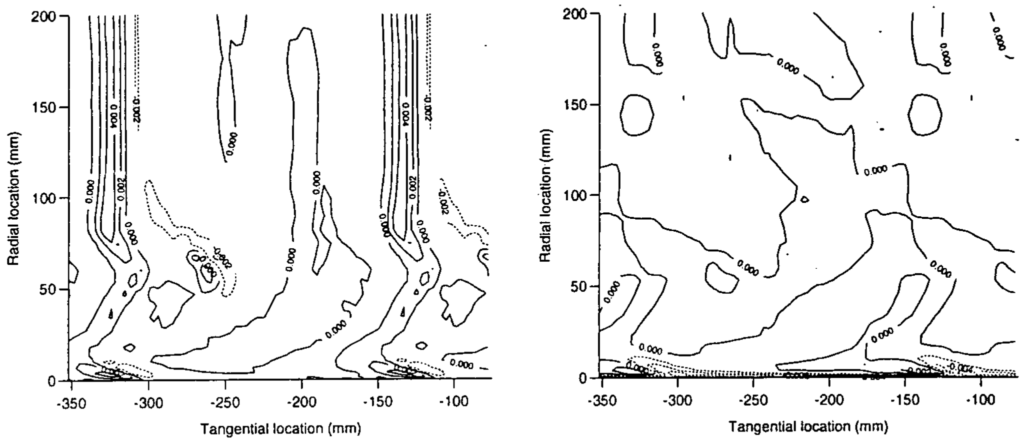

a) Velocity correlation uv/Vo^2

b) Velocity correlation uw/Vo^2

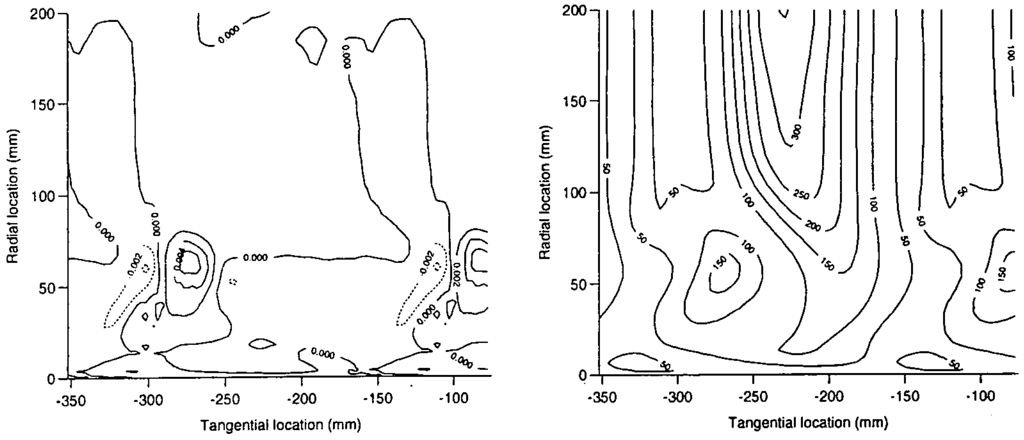

c) Velocity correlation vw/Vo^2

d) Viscosity turbulent/laminar

Figure 6.8 — Slot 10: Turbulence quantities (LSO)

Chapter VII

Overview and discussion

7.1 Experimental results

The primary aim of this work has been to produce detailed experimental data that is suitable for the validation of CFD codes and the turbulence and transition models contained within them. The data is designed to complement work carried out previously at Durham (Walsh [1987], Cleak [1989], Biesinger [1993]) and has concentrated on the development of the secondary flows and the boundary layers. In addition to measurements through the cascade, the flow at one axial chord upstream of the leading edge has been measured in detail to obtain suitable inlet conditions for calculations. Previously the only upstream measurements were taken at slot 1 where the flow is influenced by the presence of the blade leading edges and so were not entirely suitable for this.

The upstream measurements provide not only the freestream velocity but also the turbulence level and dissipation rate which though important, is rarely if ever, quoted in the open literature. The velocity measurements showed the flow to have a slight positive incidence due to deflection by the turbulence grid which, when taken into account, tends to improve the calculated blade static pressure distribution (e.g. Lien and Leschziner [1995]). The velocity and turbulence profiles in the endwall boundary layer have also been measured. The shape of the boundary layer does not conform to the standard log–law profile, though does exhibit a log–law region (*Figure 4.9*). This is thought to be due to a non–uniform velocity at the leading edge of the false endwall caused by a 'jet' effect in the flow through the turbulence grid.

Detailed hot–wire area traverses in the endwall region chart the development of the secondary flows and, to some extent, the state of the blade and endwall boundary layers. Whilst the latter measurements were restricted by how close the hot–wire could approach the surface, the addition of intermittency measurements has ensured that the boundary layer states have been fully determined. The development of the secondary flows is perhaps best shown by the secondary velocity vectors which, starting at slot 1 (-9% C_{ax}), show the horseshoe vortex forming around the leading edge. By slot 3 (23% C_{ax}) the cross–passage pressure gradient is well established and the pressure side leg of the horseshoe vortex has merged with the beginnings of the passage vortex and has grown considerably. Since the flow has only been turned a little by this point the passage vortex is still close to the pressure surface and the much smaller suction side leg of the horseshoe vortex is still clearly visible in the endwall/suction surface corner.

Between slots 3 & 5 (55% C_{ax}) most of the turning of the flow occurs so the passage vortex continues to grow and crosses to the suction surface. From here onwards it begins to decay but continues to be convected towards and then along the suction surface and continues this spanwise migration even downstream of the trailing edge. The growth and decay of turbulence associated with the passage vortex follows a similar pattern. Upstream of the blades the turbulent k.e. is relatively low in the freestream and increases uniformly in the endwall boundary layer. The action of the passage vortex rolls up the boundary layer and induces low turbulence freestream fluid down the pressure surface. By slot 5 most of the turbulence is concentrated in a core close to the suction surface and the peak values have increased considerably.

As the passage vortex moves away from the endwall, the growth of the corner vortex produces a separate turbulent peak in the endwall/suction surface corner. The turbulence levels have also increase along the suction surface by slot 6 (71% C_{ax}) possibly indicating transition of this boundary layer. As with the secondary k.e., the turbulence has decayed considerably by slot 8 (97% C_{ax}) and continues to do so to slot 10. At its peak the turbulence reaches 34% of inlet velocity and has decayed to 14% at slot 10 which is consistent with the findings of others (e.g. Moore et al [1987], Langston et al [1977], Zunino et al [1987]). The individual turbulence intensities generally follow the same pattern as the turbulent k.e. with the spanwise component generally being the largest.

The cross velocity correlations are generally only significant where the turbulence is large. The streamwise/cross–passage ($\overline{uv}$) correlation initially becomes increasingly positive within the passage vortex, then decays from slot 5 and has become negative by slot 10. Negative regions are also found in the corner vortex and along the suction surface at slot 6 where it is consistent with a turbulent boundary layer. This is confirmed by the suction surface intermittency measurements which show transition beginning just after slot 5 except close to the endwall where the horseshoe and the passage vortices keep the flow turbulent. On the pressure surface the intermittency measurements show relaminarisation occurs over much of the surface. The lack of any significant $\overline{uv}$ values on this surface is most likely to mean that the boundary layer is too thin to extend into the traversed region.

The streamwise/spanwise ($\overline{uw}$) correlation remains negative in the passage vortex region, increasing in strength to slot 6 and then decaying. It is also negative within the corner vortex and on the endwall upstream of the passage vortex separation line. Behind this the correlation is close to zero until slot 10 where negative values begin to appear. This is consistent with the initially turbulent boundary layer being removed by the passage vortex and a new laminar boundary layer growing in its place. The endwall intermittency measurements confirm this and also show the onset of transition by slot 10. The final correlation ($\overline{vw}$) is initially negative in the passage vortex region but changes sign between slots 6 & 8. In terms of magnitude it is generally greater than the $\overline{uv}$ but smaller than the $\overline{uw}$ correlation.

Taken with the pressure measurements of Biesinger [1993] these results provide a very detailed description of the flow through the Durham cascade. Unlike most other cascade experiments, the inlet conditions are well defined and details of the turbulent structure are available within the blade passage rather than just downstream. This should allow the behaviour of turbulence models to be studied in detail, rather than simply testing whether they work or not, and so aid their design and development. It is unfortunate, however, that the slot 8 traverse was not extended further away from the endwall to completely capture the passage vortex. The reason for this was that $60mm$ was about the maximum distance that could be traversed using the endwall locating pin to support the hot-wire probe. Whilst traversing could be carried out without it (as it was at slot 10), this allows the probe to deflect and vibrate more which may affect the results.

7.2 Computational results

Two–dimensional calculations

Initial calculations were carried out in two–dimensions in order to test the grids and various aspects of the turbulence models. A simple check of the grid suitability, using three different grids, showed the results to be fairly independent of their size. The near wall spacings for the coarse and fine grids were also shown to be suitable for use with their respective turbulence models. The fine grid was, however, found to produce some oscillations in parameters such as velocity and pressure near to the blade, particularly on the suction surface. This is thought to be due to the presence of high aspect ratio cells in this region caused by the need for a very fine spacing normal to the wall which could not be matched in the axial direction without an excessive number of grid points. This makes the fine grid less than ideal but cannot easilly be avoided with a simple 'H' type grid. Either an embedded grid or a multiblock scheme with an 'O' or 'C' grid close to the blade would be better options. The latter, in particular, would also give more orthogonal grid cells in the leading and trailing edge regions.

The first turbulence model tested was a simple mixing length formulation (section 5.1.2). Though its limitations are well known (Lakshminarayana [1991]) this type of model is still widely used in industry largely because more sophisticated models are computationally expensive and can be more difficult to converge without necessarily giving better results (Gregory–Smith [1995]). The exerience of Cleak [1989] in running this model was that it produced too much dissipation of the secondary flows and produced too high losses. The higher measured inlet turbulence and length scale than he used would tend to exascerbate this problem so the effect of reducing the freestream length scale was investigated. Doing this is not unreasonable since the length scale will in reality change as turbulence grows and decays so the inlet value is unlikely to be correct.

As expected the correct length scale produced a very high turbulent viscosity and hence led to excessive loss. Reducing the length scale by a factor of ten and then one hundred improved the loss prediction considerably. The latter effectively gave laminar flow outside shear layers, so seemed to have gone too far, whilst the former seemed more reasonable but without any secondary flows to compare it is difficult to draw too many conclusions. The loss even for the lowest length scale was found to be higher than the experimental value but this is due to the assumption of fully turbulent boundary layers. This lack of ability to predict transition is a considerable problem considering the nature of the flow both on the blade surfaces and the endwall.

To investigate the effect of transition on the production of loss a number of two-dimensional mixing length calculations were carried out with various regions of the flow specified as laminar (by setting $\mu_T = 0$) and transitional (by scaling μ_T by a factor between 0 & 1). Defining regions that followed the measured intermittency on the blade surfaces was found to almost halve the loss and reduce the wake thickness significantly. Whilst the state of the suction surface boundary layer was thought to be the most important, since it is responsible for most of the loss, the state of the latter part of the pressure surface also had a considerable effect. Away from the surfaces, the specified state of the flow was found to have little effect on the overall results, not surprising in two–dimensions since little loss is produced here.

The two other turbulence models tested were high and low Reynolds number versions of the k–ϵ model. The latter is, in principle, capable of predicting transition so its performance is of particular interest. It does, however, require a much finer grid in order to fully resolve the boundary layer and problems with high aspect ratio and highly skewed cells have made it impossible to obtain a converged two-dimensional solution. The high Reynolds number version uses a wall function, so runs on the coarse grid and converged without problem. Like the mixing length model, it assumes fully turbulent boundary layers, and so would be expected to overpredict the losses to some extent, but should otherwise be superior.

A problem with all k–ϵ models that is particularly significant when there are high turbulence levels and a low dissipation rate (large length scale) is that irrotational strains due to flow turning act to generate turbulence. The effect of a modification to the standard k–ϵ formulation, the S–Ω modification (section 5.1.2), designed to alleviate this problem has been investigated. Its effect on both the k field and the total loss is dramatic, the generation of turbulence is restricted almost entirely to the boundary layers and the wake and the loss is reduced by almost 40%. Overall its inclusion produces much better results that are also significantly better than the high length scale mixing length calculation but slightly worse than the results with the length scale reduced by a factor of ten. It is important to remember, however, that this modification is not physically correct but introduces an inconsistency between the k equation and the Reynolds averaged Navier–Stokes equations.

Three–dimensional calculations

Whilst two–dimensional calculations are relatively quick to run and provide some information on how well profile loss is predicted, they give no information on the ability to predict secondary flows. Three–dimensional repeats of a number of the two–dimensional calculations have been carried out in order to examine this. An investigation of the effect of the freestream length scale showed that the higher dissipation associated with the high length scale ($9.36mm$) resulted in a weak vortex centered at mid-passage (at slot 8) and too close to the endwall. As expected the calculated loss is considerably higher than the experimental value but the secondary loss is lower when it too should be higher (due to the greater dissipation of secondary k.e.). This however, is likely to result from the way it is calculated (full area – midspan) since the midspan loss contains a large component in the freestream which, in the secondary flow region, ought to be included as secondary loss.

The calculation at the lower length scale ($0.936mm$) gave a much better prediction of the passage vortex in terms of its size, shape and position. It does, however, overpredict the strength of the secondary flows which implies that the length scale, and hence the dissipation, has been reduced too far. Being an arbitrarily chosen value, however, it can only be a coincidence that the agreement is this good. The total loss is still too high but this is mainly because the fully turbulent boundary layers produce too much profile loss, the secondary loss is approximately correct. An equivalent calculation on the fine grid produced an almost identical pattern of secondary flow and an apparantly similar pressure loss distribution though the midspan loss is significantly higher. Comparison with the equivalent 2D results show good agreement for the fine grid but less so for the coarse grid. The reason for the discrepency is not known but may indicate that the calculation was not completely converged. Otherwise the similarity of the results suggests reasonable grid independency in three dimensions as well as in two.

A final mixing length calculation (MLV) extended the use of laminar and transitional regions to three–dimensions. The regions were designed to follow the measured values reasonably well (see *Figure 5.8*) and followed the 2D practice of becoming fully turbulent away from the surfaces. The effect on the development of the secondary flows and losses associated with the passage vortex was minimal so they remain in good agreement with the experiment. The main difference is the reduced thickness of the boundary layers which is most evident on the blade, where they are thickest, but can also be seen on the endwall. Since most of the loss is produced in these high shear regions (the high turbulence in the passage vortex mainly acts to dissipate the secondary flows) their improved prediction gives much better loss results. It would also be interesting to look at the effect this has on the prediction of heat transfer, since it may be considerable, but without experimental data the results would be of limited use.

The three further calculations that were carried out used the k–ϵ model. The first two used the high Reynolds number version, one with (KSS) and the other without (KSO) the S–Ω modification, whilst the third used the low Reynolds number version (LSO). The effect of running without the S–Ω modification was found to be very similar to running the mixing length calculation with the high length scale. The considerable generation of turbulence in the freestream dissipates the secondary flows, restricts the movement of the passage vortex and leads to very high losses. Reference to the turbulent k.e. plots (*Figures 5.17 & 5.21*), in particular, shows how poor this calculation is. That other k–ϵ calculations, such as that of Cleak [1989], have been much more successful is thought to be due to the lower inlet turbulence and length scales which reduce the initial production and increase dissipation, hence avoid the explosion of turbulent k.e.

This result (KSS) suggest that there is a problem with the standard k–ϵ model. The k equation is derived directly from the Reynolds averaged Navier–Stokes equations (though with the Reynolds stresses replaced by the Boussinesq relationship) whilst the ϵ equation is based more on empirical data and so it is probably the latter that is wrong. Despite this the S–Ω modification, which improved the 2D results considerably, alters the k equation making it physically incorrect. As a result it may well produce poor solutions when applied to other types of flow. If instead the same effect could be obtained by modifying the ϵ equation, this would probably be a better approach.

The modified k–ϵ calculation and the low Reynolds number version (also run using the S–Ω modification) both produce much better results. In both cases the passage vortex has migrated well towards the suction surface but has not moved far enough from the endwall. In this they are less good than the best mixing length calculations but the strength of the vortex is better predicted, though still slightly too great. This may be explained by the low levels of turbulent k.e. in the passage vortex region which would lead to insufficient dissipation of the secondary flows. The losses are slightly higher than for the mixing length calculations largely due to the midspan values which are slightly elevated (due to high μ_T values) in the freestream as well as at the wake center. The secondary loss is slightly low for both calculations but this seems to be due to the high midspan value since the pattern of loss in the loss core is very similar to the experiment.

Though the low Reynolds number calculation should be able to predict transition, the similarity between it and the high Reynolds number calculation suggests that it does not do so very well. This is confirmed by the skin friction factor and turbulent viscosity which suggest that transition on the suction surface occurs almost immediately behind the leading edge and that there is little if any relaminarisation on the pressure surface. On the endwall there is some indication that the new boundary layer is laminar but, again, the differences are not great. The reason for the poor performance of the low Reynolds number model may be due to its over sensitivity to the high pressure gradients and curvature of the flow or more simply that the grid was not sufficiently fine or well formed. Also, another more fundamental problem, pointed out by Lien and Leschziner [1995], is that transition appears to be initiated by pressure fluctuations rather than diffusion of turbulence into the boundary layer which is the mechanism relied upon by the model.

Looking in more detail at the turbulence quantities from the better calculations (MLB, MLV, KSO & LSO) it can be seen that all yield qualitatively similar velocity correlations that generally follow the pattern of the experimental results. The exception is the streamwise/spanwise correlation which invariably fails to reproduce the negative region associated with the passage vortex. The gradients in the boundary layers are similar for each calculation except for MLV where the specified laminar and transitional regions clearly reduces their size. Conversely there is no such reduction, except perhaps on the pressure surface, for the low Reynolds number calculation confirming its failure to correctly predict transition.

Within the secondary flow regions positive and negative peaks of the velocity correlations may be seen but all are significantly lower than the experimental values. Furthermore the results from the mixing length calculations are typically half those from the k–ϵ calculations. The cause may be seen from the plots of viscosity which are much lower for the mixing length model calculations than the k–ϵ ones. The experimental values are much higher still which explains why the calculations produce too little turbulence and insufficient dissipation of secondary velocities. However, within the blade passage the negative and strongly anisotropic regions (found by Biesinger [1993]) mean that any kind of agreement was never possible for linear eddy–viscosity models. It seems that nothing less than algabraic or full Reynolds stress closure models will suffice in the secondary flow region if detail of the turbulence is required.

If such details are not required it seems that reasonable results may be obtained from both mixing length and k–ϵ models. In terms of loss development, all the calculations overpredict the growth through the cascade, mostly due to overpredicting the loss in the boundary layers. The k–ϵ models also predict too much loss in the freestream due to high turbulent viscosities which are not found in the low length scale mixing length calculations. The high length scale mixing length and standard k–ϵ calculations both give an excessive growth of viscosity in the freestream which accounts for the high losses they produce. Across the trailing edge the calculations, if anything, underpredict the loss but since the flow off the trailing edge is unsteady it cannot be expected to be modelled correctly.

The secondary k.e. grows rapidly in all calculations up to about 70% C_{ax} as the flow is turned. The growth is slightly too great in the mixing length calculations (except MLA) due to the low turbulent viscosity and slower in the k–ϵ models since the viscosity is higher. Though the flow is no longer being turned greatly the calculations then show the secondary k.e. to rise slightly or remain level up to the trailing edge but the lack of an experimental value at slot 8 (97% C_{ax}) makes comparisons here difficult. After this the secondary flows begin to decay but more slowly than the experimental rate due to the lower levels of turbulence in the vortex core. This may also be seen in the difference between loss and mixed out loss at slot 10 where the greater value from the calculations indicate that less that mixing has occured.

To summarise, reasonable results may be obtained using a simple mixing length model with a reduced freestream length scale even though details of the turbulence quantities are not, and cannot be predicted at all well. The lack of transition modelling causes losses to be overpredicted but the use of laminar and transitional regions can improve the results. However, the need to reduce the length scale and prescribe these regions limits the use of this type of calculation as a predictive tool. The high Reynolds number k–ϵ model (with S-Ω modification) performs similarly well using the correct inlet length scale but, otherwise, suffers the same limitations. The low Reynolds number model predicts transition too early and so produces similar results to the high Reynolds number version though this may in part be due to the grid.

Chapter VIII

Conclusions and future work

This chapter contains the main conclusions that may be drawn from the experimental and computational work presented in this thesis. This is followed by some recommendations as to work that may be carried out in the future.

Experimental conclusions

The following are the conclusions drawn from the experimental measurements.

- Modifications to the endwall have reduced the inlet boundary layer thickness slightly compared with results from Cleak [1989]. This is thought to be the cause of the differences in results at slot 10 (128% C_{ax}).
- The upstream measurements show that the inlet flow has a slight positive incidence ($\sim 0.7^\circ$) due to deflection by the turbulence grid.
- The generation of turbulent k.e. and shear stresses is restricted mainly to the passage and corner vortex regions. All three velocity correlations reach significant levels with the $\overline{uw}$ and $\overline{vw}$ components being the largest.
- On the suction surface, away from the secondary flow region, the flow is initially laminar and remains so up to about 60% C_{ax}. Transition occurs over the remainder of the blade so that the flow is turbulent by the trailing edge.
- Close to the endwall the flow on the suction surface is initially turbulent due to the horseshoe vortex. After the passage vortex has crossed the passage this region grows in width as the vortex grows and migrates away from the endwall. As it does so the flow behind it begins to exhibit some laminar features except in the endwall corner where the growth of a corner vortex maintains a fully turbulent flow.
- On the pressure surface the initial acceleration around the leading edge produces some laminar characteristics up to slot 3 (22% C_{ax}) by which time the

adverse pressure gradient has made the flow turbulent. From here to 80% C_{ax} relaminarisation occurs and the flow then remains laminar to the trailing edge.

- The endwall boundary layer is initially turbulent and remains so until it is rolled up into a loss core by the passage vortex. The exception is a small region just behind the leading edge and against the suction surface where reattachment of the horseshoe vortex causes some laminarisation.
- Behind and away from the passage vortex the new endwall boundary layer is very thin and highly skewed. Intermittency measurements show it to be initially laminar with some evidence of transition beginning at slot 10 (128% C_{ax}).

Computational conclusions

The following conclusions have been drawn from the various calculations.

- The best results have been obtained using the mixing length model with a reduced freestream length scale and correctly specified laminar and transitional regions. The prior knowledge required, however, suggests that this type of calculation may be of limited use as a design tool. The apparent lack of sensitivity of the results to the detail of transition (at least in 2D) though, does mean that an experienced designer may be able to specify transition well enough to obtain reasonable results.
- The laminar and turbulent regions need only be set close to the surfaces. The state of the flow away from them has little effect on the overall results unless the freestream length scale is set too high. In this case too much dissipation occurs leading to reduced secondary flows and increased losses.
- If a suitable freestream length scale is chosen reasonable results may be obtained using a fully turbulent mixing length model with the exception of the profile loss which is considerably overpredicted.
- High Reynolds number k–ϵ models do not produce significantly better results than can be achieved with a mixing length model but do so without the need to adjust inlet parameters.

- The low Reynolds number k–ϵ model failed to predict transition at all well. This may be improved with a better near wall grid but better transition modelling is also likely to be needed. If this can be achieved, low Reynolds number models will become a useful design tool.
- The prediction of the turbulence structure is poor for all calculations. Highly anisotropic and negative eddy viscosities within the blade passage (Biesinger [1993]) mean that models based on the Boussinesq concept will never succeed in this region. If accurate modelling of these turbulence quantities is required, at a minimum algebraic or full second order closure must be used.

Recommendations for future work

On the experimental side, there are a number of further pieces of experimental work that would be desirable to give a complete set of data and to clear up some minor points. The first is an extension of the slot 8 traverse in the spanwise direction to completely capture the secondary flow region. It was unfortunate that this was not done in the current work as it has made comparisons of the flow development more difficult than they should have been. Also at slot 8 it would be desirable to resolve the big difference in $\overline{uv}$ velocity correlation found between the present results and those of Cleak [1989]. Though some differences may be expected, the better agreement at earlier and later slots suggests that one set of results here are incorrect. The present results are believed to be correct because they are more consistent (Cleak [1989] found very rapid sign change in the passage vortex region that he had difficulty justifying), and agree better both with others (Zunino et al [1987]) and with the calculated results. However, the inconsistency should ideally be cleared up.

The pressure measurements used in this work (taken from Beisinger [1993]) were taken on a fairly coarse grid and do not approach the walls very closely. A repeat on the same grid and at all the slots as the hot–wire measurements would be helpfull. More useful, however, would be traverses with a minature three–hole pitot probe in the blade and endwall boundary layers. This would improve the area averaged results and provide data of use in the development and validation of transition models. Similarly, hot–wire measurements within the boundary layers would be desirable but would be difficult to achieve due to the need to rotate the probe about a suitable axis. Alternatively a technique such as laser doppler anemometry could be used though there may be difficulties with optical access to some parts of the cascade.

Further extensions to the project could include the measurement of heat transfer since this is of great importance in high pressure turbines. This would require heating of either the air, or more likely the blades and endwall but would allow validation of heat transfer predictions so add to the use of the data. More simply a tip gap could be introduced by shortening the blades and its effect on the secondary flows studied. This would be relatively easy to implement since the blades are cantilevered from the far side of the cascade so few modifications would have to be made. Tip leakage flows are, however, a popular research topic so care would have to be taken to ensure previous work is not simply repeated.

One possibility would be to carry out a computational investigation of the effect of shaping the blade tip, with the aim of reducing loss, and then to test the predictions experimentally. On a similar theme it would be interesting to design and then test an endwall profile that reduces secondary flows by modifying the near wall pressure gradient. The existing perspex section of the endwall could easilly be replaced a contoured section, or by a flexible surface whose profile could be varied, and measurements of the secondary flows could be compared with the present results. A computational design of something similar has been described by Rose [1994] though his intention was to produce a uniform static pressure in order to reduce disk leakage flows.

On the computational side, an improved mesh for low Reynolds number calculations would show whether the poor results obtained with this model were the fault of the grid or the model itself. If it seems to be the model there are a considerable number of other versions which may be tried. Sieger et al [1993], for example, found the Lam–Bremhorst [1981] model to be one of the best though whether any current model is is capable of predicting transition in such complex three–dimensional flows is questionable. There is certainly a need for further work in this area particularly as it appears to have a greater effect on the overall results than the turbulence modelling. Ultimately, however, higher order models will be needed if details of the turbulence, and quite possibly transition, are to be predicted correctly. Beyond this, the whole purpose of the experimental work was to provide data with which to design and validate turbulence and transition models so this should be encouraged.

Inserting (A.2) into (A.1) and rearranging gives:

$$U_{eff}^2 = A_{11}U_1^2 + A_{22}U_2^2 + A_{33}U_3^2 + A_{12}U_1U_2 + A_{13}U_1U_3 + A_{23}U_2U_3 \qquad (A.3)$$

Where:

$$\begin{aligned}
A_{11} &= \cos^2\alpha + k^2\sin^2\alpha \\
A_{22} &= \cos^2\theta(\sin^2\alpha + k^2\cos^2\alpha) + h^2\sin^2\theta \\
A_{33} &= \sin^2\theta(\sin^2\alpha + k^2\cos^2\alpha) + h^2\cos^2\theta \\
A_{12} &= (1-k^2)\sin 2\alpha\cos\theta \\
A_{13} &= (k^2-1)\sin 2\alpha\sin\theta \\
A_{23} &= \sin 2\theta(-\sin^2\alpha - k^2\cos^2\alpha + h^2) \qquad (A.4)
\end{aligned}$$

For a non–steady flow each component of velocity can be split up into a steady, $\overline{U}$, and fluctuating, u, component where $U = \overline{U} + u$. Inserting this into (A.3) and multiplying out gives:

$$\begin{aligned}
(\overline{U}_{eff} + u_{eff})^2 \; = \; & \left.\begin{array}{l} A_{11}\overline{U}_1^2 + A_{22}\overline{U}_2^2 + A_{33}\overline{U}_3^2 + \\ A_{12}\overline{U}_1\overline{U}_2 + A_{13}\overline{U}_1\overline{U}_3 + A_{23}\overline{U}_2\overline{U}_3 + \end{array}\right\}\overline{\mathrm{X}}^2 \\
& \left.\begin{array}{l} 2A_{11}\overline{U}_1u_1 + 2A_{22}\overline{U}_2u_2 + 2A_{33}\overline{U}_3u_3 + \\ A_{12}(\overline{U}_1u_2 + \overline{U}_2u_1) + A_{13}(\overline{U}_1u_3 + \overline{U}_3u_1) + \\ A_{23}(\overline{U}_2u_3 + \overline{U}_3u_2) + \end{array}\right\}\overline{\mathrm{Y}}\mathrm{y} \\
& \left.\begin{array}{l} A_{11}u_1^2 + A_{22}u_2^2 + A_{33}u_3^2 + \\ A_{12}u_1u_2 + A_{13}u_1u_3 + A_{23}u_2u_3 \end{array}\right\}\mathrm{z}^2
\end{aligned}$$

Or in shorthand form:

$$(\overline{U}_{eff} + u_{eff})^2 = \overline{\mathrm{X}}^2 + \overline{\mathrm{Y}}\mathrm{y} + \mathrm{z}^2 \qquad (A.5)$$

Taking square roots of both sides and expanding the R.H.S. using a power series gives:

$$\overline{U}_{eff} + u_{eff} = \overline{X}\left[1 + \frac{1}{2}\frac{(\overline{Y}y + z^2)}{\overline{X}^2} - \frac{1}{8}\left(\frac{\left(\overline{Y}y\right)^2}{\overline{X}^4} + \frac{2\overline{Y}yz^2}{\overline{X}^4} + \frac{z^4}{\overline{X}^4}\right) + \dots\right] \tag{A.6}$$

Neglecting terms with triple or higher order fluctuating velocity correlations (e.g. $u_1u_2u_3$ or $u_1^2u_2$) gives:

$$\overline{U}_{eff} + u_{eff} = \overline{X}\left[1 + \frac{1}{2\overline{X}^2}\left(\overline{Y}y + z^2\right) - \frac{1}{8\overline{X}^4}\left(\overline{Y}y\right)^2\right] \tag{A.7}$$

Time averaging (A.7):

$$\overline{U}_{eff} = \overline{X}\left[1 + \frac{\overline{z^2}}{2\overline{X}^2} - \frac{1}{8\overline{X}^4}\overline{\left(\overline{Y}y\right)^2}\right] \tag{A.8}$$

Squaring and again neglecting terms with triple or higher order fluctuating velocity correlations:

$$\overline{U}^2_{eff} = \overline{X}^2 + \overline{z^2} - \frac{1}{4\overline{X}^2}\overline{\left(\overline{Y}y\right)^2} \tag{A.9}$$

Time averaging (A.5):

$$\overline{U}^2_{eff} + \overline{u^2_{eff}} = \overline{X}^2 + \overline{z^2} \tag{A.10}$$

Subtracting (A.9) from (A.10):

$$\overline{u^2_{eff}} = \frac{1}{4\overline{X}^2}\overline{\left(\overline{Y}y\right)^2} \tag{A.11}$$

Multiplying out $\overline{\left(\mathrm{Yy}\right)^2}$ gives an expression with 45 terms. Rearranging this and factorizing yields:

$$\overline{u_{eff}^2} = \frac{1}{\mathrm{X}^2}\left(B_1^2\overline{u_1^2} + B_2^2\overline{u_2^2} + B_3^2\overline{u_3^2} + 2B_1B_2\overline{u_1u_2} + 2B_1B_3\overline{u_1u_3} + 2B_2B_3\overline{u_2u_3}\right) \tag{A.12}$$

where:

$$\begin{aligned} B_1 &= A_{11}\overline{U}_1 + \frac{1}{2}A_{12}\overline{U}_2 + \frac{1}{2}A_{13}\overline{U}_3 \\ B_2 &= \frac{1}{2}A_{12}\overline{U}_1 + A_{22}\overline{U}_2 + \frac{1}{2}A_{23}\overline{U}_3 \\ B_3 &= \frac{1}{2}A_{13}\overline{U}_1 + \frac{1}{2}A_{23}\overline{U}_2 + A_{33}\overline{U}_3 \end{aligned} \tag{A.13}$$

Equations A.11 & A.12 have been derived previously by Perdichizzi et al (1990). Taking several readings at a point, with different wire orientations (θ) makes A.8 & A.11 into two sets of simultaneous equations which may be solved for both the mean flow and Reynolds stresses.

A.2 Wire calibration

The hot–wires are calibrated or two reasons, the first is to find a relationship between E and U_{eff} and the second is to find relationships for k^2 & h^2 in the Jørgensen equation. To calibrate for the relationship between wire voltage and effective velocity is straightforward. The the wire is placed in a variable speed flow with the flow direction normal to the wire and the voltage is recorded at various velocities. In this condition the effective velocity is equal to the flow velocity so fitting a curve or spline to this data gives the relationship between E and U_{eff}.

Though this has the advantage over using the Kings law in that the accuracy of the method is limited only by experimental considerations, the relationship is only valid if the atmospheric temperature (and the temperature at which the wire is operated) remains constant between the calibration and subsequent experiments.

Small changes in temperature, however, can be corrected for by the equation:

$$E_c^2 = E_e^2 \left(\frac{T_s - T_c}{T_s - T_e} \right) \tag{A.14}$$

Where suffix 'c' refers to the calibration, suffix 'e' refers to the experiment and T_s is the wire temperature.

Calibrating for the wire constants, k^2 & h^2, is more difficult. These vary with both flow angle and magnitude so the calibration requires measurements to be made over all the velocities and angles that could be encountered during the experiment. If this includes the wire orientation where the flow is normal to the wire, this set of data can also be used to find the relationship between E and U_{eff} so this need not be done as a separate calibration. Unlike the effective velocity calibration, however, finding relationships for k^2 & h^2 requires some assumptions to be made.

Calibrations are carried out using a small, purpose built free–jet wind tunnel (*Figure A.2*). The tunnel is driven by a 5Hp variable speed motor (Allspeeds A20–M8) connected to a centrifugal fan (Watkins & Watson 'Discus' blower) with a filtered inlet. This blows air along a 305mm dia flexible tube to a short, parallel section containing a length of honeycomb to straighten the flow. The air is then accelerated through a 9:1 contraction to reduce turbulence levels and passes along a second short, straight section before exiting. The wire is located in the center of the resulting jet at approximately 1.5 diameters further downstream along with a pitot–static probe connected to a pressure transducer (CMR 200–032).

The traverse on which the wire is mounted was designed to take the probes used in the wind tunnel. It consists of a long arm mounted on a 43:1 gearbox which is driven by a 200 step/revolution stepper motor. This is used to vary the yaw angle, ϕ, (*Figure A.3*) of the probe relative to the flow and gives a step angle of 0.042°. Variation of the pitch angle, θ, is achieved using the same rotary stage as used in the wind tunnel. It and the probe are transferred between the two as a single unit which ensures that the probe always maintains the same alignment. Variation of these two angles and the tunnel speed, then allows a full calibration of the hot–wires to be carried out.

A typical calibration consists of 15 velocities, 17 yaw angles and 19 pitch angles and takes approximately 6 hours to complete. The probe is initially aligned with the flow by making use of its symmetrical response about certain angles (e.g. $\theta = 0°$ and $\phi = 45°$ for a slanted wire). Several readings are taken at either side of a nominal zero and a curve is fitted to the points to find the true maxima (or minima). This is done for both yaw and pitch and gives results that are repeatable to within ±2 steps. The angles are re–zeroed for each velocity since the flow direction changes slightly as the speed is changed.

In the calibration itself measurements are taken at intervals of approximately 3m/s and 7.5°–15°. At each point the mean wire voltage and flow velocity are found by alternately sampling the output of the hot–wire and pressure transducer (which was calibrated against a micro–manometer) at a rate of 10KHz for 1 second. The 99% confidence limit is also calculated for both the velocity and voltage measurements to ensure that there are no excessive fluctuations. If there are the measurement is repeated.

To extract the calibration data from these results is a three stage process. First the E vs. U_{eff} relationship is found from the measurements where the wire is normal to the flow. A spline is fitted to this data and is used to convert all the voltage readings to effective velocities. Whilst doing this, a correction is also made for the small fluctuations in velocity which occur between individual readings at the same nominal velocity. This spline data is also filed for later use. The second and third stages are to find relationships for k^2 & h^2, the 'constants' in the Jørgensen equation. These are often taken as fixed, single values but this is not the case.

The data from the calibration comprises of U, ϕ, θ (*Figure A.3*) and U_{eff}. From the first three, and the wire angle, α, the wire velocities, U_n, U_t & U_b can be calculated where:

$$\begin{aligned} U_n &= U(\sin\phi\cos\alpha + \cos\phi\sin\alpha\cos\theta) \\ U_t &= U(-\sin\phi\sin\alpha + \cos\phi\cos\alpha\cos\theta) \\ U_b &= U\cos\phi\sin\theta \end{aligned} \tag{A.15}$$

Inserting these into the Jørgensen equation (A.1) leaves two unknowns, k^2 and h^2, neither of which can be found without first knowing the other or eliminating it from the equation. Neither are known but each can be eliminated simply by arranging for either U_t or U_b to be zero. In practice it is easier to make $U_b = 0$, since this occurs when $\theta = 0°$ (and when $U = 0$ but this is a trivial solution), so k^2 is found first. Taking only the calibration data where $\theta = 0°$, then gives k^2 for all combinations of U and ϕ. If k^2 is also assumed to be independent of θ, fitting a bi–cubic spline to this data allows $k^2 = \text{fn}(U, \phi)$ to be evaluated anywhere within the calibration range.

Using this relationship for k^2, h^2 is then be calculated at each of the calibration points. This gives h^2 as a function of three variables (U, ϕ, θ) which makes interpolation difficult, though not impossible. However, h^2 is virtually independent of velocity, over the range of interest, so this is reduced to $h^2 = \text{fn}(\phi, \theta)$ by averaging over U. A bi–cubic spline surface is then, again fitted to allow interpolation between data points. The accuracy of these calibrations can then be checked by back substitution of the interpolated values into the Jørgensen equation and comparison with the measured U_{eff}. The results were found to be very good except at the edges of the calibration data and in regions where the wire was in the wake of one of its supports. In a properly set up experiment, however, these conditions would be avoided.

A.3 Transformation of stress coordinates

The normal, σ, and shear, τ, stresses based on a coordinate system defined by the suffixes 1, 2 & 3 (*Figure A.4*) may be rotated through an angle θ about the σ_1 direction by the following equations.

$$\begin{aligned}
\sigma_u &= \sigma_1 \\
\sigma_v &= \sigma_2 \cos^2\theta + \sigma_3 \sin^2\theta + \tau_{23} \sin 2\theta \\
\sigma_w &= \sigma_2 \sin^2\theta + \sigma_3 \cos^2\theta - \tau_{23} \sin 2\theta \\
\tau_{uv} &= \tau_{12} \cos\theta + \tau_{13} \sin\theta \\
\tau_{uw} &= -\tau_{12} \sin\theta + \tau_{13} \cos\theta \\
\tau_{vw} &= \frac{1}{2}(-\sigma_2 + \sigma_3) \sin 2\theta + \tau_{23} \cos 2\theta
\end{aligned} \qquad (A.16)$$

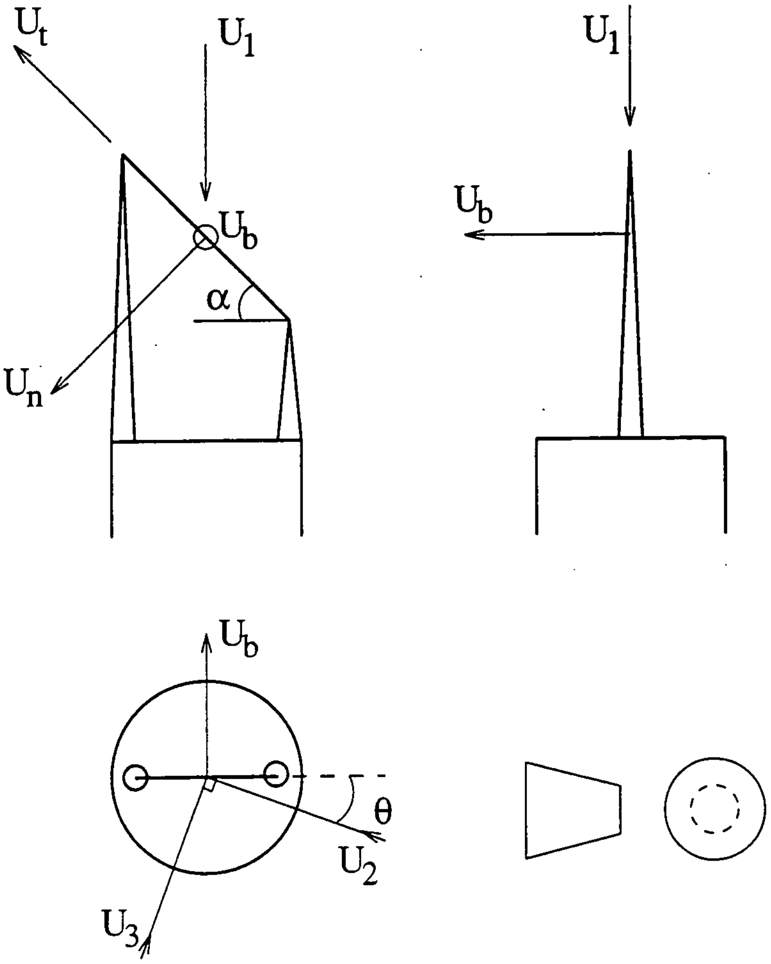

Figure A.1 — Hot–wire velocity components.

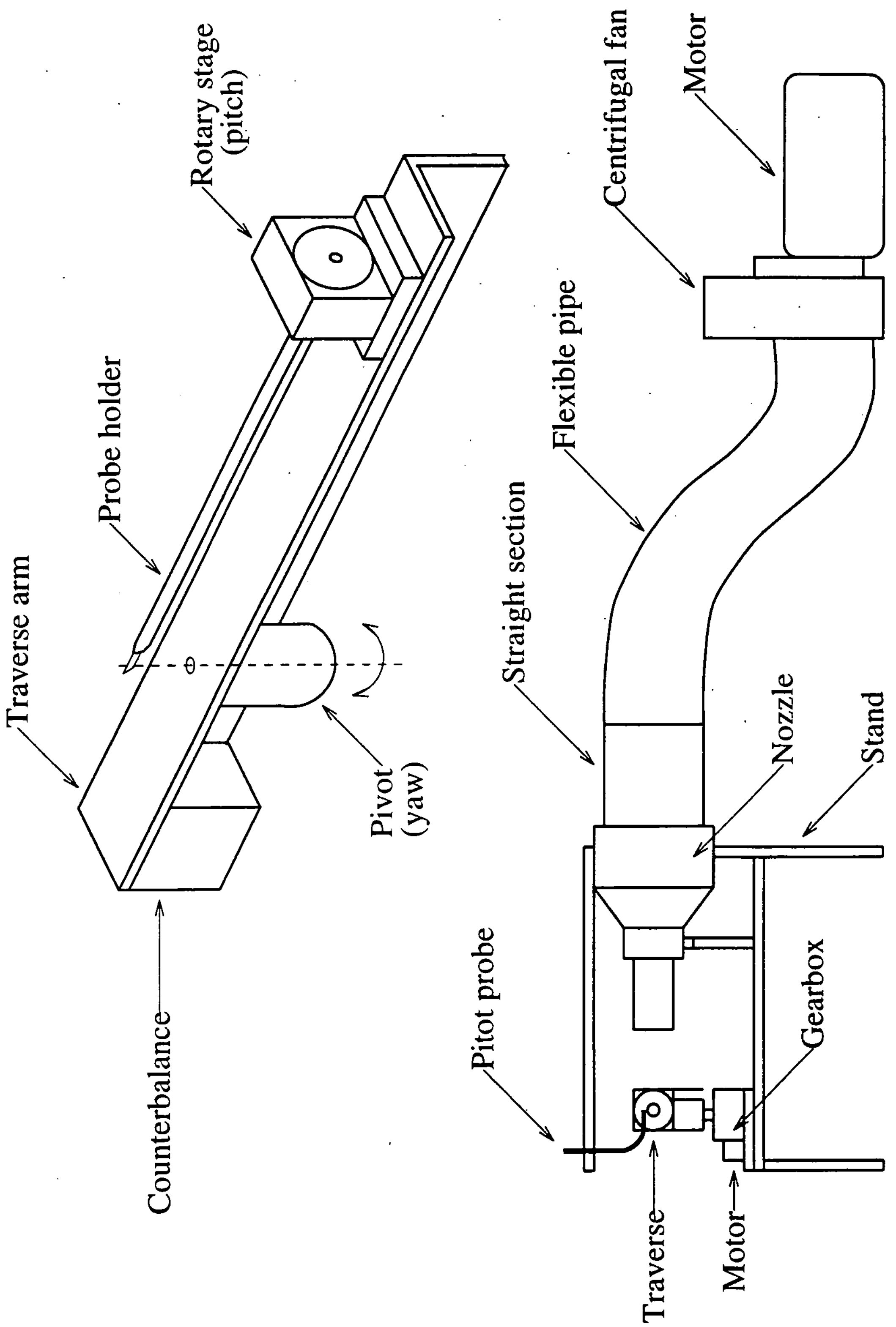

Figure A.2 — Diagram of the calibration rig.

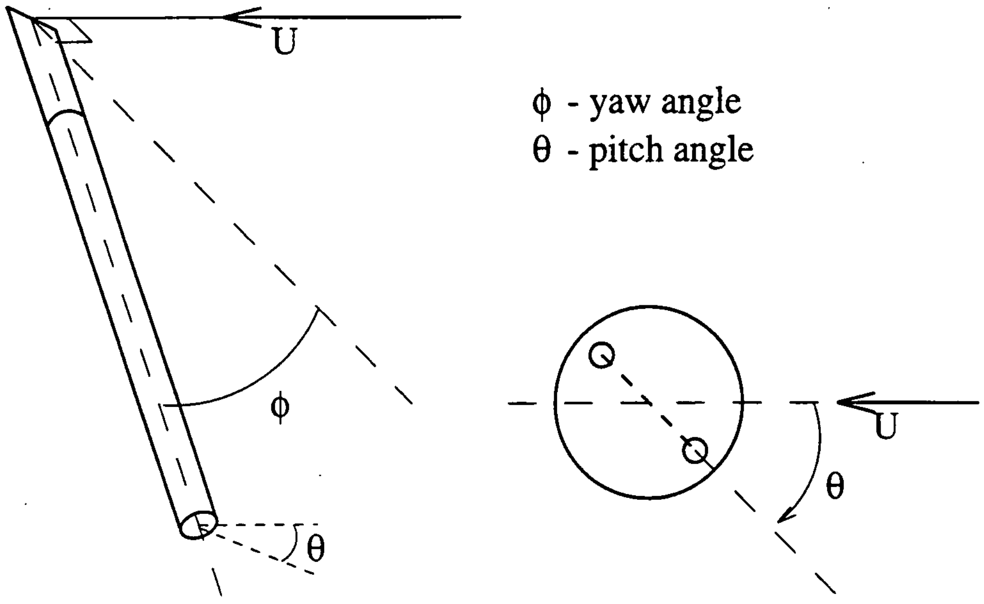

Figure A.3 — Definition of calibration flow angles.

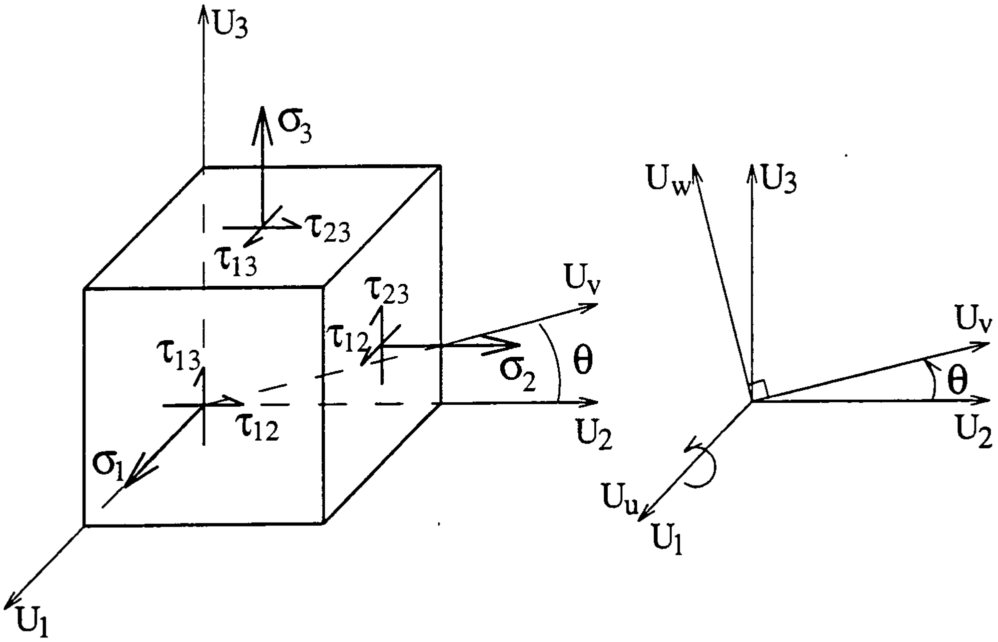

Figure A.4 — Stresses in 3–dimensions.

Appendix B

Data processing

B.1 Definitions

Turbulent k.e. coefficient, C_{tk}

$$C_{tk} = \frac{\left(\overline{u_1^2} + \overline{u_2^2} + \overline{u_3^2}\right)}{V_u^2} \qquad (B.1)$$

Normal, S_n, and shear, S_s, stresses

$$S_n = \frac{\sqrt{\overline{u_i^2}}}{V_u} \qquad S_s = \frac{\overline{u_i u_j}}{V_u^2} \qquad (B.2)$$

Total pressure coefficient, C_{p0}

$$C_{p0} = \frac{P_{0u} - P_0}{\frac{1}{2}\rho V_u^2} \qquad (B.3)$$

Static pressure coefficient, C_{ps}

$$C_{ps} = \frac{P_u - P}{\frac{1}{2}\rho V_u^2} \qquad (B.4)$$

Secondary kinetic energy coefficient, C_{sk}

$$C_{sk} = \frac{U_{ts}^2 + U_3^2}{V_u^2} \qquad (B.5)$$

where

$$U_{ts} = U_2 \cos\alpha_m - U_1 \sin\alpha_m \qquad (B.6)$$

and α_m is the midspan flow angle at that pitchwise position.

B.2 Pitch and area mass averages

Pitch averages are designated by a single bar, $\overline{\phi}$, and area averages by a double bar, $\overline{\overline{\phi}}$.

Total pressure loss coefficient

$$\overline{C_{p0}} = \frac{\int_0^s C_{p0} V_1 dy}{\int_0^s V_1 dy} \qquad \overline{\overline{C_{p0}}} = \frac{\int_0^h \int_0^s C_{p0} V_1 dy dz}{\int_0^h \int_0^s V_1 dy dz} \tag{B.7}$$

Yaw angle

$$\overline{\alpha} = \tan^{-1}\left[\frac{\int_0^s V_2 V_1 dy.s}{(\int_0^s V_1 dy)^2}\right] \qquad \overline{\overline{\alpha}} = \tan^{-1}\left[\frac{\int_0^h \int_0^s V_2 V_1 dy dz.s.h}{\left(\int_0^h \int_0^s V_1 dy dz\right)^2}\right] \tag{B.8}$$

Secondary kinetic energy coefficient

$$\overline{C_{sk}} = \frac{\int_0^s C_{sk} V_1 dy}{\int_0^s V_1 dy} \qquad \overline{\overline{C_{sk}}} = \frac{\int_0^h \int_0^s C_{sk} V_1 dy dz}{\int_0^h \int_0^s V_1 dy dz} \tag{B.9}$$

Turbulent kinetic energy coefficient

$$\overline{C_{tk}} = \frac{\int_0^s C_{tk} V_1 dy}{\int_0^s V_1 dy} \qquad \overline{\overline{C_{tk}}} = \frac{\int_0^h \int_0^s C_{tk} V_1 dy dz}{\int_0^h \int_0^s V_1 dy dz} \tag{B.10}$$

B.3 Mixed out values

By using the continuity and momentum equations, the area averages on any plane outside of the blade row may be extrapolated to a plane located at infinity. Here the flow will have 'mixed out' to give a uniform velocity and pressure field so a 'mixed out' total pressure loss coefficient, $C_{p0\infty}$, and yaw angle, α_∞, may be calculated.

Assuming $V_{3\infty} = 0$.

by continuity

$$\int_0^h \int_0^s \rho V_1 dydz = \rho V_{1\infty} sh \qquad \text{therefore} \qquad V_{1\infty} = \frac{1}{sh} \int_0^h \int_0^s V_1 dydz \tag{B.11}$$

equating tangential momentum

$$\int_0^h \int_0^s \rho V_1 V_2 dydz = \rho V_{1\infty} V_{2\infty} sh \qquad \text{therefore} \qquad V_{2\infty} = \frac{\int_0^h \int_0^s V_1 V_2 dydz}{\int_0^h \int_0^s V_1 dydz} \tag{B.12}$$

defining

$$\alpha_\infty = \tan^{-1} \left[\frac{V_{2\infty}}{V_{1\infty}} \right] \qquad \text{gives} \qquad \alpha_\infty = \tan^{-1} \left[\frac{\int_0^h \int_0^s V_1 V_2 dydz.s.h}{\left(\int_0^h \int_0^s V_1 dydz \right)^2} \right] \tag{B.13}$$

equating axial momentum

$$\int_0^h \int_0^s P dydz - P_\infty sh = \rho V_{1\infty}^2 sh - \int_0^h \int_0^s \rho V_1^2 dydz \tag{B.14}$$

also

$$\int_0^h \int_0^s C_{ps} dydz = \frac{1}{\frac{1}{2}\rho V_u^2} \int_0^h \int_0^s (P_u - P) dydz \tag{B.15}$$

and since P_u is a constant

$$\frac{1}{2}\rho V_u^2 \int_0^h \int_0^s C_{ps} dydz = P_u sh - \int_0^h \int_0^s P dydz \tag{B.16}$$

combining (B.14) & (B.16)

$$P_u sh - P_\infty sh = \rho V_{1\infty}^2 sh + \frac{1}{2}\rho V_u^2 \int_0^h \int_0^s C_{ps} dydz - \rho \int_0^h \int_0^s V_1^2 dydz \tag{B.17}$$

$$P_u - P_\infty = \rho V_{1\infty}^2 + \frac{\frac{1}{2}\rho V_u^2}{sh} \int_0^h \int_0^s C_{ps} dy dz - \frac{\rho}{sh} \int_0^h \int_0^s V_1^2 dy dz \qquad (B.18)$$

Applying Bernoulli and defining the mixed–out total pressure loss, $C_{p0\infty}$

$$C_{p0\infty} = \frac{P_{0u} - P_{0\infty}}{\frac{1}{2}\rho V_u^2} \qquad (B.19)$$

gives

$$C_{p0\infty} = 1 + \frac{1}{V_u^2} \left[V_{1\infty}^2 - V_{2\infty}^2 + \frac{1}{sh} \left(V_u^2 \int_0^h \int_0^s C_{ps} dy dz - 2 \int_0^h \int_0^s V_1^2 dy dz \right) \right] \qquad (B.20)$$

Bibliography

Ainley, D.G. and Mathieson, C.G.R., 1951.
A method of performance estimation for axial flow turbines. ARCR & N 2974.

Abu–Ghannam, B.J. and Shaw, R., 1980.
Natural transition of boundary layers – the effects of turbulence, pressure gradient and flow history. J. of Mech. Eng. Sci., Vol. 22, pp. 213–228.

Adrian, R.J., 1986.
Multi–point optical measurements of simultaneous vectors in unsteady flow–a review. Int. J. of heat and fluid flow, Vol. 7, No. 2, pp. 127–145.

Adrian, R.J., 1991.
Particle imaging techniques for experimental fluid mechanics. Annual review of fluid mechanics, Vol. 23, pp. 261–304.

Anderson, J.D., 1986.
Introduction to computational fluid dynamics. VKI lecture series.

Baldwin, B. and Lomax, H., 1978.
Thin layer approximation and algebraic model for separated turbulent flows. AIAA Paper 78–257.

Balint, J.L., Arault, M. and Schon, J.P., 1983.
Quantitative investigation of the velocity and concentration fields of turbulent flows combining visualisation and image processing. Flow visualisation III, Proc. 3rd international symposium on flow visualisation, ed. W.J. Yang, Hemisphere. pp. 254–258

Belik, L., 1975.
Secondary losses in a turbine blade cascade with low aspect ratio and large deflection. Proc. 6th Conf. on steam turbines of large power output, Plzen, Czechslovaia.

Biesinger, T.E., 1993.
Secondary flow reduction techniques in linear turbine cascades. PhD thesis, Durham University.

Boyle, M.T., Simonds, M. and Poon, K., 1989.
A comparison of secondary flow in a vane cascade and a curved duct. Trans. ASME, J. Turbomachinery, Vol, 111, pp. 530–536.

Bradshaw, P, Cebeci, T. and Whitelaw, J.H., 1981.
Engineering calculation methods for turbulent flow. Academic press, London.

Browne, L.W.B., Antonia, R.A. and Chua, L.P., 1989.
Calibration of X–probes for turbulent flow measurements. Experiments in Fluids 7, pp 201–208.

Came, P.M. and Marsh, H., 1974.
Secondary flow in cascades: Two simple derivations for the components of vorticity. J. Mech. Eng. Sci., Vol. 16, No. 6, pp. 391–401.

Carey, C., Scanlon, T.J. and Fraser, S.M., 1992.
The reduction of false diffusion in the simulation of vortex shedding. J. I.Mech.E., Vol. C6.

Chen, EW.L., Lien, F.S. and Leschziner, M.A., 1995.
Computational modelling of cascade–blade flow with linear and non–linear low–Re eddy–viscosity models. AGARD PEP Symposium, Derby, paper 3.

Chima, R.V., 1985
Inviscid and viscous flows in cascades with an explicit multiple–grid algorithm. AIAA Journal., Vol. 23, pp. 1556–1563.

Chorin, A.J., 1967.
A numerical method for solving incompressible viscous flow problems. J.Comp. Physics., Vol. 2, pp. 12–26.

Cleak, J.G.E., 1989.
Validation of viscous, three–dimensional flow calculations in an axial turbine cascade. PhD thesis, Durham University.

Cleak, J.G.E., Gregory–Smith, D.G. and Birch, N.T., 1991.
Experimental verification of a 3D turbulent flow calculation in an axial turbine cascade. AGARD PEP Symposium on Computational Fluid Dynamics in Propulsion, AGARD–CP–510, Paper No. 8.

Coupland, J., 1992.
Rolls–Royce PLC, Private communication.

Coupland, J. and Stow, P., 1993.
Turbulence modelling for turbomachinery flows. 2nd international symposium on engineering turbulence modelling and measurement, Florence.

Crowder, J.P., 1982.
Fluorescent minitufts for nonintrusive surface flow visualisation. Flow visualisation II, ed. W. Merzkirch, Hemisphere, pp. 663–667.

Dawes, W.N., 1990.
A comparison of zero and one equation turbulence modelling for turbomachinery simulations. ASME 90–GT–303.

Dawes, W.N., 1991.
The simulation of three–dimensional viscous flow in turbomachinery geometries using a solution–adaptive unstructured mesh methodology. ASME 91–GT–124.

Denton, J.D., 1975.
A time marching method for two– and three–dimensional blade–to–blade flow. ARC R&M No. 3775.

Denton, J.D., 1982.
An improved time marching method for turbomachinery flow calculation. ASME 82–GT–239.

Denton, J.D., 1993.
Loss mechanisms in turbomachines. The 1993 IGTI scholar lecture., J. Turbomachinery, Vol. 115, pp. 621–656.

Dominy, R.G., 1990.
A simple, non–intrusive technique for flow tracking. 10th symposium on measuring techniques for transonic and supersonic flows in cascades and turbomachines, V.K.I.

Dossena, V., Perdichizzi, A., Ubaldi, M. and Zunino, P., 1993.
Turbulence measurements downstream of a turbine cascade at different incidence angles and pitch–chord ratios. ASME Paper No. 93–GT–52.

Drain, L.E., 1980.
The laser doppler technique. Wiley.

Dunham, J., 1970.
A review of cascade data on secondary losses in turbines. J. Mech. Eng. Sci., Vol. 12, No. 1, pp. 48–59.

Dunham, J., 1995.
Aerodynamic losses in turbomachines. Keynote address, 85th AGARD–PEP symposium, Derby.

Elazar, Y. and Shreeve, R.P., 1989.
Viscous flow in a controlled diffusion compressor cascade with increasing incidence. ASME 91–GT–148.

Falco, R.E. and Gendrich, C.P., 1990.
The turbulent burst detection algorithm of Z. Zaric. Near–wall turbulence: 1988 Zoltan Zaric memorial conference., S.J. Kline and N.H. Afgan (eds.), Hemisphere, pp 911–931.

Gill, P.E. and Miller, G.F., 1971.
An algorithm for the integration of unequally spaced data. The computer journal, Vol. 15, No. 1, pp. 80–83.

Glynn, D.R. and Marsh, H., 1980.
Secondary flow in annular cascades. Int. J. Heat and Fluid Flow, Vol. 2, No. 1, pp. 29–33.

Graves, C.P., 1985.
Secondary flows and losses in gas turbines. PhD thesis, Durham University.

Gregory–Smith, D.G., 1995
Calculations of the secondary flow in a turbine cascade. Submitted to; An international symposium on CFD and aero–propulsion, ASME winter meeting, San Fransisco.

Gregory–Smith, D.G. and Cleak, J.G.E., 1990.
Secondary flow measurements in a turbine cascade with high inlet turbulence. ASME Paper No. 90–GT–20.

Gregory–Smith, D.G. and Graves, C.P., 1983.
Secondary flows and losses in a turbine cascade. AGARD CP–351, 'Viscous effects in turbomachines', Paper No. 17.

Gregory–Smith, D.G., Graves, C.P. and Walsh, J.A., 1988a.
Growth of secondary losses and vorticity in an axial turbine cascade. ASME J. of Turbomachinery, Vol. 110 pp1–8.

Gregory–Smith, D.G. and Okan, M.B., 1991.
A simple method for the calculation of secondary flows in annular cascades. I.Mech.E Conference on turbomachinery – Latest developments in a changing scene, Paper No. C423/008.

Gregory–Smith, Walsh, J.A., D.G., Graves, C.P. and Fulton, K.P., 1988b.
Turbulence measurements and secondary flows in a turbine rotor cascade. ASME J. of Turbomachinery, Vol. 110 pp479–485.

Gregory–Smith, D.G. and Marsh, H., 1971.
The manufacture of glass fibre rotor blades with pressure tappings. Aero. J., 75, p73.

Halstead D.E., Okiishi, T.H. and Wisler, D.C., 1990.
Boundary–layer transition and separation on a turbine blade in plane cascade. AIAA/SAE/ASME/ASEE 26th Joint Propulsion Conference, Orlando, Fl.

Hah, C., 1984.
A Navier–Stokes analysis of three–dimensional turbulent flows inside turbine blade rows at design and off–design conditions. ASME J. Eng. for gas turbines and power, Vol. 106 pp. 421–429.

Harrison, S., 1989.
Secondary loss generation in a linear cascade of high–turning turbine blades. ASME Paper No. 89–GT–47.

Hawthorn, W.R., 1955.
Rotational flow through cascades: Part I. The components of vorticity. Quart. J. Mech. and applied math., Vol. 8, Pt. 3, pp.266–279.

Hawthorn, W.R. and Armstrong, W.D., 1955.
Rotational flow through cascades: Part II. The circulation about the cascade. Quart. J. Mech. and applied math., Vol. 8, Pt. 3, pp.280–292.

Hirsch, C., 1990.
Numerical computation of internal and external flows. Vols. 1 & 2, Wiley.

Hirsch, C. and Warzee, G., 1979.
An integrated quasi–3D finite element calculation program for turbomachinery flows. J. Engineering for Power, Vol. 101, pp. 141–148.

Horlock, J.H. and Lakshminarayana, B., 1973.
Secondary flows: Theory, experiment, and application in turbomachinery aerodynamics. Annual review of fluid mechanics., vol. 5, pp. 247–280.

Jones, W.P. and Launder, B.E., 1972.
The prediction of laminarisation with a two–equation model of turbulence. Int. J. Heat and mass transfer, Vol. 15, pp. 301–314.

Jørgensen, F.E., 1971.
Directional sensitivity of wire and fibre film probes : An experimental study. DISA Information, No. 11.

Kato, M, and Launder, B.E., 1993.
The modelling of turbulent flow around stationary and vibrating square cylinders. Proc. 9th Symp. turbulent shear flows., Kyoto, pp. 10–14.

Kawai, T, Adachii, T. and Akashita, K. 1985.
Structure and decay of secondary flow in the downstream of a cascade. Bulletin of JSME, Vol. 28, No. 242, Paper 10.

Kawai, T., Shinoki, S. and Adachi, T., 1989.
Secondary flow control and loss reduction in a turbine cascade using endwall fences. JSME International Journal, Series II, Vol 32, No. 3, pp 375–387.

Kobayashi, T., Ishihara, T. and Sasaki, N., 1983.
Automatic analysis of photographs of trace particles by microcomputer system. Flow visualisation III, Proc. 3rd international symposium on flow visualisation, ed. W.J. Yang, Hemisphere. pp. 231–235

Kreyszig, E., 1983.
Advanced engineering mathematics. John Wiley & Sons.

Lakshminarayana, B., 1986.
Turbulence modelling for complex shear flows. AIAA Journal, Vol. 24, No. 12, pp. 1900–1917.

Lakshminarayana, B., 1991.
An assessment of computational fluid dynamic techniques in the analysis and design of turbomachinery – The 1990 Freeman scholar lecture. ASME J. of Fluids Engineering, Vol. 113, pp. 315–352.

Lam, C.K.G. and Bremhorst, K., 1981.
A modified form of the k–ϵ model for predicting wall turbulence. ASME J. Fluids Eng. Vol. 103, pp. 456–460.

Langston, L.S., Nice, M.L. and Hooper, R.M., 1977.
Three–dimensional flow within a turbine cascade passage. ASME J. Eng for Power, Vol. 99, No. 1, pp 21–28.

Laskaris, T.E., 1975.
Finite–element analysis of compressible and incompressible viscous flow and heat transfer problems. The physics of fluids., Vol. 18, pp. 1639–1648.

Launder, B.E. and Sharma, B.I., 1974.
Application of the energy dissipation model of turbulence to the calculation of flow near a spinning disk. Letters in heat and mass transfer, Vol. 1, pp. 131–138.

Lekakis, I.C., Adrian, R.J. and Jones, B.G., 1989.
Measurement of velocity vectors with orthogonal and non–orthogonal triple–sensor probes. Experiments in Fluids 7, pp 228–240.

Lien, F.S. and Leschziner, M.A., 1995.
Computational modelling of a transitional 3D turbine–cascade flow using a modified low–Re k–ϵ model and a multi–block scheme. ASME COGEN '95, 23–25 August, Vienna.

Marchal, P. and Sieverding, C.H., 1977.
Secondary flows within turbomachinery blading. Secondary Flows in Turbomachines, AGARD CP 214.

Marsh, H., 1976.
Secondary flow in cascades – The effect of compressibility. ARC R&M No. 3778.

Mayle, R.E., 1991.
The role of laminar–turbulent transition in gas turbine engines. ASME Paper No. 91–GT–261.

Mee, D.J., Baines, N.C. and Oldfield, M.L.G., 1990.
Detailed boundary layer measurements on a transonic turbine cascade. ASME Paper No. 90–GT–263.

Mee, D.J., Baines, N.C., Oldfield, M.L.G. and Dickens, T.E., 1992.
An examination of the contributions to loss on a transonic turbine blade. ASME J. of Turbomachinery, Vol. 114, pp155–162.

Mee, D.J., Walton, T.W., Harrison, S.B. and Jones, T.V., 1991.
A comparison of liquid crystal techniques for transition detection. AIAA 91–0062.

Moore, J., 1985.
Performance evaluation of flow in turbomachinery blade rows. AGARD–LS–140, 3D computation techniques applied to internal flows in propulsion systems.

Moore, J. and Moore, J.G., 1985.
Performance evaluation of linear turbine cascades using three–dimensional viscous flow calculations. Trans. ASME, J. Eng. Gas turbines and power, Vol. 107, pp. 969–975.

Moore, J., Shaffer, D.M. and Moore, J.G., 1987.
Reynolds stress and dissipation mechanisms downstream of a turbine cascade. ASME J. of Turbomachinery, Vol. 109. pp258–267.

Moore, J. and Smith, B.L., 1984.
Flow in a turbine cascade. Part 2: Measurement of flow trajectories by ethylene detection. ASME J. Eng. for gas turbines and power, Vol. 106, pp409–413.

Moore, J.G., 1985a.
An elliptic calculation procedure for 3D viscous flow. AGARD–LS–140, 3D computational techniques applied to internal flows in propulsion systems.

Moore, J.G., 1985b.
Calculation of 3D flow without numerical mixing. AGARD–LS–140, 3D computational techniques applied to internal flows in propulsion systems.

Mueller, T.J., 1983.
Recent developments in smoke flow visualisation. Flow visualisation III, Proc. 3rd international symposium on flow visualisation, ed. W.J. Yang, Hemisphere. pp. 30–40

Okan, M.B. and Gregory–Smith, D.G., 1992.
A simple method for estimating secondary losses in turbines at the preliminary design stage. ASME 92–GT–294.

Pankhurst, R.C. and Holder, D.W., 1968.
Wind tunnel techniques. Pitman.

Patel, V.C., Rodi, W. and Scheuerer, G., 1984.
Turbulence models for near–wall and low Reynolds number flows: A review. AIAA Journal, Vol. 23, No. 9, pp. 1308–1319.

Perdichizzi, A., Ubaldi, M. and Zunino, P., 1990.
A hot–wire measuring technique for mean velocity and Reynolds stress components in compressible flow. Measurement techniques for transonic and supersonic flows in cascades and turbines, Proceedings of 10th symposium, VKI.

Perdichizzi, A., Ubaldi, M. and Zunino, P., 1992.
Reynolds stress distribution downstream of a turbine cascade. Experimental thermal and fluid science; 5, pp338–350.

Rai, M. and Moin, P., 1991.
Direct numerical simulation of transition and turbulence in a spatially evolving boundary layer. AIAA 91–1607.

Roach P.E., 1987.
The generation of nearly isotropic turbulence by means of grids. Int. J. Heat and Fluid Flow, 8, pp 88–91.

Roach, P.E. and Brierlel, D.H., 1992.
The influence of a turbulent freestream on zero pressure gradient transitional boundary layer development. Numerical simulational of unsteady flows and transition to turbulence, ed. Pironneau et al, Cambridge university press, pp. 319–347.

Rose, M.G., 1994.
Non–axisymmetric endwall profiling in the HP NGV's of an axial flow gas turbine. ASME 94–GT–249.

Ruck, G., 1988.
Turbulence measurements with a high response pressure probe. Proc. 9th symposium on measuring techniques for transonic and supersonic flows in cascades and turbomachines, Oxford, Paper 7.

Rodi, W., 1975.
A new method of analysing hot–wire signals in highly turbulent flow, and its evaluation in a round jet. DISA Information, No. 17.

Savill, A.M., 1993.

A synthesis of T test case predictions. Numerical simulation of unsteady flows and transition to turbulence, eds. Pironneau, Rodi, Rhyming, Savill and Truong, Cambridge.

Savill, A.M., 1994.

Transition modelling for turbomachinery II, an updated summary of ERFCOTAC transition SIG progress. 2nd workshop of the BRITE–EURAM AERO–CT92–0052 project, VUB, Brussels.

Schlicting, H., 1978.

Boundary layer theory, 7th ed. McGraw–Hill, New–York.

Schmidt, R.C. and Patankar, S.V., 1988.

Two–equation low–Reynolds number turbulence modelling of transitional boundary layer flows characteristic of gas turbine blades. NASA CR–4145.

Schodl, R., 1980.

A laser–two–focus (L2F) velicometer for automatic flow measurements in the rotating components of turbomachines. ASME J. Fluids Engineering, Vol 102, pp. 412–419.

Sharma, O.P. and Butler, T.L., 1986.

Predictions of endwall losses and secondary flows in axial flow turbine cascades. ASME 86–GT–228.

Sieger, K., Schulz, A., Crawford, M.E. and Wittig, S., 1992.

Comparitive study of low–Reynolds number k–ϵ turbulence models for predicting heat transfer along turbine blades with transition. Int. Symposium on heat transfer in turbomachinery, Athens.

Sieger, K., Schulz, A., Crawford, M.E. and Wittig, S., 1993.

An evaluation of low–Reynolds number k–ϵ turbulence models for predicting transition under the influence of free–stream turbulence and pressure gradient. 2nd international symposium on engineering turbulence modelling and measurement, Florence.

Sieverding, C.H., 1985.
Recent progress in the understanding of basic aspects of secondary flows in turbine blade passages. Trans. ASME, J. Eng. Gas Turbines and Power, 107, pp 248–252.

Sieverding, C.H. and Van den Bosch, P., 1983.
The use of coloured smoke to visualise secondary flows in a turbine–blade cascade. Journal of Fluid Mechanics, Vol. 134, pp. 85–89.

So, R.M.C., Lai, Y.G. and Zhang, H.S., 1991.
Second–order near–wall turbulence closures: A review. AIAA Journal, Vol. 29, No. 11, pp. 1819–1835.

Spalart, P.R., 1988.
Direct simulation of a turbulent boundary layer up to $R_\theta = 1410$. J. of fluid mechanics, Vol. 187, pp. 61–98.

Speziale, C.G., 1991.
Analytical methods for the development of Reynolds–stress closures in turbulence. Annual review in fluid mechanics, Vol. 23, pp. 107–157.

Squire, H.B. and Winter, K.G., 1951.
The secondary flow in a cascade of aerofoils in a non–uniform stream. J. Aero. Sci., Vol. 18, pp. 271.

Stark, U and Bross, S., 1995.
Endwall boundary layer separations and loss mechanisms in two compressor cascades of different stagger angles. 85th NATO AGARD–PEP Symposium, Derby.

Stinebring, D.R., 1983.
Development of the liquid crystal/skin friction measurement device. Flow visualisation III, Proc. 3rd international symposium on flow visualisation, ed. W.J. Yang, Hemisphere. pp. 49–54

Stow, P., 1985.
Turbomachinery blade design using advance calculation methods. NATO ASI series E: Applied sciences – No. 97A, Thermodynamics and fluid mechanics of turbomachinery, pp. 923.

Tennekes, H. and Lumley, J.L., 1978.

A first course in turbulence. MIT press, Cambridge, Massachusetts.

Treaster, A.L. and Yocum, A.M., 1979.

The calibration and application of five–hole probes. ISA Transactions, Vol 18, No. 3, pp. 23–34.

Turner, J.R., 1957.

An investigation of the end–wall boundary layer of a turbine–nozzle cascade. Trans. ASME, 79, PP 1081

Van Dyke, M., 1982.

An album of fluid motion. Parabolic press, California.

Véret, C., 1983.

Flow visualisation by light sheet. Flow visualisation III, Proc. 3rd international symposium on flow visualisation, ed. W.J. Yang, Hemisphere. pp. 106–112

Walker, G.J., 1992.

The role of laminar–turbulent transition in gas turbine engines – a discussion. ASME Paper No. 92–GT–301.

Walker, G.J. and Solomon, W.J., 1992.

Turbulent intermittency measurement on an axial compressor blade. 11th Australian fluid mechanics conference, University of Tasmania, Hobart, Australia.

Walsh, J.G.C., 1987.

Secondary flows and inlet skew in axial flow turbine cascades. PhD thesis, Durham University.

Walsh, J.A. and Gregory–Smith, D.G., 1987.

The effect of inlet skew on the secondary flows and losses in a turbine cascade. Proceedings of the I. Mech E. International Conference 'Turbomachinery – Efficiency Prediction and Improvement', Paper No. C275/87.

Wang, Q., Zhu, G. and Wu, C.H., 1985.

Quasi–three–dimensional and full three–dimensional rotational flow calculations in turbomachines. J. Engineering for Power, Vol. 107, pp. 277–285.

Yang, Z. and Voke, P.R., 1993.
Large eddy simulation studies of bypass transition. 2nd International symposium on engineering turbulence modelling and measurements, Florence.

Yang, Z. and Voke, P.R. and Savill, A.M., 1994.
Mechanisms and models of boundary layer receptivity deduced from large–eddy simulation of bypass transition. 1st ERCOFTAC workshop on LES, Guildford.

Yavuzkurt, S., 1984.
A guide to uncertainty analysis of hot–wire data. Trans. ASME, J. Fluids Eng., 106, p 181.

Zunino, P., Ubaldi, M. and Satta, A., 1987.
Measurements of secondary flows and turbulence in a turbine cascade passage. ASME Paper No. 87–GT–132.